

**DEFECTS IN LIQUID CRYSTAL POLYMERS:  
THEIR ORIGINS AND BEHAVIOR IN MAGNETIC  
AND FLOW FIELDS**

by

Janelle Gunther

Submitted to the Department of Materials Science and  
Engineering

Program in Polymer Science and Technology

in partial fulfillment of the requirements for the degree of  
Doctor of Philosophy

at the

MASSACHUSETTS INSTITUTE OF TECHNOLOGY

June 1997

© Massachusetts Institute of Technology, 1997. All Rights Reserved.

Author .....

.....  
Janelle Gunther  
May 2, 1997

Certified by ...

.....  
Edwin L. Thomas  
Morris Cohen Professor of Materials Science and Engineering  
Thesis Supervisor

Accepted by .....

.....  
Linn W. Hobbs  
John F. Elliott Professor of Materials  
Chairman, Departmental Committee on Graduate Students

MASSACHUSETTS INSTITUTE  
OF TECHNOLOGY

- SCIENCE

JUN 16 1997

# DEFECTS IN LIQUID CRYSTAL POLYMERS: THEIR ORIGINS AND BEHAVIOR IN MAGNETIC AND FLOW FIELDS

by

Janelle Gunther

Submitted to the Department of Materials Science and Engineering  
Program in Polymer Science and Technology

on May 2, 1997,

in partial fulfillment of the requirements for the degree of  
Doctor of Philosophy

## Abstract

Pattern formation and evolution in liquid crystal polymers is studied in both static situation as well in applied magnetic and flow fields. Observations of nucleation and growth of nematic domains in an isotropic matrix under static conditions were used to establish the origins of the most common types of point defects. The patterns describing the director field distribution were revealed using a solidification induced banding method on quenched samples. At a low percent conversion of isotropic to nematic, the defect density is dominated by domain density and by anchoring conditions between the nematic domains and the isotropic matrix. At higher percent conversions, the defect density is controlled by domain-domain interaction events. The defect density rises as the domains nucleate and impinge but decreases after the generation of defects of negative strengths and an annihilation process begins. Larger domains created in the coalescence process can then grow and impinge and continue defect generation via domain interaction. The absence of negative strength defects during the preimpingement phase indicates these defects arise solely due to the domain-domain coalescence during the growth process.

The subsequent effects of both magnetic fields and flow fields on defect structure are also examined. With respect to the former, a solution of the director orientation distribution function is presented for Néel inversion walls created in a liquid crystal by application of a magnetic field. The theoretical model is used to simulate director trajectories across walls as a function of both the elastic anisotropy and the orientation of the wall with respect to the applied field. The gradual transition of the defect structures from Néel bend walls to Néel splay walls as the angle between the wall and the magnetic field is varied is also presented. Experimental micrographs obtained via atomic force microscopy on a thermotropic liquid crystalline polymer are used to test and evaluate the theoretical model. Visualization of director textures using the lamellar decoration technique shows the theoretical and experimental results to be in good agreement. The results were used to determine that the sample had an elastic anisotropy of 0.5, implying that  $k_{11} = 3k_{33}$ .

The effects of flow on the disclination textures were studied with an optical shearing cell. Flow visualization experiments were used to study curvature driven motion in disclination loops created during flow. Theories of differential geometry were used to predict the way the line curvature should evolve over time. Theoretically the relationship between velocity and local curvature is linear. Experimentally, deviations from the theory sometimes occurred due to forces of attraction between nearby disclinations. Even though disclination evolution in both small molecular and polymer liquid crystals obeyed similar physical laws, several significant differences were observed. Disclinations in the polymer systems generally displayed initially highly contorted contours. In the small molecule liquid crystals however, the loop contours consistently displayed very simple shapes. In the polymer system, the complex line shape reflects the many prior loop-loop coalescence events due to the greater density of loops than in the low molar mass liquid crystal. Moreover, the reduction of regions of high loop curvature is inherently slower in the polymer liquid crystal due to the higher viscosity of the medium. In addition, the motion of the disclination contour may also be affected by a possible reduction in the mobility of disclinations due to the presence of lower molecular weight components at the defect core which themselves must diffuse along with the line defect.

Thesis Supervisor: Edwin L. Thomas

Title: Morris Cohen Professor of Materials Science and Engineering

### **Acknowledgments:**

It is hard to believe that my 8+ years at MIT are coming to an end! Before departing there are many people I would like to thank. First I would like to express my appreciation to my advisor Professor Edwin Thomas, for his enthusiasm and support over the years. His excitement for scientific research made an indelible impression on me when I came to him as a sophomore in September of 1989 to inquire about undergraduate research opportunities in his group. Since that time he has taken great care in my professional development, something that has added significantly to my positive experience at MIT. As I reflect on the last 8 years I have worked for him, I am beginning to understand the advice given to me by one of his former students. One person in particular suggested that if I wanted to start research as a undergraduate I should “go work for Ned Thomas”. That was it. No “ifs”, “ands” or “buts”, just “do it”. When I look back now, if I had to do it over again I wouldn’t have done anything differently. The lessons I have learned from Ned about academics, research, and group management are invaluable and will serve a foundation for some day in the future when I start my own research group.

I am also very grateful to Professor Michael Rubner for his support, especially of my desires to become involved with teaching. The first time we worked together was in the Fall of 1992 when I was a grader for his course in Polymer Chemistry. He gave me his full support when I expressed an interest in also running review sessions and holding office hours in addition to my regular duties. I was honored when he asked me to become a full-time graduate teaching assistant for him in the fall of 1995. The marvelous example he set in the classroom is something to which I aspire. His continued advice over the years is something that I have appreciated a great deal.

There are many other people that have been instrumental in my career at MIT. I am very grateful to Professor Robert Rose for his guidance and support over the years. He has been one of the most influential professors I have interacted with and has been instrumental in my decision to become a professor.

I would also like to thank the members of my committee: Professors Robert Armstrong, Ken Russell and Chris Scott for their advice and suggestions. Professor Sam Allen was also very instrumental in my research on curvature driven motion of disclination loops. Scott Clingman (Cornell University, Professor Chris Ober’s group) was a main driving force in this research through the superb polymers he synthesized for me. I don’t know what I would have done without him. I owe you one Scott!

I also could not have done this without the continual support of my friends and family. I would like to thank Leslie Lawrence, Marshall Hughes, Dongsik Yoo and Barbara Dirsa for their friendship over the years. A big thank-you is also due to Kevin McGinty, my piano teacher, who was not only a superb teacher but a good friend as well. He was one of the main people who helped me maintain my sanity while finishing my degree. The love and support of my parents, Paul and Lynda Gunther, helped pull me through the difficult moments. To all my brothers and sisters: Jordan, Jenessa, Jilenne, Julia, Jansen, Justus, and Jesse...yes! I am now Dr. Gunther! I am deeply indebted to my brother Jordan who spent nearly one week of his summer vacation helping me finish the final corrections on my thesis. I couldn’t have done it without you! Finally, I would like to thank the Lord for his love and blessings and without whom none of this would have been possible.



## Table of Contents

Abstract .....	2
Acknowledgments: .....	4
Table of Contents .....	5
List of Figures .....	7
List of Tables .....	16
Chapter 1 Background On Liquid Crystals.....	17
1.1 Applications .....	17
1.2 Introduction.....	18
1.3 Defect Structures in Nematic Liquid Crystals .....	21
1.3.1 Defect Morphology .....	21
1.3.2 Defect Interaction.....	25
1.3.3 Non-Equiconstant Case.....	27
1.4 Static Situation in Two-Dimensions - Schlieren Textures.....	28
1.5 The Effect of Magnetic Fields on Defect Textures.....	28
1.6 The Effect of Flow Fields on Defect Textures.....	29
1.6.1 Defect Walls formed by Flow Fields .....	29
1.7 Disclination Loops and Threads .....	32
1.8 Liquid Crystal Rheology .....	32
1.8.1 Leslie-Ericksen theory .....	32
1.8.2 Shear Flow of Nematics.....	34
1.8.3 Tumbling and Flow Aligning Nematics .....	35
1.8.4 Shear Flow Visualization .....	36
1.9 Introduction to the Thesis .....	40
Chapter 2 Experimental Techniques .....	62
2.1 Introduction.....	62
2.2 Light Microscopy.....	62
2.2.1 Use of Compensators .....	63
2.2.2 Solidification-Induced Banding .....	64
2.3 Atomic Force Microscopy .....	64
2.4 Optical Shearing Apparatus .....	65
Chapter 3 Defect Generation Mechanisms .....	74
3.1 Introduction.....	74
3.2 Background .....	74
3.3 Determination of Anchoring Conditions .....	77
3.4 Materials .....	79
3.5 Experimental Procedure.....	79
3.6 Early Stages of Domain and Defect Development .....	80
3.7 Middle Stages of Domain and Defect Development .....	81
3.8 Late Stages of Domain and Defect Development.....	81
3.8.1 Formation of the $s=-1$ defect.....	82
3.8.2 Formation of $s=-1/2$ defects .....	83
3.8.3 Formation of the $s=+1/2$ defect.....	85
3.8.4 Domain Recombination .....	85

3.8.5 Implications for Materials Parameters .....	86
3.9 Summary .....	86
Chapter 4 Computer Simulations of Static Defect Textures.....	115
4.1 Introduction.....	115
4.2 Background.....	115
4.3 Computer Methods.....	118
4.4 Director trajectories and Polarized Light Simulations for Individual Point Defects.....	119
4.5 Repulsion of Defects of Similar Sign: A single $s=+2$ or two $s=+1$ Defects? .....	119
4.6 Defect Generation Mechanism Experiments, Computer Simulations and the Implications for Defects of High Strength.....	122
Chapter 5 The Effect of Magnetic Fields on Defect Structure .....	153
5.1 Introduction.....	153
5.2 Theoretical Background.....	154
5.3 Sample Preparation .....	160
5.4 Results and Discussion .....	161
5.5 Summary .....	164
Chapter 6 Curvature Driven Motion in Liquid Crystal Polymers.....	181
6.1 Introduction.....	181
6.2 Curvature Driven Motion.....	181
6.2.1 Background.....	181
6.2.2 Mathematical Algorithms for Studying Curvature Motion .....	187
6.2.3 Introduction.....	187
6.2.4 Algorithms of Differential Geometry - The Marker Method.....	188
6.2.5 Algorithms of Differential Geometry - The Level Set Approach.....	188
6.3 Evolution of Disclination Loops in Liquid Crystals .....	189
6.3.1 Introduction.....	189
6.3.2 Experimental Procedure.....	191
6.3.3 Experimental Results .....	192
6.4 Curvature Measurement Algorithms.....	193
6.4.1 Introduction.....	193
6.4.2 Error Analysis .....	194
6.4.3 Curvature Motion in Liquid Crystals.....	196
6.5 Summary .....	199
Chapter 7 Summary .....	227
7.1 List of Conclusions .....	227
7.1.1 Defect Generation Mechanisms.....	227
7.1.2 Magnetic Field Effects.....	227
7.1.3 Curvature Driven Motion of Disclination Loops.....	228
7.2 Thesis Research .....	228
7.3 Suggestions for Future Work.....	229

## List of Figures

Figure 1.1: This schematic emphasizes the interconnections between structure, properties, processing and performance. The defect placed at the center of the pyramid can have a strong influence on all the other parameters. ....	47
Figure 1.2: a) A schematic depicting a rod-like liquid crystal with mesogens in the main-chain. b) A similar material but with the mesogens in the side-chain. c) A disk-like main-chain liquid crystal. c) A disk-like side-chain liquid crystal .....	48
Figure 1.3: Schematics depicting the main liquid crystalline phases a) nematic b) cholesteric c) smectic d) columnar .....	49
Figure 1.4: Examples of various types of defect ‘textures’. a) A schlieren texture as seen in crossed polarized transmitted light using the nematic liquid crystal DHMS-7,9. The black brushes emanate from the cores of the defects. b) A threaded texture. The defects are disclination lines and loops that are viewed with crossed polarized light with the polymer Vectra B950. ....	50
Figure 1.5: A schematic depicting the Volterra process for the generation of a defect (in this case an $s=-1/2$ ). a) A monodomain is cut along a surface that is bounded by a line L. b) The surfaces marked S1 and S2 of the cut are moved apart and excess material is put in the gap. c) The material is allowed to relax, thus producing the line defect. (after Volterra [10])	51
Figure 1.6: a-c) Schematics depicting splay, twist, and bend distortions pictorially. d-f) Graphical representations of the corresponding distortions. The splay is related to the divergence of the director while twist and bend are respectively the parallel and perpendicular components of the curl of the director field. (after Frank [12]) .....	52
Figure 1.7: A schematic depicting the geometry used in generating 2D director field distribution equations. The angle $\theta$ represents the angle between the director field and the frame of reference (the x axis). The angle $\phi$ is the angle between the director and a polar line along which the measurements are made. The components of the director are indicated below the schematic. ....	53
Figure 1.8: Plots of the director field distribution for various values of s and c. (after Frank [12]) .....	54
Figure 1.9: Plots depicting changes in the director field distribution as a function of elastic anisotropy for an $s=+1/2$ defect and $s=-1/2$ defect. (Hudson and Thomas [23]) In all cases the director field distribution reorients in order to minimize the more costly distortion.	55
Figure 1.10: Schematics depicting the three main types of walls. a) a twist wall that involves out-of-plane deformations b) a Néel bend-splay wall. The director is confined to the	

zx plane. The transition across the wall occurs mainly through bend deformations. c) a Néel splay-bend wall. The director is again confined to the zx plane. The transition across the wall occurs mainly through splay deformations. . . . . 56

Figure 1.11: a) The director field distribution for a thin thread ( $s=|1/2|$ ) (after Mackley [30]) . . . . . 57

Figure 1.12: A diagram depicting simple shear flow in a nematic . . . . . 58

Figure 1.13: a) A typical curve of log viscosity vs log shear rate for a polymer. Region I is the low shear rate region where the apparent viscosity rapidly decreases with increasing shear rate. Region II is the plateau region (Newtonian) and region III is the high shear rate region (shear thinning). The exact location of each region will depend on the material. b) Actual plots for some lyotropic liquid crystals.[32] . . . . . 59

Figure 1.14: A diagram depicting the likely changes that occur in the various regions.[32] 60

Figure 2.1: An example of the color chart used for determining molecular orientation in conjunction with a quarterwave plate and a first order red plate [4]. . . . . 69

Figure 2.2: Schematics depicting the use of compensators for determining molecular orientation. It is assumed that the original sample has a light gray color.. a) An  $s=+1, c=$  defect. b) The color change that occurs when a quarterwave plate is inserted in the optical path. c) The color change for a first order red plate. d) An  $s=+1, c=0$  defect. e) and f) The changes for a quarterwave plate and first order red plate respectively. Note that the color shifts for the  $s=+1, c=$  defect are the opposite those of the  $s=+1, c=0$  defect. . . . . 70

Figure 2.3: A schematic depicting the solidification induced banding technique. a) A sample in the nematic state before quenching. b) After quenching, bands form normal to the average director. In the light microscopy these would appear as alternating dark and light stripes which provide the useful contrast. The spacing is typically 2-10 microns. . . . . 71

Figure 2.4: A schematic depicting the use of the lamellar decoration technique. a) The sample is annealed in the nematic state to allow the defect texture to coarsen. b) The sample is then quenched at a rate greater than 10 oC/sec to produce a glassy nematic. c) In the final step, the sample is annealed above the  $T_g$  but below the  $T_m$  to allow thin lamellae to grow normal to the director. These protrude a few nanometers from the surface of the sample. The typical lamellar spacing is 30 nm [16]. . . . . 72

Figure 2.5: A schematic of the CSS 450 Shear cell and the operating parameters . . . . . 73

Figure 3.1: a) A fine schlieren texture observed in the polymer B-ET after cooling below the isotropic to nematic transition temperature [7] . . . . . 90

Figure 3.2: a) A schematic depicting homeotropic anchoring. b) homogeneous anchoring

Figure 3.3: (following page) a) Nematic domains that appear during early stages of nucleation and growth. Each contains a single  $s=+1$  defect. b) The corresponding color shifts for insertion of a quarter wave plate. c) The corresponding color shifts for insertion of a first order red plate. These results were used to determine that the director was parallel to the boundary of the domains (homogeneous anchoring conditions). . . . . 92

Figure 3.4: Chemical structure of DHMS-7,9, a random liquid crystal copolyether. The transition temperatures are as follows:  $T_g=20$  oC,  $T_{xn}=90$  oC,  $T_{ni}=170$  oC. . . . . 94

Figure 3.5: Schematics depicting the structure of point defects that lie at the surface of a film.[9] a) The top view of an  $s=+1$   $c=\pi/2$  defect. b) The corresponding side view. c) The top view of an  $s=-1$  defect. d) The corresponding side view. . . . . 95

Figure 3.6: Image of nematic droplets that appear during early stages of domain development. The bright spots are indicative of liquid crystalline ordering. However it is still too early in the transformation process to determine the exact morphology within the droplets. . . . . 96

Figure 3.7: Schematics depicting the four possible droplet morphologies. a) Tangential configuration, homogeneous anchoring. b) Toroidal configuration, homogeneous anchoring. c) ‘Hedgehog’ configuration, homeotropic anchoring. d) Axial configuration, homeotropic anchoring. . . . . 97

Figure 3.8: Example of nematic domains that appear during slightly later stages of domain development. At this stage, a defect can be seen inside each domain. These are of the  $s=+1$ ,  $c=\pi/2$  type as evidenced by the four brush pattern and by banding experiments as well as optical analysis with compensators. . . . . 98

Figure 3.9: The director field distribution within middle stage nematic domains. The molecules are parallel to the boundary of the domain which indicates that the anchoring conditions are homogeneous. . . . . 99

Figure 3.10: a) An image of several large domains formed by many coalescence events. b) The corresponding schematic indicating, by color, the location and type of the various defects. Note that the  $s=|1/2|$  defects are located exclusively at the boundaries while the defects of the type  $s=|1|$  are located towards the center of the domains that just coalesced. . . 100

Figure 3.11: a) An image taken 20 seconds after Figure 3.10a. b) The corresponding schematic indicating the location and types of defects. The dotted line indicates the region where the domains coalesced and the  $s=-1$  defect was created. . . . . 101

Figure 3.12: Schematics illustrating how the  $s=-1$  is incompatible with the nematic domains formed at early stages of domain development. a) homogeneous anchoring. b) homeotropic

anchoring ..... 102

Figure 3.13: A model for the formation of an  $s=-1$  defect from the coalescence of two  $s=-1/2$  defects. The label “I” refers to the isotropic phase between the domains. a) A schematic showing two  $s=-1/2$  defects in close proximity, but in adjacent domains separated by a thin region of isotropic material. b) The state of the system after domain coalescence. The  $s=-1/2$  have coalesced to form an  $s=-1$  defect. .... 103

Figure 3.14: A video sequence depicting the formation of an  $s=-1$  defect. Time is indicated in seconds. The  $s=-1$  defect is attracted to the  $s=+1$  defect located near the center of one of the coalescing domains. These eventually annihilate each other. .... 104

Figure 3.15: a) This schematic depicts the repulsive force field that exists between two  $s=+1$ ,  $c=\pi/2$  defects in close proximity. If this ensemble is placed within a domain, the homogeneous anchoring conditions are not satisfied at all locations along the boundary. The arrows mark the problematic locations. b) If homogeneous anchoring is imposed on the ensemble then two new topological defects must be created. These defects are clearly of the  $s=-1/2$  type indicated by the arrows. .... 105

Figure 3.16: a-c) a series of images depicting the formation of two  $s=-1/2$  defects from the coalescence of two  $s=+1$  defects. Images taken 10 seconds apart. d-f) The corresponding maps of the director field distribution. g-i) The corresponding maps of the solidification-induced banded texture. .... 106

Figure 3.17: Two separate examples of a  $s=-1/2$  defect formed by the coalescence of three domains each containing a pair of  $s=+1/2$  defects. d-f) The corresponding maps of the director field distribution. g-i) The corresponding maps of the solidification-induced banded texture. Compare the pattern in “i” with the images in a and b. There is good agreement between experimental results and the proposed model. .... 107

Figure 3.18: a) A schematic depicting the incompatibility of a single  $s=+1/2$  defect within a nematic domain formed at early stages. The geometry of this defect make it impossible for the homogeneous anchoring conditions to be satisfied in all locations along the boundary. .... 108

Figure 3.19: Images showing the two possibilities for domain recombination. .... 109

Figure 3.20: A video sequence depicting recombination of many small droplets with a single  $s=+1$   $c=\pi/2$  into a single  $s=+1$ ,  $c=\pi/2$  defect. .... 110

Figure 3.21: Video sequence showing recombination to a pair of  $s=+1/2$  defects (1cm=60microns) ..... 111

Figure 3.22: A plot of ellipticity vs defect type. No correlation exists between these two quantities. However, approximately 90% of the domain reconfiguration events led to the formation of a single  $s=+1$  defect. .... 114

Figure 4.1: Two images from reference [2] depicting possible high strength defects. a) A micrograph of CPB combined with a droplet of DSCG|H<sub>2</sub>O|EG. Possible defects with  $s=+4, +2, +1/2$ , are indicated by the arrows. b) A micrograph of MBBA combined with a droplet of DSCG|H<sub>2</sub>O|EG. Singularities from  $s=|1|$  to  $s=|4|$  were reported. . . . . 126

Figure 4.2: a) An image of a cholesteric droplet showing a disclination line. The sample thickness is 150 microns[4]. b) A schematic depicting the director field distribution on the surface of the cholesteric droplet. The singularity point marked by the arrow is an  $s=+2$  defect. . . . . 127

Figure 4.3: a) An example of an  $s=+3/2$  defect from reference [1]. The circled region actually appears to be an  $s=+1$  and an  $s=+1/2$  defect connected by a short line defect. It is not clear that the defects occupy the same core region. b) A defect reported by the authors to be of type  $s=+2$ . This actually appears to be two  $s=+1$  defects in close proximity. . . . 128

Figure 4.4: The linear colormap used for producing the simulated polarized light images  
129

Figure 4.5: a) Simulation of the director field distribution for an  $s=+1/2$  defect. b) The corresponding polarized light simulation . . . . . 130

Figure 4.6: a) Simulation of the director field distribution for an  $s=-1/2$  defect. b) The corresponding polarized light simulation . . . . . 131

Figure 4.7: a) Simulation of the director field distribution for an  $s=+1, c=0$  defect. b) The corresponding polarized light simulation . . . . . 132

Figure 4.8: a) Simulation of the director field distribution for an  $s=+1, c=\pi/4$  defect. b) The corresponding polarized light simulation . . . . . 133

Figure 4.9: a) Simulation of the director field distribution for an  $s=+1, c=\pi/2$  defect. b) The corresponding polarized light simulation . . . . . 134

Figure 4.10: a) Simulation of the director field distribution for an  $s=-1$  defect . b) The corresponding polarized light simulation . . . . . 135

Figure 4.11: a) Simulation of the director field distribution for an  $s=+3/2$  defect. b) The corresponding polarized light simulation . . . . . 136

Figure 4.12: a) Simulation of the director field distribution for an  $s=+2$  defect. b) The corresponding polarized light simulation . . . . . 137

Figure 4.13: a) Simulation of the director field distribution for an  $s=-3/2$  defect. b) The corresponding polarized light simulation . . . . . 138

Figure 4.14: a) Simulation of the director field distribution for an  $s=-2$  defect. b) The cor-

responding polarized light simulation .....	139
Figure 4.15: a) Simulation of the director field distribution for an $s=+4$ defect. b) The corresponding polarized light simulation .....	140
Figure 4.16: A plot of reduced energy vs normalized separation distance for two $s=+1$ defects .....	142
Figure 4.17: A simulation of the director field distribution for two $s=+1$ , $c=\pi/2$ defects in the same location. ....	143
Figure 4.18: Two $s=+1$ , $c=\pi/2$ defects with $d/R=0.022$ . The two cores are indistinguishable in the polarized light simulation. ....	144
Figure 4.19: Two $s=+1$ , $c=\pi/2$ defects with $d/R=0.044$ . The two cores are indistinguishable .....	145
Figure 4.20: Two $s=+1$ , $c=\pi/2$ defects with $d/R=0.177$ . The cores are barely distinguishable. ....	146
Figure 4.21: Two $s=+1$ , $c=\pi/2$ defects with $d/R=0.266$ . The cores are easily distinguished. ....	147
Figure 4.22: Two $s=+1$ , $c=\pi/2$ defects with $d/R=0.355$ .....	148
Figure 4.23: Two $s=+1$ , $c=\pi/2$ defects with $d/R=0.444$ .....	149
Figure 4.24: Incompatibility of an $s=+3/2$ with anchoring conditions and droplets formed at early stages. This can be seen by the variation of the director angle with respect to the circular boundary. ....	150
Figure 4.25: a) A schematic showing a domain with a single $s=+1$ $c=\pi/2$ defect that is about to coalesce with a domain containing a pair of $s=+1/2$ defects. b) The domains just after coalescence. Two sharp cusps form in the regions marked by the arrows. The homogeneous anchoring is violated in these regions. c) Two new topological defects of the type $s=-1/2$ are formed in front of the cusps in order to satisfy the anchoring conditions. ....	151
Figure 5.1: Schematics depicting the three main types of walls. a) a twist wall that involves out-of-plane deformations b) a Néel bend-splay wall. The director is confined to the $zx$ plane. The transition across the wall occurs mainly through bend deformations. c) a Néel splay-bend wall. The director is again confined to the $zx$ plane. The transition across the wall occurs mainly through splay deformations. ....	168
Figure 5.2: The chemical structure of TPP5, a liquid crystal polyester. The crystal to nematic transition temperature is 148 oC and the nematic to isotropic transition temperature is 180 oC. TPP5 is ( 1-(4-hydroxy-4'-biphenyl)-2-(4-hydroxyphenyl)propane with 1,5-dibro-	



mopentane) ..... 169

Figure 5.3: A series of plots showing the director trajectory across a wall as a function of  $\theta$ , the angle between the wall (W) and the applied field(H). In all cases (equiconstant case) 170

Figure 5.4: An AFM image depicting a portion of a Néel wall. The numerical labels indicate the value (in degrees) of  $\theta$ , which is the angle between the wall and the applied field. The lines drawn normal to the centerline of the wall separate segments of differing  $\theta$ . The straight segment with  $\theta = 0$  was used for the mathematical analysis of the director field distribution. .... 171

Figure 5.5: a) A rough map of the director field distribution produced by hand tracing lines normal to the lamellae in the AFM micrograph of Figure 5.4. .... 172

Figure 5.6: a) A series of plots showing variations in  $\theta$  with  $\theta_0$  fixed at 0.5. Large changes in  $\theta$  produce noticeable changes in the director trajectory. Changes of only a few degrees have less of an effect. .... 176

Figure 5.7: b) An additional example of a "bad fit" between data and experiment. In this case,  $\theta_0 = 0.5$  and  $\theta = 0.5$ . The thick and thin lines represent the simulation and data respectively. The mismatch is again most evident in the regions close to the centerline of the wall. The large mismatch in  $\theta$  produced a more noticeable difference visually than did the mismatch seen in Figure 5.7a. This is also supported by the larger value of the rms error in this simulation which was 2.96. .... 179

Figure 6.1: A schematic depicting the geometry used for the basis of the early curvature driven boundary motion algorithms (after R. Courant). .... 203

Figure 6.2: a) A schematic depicting a curve with a low marker density. b) An identical curve with a high marker density. The arrows indicate the direction of motion of the curve segment at that location. The local motion is toward the center of curvature. A higher marker density would yield a more accurate solution as can be seen pictorially in the two schematics. .... 204

Figure 6.3: A schematic depicting the basic elements of the level set algorithm. a) This schematic shows a view of a two-dimensional circular surface that lies in the xy plane. The arrows indicate the direction of motion of the curves. b) This schematic depicts the cone-shaped level set function. The moving front (schematic a) is the intersection of the surface and the xy plane. Other slices of the level set function taken at different heights along the z axis represent the front at different times. .... 205

Figure 6.4: A series of two dimensional simulations produced with Surface Evolver that depict a complex curve evolving under its curvature. The first simulation (i=0 iterations) depicts the original curve. Initially, the high curvature regions (i.e. the sharp points) become smoother (i=10 iterations). In subsequent simulations the curve evolves first to an elliptical

shape and then to a circular one before it disappears (at  $i=70$  iterations). . . . . 206

Figure 6.5: The chemical structure of 8CB and DHMS-7,9 . . . . . 207

Figure 6.6: a) Examples of typical disclination loops in 8CB. Three disclination loops are identified by the arrows. b) An example of a typical disclination loop in the polymer DHMS-7,9. The arrow marks the location of the loop that is analyzed in this chapter. Note that the disclination loops in the polymer are much more irregular and jagged . . . . . 208

Figure 6.7: Several examples depicting disclination loop evolution in 8CB . . . . . 209

Figure 6.8: A series of images depicting disclination loop evolution in the polymer DHMS-7,9. (see the Following Pages). The first image shows the sample while it is being sheared between two coverslips. The disclination density is high enough so that no individual defect contours can be traced. After cessation of shear, the sample relaxes and the texture coarsens. This is evidence by a dramatic decrease in the disclination density with time. The second image shows the sample 30 seconds after cessation of shear. At this point, small segments of the disclination contours can be traced. After an additional 30 seconds (image 3), several large and irregularly shaped disclinations can be seen. Region “A” contains some high curvature segments while region “B” contains more gently curved segments. These two regions will be used for a subsequent mathematical analysis. The fourth image shows the system after about 30 minutes. . . . . 210

Figure 6.9: A schematic showing the circular contours used to test the curvature measurement algorithms. The  $xy$  coordinates of each contour was subsequently obtained using NIH-Image. The large circle represents the contour at  $t=t_0$  while the smaller circle represents the contour at a later time after it has evolved solely due to curvature forces. The second smaller circle is identical to the other except that it is shifted laterally. . . . . 217

Figure 6.10: A plot of Velocity vs. Curvature for the contours of Figure 6.9. The data points should ideally be at the same  $(x,y)$  location since the radius of curvature of the circles does not change. The small deviation seen here is a result of the point digitization process made with NIH-Image as well as the curvature measurement algorithm itself. . . . . 218

Figure 6.11: The first schematic represents digitized data taken from Figure 6.8c. The subsequent images are simulations of loop evolution made with the Surface Evolver program. The label “ $i$ ” refers to the number of iterations of the program. . . . . 219

Figure 6.12: A plot of velocity vs. curvature for the theoretical loop evolution shown in Figure 6.11. The data fits a straight line remarkably well, indicating that the curvature measurement algorithm can yield results that are expected from mathematical theories. . . 221

Figure 6.13: The above schematic shows a loop evolution process in 8CB. The data was digitized with NIH-Image. Some lateral shift can be seen in the image. However it is clear that the high curvature regions (i.e. the ends of the ellipses) are evolving more rapidly than the low curvature regions. . . . . 222

Figure 6.14: A plot of velocity vs. curvature for 8CB based on the digitized images in Figure 6.13. The data does not fit a straight line plot. Rather, a leveling-off occurs in the high curvature regime. This is most likely a result of fluid drag and possibly even molecular diffusion that can oppose the direction of motion of the curvature driving force. . . . . 223

Figure 6.15: a) A series of digitized loop contours for the polymer DHMS-7,9. Some lateral shift as well as rotation is evident. b) The curves overlay somewhat when shifted and rotated. . . . . 224

Figure 6.16: A plot of velocity vs curvature for DHMS-7,9 based on the digitized data shown in Figure 5.15. A significant amount of scatter can be seen even for a small number of data points. This is most likely a result of the lateral shifting that occurred. . . . . 225

Figure 6.17: A series of schematics depicting how loop coalescence could lead to the formation of new disclination loops with many regions of high curvature along their contours. . . . . 226

## List of Tables

A list of Figure numbers and the corresponding $d/R$ value .....	121
Examples of local, global, and independent properties that affect the speed function of a moving boundary or surface. ....	182
Molecular weight and transition temperatures for the 8CB and DHMS-7,9 samples used in this study .....	191

# Chapter 1

## Background On Liquid Crystals

### 1.1 Applications

In recent years, the interest in high performance materials has prompted a great deal of research in liquid crystal polymer systems[1][2]. The applications that most readily come to mind are liquid crystal displays and high strength fibers such as Kevlar®. However, liquid crystals are actually used in a very wide array of applications. In the food packaging industry, certain liquid crystal polymers are used for their excellent barrier properties to oxygen[3]. Ten micron thin films of certain multiaxially oriented liquid crystal polymers have the same barrier properties as a 50 micron film of polyethylene vinyl alcohol. This difference translates to improved performance and reduced costs.

Liquid crystals are also used quite extensively for nonlinear optics and electronic devices [4][5][6]. Side-chain ferroelectric liquid crystalline polymer films are currently being used for displays and electrical sensors[5]. Although the polymers have a lower figure of merit than do ceramics, the former offers promises of greater durability in sensor applications. A particularly interesting application is the use of liquid crystal polymers in the fabrication of re-programmable diffraction gratings[6]. Reversible patterns are created in the material by using lasers to write transparent lines on either an opaque or aligned background. This can produce either amplitude or phase modulated devices respectively. Although exposure times are still rather long, these devices offer advantages of reversibility as well as lower production costs since no wet-lab chemistry is involved. This application is of particular interest for this thesis because variations in the performance of these diffraction gratings were produced by making significant changes in the morphology of the sample, particularly in the defect structure.

Morphology, or the structure of a material, is profoundly affected by the presence of defects. All practical materials contain many defects which can affect not only structure or morphology but also processing, properties, and performance. The relationship between these parameters is depicted in the schematic of Figure 1.1. Anything that affects one of these parameters certainly affects all the others. In the schematic a defect has been placed at the center of the tetrahedron to emphasize that defects can have a profound influence on all aspects of the liquid crystal system.

Currently a great deal is known about how defects affect the structure of a liquid crystal. However the relationship between defects and the other parameters in the pyramid is not as clear. In order for research on liquid crystals, or any material, to progress effectively, it is essential to understand the connections between defect behavior and structure, properties, processing, and performance. One issue that is essential to understand is how the defects are generated and what affects their behavior once they are formed. This thesis will address the issue of defect generation in liquid crystals and discuss several ways various defects can evolve under a variety of conditions. Chapter three will discuss the generation of defects during the isotropic to nematic transition. Mechanisms of formation for the most common types of defects will be presented. Chapter five will address the ways in which the director field distribution changes upon subjecting a polymer to an applied magnetic field. The effects of flow fields on defect textures will be discussed in chapter 6. Curvature driven motion of disclination loops will be discussed from both an experimental and theoretical point of view.

## **1.2 Introduction**

A liquid crystal is a material that is in an intermediate state between a liquid and a crystal. That is, it can possess the fluidity of a liquid under certain conditions, but at the same time have anisotropy in certain properties [7]. In order for a substance to exhibit liquid crystallinity, an anisotropy in shape must be present. This is typically accomplished by adding stiff, shape persistent moieties, or mesogens, into the chemical structure. It is the mesogens that are responsible for imparting the liquid crystalline properties to the system.

The mesogens can be linked or separated by flexible spacers. The schematics shown in Figure 1.2 depict several of the ways in which shape anisotropy is created. The first schematic (1.2a) shows a rod-like liquid crystal that could be synthesized by adding para-linked benzene rings or other stiff chemical units into the backbone of the structure. This type of structure is known as a “main-chain” liquid crystal. A similar structure, but with the rods placed in pendent groups from a flexible polymer backbone, would be known as a “side-chain” liquid crystal (Figure 1.2b). Structural differences such as main-chain or side-chain LCP’s lead to vastly different properties[8]. It is also possible to incorporate disk-like mesogens into the structure as shown in Figure 1.2c and d.

Liquid crystals can also be classified into different categories according to what type of external influence causes the transition to the mesophase region. Thermotropic liquid crystals are those for which the mesophase state is induced by changes in temperature. In lyotropic liquid crystal systems the mesophase state is induced by changes in the concentration of an appropriate solvent.

An additional classification scheme differentiates between liquid crystals according to the way in which the molecules are ordered. In nematic liquid crystals the molecules have a high degree of orientational order, but no long range translational order. The fluidity of the nematic phase is a result of the fact that the molecules can remain approximately parallel while they slide past each other. A diagram depicting nematic ordering is shown in Figure 1.3a. The diagram shows how the locally preferred direction changes from point to point within the sample, but on average the long axes of the molecules tend to point in the same direction. The average direction of the long axes of the molecules defines a parameter known as the director,  $n$ . The director is a nonpolar vector for which  $+n$  and  $-n$  are equivalent. It is possible to quantify the degree of order in a nematic liquid crystal by defining the parameter “ $S$ ”, known as the order parameter:

(1.1)

$$S = \frac{1}{2} \langle 3 \cos^2(\theta) - 1 \rangle$$

The variable  $\theta$  represents the angle between the individual molecular axes and the director. The brackets indicate that an average value is being taken. The above relation is only valid when the following two criteria are satisfied: First, that the distribution function is cylindrically symmetric about the director. Second, that the directions  $+n$  and  $-n$  are equivalent. A value of  $S=1$  indicates perfect alignment of the molecules. A value of  $S=0$  would be indicative of an isotropic state. In nematic liquid crystals,  $S$  is strongly temperature dependent. Typical values of  $S$  range from 0.6 to 0.8.

A cholesteric liquid crystal is very similar to a nematic in that it has a high degree of orientational order, except that the director has undergone twist as shown in Figure 1.3b. This type of liquid crystal is often referred to as a chiral nematic due to the presence of chiral centers in the backbone of the structure. A cholesteric or chiral nematic liquid crystal will, on a local scale, look very similar to a nematic. However in the case of the cholesteric, the director will twist in a helical pattern due to the presence of the chiral centers. This necessitates the formation of a new description for the director which is shown below:[9]

(1:2)

$$n_x = n \cos\left(\frac{2\pi z}{\lambda} + \phi\right) \quad n_y = n \sin\left(\frac{2\pi z}{\lambda} + \phi\right) \quad n_z = 0$$

where  $\phi$  is determined by the coordinate system and the director orientation and  $\lambda$  is the pitch of the helix. The helical nature of cholesterics makes them able to selectively reflect circularly polarized light[7].

Smectics are another type of liquid crystal that have a variety of stratified structures and also have one-dimensional long range translational order and long-range orientational order [11]. Within each particular layer, the molecules are parallel to each other, but the lateral distance between each molecule and its neighbors varies in a liquid-like way throughout the layer. A general characteristic of smectics is that there is less attraction between the layers than between molecules so that the layers are able to move past each other more easily. The schematic shown in Figure 1.3c shows an example of the smectic A



phase, where the molecules are aligned along the normal to the layers. Various other types of smectic phases exist which have other specific types of alignment.

A fourth liquid crystalline phase is known as the columnar phase, shown in Figure 1.3d. In this type of liquid crystal the disk-like mesogens form hexagonally ordered stacks that have two-dimensional long range ordering [7].

## 1.3 Defect Structures in Nematic Liquid Crystals

### 1.3.1 Defect Morphology

A particular liquid crystalline texture is defined by the number, types, and arrangements of the defects it contains. These defects produce large scale distortions whose length scale is comparable to the wavelength of visible light. Thus they can be easily viewed using a polarizing light microscope. An example of a typical “schlieren” texture is shown in Figure 1.4a. This depicts the state of a thin film of a liquid crystal polymer just 5 minutes after it was cooled through the nematic to isotropic transition temperature. The defects are represented by the black points that have dark ‘brushes’ emanating from them. The structure of these defects will be described in more detail in following paragraphs. The image in Figure 1.4b is an example of a ‘threaded’ texture in the liquid crystal Vectra B950. This texture is typically found in thicker liquid crystal samples (i.e. 30 microns or greater) in static situations as well as under appropriate shearing conditions. The structure of the threaded texture will be discussed in greater detail in section 1.7. The evolution of threads will be treated from both a theoretical and experimental point of view in Chapter 6. Next I present an introduction to the basic defect structures and the theories used to describe them in both static situations as well as under applied fields and constraining influences.

The ground state of a liquid crystal is a defect-free monodomain. Line defects can then be introduced by the Volterra process[12]. First, the monodomain is cut along an arbitrary surface that is bounded by a line  $L$  [13] as shown in Figure 1.5a. The surfaces marked  $S1$  and  $S2$  of the cut are moved with respect to each other by either translation, rotation, or both [9] (Figure 1.5b). This process leads to the production of empty space. Next the

empty space is filled with defect free material. Rather than creating a void, it is also possible to create excess material that must be removed. In the final step of the Volterra process, the sample is allowed to relax. The relaxation process produces a line discontinuity along L as shown in Figure 1.5c.

Before developing a framework for describing molecular orientation in the vicinity of a defect, it is important to discuss the continuum theory for deformations in nematic liquid crystals. Nematics have low viscosities and can be deformed by small external forces. A continuum theory was developed by Frank [14] and deGennes [15] to describe deformations in nematics. This theory can be used to developed the following expression for the free energy per unit volume of a nematic:

(1.3)

$$F = \frac{1}{2}k_{11}(\nabla \cdot n)^2 + \frac{1}{2}k_{22}(n \cdot \nabla \times n)^2 + \frac{1}{2}k_{33}(n \times \nabla \times n)^2$$

where  $n$  represents the director and  $k_{11}$ ,  $k_{22}$ , and  $k_{33}$  are the Frank elastic constants known respectively as splay, twist, and bend. Each of these constants describes a specific type of distortion (see Figure 1.6). The first three schematics (Figure 1.6 a-c) depict the distortions in terms of their specific effects on the liquid crystal molecules. The next three schematics (Figure 1.6 d-f) depict the distortions graphically for splay, twist, and bend respectively. Splay represents the divergence of the director which is represented by  $\nabla \cdot n$  or equivalently:  $\frac{\partial n_x}{\partial x} + \frac{\partial n_y}{\partial y}$ . Twist on the other hand is described by the parallel component of the curl of the director:  $n \cdot \nabla \times n = \frac{\partial n_y}{\partial x} - \frac{\partial n_x}{\partial y}$  while bend is the perpendicular component of the curl of the director:  $n \times \nabla \times n = \frac{\partial n_x}{\partial z} + \frac{\partial n_y}{\partial z}$ . The above equations form the basis for the theoretical treatment of defects and textures in nematics. For distortions to be stable, they must result in a relative minimum in the free energy expression.

For nematic polymers of the semiflexible type, the Frank elastic constants are on the order of  $10^{-6}$  dynes[16]. These constants depend on molecular structure in many ways. For example,  $k_{11}$  is predicted to be a strong function of molecular length  $L$  (i.e. molecular weight). A model based on elastic entropy developed by Meyer predicts that  $k_{11}$  should be proportional to  $L$ [17]. The model developed by deGennes is based on elastic energy rather

than entropy and predicts that  $k_{11}$  should vary as  $L^2$ . The variation of the splay constant with molecular weight is a particularly interesting problem that has not yet been explored experimentally. By carrying out such a study, it should be possible to determine the dominating mechanism contributing to splay. For the case of LCP's with mesogens and flexible spacers in the backbone, it is still not known whether chain folding in LCP's (termed "hairpins" by deGennes) [18] or aggregation of chain ends is dominant. In the former case, the splay constant would be independent of molecular weight, while in the latter case, the splay constant should increase with molecular weight. Clearly this is an interesting problem and deserves further exploration. In the same paper by deGennes [18] it is found that the bend elastic constant,  $k_{33}$ , is dominated by chain rigidity while the twist constant ( $k_{22}$ ) is primarily a function of the interaction between chains. In thermotropic liquid crystals,  $k_{22}$  is found not to vary much among different samples. The variation in  $k_{22}$  for lyotropic systems can be explained by the changing interactions between polymer chains induced by various solvents [19]. In addition, the temperature dependence of the elastic constants are of the form  $k=cS^2(T)$ , where  $S(T)$  represents the temperature dependence of the order parameter [20].

Molecular orientation in the neighborhood of a disclination can be described by first making some simplifications of the previous equation. Assuming the director is confined to the x-y plane, a schematic shown in Figure 1.7 can be drawn. Note that in the two-dimensional case there are no twist distortions. The components of the director then become  $n_x = \cos(\phi)$ ,  $n_y = \sin(\phi)$ , and  $n_z = 0$ , with  $\phi$  representing the angle between the director and the polarization direction of the incident light. Then by assuming  $k_{11}=k_{33}=k$  (elastic isotropy) and that  $k_{22}=0$  the equation reduces to:

(1.4)

$$F = \frac{1}{2}k(\nabla\phi)^2$$

The free energy of the system is minimized in the absence of body torques when the following condition holds:

(1.5)

$$\frac{\partial^2 \phi}{\partial x^2} + \frac{\partial^2 \phi}{\partial y^2} = 0$$

When this result is combined with the previous equation, the expression reduces to:

(1.6)

$$\nabla^2 \phi = 0$$

Solutions of this last equation have the form:

(1.7)

$$\phi = s\alpha + c$$

where  $s$  is the defect strength,  $\alpha$  is equal to  $\arctan\left(\frac{y}{x}\right)$  and  $c$  is a constant.

Several plots for various values of  $s$  and  $c$  are shown in Figure 1.8. The disclination lines are shown as small dots indicating that they lie along the  $Z$ -axis (out of the page). In addition, the director changes its orientation by  $2\pi s$  upon traversing the line. The defect strength can also be defined as the number of rotations that the director undergoes as it traverses a path known as the Frank-Nabarro circuit. This circuit is defined as a circular counterclockwise path taken around the defect. Begin by marking a point on the disclination and follow the director orientation as a function of angular distance from that point. Consider an  $s=-1$  defect for example. In traveling through the first quadrant, the director has undergone a rotation of  $\frac{\pi}{2}$ . After traversing all quadrants, the director has made a total rotation of  $2\pi$ . This indicates that the defect has a strength of  $|1|$ . The sign of the strength depends on the direction of rotation with respect to the circuit. If the director rotates in the opposite sense of the circuit then the strength is of negative sign, otherwise it is positive. Thus, for an  $s=-1$  defect the sense of rotation is opposite that of the circuit.

In two-dimensions these defects are points. In three dimensions they can either be points or lines depending on the anchoring conditions. For the special anchoring condi-

tions of homeotropic at the substrate/liquid crystal interface and homogeneous at the free surface, the morphology is characterized by point defects at the surface of the sample [20]. If the anchoring conditions depart from this significantly then the 'points' seen in the schlieren texture will actually represent line defects passing through the thickness of the film.

### 1.3.2 Defect Interaction

Disclinations of strength  $s = \pm 1$  and  $s = \pm \frac{1}{2}$  are usually the only type observed [7]. Their interactions with each other can be described in the following way for a two-dimensional case. The deformation energy,  $W$ , of an isolated defect in a circular region of radius  $R$  and unit thickness is [24]

(1.8)

$$W = W_c + \pi k s^2 \ln\left(\frac{R}{r_c}\right)$$

where  $W_c$  is the unknown energy of the core region of radius  $r_c$ ,  $k$  is an elastic constant and  $s$  is the defect strength. Since  $k_{11}=k_{33}=k$ , the director field due to the presence of  $i$  defects of strength  $s_i$  with the  $i$ th defect located at coordinates  $x_i$  and  $y_i$  is given by:

$$\phi = \sum_i s_i \arctan\left(\left(\frac{y - y_i}{x - x_i}\right) + const\right)$$

The energy for a pair of disclinations separated by a distance  $r_{12}$  becomes:

(1.9)

$$W = \pi k(s_1 + s_2)^2 \ln\left(\frac{R}{r_c}\right) - 2\pi k s_1 s_2 \ln\left(\frac{r_{12}}{2r_c}\right)$$

The interaction energy is given by the second term of the above equation. The force between disclinations is then the partial derivative of  $W$  with respect to the separation distance. This yields:

(1.10)

$$Force = \frac{-2\pi k s_1 s_2}{r_{12}}$$

Thus, when the strengths of the defects have opposite signs, the defects are attracted and either disappear completely or form a new defect with a strength  $s' = s_1 + s_2$ . Defects of the same sign repel each other. The force between disclinations is inversely proportional to the distance between them. Defects of opposite sign at an initially large value of  $r_{12}$  will move towards each other slowly but as the distance between them decreases, they will begin to move together more rapidly.

Defects are not only affected by the presence of other defects but also by constraining surfaces. Molecular orientation near a surface can be determined by adding a surface energy term to the free energy expression in section 1.3.1 (equation 1.3). The liquid crystal is only affected by the anisotropic component of the surface tension which has the following form:

(1.11)

$$\gamma = \frac{A}{2} \sin^2(\phi - \phi_s)$$

where the preferred orientation of the surface is  $\phi_s$ . The free energy could then be modified by adding the term  $\gamma\delta(z)$ . There are two main situations to consider. First, if the

anchoring energy is strong, so that the orientation at the surface is very close to  $\phi_s$ , then the surface behaves like a defect of the opposite strength. As a result the surface repels the defect with a force of  $\frac{\pi k s^2}{d}$ , where  $d$  is the distance between the disclination and the surface[7]. If, on the other hand, the disclination is close to the surface and the distortional energy is much larger than the surface energy, then the defect becomes attracted to the surface. This situation has been addressed theoretically by Meyer [25] who determined that the equation for the director field distribution in this situation is:

(1.12)

$$\phi = \phi_s + \arctan\left(\frac{(z + z_o)}{x}\right)$$

where the disclination appears at  $x=0$  and  $z_o = -\frac{k}{A}$ , with  $k$  being a combination of the elastic constants.

### 1.3.3 Non-Equiconstant Case

Up to this point, the underlying assumption has been that all the elastic constants are equal. As mentioned earlier this was originally done by Frank to obtain analytical solutions for the director field distribution. However in practice, the three elastic constants are usually not equal. The splay and bend constants are typically two to four times larger than the twist constant in liquid crystal polymers. A new quantity,  $\epsilon$ , known as the elastic anisotropy, reflects the relative magnitude of the bend and splay constants:

(1.13)

$$\epsilon = \frac{(k_{11} - k_{33})}{(k_{11} + k_{33})}$$

When the bend and splay constants are equal, the elastic anisotropy,  $\epsilon$ , has a value of zero. The upper limit of  $\epsilon$  is 1.0, which results when  $k_{11}$  is much larger than  $k_{33}$ . This would be found for extremely flexible high molecular weight systems where bend distortions are more energetically favorable leading to the low  $k_{33}$  value. The lower limit of  $\epsilon$  is

-1.0, which would be expected when  $k_{33}$  is much larger than  $k_{11}$  or when the molecules are very stiff. Intermediate values of  $\epsilon$  can be obtained by minimizing the total free energy as described by equation 1.3, but assuming that  $k_{11} \neq k_{33}$ . This yields the following second order non-linear partial differential equation for the director field  $\phi(\theta)$  about the defect:

(1.14)

$$0 = \frac{\partial^2 \phi}{\partial \theta^2} (1 + \epsilon \cos 2(\phi - \theta)) + \left( 2 \frac{\partial \phi}{\partial \theta} - \left( \frac{\partial \phi}{\partial \theta} \right)^2 \right) \epsilon \sin 2(\phi - \theta)$$

This equation has been solved numerically by Hudson and Thomas [25] for static situations. These authors found that the elastic anisotropy had a strong effect on the structure of the  $s=+1/2$  defect. Examples depicting this are shown in Figure 1.9. In all cases, the director field rearranges itself in order to reduce the presence of the more costly distortion.

## 1.4 Static Situation in Two-Dimensions - Schlieren Textures

The schlieren texture refers to a grouping of the aforementioned disclinations (Figure 1.4a). The defect cores are represented by the black points which have either two or four dark brushes emanating from them. The brushes are black which means that the director field within them is either parallel or perpendicular to the polarizer or analyzer respectively. The number of brushes is four times the strength of the defect.

Thus, a defect of strength  $s = \pm \frac{1}{2}$  will have two brushes while one with  $s = \pm 1$  will have four brushes. The motion of these brushes under rotating crossed polars will be determined by both the sign and magnitude of the defect strength. Defects of positive strength have brushes that rotate in the same sense as the crossed polars. Brushes associated with defects of negative strength will rotate in the opposite sense. The speed of brush rotation will be twice as fast for defects of half-integer strength as it will for integer strength defects.

## 1.5 The Effect of Magnetic Fields on Defect Textures

Magnetic fields are capable of aligning liquid crystal polymers that have a net positive dia-



magnetic anisotropy. If this quantity is negative, then the polymer orients perpendicular to the field. The director field distribution surrounding such walls can be determined mathematically by developing a free energy expression based on the equations of Frank [7]. This new equation has the following form:

(1.15)

$$F = \frac{1}{2}k_{11}(\nabla \cdot n)^2 + \frac{1}{2}k_{22}(n \cdot \nabla \times n)^2 + \frac{1}{2}k_{33}(n \times \nabla \times n)^2 - \frac{1}{2}\chi_a(n \cdot H)^2$$

where  $H$  is the magnetic field strength and  $\chi_a$  is the magnetic susceptibility anisotropy. The linear elastic term tends to disperse the distortions while the nonlinear magnetic term tends to localize them. The competition between these two forces is what leads to the creation of defect “walls”. A schematic depicting the three main types of walls is shown in Figure 1.10. The first type is a twist wall where the field is along the  $z$  axis and the director is confined to the  $yz$  plane and twists about the  $x$  axis. As indicated in Figure 1.10a, the director has to twist out of the plane of the page by a factor of  $\pi$  as it crosses the wall. Twist walls are analogous to Bloch walls in magnetic-spin systems [26]. The other two types of walls are referred to as Néel walls, the main difference between them being the proportions of bend and splay distortions they exhibit. A schematic of a Néel bend-splay wall is shown in Figure 1.10b. The field is again applied along the  $z$  direction, however the director remains confined to the  $xz$  plane. The transition of the director through an angle of  $\pi$  takes place primarily through bend distortions. For the Néel splay-bend wall, on the other hand, the transition takes place mostly through splay distortions (see Figure 1.10c).

The structure of a wall defect is highly dependent upon the elastic anisotropy. This will be addressed from both a theoretical and experimental point of view in chapter 5.

## 1.6 The Effect of Flow Fields on Defect Textures

### 1.6.1 Defect Walls formed by Flow Fields

Flow fields are also capable of producing defect walls, but under very specific conditions. If a two-dimensional situation is assumed, then flow can be of the shear or extensional type (or both). Several materials parameters as well as flow conditions will determine whether or not the production of defect walls will be analogous to those formed in magnetic fields.

This issue can be addressed by beginning with an expression describing arbitrary flow in the x direction in terms of a rate of strain tensor:

$$d_{ij} = \begin{bmatrix} \dot{\epsilon} & \dot{\gamma} \\ \dot{\gamma} & \dot{\epsilon} \end{bmatrix} \quad (1.16)$$

where the magnetic and director field distributions are defined as:

$$H = H[\cos(\phi_H), \sin(\phi_H)] \quad n = [\cos\phi, \sin\phi] \quad (1.17)$$

A torque balance can be used to define the director orientation in the following way:

$$\frac{\partial}{\partial x_j} \Pi_{ij} + f_i + f'_i = \lambda n_i \quad (1.18)$$

where the components of the Euler-Lagrange equation are defined as:

$$\Pi_{ij} = \frac{\partial g}{\partial n_{i,j}} \quad f_i = \frac{\partial g}{\partial n_i} \quad f'_i = (\alpha_3 - \alpha_2)N_i + (\alpha_3 + \alpha_2)d_{ij}n_{ij} \quad (1.19)$$

where  $\Pi_{ij}$  is the curvature stress tensor,  $f_i$  is the elastic and magnetic body curvature force,  $f'_i$  is the flow body curvature force and  $\lambda$  is the Lagrange multiplier.

These parameters are related to the free energy density as well as the director field:

(1.20)

$$N = \dot{n} - \omega \times n \quad g = \frac{1}{2}k(\nabla\phi)^2 - \frac{1}{2}\chi_a H^2 \cos^2(\phi - \phi_H)$$

where  $g$  is the elastic and magnetic free energy density and  $N_i$  is the vorticity of the director relative to that of a volume element:

When the previous equations are inserted into the Euler-Lagrange expression, the following differential equation can be written to describe the director field distribution:

(1.21)

$$0 = \left[ (\alpha_2 - \alpha_3) \frac{\partial}{\partial t} - k \left( \frac{\partial^2}{\partial y^2} + \frac{\partial^2}{\partial y^2} \right) \right] \phi + \chi_a H^2 \sin(\phi - \phi_H) \cos(\phi - \phi_H)$$

(1.22)

$$- 2(\alpha_3 + \alpha_2) \dot{\epsilon} \sin\phi \cos\phi + \underline{2\alpha_3 \dot{\gamma} \cos^2\phi - 2\alpha_2 \dot{\gamma} \sin^2\phi}$$

Each component represents a torque on the director. Each term can be set to zero when the director is oriented along the shear, stretch, or magnetic field directions.

When the external field is exclusively of the extensional type, then the equations are analogous to those for magnetic field alignment. In this case, the characteristic length which describes the size of the distorted region becomes:

(1.23)

$$\xi = \left( \frac{k}{2(\alpha_3 + \alpha_2)\dot{\epsilon}} \right)^2$$

The underlined term in equation 1.23 introduces asymmetry into the director distribution surrounding the defect walls that were created during shear flow. As a result, the wall will not be symmetrical about its center. This is a complicated situation that has not yet been addressed from a modeling point of view.

## 1.7 Disclination Loops and Threads

When the thickness of a sample with a schlieren texture is increased beyond about 50 microns, the morphology becomes more complicated. The disclinations that appeared before in an end-on view now exist in three-dimensions as a ‘threaded texture’ which consists of loops and lines. There are two main types of defect lines [30]. Those called ‘thins’ are disclinations of  $s = \pm\frac{1}{2}$ . A schematic of one is shown in Figure 1.11. ‘Thicks’ are the other type of thread that are disclinations of the type  $s = \pm 1$ . Threads of the type  $|1/2|$  can either form closed loops or end at surfaces [28]. The lines with a strength  $s=|1|$  can form closed loops, end at surfaces or at the  $s=|1/2|$  lines.

Although threads can be seen under static conditions, their structure and behavior is generally discussed within the context of shear flow visualization experiments. These will be reviewed in detail in section 1.8.4.

## 1.8 Liquid Crystal Rheology

### 1.8.1 Leslie-Ericksen theory

The Leslie-Ericksen theory is a continuum mechanics theory that has been used for both small molecule and polymeric nematics to predict how director and velocity fields are affected by flow, electric, and magnetic fields [7]. The x-y component of the Leslie-Erick-

sen constitutive equation (which is the relevant component for shear flow of nematics) is shown below:

(1.24)

$$\begin{aligned} \sigma_{ih} = & \alpha_1 n_i (n_k A_{kl} n_l) n_j + \alpha_2 n_i N_j + \alpha_3 n_j N_i + \alpha_4 A_{ij} \\ & + \alpha_5 n_i n_k A_{kj} + \alpha_6 n_j n_k A_{ki} \end{aligned}$$

where  $\alpha_i$  describes the viscous torque coefficients, A represents the rate of deformation tensor, and N is the relative director angular velocity. For shear flow this equation becomes:

(1.25)

$$\sigma = g(\theta) \gamma'_g$$

where

(1.26)

$$g(\theta) = \alpha_1 \cos^2(\theta) \sin^2(\theta) + \eta_1 \sin^2(\theta) + \eta_2 \cos^2(\theta)$$

where  $\eta_1$  and  $\eta_2$  are the viscosities measured for the director in the homeotropic (normal to the surface) and planar configurations (parallel to the surface) respectively, and  $\theta$  is the orientation of the director with respect to the vertical direction. These equations clearly show that the viscoelastic response of the material is strongly related to the director field behavior. An analysis of the Leslie-Ericksen equations leads to the development of the Ericksen number [29]:

(1.27)

$$Er = \frac{(n\dot{\gamma})}{\left(\frac{k}{a^2}\right)} = \frac{\text{viscous stress}}{\text{elastic stress}}$$

where  $\eta$  is a combination of the Leslie coefficients,  $k$  is a combination of elastic constants,  $\dot{\gamma}$  is the shear rate and  $a$  is the sample thickness. This dimensionless parameter describes the relative magnitude of viscous stresses that tend to rotate the director and elastic stresses that tend to impose boundary conditions on the director.

The Ericksen number has important implications for studies of disclinations in nematic systems. For examples, Mather et al. [30][31] have found that in small molecule nematics, the dimensionless disclination density,  $\rho_A$ , depends on the Ericksen number,  $Er$ , for a certain range of  $Er$  in the form of a power law:

(1.28)

$$\rho_A h = \alpha(Er)^\beta$$

where  $\rho_A$  is the length per unit area of disclinations projected on the velocity-vorticity plane and  $h$  is the sample thickness, In addition, the exponent  $\beta$  provided insight into the dimensionality of the disclination textures. A value of  $\beta = 0.5$  suggested a two-dimensional length scale, while values of  $\beta = 1$  suggested a three-dimensional length scale.

### 1.8.2 Shear Flow of Nematics

A diagram depicting simple shear flow of a nematic polymer is shown in Figure 1.12. The flow direction is along the x-axis, the velocity gradient is along the y-axis and the vorticity direction is along the z-axis. The alignment of the liquid crystal polymer can be affected by shear flow. If the director is fixed within the shear plane (the x-y plane) then it will be subjected to a viscous torque described by the following equation[32]:

(1.29)

$$\Gamma_{vis} = \left( \alpha_3 \sin^2 \theta - \alpha_2 \cos^2 \theta \right) \dot{\gamma}$$

where  $\tau_{vis}$  is the viscous torque density,  $\alpha_2$  and  $\alpha_3$  are Leslie coefficients,  $\theta$  is the director orientation with respect to the velocity gradient direction, and  $\gamma_1 = \alpha_2 - \alpha_3$  is the twist viscosity.

The viscous torque encounters a resistance that stems from the energetic penalty of creating curvature in the director (i.e. bend and splay). This leads to the generation of an elastic torque described by

$$\tau_{el} = h(\theta) \frac{d^2}{dy^2}(\theta) + \frac{1}{2} h'(\theta) \left( \frac{d\theta}{dy} \right)^2 \quad h' = k_{11} \sin^2(\theta) + k_{33} \cos^2(\theta) \quad (1.30)$$

where  $\tau_{el}$  is the elastic torque density and  $k_{11}$  and  $k_{33}$  are the bend and splay elastic constants. Thus it is evident that such fundamental parameters as  $k_{11}$  and  $k_{33}$  affect not only observed defect textures, but presumably also have an effect on the material's viscoelastic responses. If it is assumed that the angular moment of inertia of the director is small, then the viscous and elastic torque densities are equal. It is then possible to solve for the velocity  $v(y)$  and director field using the Leslie-Ericksen constitutive equation.

### 1.8.3 Tumbling and Flow Aligning Nematics

The Leslie coefficients  $\alpha_1$  and  $\alpha_2$  are important material parameters. They can be combined in the ratio,  $\lambda$ , to define the transition between tumbling and flow-aligning behavior[33]:

$$\lambda = \frac{-\alpha_3 - \alpha_2}{\alpha_3 + \alpha_2} \quad (1.31)$$

Tumbling refers to rotation of the director either in or out of the shear plane. Flow-aligning refers to the case where the shear flow aligns the director at a small angle with

respect to the flow direction within the shear plane. When  $\lambda < 0$  the director “tumbles”, but when  $\lambda > 0$  the director becomes “flow-aligned”. The tumbling behavior of the director in certain situations is thought to be the reason why certain polymers show very large disclination densities during shear. In fact, Mather et al. [31] found that a small molecule tumbling nematic, 4,4'-n-octalcyanobiphenyl (8CB), had disclination densities about 10 times that of a related flow aligning small molecule nematic, 4,4'-n-pentylcyanobiphenyl (5CB) which has only a slightly lower molecular weight.

#### 1.8.4 Shear Flow Visualization

A review of the general subject of rheological behavior of liquid crystalline polymers can be found in a paper by Asada and Onogi [32]. A typical curve of log viscosity vs. log shear rate is shown in Figure 1.13a. Three distinct regions can be seen in the curve. Region I is the low shear rate region where the apparent viscosity rapidly decreases with increasing shear rate. Region II is the plateau region (Newtonian) and region III is the high rate region (shear thinning). The exact location of each region will depend on the particular system being examined. The flow properties are strongly affected by the texture of the liquid crystal. In addition, region I has also been shown to be sensitive to sample history. Asada and Onogi make the statement that “disregard of the [liquid crystal] texture often causes misunderstanding or disagreement among investigators. [with respect to rheological properties] This is why we have to utilize rheo-optical techniques for studying liquid crystal systems.”

Although most of the experiments in their paper discuss lyotropic systems, many of the principles are equally applicable to thermotropic systems. Plots of  $\log \eta$  vs  $\log \dot{\gamma}$  for polybenzyl-L-glutamate (PBLG) in m-cresol and hydroxypropylcellulose (HPC) in water are shown in Figure 1.13b. The three regions are readily apparent in these plots. A diagram depicting the likely changes that occur in the director texture of both nematic and cholesteric polymers is shown in Figure 1.14. The authors explain that in a nematic system under quiescent conditions, the overall director distribution is random as a result of point and line defects. When a shear force above a certain magnitude is applied, the molecules are forced to orient in a certain direction and the randomizing effect of the disclinations seems



to be overcome by the shear field. Then a continuous phase (region II) appears that contains small numbers of anisotropic domains. A monodomain continuous phase eventually appears when the orientational effect due to shear force overcomes the effect of the disclinations. The situation is similar for cholesteric systems. Changes in bulk structure roughly correspond to the three regions of viscoelastic behavior. Optical methods are sensitive to local structure, but rheological quantities reflect an overall state of a sample. Thus it is important to consider both rheology and optical properties when studying liquid crystal systems. Certainly direct observation of textural changes during shear will be important for further understanding of the unique rheological behavior of liquid crystals. Shear flow visualization research, begun in the early 1970's and becoming an increasingly popular area of research, refers to the direct examination of shearing processes on sample texture using a shear cell in conjunction with an optical microscope.

The first shear flow visualization work, done by Wahl and Fischer [35][36] relied upon a torsional shear cell. Samples were placed between two parallel plates whose separation was controlled by three fine threaded screws. The bottom plate was attached to a tube in order to produce the shearing action. No provisions were made for temperature control. They performed measurements on a small molecule liquid crystal, 4-methoxybenzylidene-4'-n-butylaniline (MBBA) at room temperature and observed a system of concentric dark and light rings superposed by a dark cross indicating the orientation of the crossed polarizers. At high values of angular velocity and plate separation, they observed the production of disclination lines. They noted that the lines grew in length as they followed the path of the sheared liquid. In addition it was observed that the disclination lines interacted with each other. However no specific information was given as to the nature of the interaction.

In the early 1980's another type of shear cell was developed by Graziano and Mackley [37][38]. Their shearing apparatus consisted of two parallel glass disks where the bottom disk could be rotated, thereby creating a shear flow in the sample. Due to the difficulties in determining an accurate value of the plate separation, they did not cite values for  $\dot{\gamma}$ , although angular velocity could be adjusted from 0.005 to 0.01 rev/sec. Temperature control was made possible in their system by using electrical foil heaters on either side of the glass plates. In their work, Graziano and Mackley studied the effects of controlled shear

programs on the microstructure of various LCP's. They found that shear had a significant effect on the microscopic textures of the LCP's they examined. In particular, they noted that increasing the molecular weight had a similar effect to increasing the shear rate. An increase of either quantity increased the likelihood of transition from a thin threaded texture to the worm texture and eventually to the ordered texture. They defined the worm texture as a sample filled with short and dark lines with a diameter of about 2 microns. These "worms" continually change shape while flowing along the streamlines. However, the authors noted that the information obtained was not sufficient to determine the cause or formation mechanism of these textures.

Graziano and Mackley also carried out studies using the small molecule MBBA and made the observation that a significant difference exists between disclination behavior during flow and during static relaxation. Defect loops subjected to shear had a very sharp contrast, suggesting very severe and localized director distortions. In addition the loops appear to affect alignment only of molecules within a small region around them. Loops elongated, deformed, and tumbled during flow, but never broke apart or split open. During flow both thick and thin lines interacted with their surroundings in a complicated way, but this "interaction" was not described in detail. The number density of both types of lines was found to increase with the shear rate. Upon cessation of shear, thick loops with nodes were seen to split apart and all loops were noticed to relax at a slower rate than the rest of the sample.

In a subsequent paper by Alderman and Mackley [37] with a similar apparatus, shearing was found to result in both multiplication of disclinations as well as a decrease in the distance between individual disclinations. They observed that at initially low angular velocities ( $\omega < 1.0$  rad/sec), the shear only perturbs individual disclinations. In other words, disclinations move but do not deform. When the angular velocity was increased above 0.1 rad/sec, but kept below 1 rad/sec, a sudden increase in the number of disclinations occurred (termed "multiplication"). When  $\omega$  was increased above 1 rad/sec, pure birefringence was observed. Values for  $\dot{\gamma}$  were not cited due to reasons stated earlier. The dense disclination texture was observed only when the material relaxed at extremes in the oscillatory shear cycle. The authors note that the dense disclination texture occurs at a

sharp transition and that the evolution is difficult to interpret. They cite Marrucci [41] and Wissbrun [39] in suggesting that the saturation of birefringence indicates that the material is fully aligned in the direction of flow.

Work by De'Neve, Navard, and Kleman [40] utilized a sliding plate apparatus for rheo-optical studies at low shear rates and also used microtomed capillary extrudates for examination of texture changes at high shear rates. They measured the variation in total light flux transmitted  $\Phi_t$  through the sample as a function of shear strain  $\gamma$  at various shear rates  $\dot{\gamma}$ . It was found that a sudden decrease in  $\Phi_t$  occurred at a well defined shear strain. Above this shear strain, damped oscillations of  $\Phi_t$  were observed. They explain this sudden change by showing that at this critical shear strain, there is a sudden increase in the defect density, reminiscent of the thread to worm texture transitions observed by Graziano and Mackley [36]. The oscillations were thought to be a result of alternating creation and annihilation of defects. A diagram of shear strain vs. the log of the shear rate shows the existence of three types of textures. Their principal conclusion was that the defect texture observed seemed to be a signature of the flow mechanism. The worm-like texture was said to be compatible with tumbling. The ordered texture was compatible with flow aligning. Marrucci and Maffettone [42][43] have described a two-dimensional model used to obtain predictions of transient rheological responses at high shear rates. Their model predicted that between tumbling and non-tumbling regimes, an intermediate range of shear rates exists where the director continuously oscillates between two orientations close to the shear directions. Among their other predictions is that at high shear rates, the oscillation of both tangential and normal stresses damps down towards a steady state value. At low shear rates, damping is not expected unless interactions between domains is considered. Although the authors did not conduct flow visualization studies, their results do suggest that the defects have a significant correlation with rheological properties.

In a more recent paper by Marrucci and Maffettone [43] they state that the behavior of LCP's in shear flow appears to be dominated by tumbling and by the dynamics of the defects. They developed a model of defect dynamics under shear flow that compares well with viscosity curves obtained by Onogi and Asada. In their paper, Marrucci and Maffettone also state that in lyotropic LCP's it has been proven that a negative normal stress marked the transition from tumbling to flow aligning, a non linear phenomenon that

occurs when shear rates become large enough[44]. However, negative normal stresses are not observed very often in thermotropic polymers.

Shear flow of LCP's has also been examined using conoscopy in conjunction with a shear cell by Srinivasarao et. al. [45]. Conoscopy is performed by inserting a Bertrand lens into the optical path, allowing one to see an optical diffraction pattern when looking into the microscope eyepiece. By looking at the symmetry of the conoscopic interference figures, they were able to detect the change from flow aligning to non flow aligning limits.

Work By Mather and the late Professor Pearson [29] examined the shear flow behavior of tumbling and flow aligning nematic liquid crystals. They built a shear cell that was capable of measuring the stress normal in the sample. Their work focused on shear flow behavior in 4,4'-n-pentylcyanobiphenyl (5CB) and 4,4'-n-octylcyanobiphenyl (8CB). They performed the first direct measurements of disclination density in nematic liquid crystals under shear flow. Their pioneering research has opened the way for a greater understanding of and increased opportunities for direct observations of disclination lines and their dynamics in polymer systems.

## **1.9 Introduction to the Thesis**

The primary goal of this thesis is three-fold: to understand the mechanisms by which the various point defects are created during the isotropic to nematic transition and how they subsequently interact both with each other and in applied magnetic and flow fields. Several very specific questions will be addressed. First, is there one underlying mechanism for the generation of point defects or are their individual mechanisms for each type? Secondly, how can one model the structural changes that occur in the final defect texture after a magnetic field is applied to a thin film sample? Thirdly, what forces play a role in the evolution of disclination loops and how can this be modeled theoretically?

The experimental techniques used in this thesis are described in chapter two. The use of optical compensators for determination of anchoring conditions and director field distribution is explained in the section on optical microscopy. A new decoration technique known as solidification-induced banding which is used extensively in this work is also

described in this chapter. A detailed description of the parallel-plate shearing apparatus is also included.

The defect generation mechanisms are discussed in chapter 3. Three regimes of nematic domain development are identified and described with videomicroscopy as well as solidification-induced banding techniques. The origins of the principal types of disclinations (i.e.  $+1/2$ ,  $-1/2$ ,  $+1$ ,  $-1$ ) are discussed individually. Mathematical analysis of domain ellipticity is also described and related to the relative magnitude of the elastic anisotropy.

Chapter 4 describes a series of programs designed to simulate director field distributions and the associated polarized light images. In the first section of the chapter, the programs are used to produce simulations for defects with strengths ranging from  $-1/2$  to  $+4$ . In the second section of the chapter, the programs are used to address the controversy surrounding the nature of defects of high strength (i.e.  $s > 1$ ). The results from the computer simulations are combined with the results of chapter 3 to show that these high strength defects cannot normally exist in static situations for the polymer system used in this work.

Chapter 5 describes the effect of magnetic fields on the structure of Néel walls. Mathematical techniques for determining director trajectories as a function of elastic anisotropy are described in detail. Several other techniques are described whereby the elastic anisotropy can be extracted directly from AFM micrographs. The results of these techniques compare favorably with other methods of determining the elastic anisotropy.

Chapter 6 describes the curvature motion of disclination loops of both small molecule and polymer liquid crystals after cessation of shear flow. An understanding of how line tension affects the morphology of these defects can be gained by studying the way in which the local curvature evolves over time. Theories of differential geometry were used along with a level set computer method to determine a relationship between velocity and curvature for the systems examined in this thesis. Experimental results describing a linear relationship between velocity and local curvature compared favorably with the experiments on both polymers and small molecules. Although the line tension led to a similar curvature evolution process, the morphology of the disclinations was significantly different between the small molecules and the polymer examined. The polymer was characterized by irregularly shaped disclination loops with typically several regions of high

curvature in each one. The disclination loop structures seen in the small molecule system were always much simpler, typically circular, oval or extended lines. Such structures appeared in the polymer system only over much longer time periods. These findings will be discussed from both an experimental and theoretical point of view in that chapter.

- [1] Rojstaczer, S.R. and Stein, R.S., "Effect of Thermal History on the Nematic State of a Thermotropic Liquid Crystal Polymer", *Macromolecules*, **23**, 4863-4867, 1990
- [2] Williams, D.R.M. and Halperin, A., "Nematic Polymers: hairpins, ringlets, and excimer fluorescence.", *J. de Phys. II, France*, **3**, 68-89, 1990
- [3] *In Science*, **273**, 100, 1996
- [4] Chandrasekhar, S. and Ranganath, C.S., "The Structure and Energy of Defects in Liquid Crystals", *Adv. Phys.*, **35**(6), 507-596, 1986
- [5] Blackwood, K.M., "Device Applications of Side-Chain Ferroelectric Liquid Crystalline Polymer Films", *Science*, **273**, 909-912, 1996
- [6] Elston, S.J. and Ulrich, D.C., "Pulsed Laser Written Diffraction Gratings in Liquid Crystal Polymers", *J. Modern Optics.*, **42**(5), 1023-1035, 1995
- [7] Chandrasekhar, S., Liquid Crystals, Cambridge Univ. Press, Cambridge, 1996
- [8] Kleman, M., "Defects in Liquid-Crystalline Polymers", *MRS Bulletin.*, September 1995
- [9] Allen, S.M and Thomas, E.L., The Structure of Materials, John Wiley and Sons, New York, 1996
- [10] Volterra, V., *Ann. Ecole Normale Super. (Paris)*, **3**, 400, 1907
- [11] Demus, D. and Richter, L., Textures of Liquid Crystals., Verlag Chemie, Weinheim, 1978
- [12] Frank, C., "On the Theory of Liquid Crystals", *Discuss. Faraday Soc.*, **25**, 19-28, 1958
- [13] deGennes, P.G., 1974, The Physics of Liquid Crystals, Oxford University Press, Oxford, 1974
- [14] Zheng-Min, S. and Kleman, M., "Measurement of the Three Elastic Constants and the Shear Viscosity  $\gamma_1$  in a Main-Chain Nematic Polymer", *Mol. Cryst. Liq. Cryst.*, **111**, 321-328, 1984
- [15] Meyer, R., Macroscopic Phenomena in Nematic Polymers, Polymer Liquid Crystals, ed. A. Ciferri, W.R. Krigbaum and R.B. Meyer, Academic Press, 1982

- [16] deGennes, P.G., "Polymeric Liquid Crystals: Frank Elasticity and Light Scattering", *Mol. Cryst. Liq. Cryst. Lett.*, **34**, 177, 1977
- [17] DuPre, D.B. and Duke, R.W., "Temperature, Concentration and Molecular Weight Dependence of the Twist Elastic Constant of Cholesteric Poly- $\gamma$ -benzyl-L-glutamate", *J. Chem. Phys.*, **63**, 143, 1975
- [18] Saupe, A., "Temperature Dependence of the Elastic Constants of a Nematic Liquid Crystal", *Z. Naturforsch.*, **15a**, 810, 1960
- [19] Ding, D.K. and Thomas, E.L., "Structures of Point Integer Disclinations and Their Annihilation Behavior in Thermotropic Liquid Crystal Polyesters", *Mol. Cryst. Liq. Cryst.*, **241**, 103-117, 1995
- [20] Nehring, J. and Saupe, A., *J. Chem. Soc. Faraday Trans. II*, 1972, 68, 1
- [21] Mazelet, M. and Kleman, M., "Observation of Defects in a Polyester Nematic Phase: 2", *Polymer*, **27**(5), 714-720, 1986
- [22] Meyer, R.B., "The Interaction Between a Disclination in a Nematic Liquid Crystal and a Rubbed Surface", *Sol. St. Commun.*, **12**, 585-588, 1973.
- [23] Hudson, S.D. and Thomas, E.L., "Frank Elastic Constant Anisotropy Measured From TEM Images of Disclinations", *Phys. Rev. Lett.*, **62**(17), 1993-1996, 1989
- [24] Kleman, M., Points, Lines, and Walls, Wiley, Chichester, 1983
- [25] Stephen, M.J. and Straley, J.P., *Rev. Mod. Phys.*, **46**, 617, 1974
- [26] Graziano, D.J. and Mackley, M.R., "Disclinations Observed During the Shear of MBBA", *Mol. Cryst. Liq. Cryst.*, **106**, 73-79, 1984
- [27] Marrucci, G., "Rheology of Liquid Crystalline Polymers", *Pure Appl. Chem.*, **57**, 1545-1552, 1985
- [28] Mather, P.T., Ph.D. thesis, University of California at Santa Barbara, Department of Materials, June 1994
- [29] Mather, P., Grizzuti, N., Heffner, G., Ricker, M., Rochefort, W.E., Seitz, M., Schmidt, H-W and Pearson, D.S., "Synthesis and Characterization of a Semiflexible Liquid Crystalline Polyester with a Broad Nematic Region", *Liq. Cryst.*, 1995



- [30] Leslie, P.M., "Some Constitutive Equations for Liquid Crystals", *Arch. Rat., Mech. Anal.*, **28**, 265-270, 1966
- [31] Larson, R.L., "Roll-Cell Instabilities in Shearing Flows of Nematic Polymers", *J. Rheol.*, **37**(2), 175, 1993
- [32] Asada, T. and Onogi, S., "Rheology and Rheo-Optical Studies of a Polyester Liquid Crystal", *Polym. Eng. Rev.*, 3(2-4), 323-353, 1983
- [33] Wahl, J. and Fischer, F., *Mol. Cryst. Liq. Cryst.*, **22**, 359-373, 1973
- [34] Wahl, J. and Fischer, F., "A New Optical Method for Studying the Viscoelastic Behavior of Nematic Liquid Crystals", *Optics Comm.*, **5**, 341-346, 1972
- [35] Graziano, D.J., Ph.D. Thesis, University of Cambridge, 1983
- [36] Graziano, D.J. and Mackley, M.R., "Shear Induced Optical Textures and Their Relaxation Behavior in Thermotropic Liquid Crystalline Polymers", *Mol. Cryst. Liq. Cryst.*, **106**, 73-79, 1984
- [37] Alderman, D. and Mackley, M.R., "Optical Textures Observed During the Shearing of Thermotropic Liquid-Crystal Polymers", *Faraday Discuss. Chem. Soc.*, 1985, 79, paper 12
- [38] Marrucci, G., paper presented at the Int. Congr. Rheology, Acapulco, 1984
- [39] Wissbrun, K.F., "A Model for Domain Flow of Liquid-Crystal Polymers", *Faraday Discuss. Chem. Soc.*, 1985
- [40] De'Neve, T., Navard, P., and Kleman, M., "Shear Rheology and Shear-Induced Textures of a Thermotropic Copolyesteramide", *J. Rheol.*, **37**, 515-529, 1991,
- [41] Marrucci, G. and Maffetone, P.L., *Macromolecules*, 1989, **22**, 4076
- [42] Marrucci, G. and Maffetone, P.L., *J. Rheol.*, **34**(8), 1217-1244, 1990
- [43] Marrucci, G. and Maffetone, Proceedings of Cafri meeting on Liquid Crystal Polymers, June 1993
- [44] Larson, R.G., "Arrested Tumbling in Shearing Flows of Liquid Crystal Polymers", *Macromolecules*, **23**, 3983-3992, 1989

[45] Srinivasarao, M., Garag, R.O., Winter, H.H., and Stein, R.S., "Rheo-Optical Properties of a Thermotropic Liquid Crystalline Polymer", *Mol. Cryst. Liq. Cryst.*, **223**, 29-39, 1992

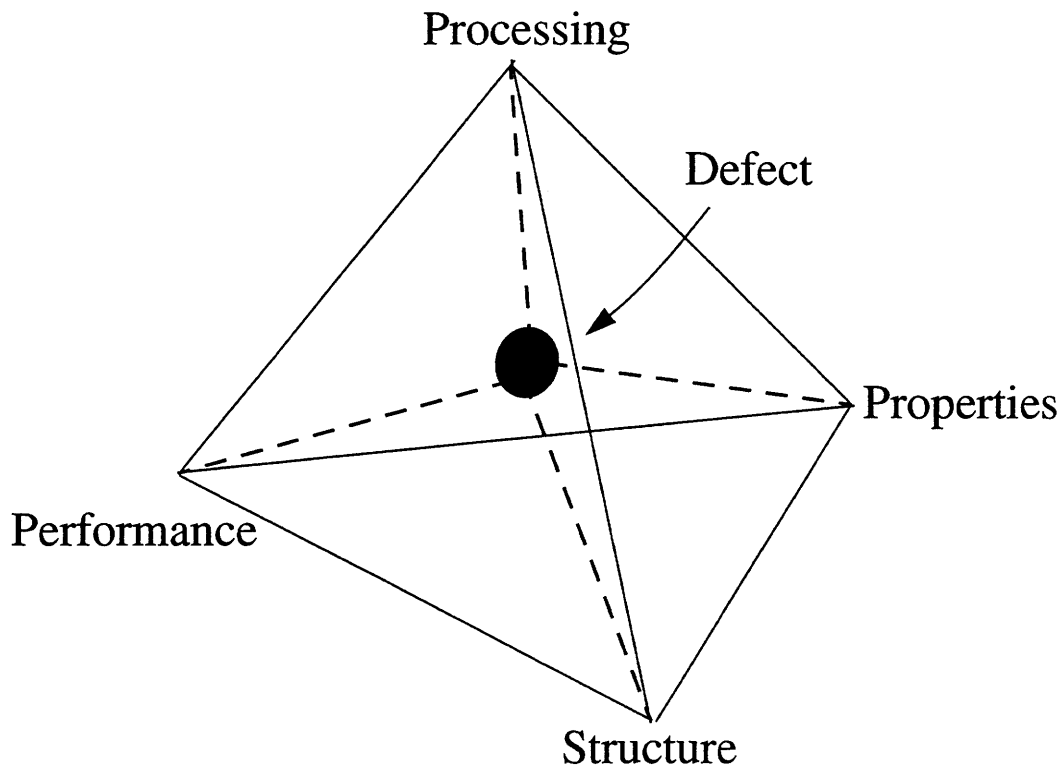


**Figure 1.1:** This schematic emphasizes the interconnections between structure, properties, processing and performance. The defect placed at the center of the pyramid can have a strong influence on all the other parameters.

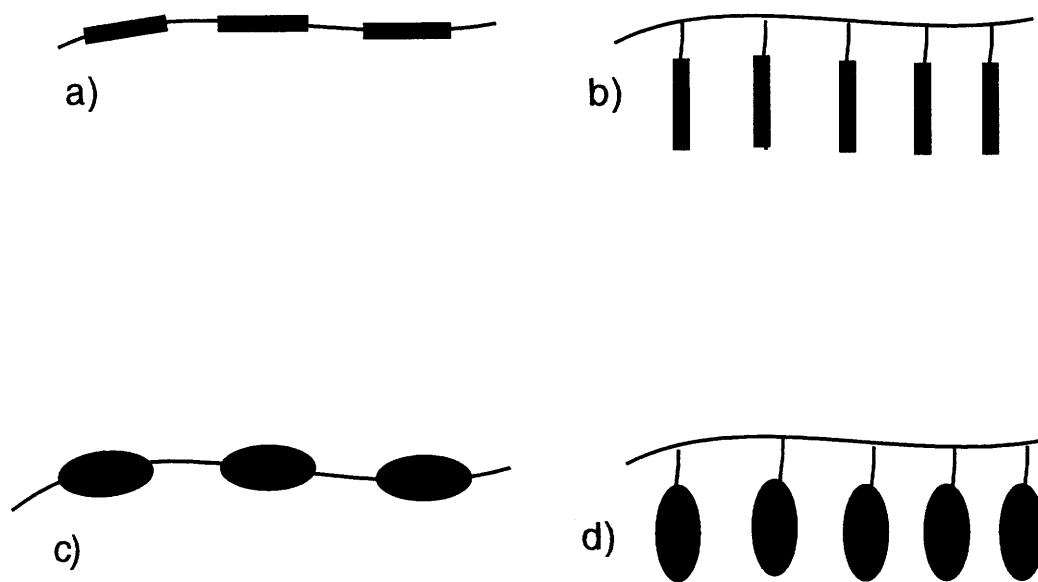


**Figure 1.2:** a) A schematic depicting a rod-like liquid crystal with mesogens in the main-chain. b) A similar material but with the mesogens in the side-chain. c) A disk-like main-chain liquid crystal. d) A disk-like side-chain liquid crystal

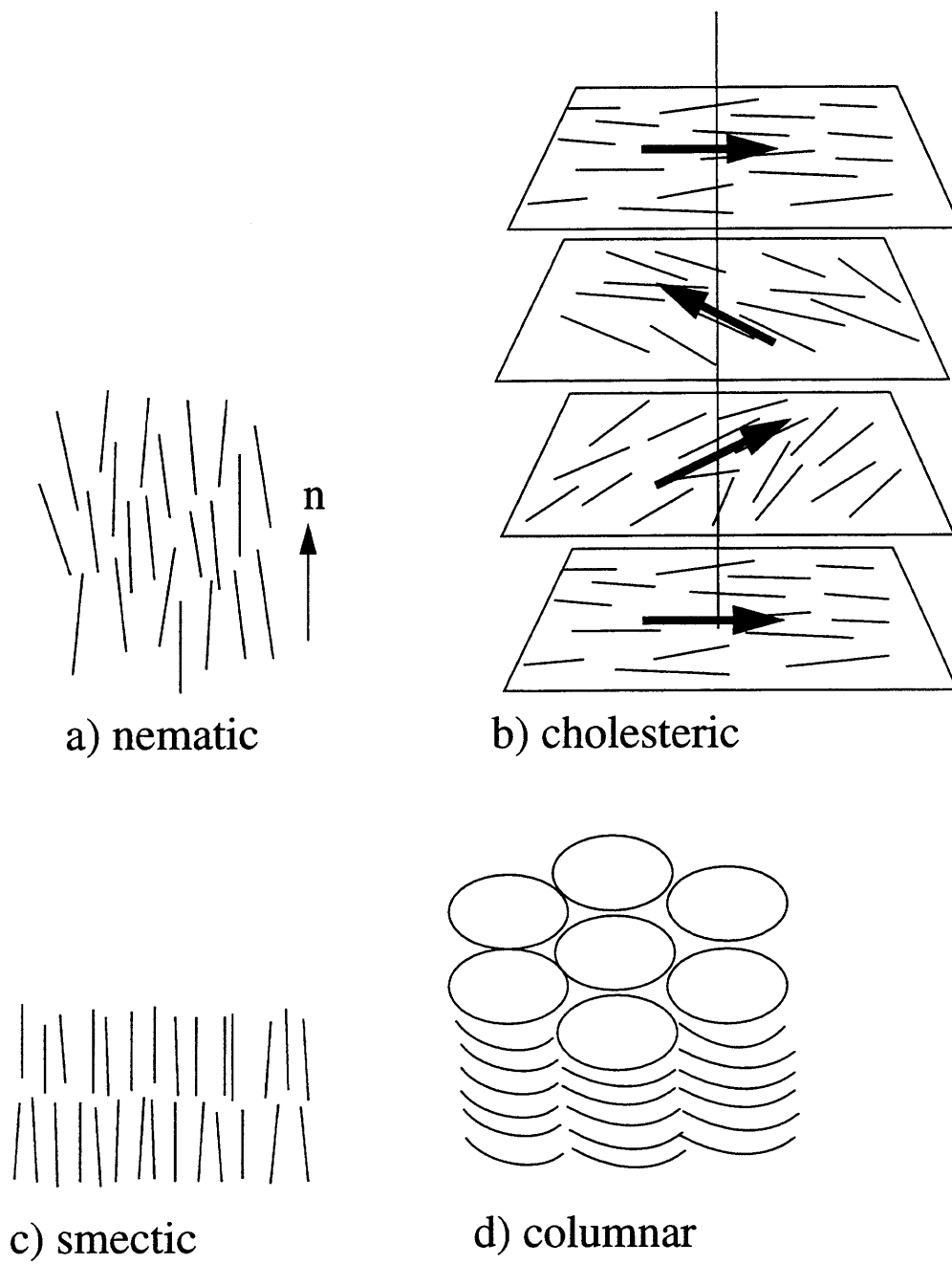
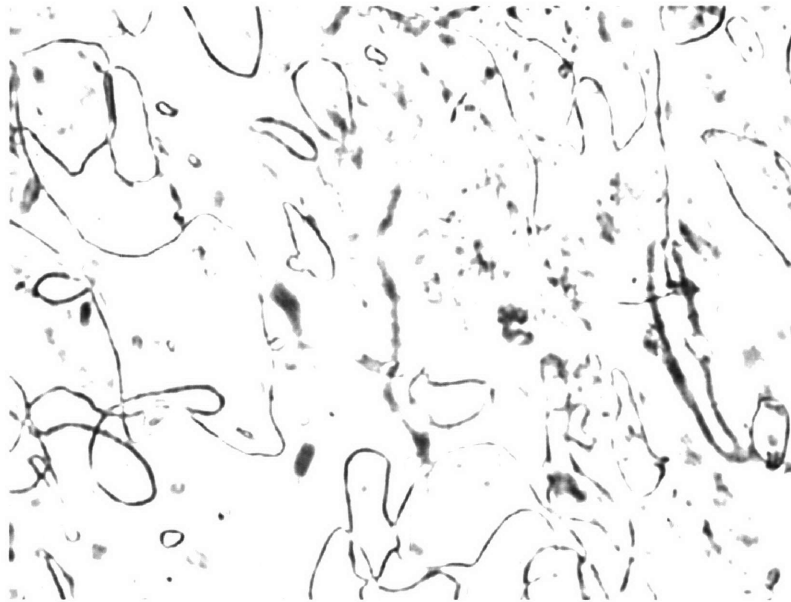


**Figure 1.3:** Schematics depicting the main liquid crystalline phases a) nematic b) cholesteric c) smectic d) columnar



— 10  $\mu\text{m}$



— 50  $\mu\text{m}$

**Figure 1.4:** Examples of various types of defect ‘textures’. a) A schlieren texture as seen in crossed polarized transmitted light using the nematic liquid crystal DHMS-7,9. The black brushes emanate from the cores of the defects. b) A threaded texture. The defects are disclination lines and loops that are viewed with crossed polarized light with the polymer Vectra B950.

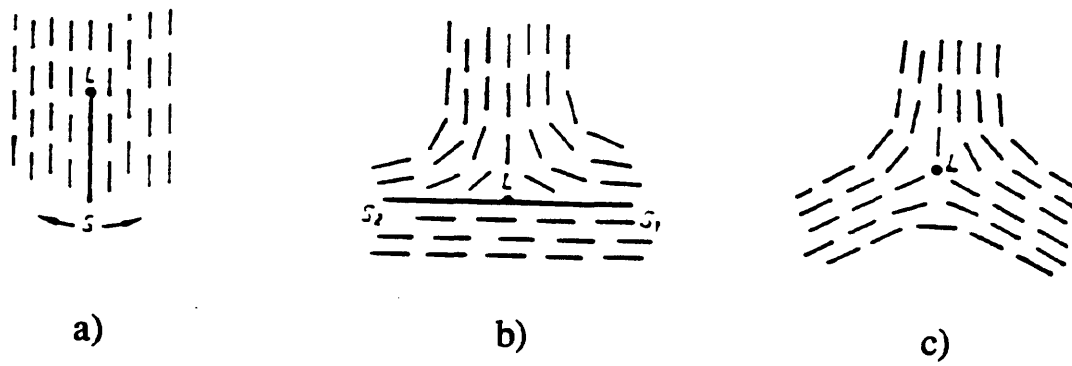
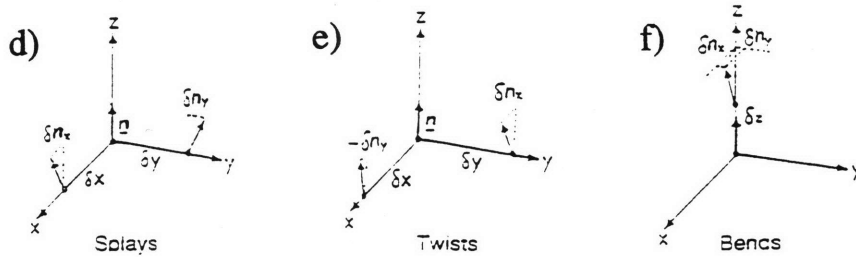
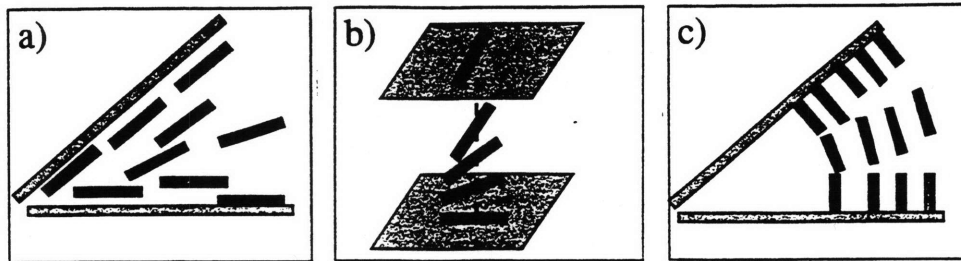


**Figure 1.5:** A schematic depicting the Volterra process for the generation of a defect (in this case an  $s=-1/2$ ). a) A monodomain is cut along a surface that is bounded by a line L. b) The surfaces marked  $S_1$  and  $S_2$  of the cut are moved apart and excess material is put in the gap. c) The material is allowed to relax, thus producing the line defect. (after Volterra [10])



$$\text{Splay} \Rightarrow K_{11} \quad \text{Twist} \Rightarrow K_{22} \quad \text{Bend} \Rightarrow K_{33}$$

**Figure 1.6:** a-c) Schematics depicting splay, twist, and bend distortions pictorially. d-f) Graphical representations of the corresponding distortions. The splay is related to the divergence of the director while twist and bend are respectively the parallel and perpendicular components of the curl of the director field. (after Frank [12])



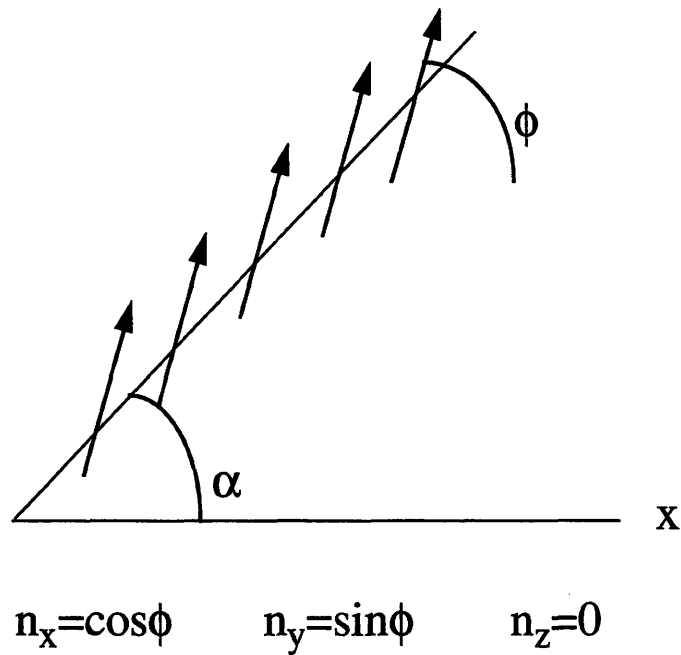


**Figure 1.7:** A schematic depicting the geometry used in generating 2D director field distribution equations. The angle  $\phi$  represents the angle between the director field and the frame of reference (the x axis). The angle  $\alpha$  is the angle between the director and a polar line along which the measurements are made. The components of the director are indicated below the schematic.

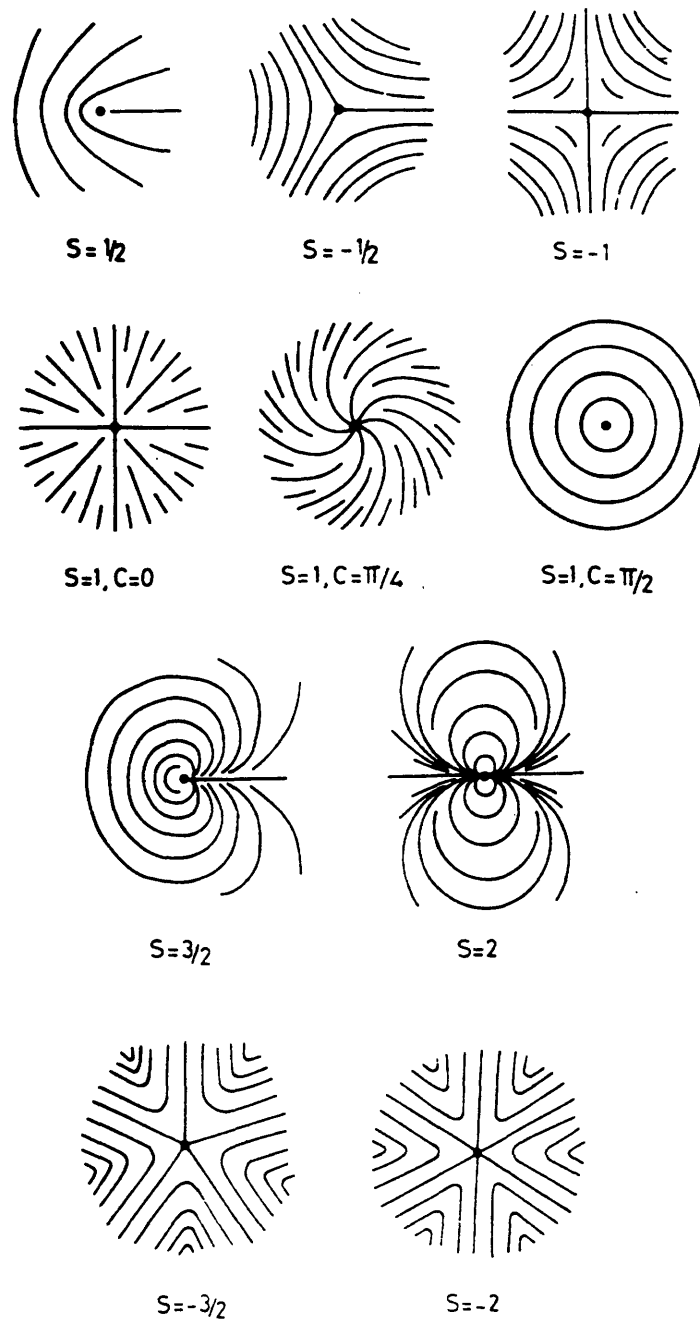


**Figure 1.8:** Plots of the director field distribution for various values of  $s$  and  $c$ . (after Frank [12])

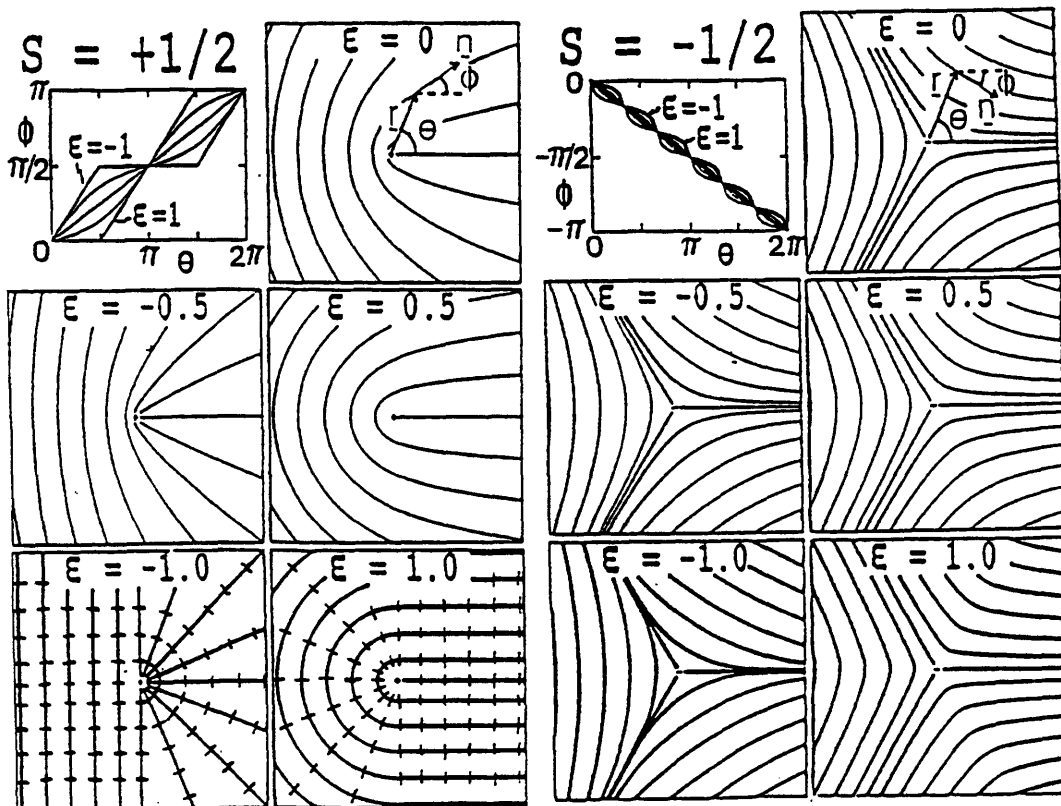


**Figure 1.9:** Plots depicting changes in the director field distribution as a function of elastic anisotropy for an  $s=+1/2$  defect and  $s=-1/2$  defect. (Hudson and Thomas [23]) In all cases the director field distribution reorients in order to minimize the more costly distortion.

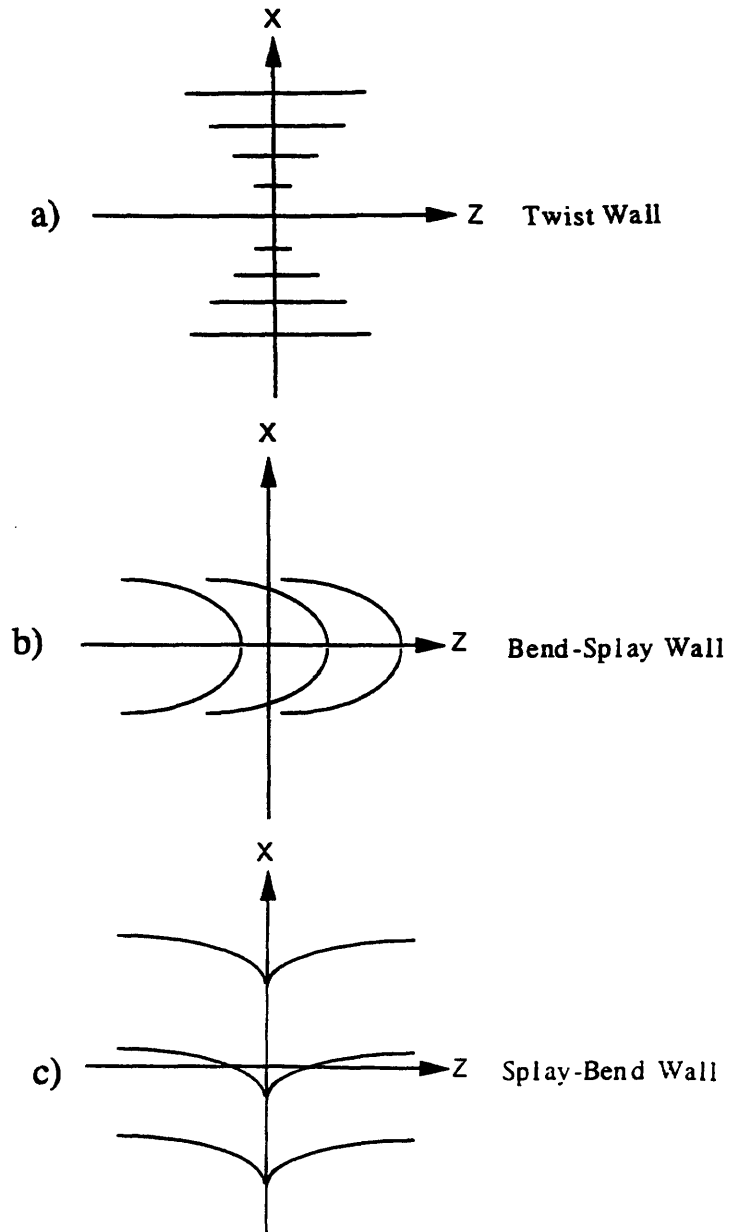


**Figure 1.10:** Schematics depicting the three main types of walls. a) a twist wall that involves out-of-plane deformations b) a Néel bend-splay wall. The director is confined to the  $xz$  plane. The transition across the wall occurs mainly through bend deformations. c) a Néel splay-bend wall. The director is again confined to the  $xz$  plane. The transition across the wall occurs mainly through splay deformations.

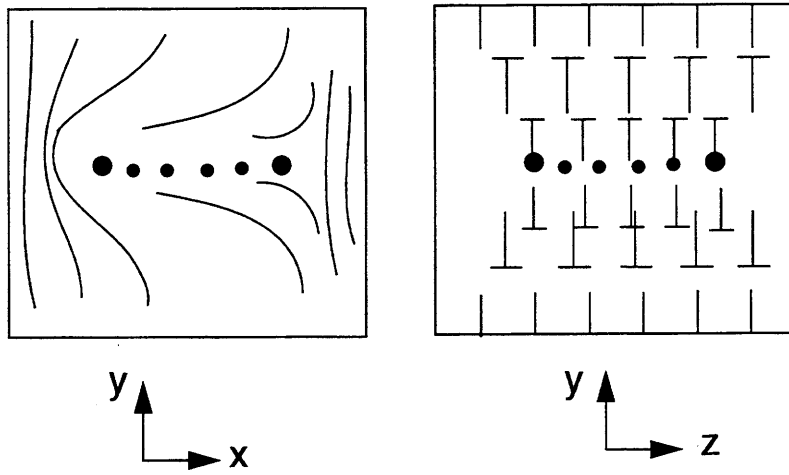


**Figure 1.11:** a) The director field distribution for a thin thread ( $s=1/2$ ) (after Mackley [30])

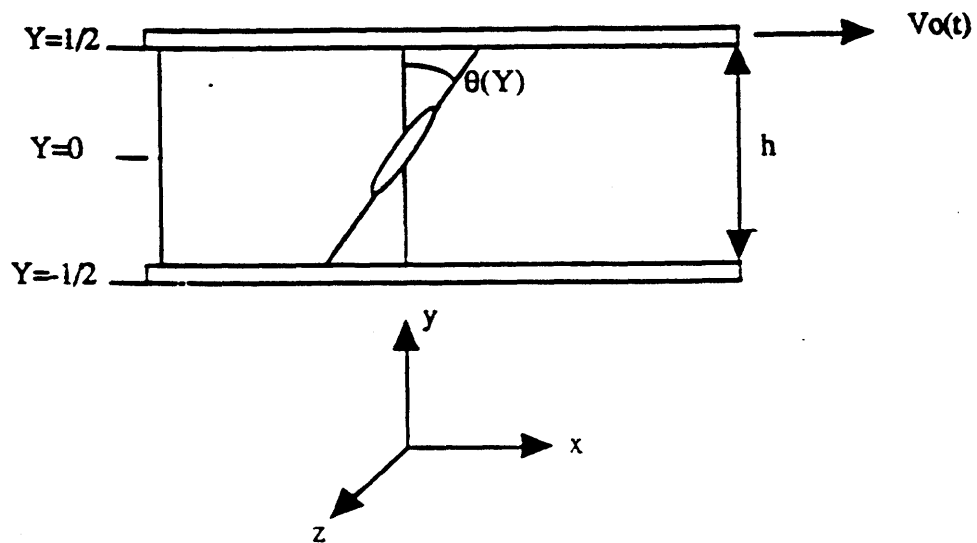


**Figure 1.12:** A diagram depicting simple shear flow in a nematic

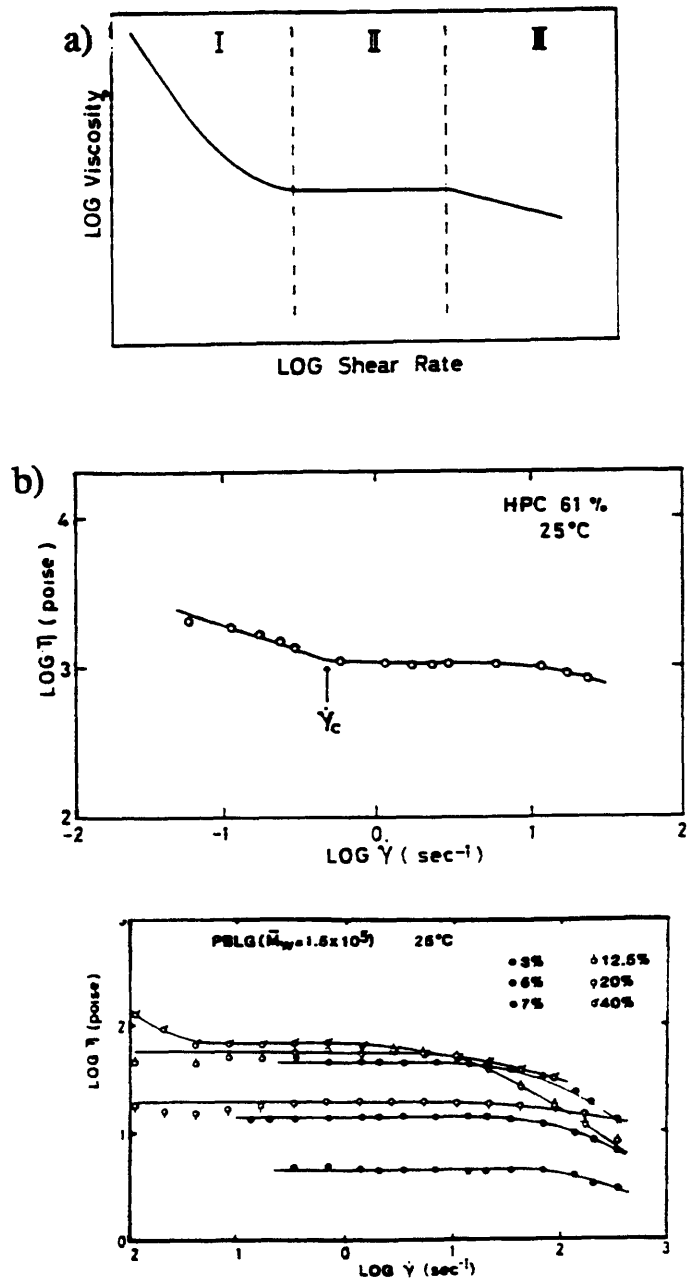


**Figure 1.13:** a) A typical curve of log viscosity vs log shear rate for a polymer. Region I is the low shear rate region where the apparent viscosity rapidly decreases with increasing shear rate. Region II is the plateau region (Newtonian) and region III is the high shear rate region (shear thinning). The exact location of each region will depend on the material. b) Actual plots for some lyotropic liquid crystals.[32]

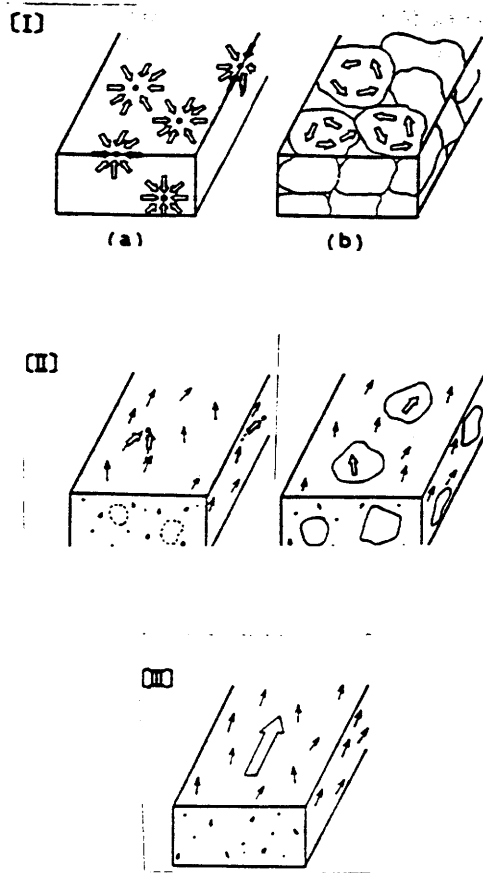


**Figure 1.14:** A diagram depicting the likely changes that occur in the various regions.[32]





Institute Archives and Special Collections  
Room 14N-118  
The Libraries  
Massachusetts Institute of Technology  
Cambridge, Massachusetts 02139-4307

**There is no text material missing here.  
Pages have been incorrectly numbered.**

# Chapter 2

## Experimental Techniques

### 2.1 Introduction

There are many techniques that can be used to study the defect texture of liquid crystals. These include polarizing optical microscopy, electron microscopy (SEM and TEM), atomic force microscopy (AFM) and in-situ shear visualization[1][2]. This chapter describes the particular techniques used in this thesis.

### 2.2 Light Microscopy

Light microscopy has several modes of operation, which are used extensively in this research. Transmission bright and dark field light microscopy give information based on differences in scattering of light. The phase contrast mode gives information on differences in refractive index, which is useful for determining the structure of two-phase systems. Interference contrast relies on variations in differential phase shifts of transmitted or reflected light to give information on the surface structure of a sample. One of the most important modes to be used in this research is polarized transmitted light microscopy. Information on the orientation of the sample can be obtained by placing it between crossed polars [3]. When natural light is incident on an ideal linear polarizer, with a transmission axis  $P$ , only light with a component of  $E$  parallel to  $P$  will be transmitted. This transmitted light then approaches a second ideal polarizer (called an analyzer) with a transmission axis  $A$  oriented at an angle  $\theta$  with respect to  $P$ . If the amplitude of the electric field transmitted by the polarizer is  $E_o$ , then only the component  $E_o \cos(\theta)$  parallel to  $A$  will be transmitted and reach the detector (the microscope eyepiece for example). If  $P$  and  $A$  are perpendicular, then no light will reach the detector. If an optically anisotropic sample is placed between  $P$  and  $A$  then the direction of the light will be changed as it passes through the

sample.

As discussed in Chapter 1, the strength of a defect can be determined by the number of dark brushes that emanate from the core of the defect. In order to determine the sign of a defect the polarizer and analyzer must be rotated relative to the sample. When the direction of brush rotation is the same as that of P and A then the sign is said to be positive. It is negative when the brushes rotate in the opposite direction. The speed with which the brushes rotate relative to P and A is also important. Half integer defects ( $s=|1/2|$ ) rotate twice as fast as P and A while integer defects ( $s=|1|$ ) rotate at the same speed.

### 2.2.1 Use of Compensators

Crossed polars alone only tell whether the optical axis of the sample is parallel or perpendicular to the polarizer. In order to distinguish between these situations one must make use of optical compensators. These are commonly known as quarterwave plates and first order red plates. The first order red plate and the quarterwave plate magnify or reduce the path differences of the specimen by approximately 550 and 140 nm respectively. Liquid crystals of the main-chain type generally have a smaller index of refraction (fast component) along the main molecular axis. As a result, when the molecular axis (and thus the director) is parallel to the fast component of the quarterwave plate, the interference color shifts to a larger wavelength. In samples of approximately 5 micron thickness this would appear as a change from gray to yellow. If the molecular axis was perpendicular to the fast component of the quarterwave plate then the interference color would shift to a lower value (e.g. gray to blue)[3]. The effect of the first order red plate is exactly the opposite. Both types of compensators are useful for determining the molecular orientation around defect cores as well as determining anchoring conditions.

An example of how this is accomplished is shown in Figure 2.1 [4]. The color of the sample under crossed polars only is located on a color chart such as the one shown in Figure 2.1. The first example (Figure 2.2a) shows a defect of the type  $s=+1$ ,  $c=\frac{\pi}{2}$ . It is assumed that the fast component is along the main molecular axis. When this is true, a quarterwave plate would produce the pattern shown in Figure 2.2b. A first order wave plate would have the opposite effect (Figure 2.2c). If the defect were an  $s=+1$ ,  $c=0$  type

instead, a quarterwave plate would have produced the pattern shown in Figure 2.2e. A first order wave plate would have produced the pattern show in Figure 2.2f.

### **2.2.2 Solidification-Induced Banding**

It is well known that shear or extensional flow can induce a banded texture in both lyotropic and thermotropic liquid crystals.[5][6][7][8][9] The bands are an optical effect that arises as a result of the zig-zag pattern that the molecules form. In an optical microscope these appear as alternating dark and light stripes. Within the last few years, several authors have reported that bands can also form upon quenching a liquid crystal that has not been subjected to shear.[11][12][13][14] The bands form normal to the director which provides the contrast in the optical microscope. The exact mechanisms by which the bands form is still not clear, but is most likely a result of anisotropic volume changes than occur upon quenching.

The solidification-banding technique can be used to study the director field distribution in liquid crystals that are not amenable to the lamellar decoration technique. Figure 2.2 shows several schematics that depict the way in which a banded texture can be used as an alternative means of decorating the director field distribution.

## **2.3 Atomic Force Microscopy**

Atomic Force Microscopy (AFM), is a high resolution technique that is non-destructive, thus making it possible to conduct evolutionary or dynamic studies of a sample. In this type of microscopy, a piezoelectric scanner performs a raster scan in the X-Y plane parallel to the surface of the sample. The topography of a sample is measured by sensing the deflection of a cantilever that is held either in contact or slightly above the moving sample. Circuitry within the AFM translates the recorded deflections into a topographic map of the surface. [15] The lamellar decoration technique developed by Wood and Thomas [16] can be used to provide a constrast mechanism for AFM. In this technique a sample is prepared in the nematic state and then quenched to room temperature. It is then subsequently

annealed at a temperature that is above the glass transition temperature but below the melting temperature. This makes it possible for small lamellae to grow normal to the director. In general these lamellae appear edge-on at the surface of the sample and protrude a few nanometers above the surface, making it possible to study the defect topology. This is illustrated in Figure 2.4.

## **2.4 Optical Shearing Apparatus**

A new type of in-situ flow visualization apparatus known as an Optical Shearing Apparatus or shear cell was also used in this work. This machine was developed by Dr. Malcolm Mackley of Cambridge University, UK in conjunction with Linkham Scientific Instruments, Ltd. This machine is unique in that it enables visualization of microstructural responses to shear in situ. Such studies have been relatively rare.

A schematic of this apparatus is shown in Figure 2.5. It has been designed to fit on any optical microscope and can span temperature ranges from room temperature to 450 C. The sample is placed between two quartz windows which are in close thermal contact with a silver block heater. The bottom window is attached to a metal disk which can rotate under the control of a stepper motor. The top window is fixed to a removable lid section to allow for easy cleaning and sample loading. The stepper motor is micro-stepped which allows for a resolution of 25,600 steps per revolution to be achieved. The motor can produce three types of shearing modes: steady shear, step movement at a constant shear rate, and an oscillatory mode with constant frequency and amplitude. It is also possible to sweep frequency or shear in oscillatory mode. The gap between the quartz windows can be set from 10 microns to 2500 microns with an accuracy of about 5 microns. It is controlled by a second stepper motor and several micrometers. The speed at which the lid moves up and down can also be adjusted. Reference positions for the upper and lower lid are set by sensors in the body and lid.

The machine is driven from a windows application on a PC. The electronics are housed separately, so only a simple connection through the computer's serial port is necessary. On-screen control is provided for setting the main gap and the temperature limits and

rates. The temperature can be programmed with up to nine ramps (heat or cool to a specified limit) but can also be held, raised or lowered instantly, thus allowing the user to hold the temperature or to repeat part of a temperature cycle when a particular event has occurred. All the motor functions are programmable and are entered using a spreadsheet, the contents of which may be saved and recalled for future use. The motor's velocity, amplitude, and frequency can all be changed while the shear cell is running, by typing a new value into one of the rows of the spreadsheet. A separate 'jog' function allows the user to control both the gap setting motor and the main motor in small increments enabling easier set up of the sample both physically and optically. Table 1 lists the possible functions and speeds that are available. The shear rate and strain ranges shown in the table are based on a window observation radius of 7.5mm and a gap variation of 10 to 2500 microns. Not all combinations of frequency and amplitude are possible in oscillatory mode since the system cannot follow both high amplitude and high frequency.

A careful cleaning procedure is followed to help ensure that the gap calibration will be as precise as possible. First, the quartz windows are soaked in an appropriate solvent (chloroform in this case) in order to remove excess polymer. Then the windows are subsequently rinsed with a sequence of ethanol and dish soap/water. This cycle is repeated until all residue is removed. If some residue remains even after 3 cycles, the windows are left in a bath of KOH and Y ethanol overnight. Following this treatment, the windows would then be subjected to one cycle of the above cleaning procedure. Before performing the gap calibration, the window holders inside the machine are cleaned using Dust-Off spray. Tiny particles of dust must be removed from these holders as well as the plates themselves in order to insure parallelism. Even small amounts of dust underneath a window can cause the upper lid to wobble when working at very small gaps. The electronic calibration procedure is carried out at the temperature used in the experiments to take into account the effects of thermal expansion. Initial work with this apparatus showed that a calibration at room temperature did not yield the same gap as a calibration carried out at elevated temperatures (250 C for example).

To date, sample loading remains problematic due to the creation of air bubbles as the sample spreads out on the plates. To minimize this problem, a small disk of sample is made by melting the polymer on a hotstage. The small lump of sample is then pressed into

a small disk shape to eliminate air bubbles. Once the disk is formed it is loaded onto the center of the bottom plate and the gap is closed to the desired setting. The amount of sample needed for an experiment depends primarily on the gap setting. Typical amounts used for an experiment range from 30 to 100 mg.

- [1] Freeman, W.J., Characterization of Polymers, in Encyclopedia of Polymer Science and Technology, Vol.3, p. 304, Mark, H.F., Bikales, N.M., Overberger, C.G., Menges, G., and Kroschwitz, J.I., eds., New York:John Wiley and Sons, 1985
- [2] Hobbs, S.Y., "Polymer Microscopy", *J. Macromol. Sci. Rev.Macromol. Chem.*,**19**, 221, 1980
- [3] Hecht, E., Optics, Addison-Wesley, Reading, MA, 1987
- [4] Zeiss Axioskop operating manual
- [5] Kiss, G. and Porter, R.S., "Rheo-Optical Studies of Liquid Crystalline Solutions of Helical Polypeptides", *Mol. Cryst. Liq. Cryst.*, **60**, 267-280, 1980
- [6] Marrucci, G. and Grizzuti, N., and Buonauro, A., "Band Formation in Sheared HPC Solutions. Effects of Sample Thickness", *Mol. Cryst. Liq. Cryst.*, *B*, **153**, 263 , 1987
- [7] Marsano, E. and Carpaneto, L., and Cifferi, A., *Mol. Cryst. Liq. Cryst.*, *B*, **155**, 267, 1988
- [8] Chen, S. and Qian, R., "A Study of Band Texture Formation of Nematic Solutions of Poly(1,4-phenyleneterephthalamide) in sulfuric acid", *Makromolek. Chem.*, **191**, 2475, 1990
- [9] Qian, R. and Chen, S., "Band Texture Formation of Sheared Polymeric Liquid Crystalline State", *Makromolek. Chem., Macromolek. Symp.*, **53**, 345, 1992
- [10] Navard, P., "Formation of Band Textures in Hydroxypropylcellulose Liquid Crystals", *J. Polym. Sci. Polym. Phys.*, **24**, 435, 1986
- [11] Chen, S., Du, C., Jin, Y., Qian, R., and Zhou, Q., *Mol. Cryst. Liq. Cryst.*, **188**, 197, 1990
- [12] Hoff, M., Kellar, A., Odell, J.A., and Percec, V., *Polymer*, **34**, 1800, 1993
- [13] Chen, S., Song, W., Jin, Y., and Qian, R., *Liq. Cryst.*, **15**, 247, 1993
- [14] Wenhui, S., Shouxi, C., Yongze, J., and Renyuan, Q., *Liq. Cryst.*, **19**(5), 549, 1995
- [15] Nanoscope III AFM Manual
- [16] Wood, B.A. and Thomas, E.L., "Are Domains of Liquid Crystalline Polymers Arrays of Disclinations?", *Nature*, **324**, 655-657, 1986



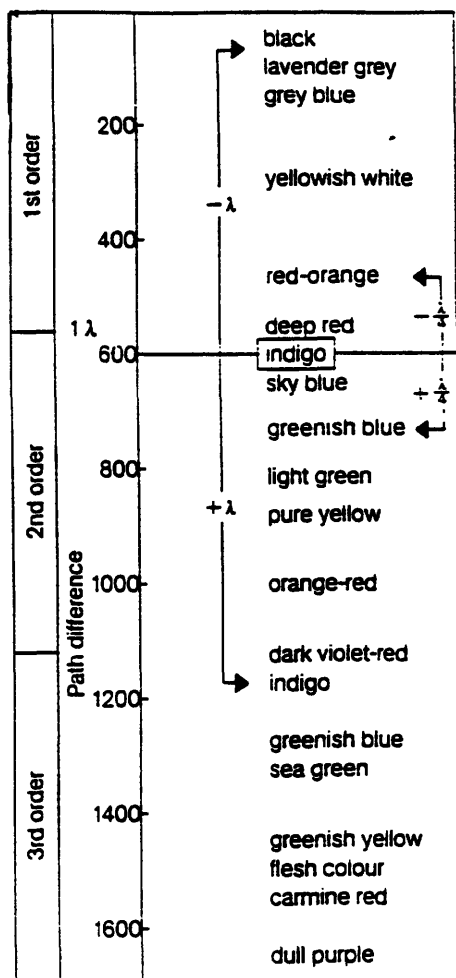
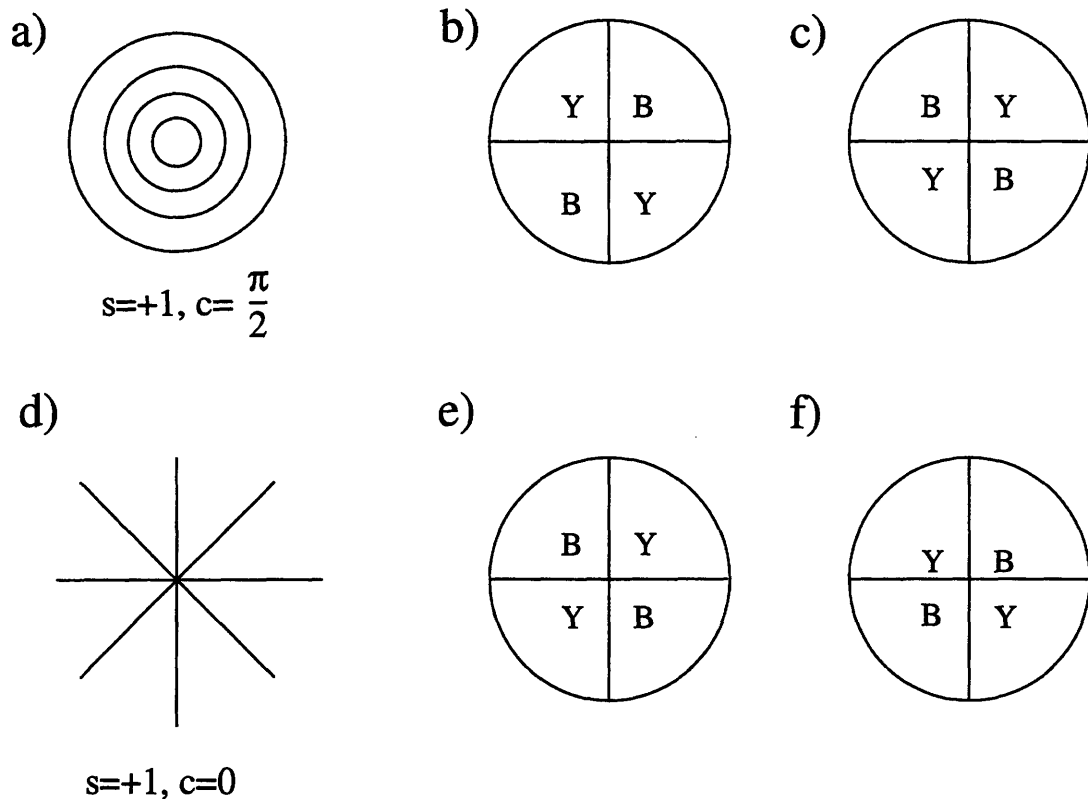


**Figure 2.1:** An example of the color chart used for determining molecular orientation in conjunction with a quarterwave plate and a first order red plate [4].

Director Field Distribution      Quarterwave plate      First order red plate



Y=yellow, B=blue

**Figure 2.2:** Schematics depicting the use of compensators for determining molecular orientation. It is assumed that the original sample has a light gray color. a) An  $s=+1, c=\frac{\pi}{2}$  defect. b) The color change that occurs when a quarterwave plate is inserted in the optical path. c) The color change for a first order red plate. d) An  $s=+1, c=0$  defect. e) and f) The changes for a quarterwave plate and first order red plate respectively. Note that the color shifts for the  $s=+1, c=\frac{\pi}{2}$  defect are the opposite those of the  $s=+1, c=0$  defect.

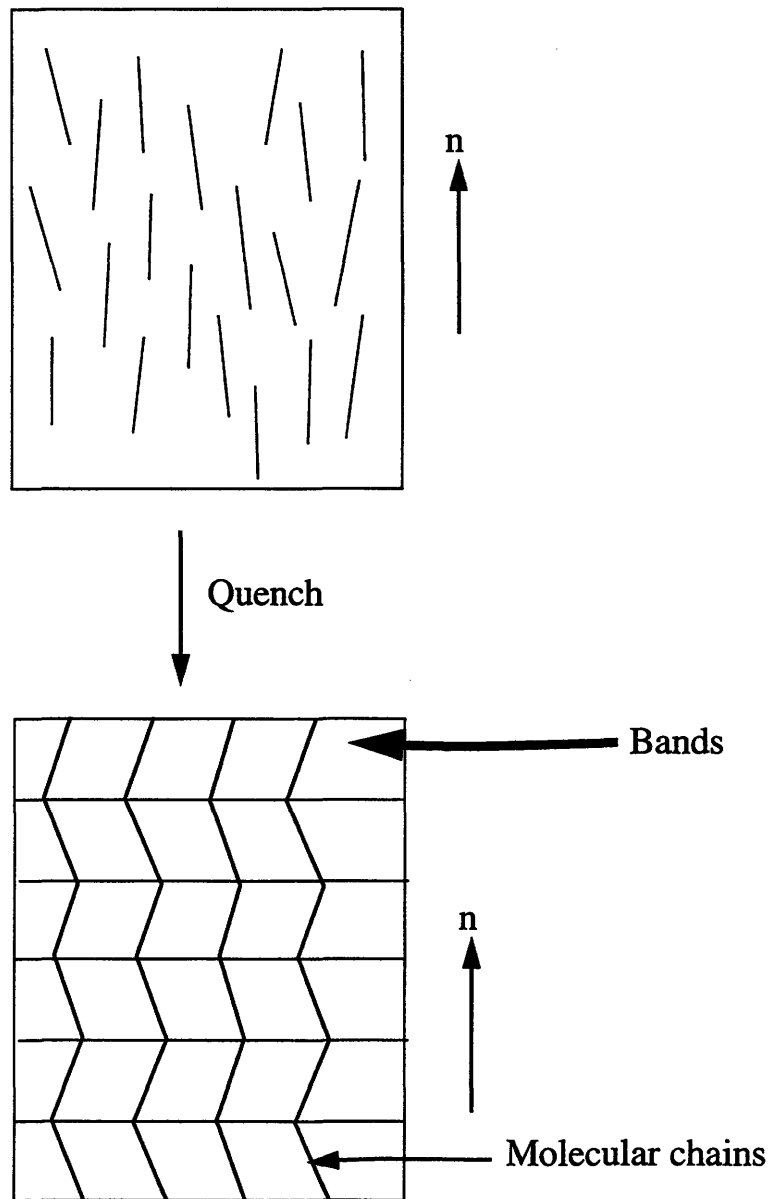


**Figure 2.3:** A schematic depicting the solidification induced banding technique. a) A sample in the nematic state before quenching. b) After quenching, bands form normal to the average director. In the light microscopy these would appear as alternating dark and light stripes which provide the useful contrast. The spacing is typically 2-10 microns.

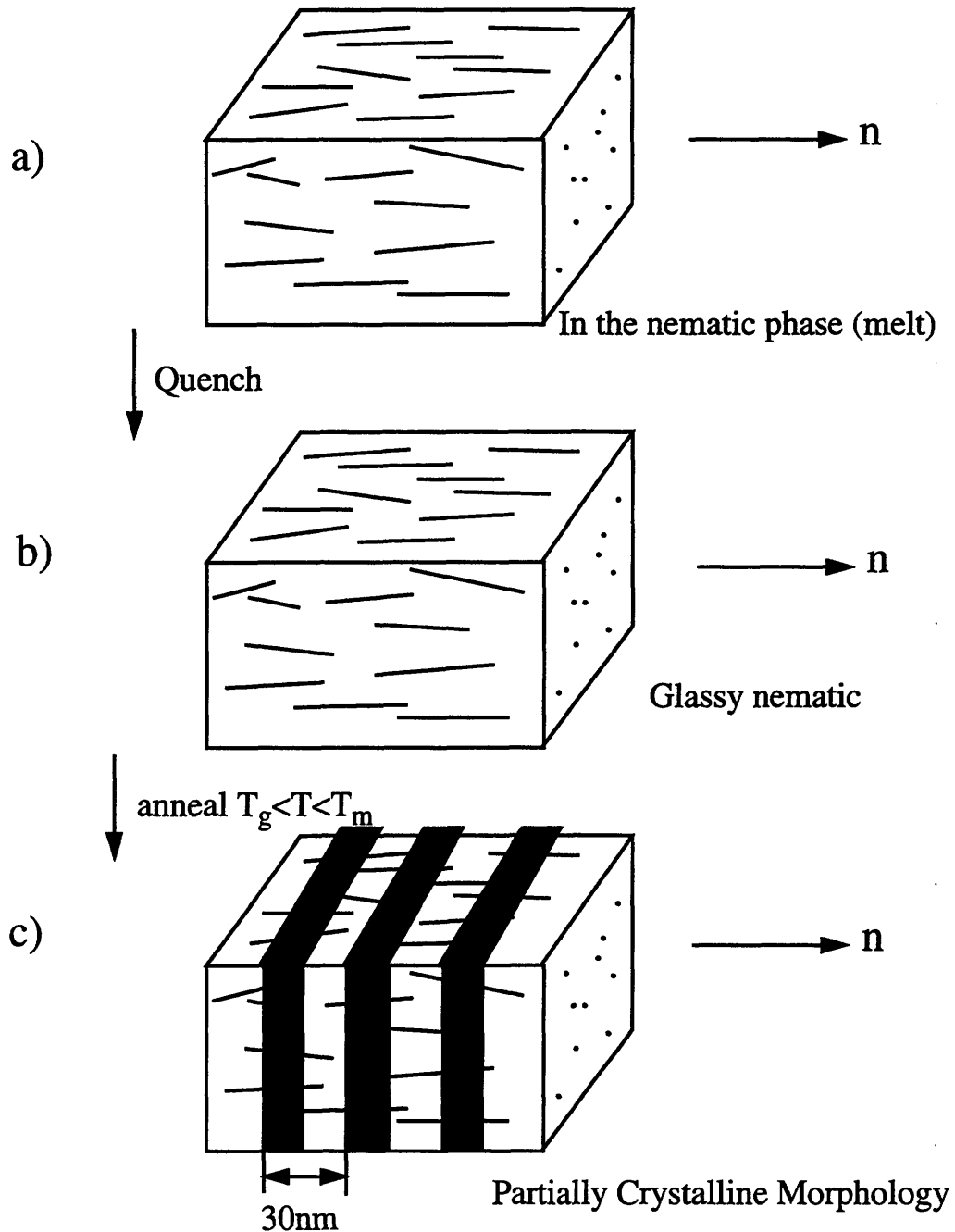
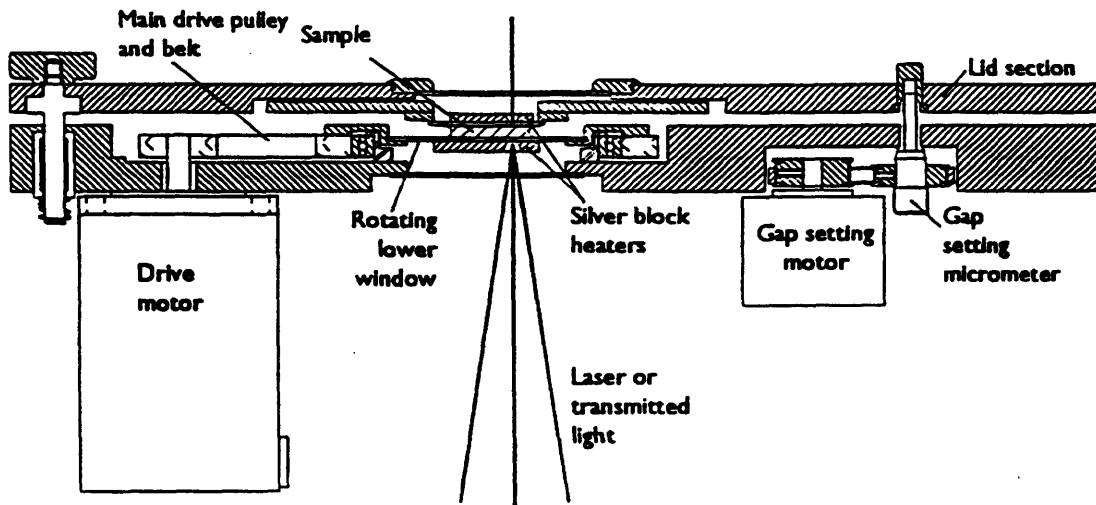


**Figure 2.4:** A schematic depicting the use of the lamellar decoration technique. a) The sample is annealed in the nematic state to allow the defect texture to coarsen. b) The sample is then quenched at a rate greater than  $10^\circ\text{C}/\text{sec}$  to produce a glassy nematic. c) In the final step, the sample is annealed above the  $T_g$  but below the  $T_m$  to allow thin lamellae to grow normal to the director. These protrude a few nanometers from the surface of the sample. The typical lamellar spacing is 30 nm [16].



	Unit	Range	Resolution	
Velocity	(rads/sec)	0.001 - 10	0.001 rads/sec	ShearRate ( $S^{-1}$ ) 0.003 - 7500
Amplitude	(rads)	0.001 - 1	0.001 rads	Strain (%) 0.3 - 300
Frequency	(Hz)	0.1 - 10	0.1 Hz	
Gap Setting	( $\mu m$ )	10 - 2500	1 $\mu m$	
Limit Temperatures	( $^{\circ}C$ )	ambient - 450	1 $^{\circ}C$	
Heating Rates	( $^{\circ}C/min$ )	1 - 30	1 $^{\circ}C/min$	
Hold Times	(mins)	1 - 9999	1 min	

**Figure 2.5:** A schematic of the CSS 450 Shear cell and the operating parameters

# Chapter 3

## Defect Generation Mechanisms

### 3.1 Introduction

The current study reports an approach for determining the origin of the various types of disclinations in a nematic liquid crystal polymer. It uses a combination of optical microscopy and solidification-induced banding to follow the development of nematic domains as the sample is cooled below the symmetry breaking phase transition (the isotropic to nematic transition temperature). The nucleation and growth process of nematic domains forming from an isotropic phase is, in general, very difficult to visualize due to the rapidity of the phase transition. This difficulty is overcome by working with low molecular weight polymers having a high polydispersity. A low molecular weight gives the sample a reasonable viscosity and relatively high transparency which makes defect structure and dynamics easier to determine. The high polydispersity in molecular weight (i.e. 2-2.5) leads to the development of isolated nematic domains that form in an isotropic matrix. Defect generation and interaction mechanisms can be studied more conveniently when there are a relatively low number of defects within a single domain.

Three regimes of domain and defect development were identified. These are characterized according to the defect morphology present at that particular time.

### 3.2 Background

When a material is subjected to a symmetry breaking phase transition, topological defects are created. The study of these defects and their dynamic behavior has been an active area of research. This is due in part to the universality of symmetry breaking phenomena. The analogies that exist in cosmology, particle physics, condensed matter physics and liquid crystal systems have been well documented in the literature.[1][2][3][4] Liquid crystals are a particularly interesting system to study because they are easy to work with and their

time scales are within experimental reach. A great deal of work has addressed the characterization of defects in liquid crystal polymers as well as their dynamic behavior (Chapter 1).

However, there have been relatively few studies on the origins of these defects. Two recent papers have addressed the formation of disclination string networks. The first of these utilized a small molecule liquid crystal (5 CB in particular) as a means for evaluating theories of cosmic string formation. (Chuang et al.[5]) The authors note that the generation of defects that are produced in symmetry breaking phase transitions is an important problem in cosmology, particle physics, and condensed matter physics. In cosmology in particular, the big bang theories automatically lead to defect production as the universe cools through a symmetry breaking phase transition. The Kibble mechanism was put forth to explain the scaling and dynamical behavior of these cosmological defects [1]. The theories associated with the dynamical phenomena of cosmological defects are difficult to test, however. This is primarily because the length and time scales of these defects are beyond human reach. Liquid crystals were used by Chuang et al because their time scales are within experimental reach and are much easier to work with than systems such as liquid helium that have related defects. The authors used a pressure cell to force an isotropic to nematic transition in the liquid crystal. In their work they made simulations and observations of defect texture coarsening and also studied the string density scaling behavior. Their results supported the scaling laws of the Kibble mechanism.

Another related study of string formation was reported by Bowick et al. [6] They also used the small molecule liquid crystal 5CB in their work. Their experimental system was slightly different. Instead of using a pressure cell, they worked with droplets on an untreated glass slide. The sample was heated with an illuminator, the intensity of which was reduced in order to induce the isotropic to nematic transition. The nucleation of defect strings was followed with a CDD camera and video recorder They were primarily interested in studying the production of string defects and determining the probability of their formation. They found that the number of string defects formed per nematic droplet agreed with numerical simulations based on theories from the Kibble mechanism.

In the preceding studies it could be seen that during a temperature quench, nematic droplets began to nucleate and coalesce. After coalescence was complete the sample was

characterized by a dense tangle of disclination strings. However no comments were made as to the changes in morphology before, during and after coalescence. The strings appeared only after many domains had coalesced, but the mechanisms by which this occurred were not commented upon. This is most likely a result of the fact that the isotropic to nematic transition occurs in approximately 30 ms for the liquid crystals that were used. This would have made it difficult, if not impossible, to study the nucleation and growth process in detail.

Although defect generation mechanisms have not been addressed in polymer systems, several micrographs depicting nucleation and growth of domains have been shown and commented upon in a Faraday Discussion meeting. [7] Several micrographs supplied by T.J. Lemmon showed a fine schlieren texture that was observed when the liquid crystal polymer was cooled below the isotropic to nematic transition temperature. (see Figure 3.1a). The extinction directions of this texture vary rapidly with position so that no domains exist. During initial stages of annealing, the texture begins to coarsen. This is evidenced by the growth of what they refer to as ‘centers’ that contain a defect in the middle (Figure 3.1b). As annealing continues, additional centers nucleate while others continue to grow (Figure 3.1c). The large domains were presumably created by a combination of normal growth as well as coalescence. Although the members of the discussion group did not comment upon the defect structure within the coarsening centers, a close examination of micrograph 3.1c yields some important information about nematic phase development. A single brush pattern can be seen inside each of the smallest centers. Several of these are marked by solid black arrows. These defects appear to be of the four-brush pattern exclusively. Several of the slightly larger domains (marked with a dotted arrow) have multiple defect points within them. The two large centers seem to contain a large number of defect points. Unfortunately the micrograph is not clear enough for the defect types to be distinguished. In spite of this the micrograph does indicate that perhaps additional defects are being created during the domain coalescence process. This provided an impetus for the current study which examines nematic domain development in detail.

Eventually the coarsening centers dominate the sample, leaving only small isolated knot-like regions behind (Figure 3.1d). A fully coarsening sample (Figure 3.1e) shows a multidomain texture. The authors of this study stated specifically that “it has not yet been



possible to follow the complete sequence in thicker specimens, where the fine microstructures are superimposed leading to a confused texture”.

This chapter extends some of the notions implied in the study that was just described. The complete cycle of nematic domain development will be discussed in detail with an emphasis on the defect structure. Mechanisms will be presented that provide explanations for how all of the most common disclinations are created in a specific polymer system.

### **3.3 Determination of Anchoring Conditions**

The samples used for the work in this chapter aligned normal to the plane of the pre-cleaned coverslips that were used as substrates. This is referred to as homeotropic anchoring (Figure 3.2a). To prove this was the case, a small amount of sample was placed between two coverslips which were then heated above the nematic to isotropic transition temperature. This sandwich assembly was then pressed together so the polymer would form a thin film of approximately 10-20 microns. The temperature was then lowered to the specific temperature used in the experiments. The elimination of all birefringence was used as proof of the homeotropic anchoring conditions between the sample and coverslip. In this situation all the molecules are oriented normal to the surfaces which makes the sample appear black under crossed polarizers. This state could be distinguished from the disordered isotropic phase by applying a small amount of pressure to the coverslip assembly. This caused some of the molecules to go out of the homeotropic alignment, which resulted in the appearance of bright flashes of light. Upon releasing the pressure, the system relaxed back to the homeotropic state.

The use of a dual-coverslip assembly has advantages in that there are only two boundary conditions to consider: nematic/substrate and nematic/isotropic. However, this experimental setup does not allow one to use high resolution techniques for examining surface details by Atomic Force Microscopy for example. It eliminates the possibility of using the upper limits of the optical microscope due to the very short working distances of the higher magnification lenses. For this reason it was necessary to determine the anchoring conditions between the nematic and the free surface (air). Thin film samples prepared on a

single coverslip showed a high degree of birefringence after cooling below the isotropic to nematic transition temperature. This indicated that the molecules could not have been homeotropically aligned with respect to the free surface otherwise all birefringence would have been eliminated. As will be discussed in more detail later, these results were confirmed by solidification induced banding techniques.

Optical analysis using both quarter wave plates and first order wave plates was used to determine that the anchoring between the isotropic and nematic phases was homogeneous (Figure 3.2b). Individual nematic droplets that formed in the isotropic phase displayed a four brush pattern at specific times during the nucleation and growth process. An example of this is shown in Figure 3.3a. The domains seen in the optical micrograph are surrounded by isotropic liquid. The corresponding color shifts for the quarter wave plate and first order red plate are shown in Figures 3.3b and 3.3c respectively. When a quarterwave plate is used the interference colors shift to blue in the first and third quadrants and to yellow in the second and fourth quadrants. In a gray scale image, a shift to yellow appears as a change to a lighter shade of gray. A shift to blue would appear in a gray scale image as a shift to a darker shade of gray. The opposite effect occurs when the first order wave plate is used. These results indicate that the molecules are parallel to the boundary between the nematic and isotropic phase.

The anchoring conditions are an important element of these experiments because they determine the nature of the defects. For example it is known that the anchoring conditions presented here give rise to point defects at the surface of the film. [8][9] A schematic depicting this morphology is shown in Figure 3.4. The first two schematics show an  $s=+1$   $c=\pi/2$  defect and an  $s=-1$  defect from the top view (Figure 3.4a and b respectively). The next two schematics show the corresponding side views of these defects. Note that most of the distortion in the director field takes place in a thin layer close to the surface of the film. This means, in effect, that the system behaves like a two-dimensional thin film since the range of the distortions is very low. For this reason, the defect generation mechanisms presented in this chapter will be discussed in a two-dimensional context.

### 3.4 Materials

Experiments were conducted on the thermotropic nematic liquid crystal polymer DHMS-7,9 which has the structure shown in Figure 3.5. This material has several characteristics that make it ideal for morphological studies. The substitution of an ether group in place of an ester avoids problems associated with transesterification reactions that occur in polyester LCP's. This is a particularly important point for dynamical studies because transesterification reactions add another relaxation mechanism to the system. Another important characteristic of DHMS-7,9 is its relatively low melting temperature (approx. 90 °C). This is brought about by attaching a methyl group to the stilbene mesogen, using an odd number of CH<sub>2</sub> groups in the spacer, and by having a random copolymer of 50% of 7 and 50% of 9 methylene unit monomers. It should also be noted that the stilbene mesogen gives rise to a nematic phase with a wide temperature range, which makes it relatively easy and convenient to study temperature dependent phenomena.[11] [12] [13] [14]

### 3.5 Experimental Procedure

Thin film samples (5-10 microns) were prepared in the nematic state at 140 °C by blade shearing on a pre-cleaned coverslip. The film was then annealed in the isotropic state (T= 170 °C) for five minutes to eliminate all defects from the system. The system was then cooled at 30 °C/min to 140 °C where all subsequent experiments were conducted. The nucleation and growth of nematic domains in an isotropic matrix was followed using several methods.

Videomicroscopy experiments were performed to follow the nucleation and growth in real time. A hot stage from Linkham Scientific Instruments was used to maintain the sample temperature. A Zeiss Axioskop polarizing optical microscope was used in conjunction with a DAGE-MTI CCD72 CCD camera and a DT55EZ frame grabber board to view the sample and record data. This type of experimental setup was limited to a magnification of 320x because of the long working distances required for hot stage use. Longer experimental runs were recorded using a TV monitor and vcr. Selected frames were later digitized with the framegrabber.

In order to use the upper magnification limits of the light microscope (i.e. 1000x), a series of annealing and quenching steps were used to view the sample at room temperature with the higher magnification lenses. The samples were prepared using the experimental procedure described previously. Next they were annealed in the nematic state for a specific length of time and then quenched into cold water. The quenching process caused bands to develop normal to the director (refer to Chapter 2). These bands map the director field distribution and provide a contrast mechanism in the light microscope. The solidification-induced banding method was used for this particular sample because it was of a lower molecular weight (6000 g/mol) and would not provide useful contrast for AFM by lamellar decoration.

### 3.6 Early Stages of Domain and Defect Development

At very early times, typically 1-10 seconds after cooling through the isotropic to nematic transition temperature, small nematic domains appear in the isotropic matrix. Under crossed polars these appear as bright white droplets in a black background. An image of these is shown in Figure 3.6. The droplets have reached a diameter of 0.5 microns by the time they appear with the intensity shown in the micrograph. At this point the domains are still too small for any defects to be detected within them. However, the fact that they can be distinguished from the disordered isotropic background indicates that liquid crystalline ordering is taking place within each domain. At early stages we assume the situation to be three-dimensional with droplets that are completely surrounded by isotropic liquid.

Several possible domain morphologies exist for such a system[15]. Schematics of the various possibilities are shown in Figure 3.7. The first two droplet structures (Figure 3.7a and 3.7b) are for homogeneous anchoring between the nematic and the isotropic matrix. In both cases the director is everywhere parallel to the interface. Which arrangement actually occurs depends on the elastic anisotropy of the system. The first schematic (Figure 3.7a) has mainly splay distortions while the second (Figure 3.7b) has mainly bend distortions. The former would be more probable in the limit of low  $\epsilon$  (approaching -1), while the latter would be more likely for high  $\epsilon$  (approaching +1). For homeotropic anchoring there are also two possible arrangements shown in Figures 6c and d (low and high  $\epsilon$  respectively).

For the particular system examined in this thesis, the schematic shown in Figure 3.7b is likely the actual morphological case. Not only are the anchoring conditions homogeneous, but the results to be discussed later in the chapter show that bend distortions are much more favorable than splay for this system.

### 3.7 Middle Stages of Domain and Defect Development

At slightly later times it becomes possible to detect defects within individual domains. Examples are shown in Figure 3.8. Note that there is a single defect within each domain. These defects are exclusively of the  $s=+1$  type as evidenced by the four brush pattern and the fact that the brushes rotate in the same sense as the polarizers. Optical analysis with a quarter wave plate and first order wave plate was used to determine that the defect was of the  $s=+1$ ,  $c = \frac{\pi}{2}$  type. A schematic showing the actual director field distribution for this situation is shown in Figure 3.9. By the time these defects can be detected, the droplets have reached a diameter of 1.5 microns. During this stage, they are still small enough so that no coalescence has occurred.

### 3.8 Late Stages of Domain and Defect Development

At later times, the third stage of domain and defect development begins. Once the domains become large relative to the thickness of the film, the situation becomes pseudo two-dimensional. It is not a true two-dimensional system because the system is not anchored between two substrates. This regime is characterized by the appearance of defects of negative strength which appear only after many domains have coalesced.

A typical example of a large domain formed by coalescence events is shown in Figure 3.10a. This light micrograph depicts three large domains that each contain many defects of various types. The banding technique was used to prepare the samples, so the textures seen in the micrograph are normal to the director field distribution. The corresponding schematic shown in Figure 3.10b indicates, by symbols, the location and type of each defect. The  $s=-1/2$  defects are located exclusively at the domain boundaries, while the  $s=+1$  and

$s=-1$  defects are always located some distance away. It is also interesting to note that the  $s=+1/2$  defects are very rare.

The region marked by the arrows is of particular interest because two  $s=-1/2$  defects are located in close proximity, but in separate domains. Since defect strengths add mathematically, one might expect an  $s=-1$  defect to be located in that region after the larger domains coalesce. This is indeed the case, as shown by the micrograph and corresponding schematic in Figure 3.11a and b respectively. This new defect is located exactly along the line of coalescence which is indicated by the arrows. Defects of the  $s=-1$  type are always located along lines of coalescence of the two domains. This suggests that they are created only in the coalescence process since their geometry makes it impossible for them to be generated within droplets at early stages of nucleation and growth. This is explained pictorially by the schematic in Figure 3.12. When an  $s=-1$  defect is placed within a droplet, the director field distribution will have a varying orientation at different locations along the boundary. This would not satisfy the anchoring conditions present in this system at early times.

### 3.8.1 Formation of the $s=-1$ defect

Several models and experimental results will be presented that illustrate various ways an  $s=-1$  can be formed during late stages of domain development.

As was mentioned in the preceding section, an  $s=-1$  defect can be formed from the coalescence of two  $s=-1/2$  defects that exist at the boundaries of different domains (refer back to Figures 3.10 and 3.11). A model for this process is shown in Figure 3.13. The first schematic describes the change in the actual director field distribution while the second shows the change in the banded texture which compares directly with the light micrographs. This is the simplest type of  $s=-1$  generation event and is based on the notion that the superposition of solutions to the nonlinear partial differential equation described in Chapter 1 can be used to describe defect interactions. These results also describe why the  $s=-1$  defects are located along lines of coalescence.

The  $s=-1$  defects can also be created by other coalescence events. A video sequence of one of these is shown in Figure 3.14. This video sequence shows a slightly more complex coalescence event that leads to the creation of an  $s=-1$  defect. In this particular situation, a domain with a pair of  $s=+1/2$  defects is coalescing with a larger domain that has both an  $s=-1/2$  and  $s=+1$  defect on one end. The locations of the original defect cores are labelled in the first image of the series. At the instant the domains coalesce, strong distortions develop in the director field as evidenced by the variations in birefringence near the cusp-like region marked in the second image. It is evident that a defect has been created just ahead of the cusp. However at this time ( $t=80$  seconds after coalescence) the strength of the defect is not clear. After 90 seconds (Figure 3.14 c), the distortions in the director field become even stronger. In addition, the cusp is still distinguishable but the defect strength is not. An interesting change takes place at 110 seconds (Figure 3.14 d). By this time, the cusp has become flat and the new defect can finally be identified as an  $s=1/2$  defect. Further annealing over 340 seconds (Figure 3.14 e-k) showed that the new defect was an  $s=-1$  since it was attracted to the original  $s=+1$  defect which it subsequently annihilated.

### 3.8.2 Formation of $s=-1/2$ defects

Defects of this type normally do not appear for homeotropic (also referred to as ‘normal layers’) anchoring conditions. However, Nehring and Saupe [10] have observed that  $s=1/2$  lines form in normal layers when the molecules are able to orient parallel to a free surface. The free surface is represented by the interface between the nematic phase and air.

Defects of the  $s=-1/2$  type are almost always found at domain boundaries. This can be explained using the schematics shown in Figure 3.15. Recall that the specific anchoring conditions of the system examined in this chapter give rise to point defects at the surface of the film in large domains formed in the late stages of the isotropic to nematic transition. This in effect concentrates the distortions in the director field at the top surface. It is for this reason that the following descriptions are discussed in two dimensions

Since defects of the  $s=+1$ ,  $c=\pi/2$  type are the only ones formed during early stages of domain development, coalescence events between these are extremely frequent. When two of these coalesce, as depicted in Figure 3.15a, a repulsive force field is formed between

them. This occurs because defects of opposite sign repel each other. If this ensemble is then incorporated into a domain, problems arise with the anchoring conditions. The anchoring conditions are maintained at the ends of the elliptical domain, but are violated along the sides. This situation cannot occur in a system with strong anchoring conditions. In order to maintain uniform anchoring conditions and the repulsive force field, the system creates two new topological defects between the two original ones (Figure 3.15b). This schematic indicates clearly that the new defects are of the  $s=-1/2$  type. This explains not only how they are created, but why they are always located near domain boundaries.

An experimental example used to validate this model is shown in Figure 3.16. The first three images (Figure 3.16a-c) show two  $s=+1$  defects after they have coalesced and produced the  $s=-1/2$  defects along the boundary. Each image was taken approximately 10 seconds apart using a sequential annealing and quenching procedure. The schematics of Figures 3.16 d-f show the changes in the director field distribution. The last three images (Figure 3.16g-i) show the changes in the banded texture which can be compared directly with the micrographs. As the system is annealed further, the  $s=-1/2$  defects move closer to the domain boundary. When the sample is viewed while it is actually in the nematic state under crossed polars, the movement of an  $s=-1/2$  defect would appear as a pair of black brushes that move from between the  $s=+1$  defects directly over to the domain boundary. It is difficult to capture such an event because the creation and resulting movement of the  $s=-1/2$  defects is very rapid (i.e. 20-30 seconds) in this particular situation. If one waits too long, then the  $s=-1/2$  will have moved over to the boundary. At that point it would be difficult to identify the defect since the brushes become somewhat obscured when they are at the domain boundary. Both real-time videomicroscopy and sequential annealing and quenching were used to determine what existed was indeed a pair of  $s=-1/2$  defects and not an  $s=-1$  with two brushes obscured along the domain boundary.

In rare cases, an  $s=-1/2$  defect can be 'trapped' in the middle of a domain. An example of this is shown in Figure 3.17a-b. This particular domain was formed from the coalescence of three smaller ones, each of which contained a pair of  $s=+1/2$  defects. Models for both the director field distribution and the banding patterns of such an ensemble are shown in Figures 3.17 c and f respectively. The next two schematics describe the state of the system just as the domains coalesce. Three sharp cusps can be seen in the areas marked by the



arrows just after coalescence occurs. In these regions the homogeneous anchoring conditions are violated (Figure 3.17 d and g). At the tip of the cusps, the anchoring is homeotropic. In order to convert these regions to homogeneous anchoring, the director field forms smooth continuous lines in front of the cusps. When this is done with successive groups of molecules in each of the three regions, a pinching-in occurs at the center of the domain. This process is likely responsible for the creation of an  $s=-1/2$  defect at the center of the small domain (refer to Figures 3.17 f and i).

### 3.8.3 Formation of the $s=+1/2$ defect

Defects of the  $s=+1/2$  type generally do not appear until very late stages of domain development. Not only is its geometry incompatible with an early stage domain (Figure 3.18), but the asymmetry of a single  $s=+1/2$  makes it difficult if not impossible for it to be created from the coalescence of individual nematic domains. The  $s=+1/2$  defects appear in large domains after annihilation events have caused the defect structure to completely reconfigure. During all regimes of domain development, but especially during late times, it is clear that the sum of the strengths of all the defects within an individual domain always sums to one. This is presumably due to the differing anchoring conditions between the substrate and the free surface. This leaves only two possibilities for the end result of defect recombination: either a single  $s=+1$  defect or a pair of  $s=+1/2$  defects. Examples of these possibilities are shown in Figure 3.19a and b respectively.

### 3.8.4 Domain Recombination

A series of images describing the complete domain development cycle are shown in Figures 3.20 and 3.21. The first series (Figure 3.20) shows how recombination events can lead to the development of a large domain with a single  $s=+1$  defect inside. The second series (Figure 3.21) shows how recombination can lead to the development of a pair of  $s=+1/2$  defects at extreme edges of the large droplet.

Nearly 400 such domains were analyzed with the NIH-Image software package. The particle analysis functions were used to determine the ellipticity of domains that contained either a single  $s=+1$  or a pair of  $s=+1/2$  defects. The results are shown in Figure 3.22. No correlation was found between ellipticity and domain type. It was also discovered that

reconfiguration led to the development of a  $s=+1$  defect approximately 90% of the time. It was initially thought that the  $s=+1/2$  defects might be more energetically favorable within more elliptical shaped domains since this configuration would cause less strain in the director field than a single  $s=+1$  defect within a domain of the same ellipticity.

### 3.8.5 Implications for Materials Parameters

A domain with a single  $s=+1$  defect contains pure bend distortions if it can reconfigure to a circular configuration, which it can over long periods of time (i.e. one hour of annealing). A domain containing a pair of  $s=+1/2$  defects on the other hand will always contain both bend and splay distortions, regardless of the domain ellipticity. This indicates that the polymer used in these experiments prefers bend distortions over splay. This would result in an elastic anisotropy greater than zero. The actual value is likely to be higher considering how frequently reconfiguration leads to development of defects with primarily bend distortions.

## 3.9 Summary

This chapter describes a mechanism whereby the origins of point (or line) defects can be explained. The mechanisms are reported for a liquid crystal polymer system under quiescent conditions. In addition the anchoring conditions are very specific: homeotropic anchoring between the coverslip and the nematic phase and homogeneous between the isotropic and nematic phase as well as between the nematic phase and the free surface (air).

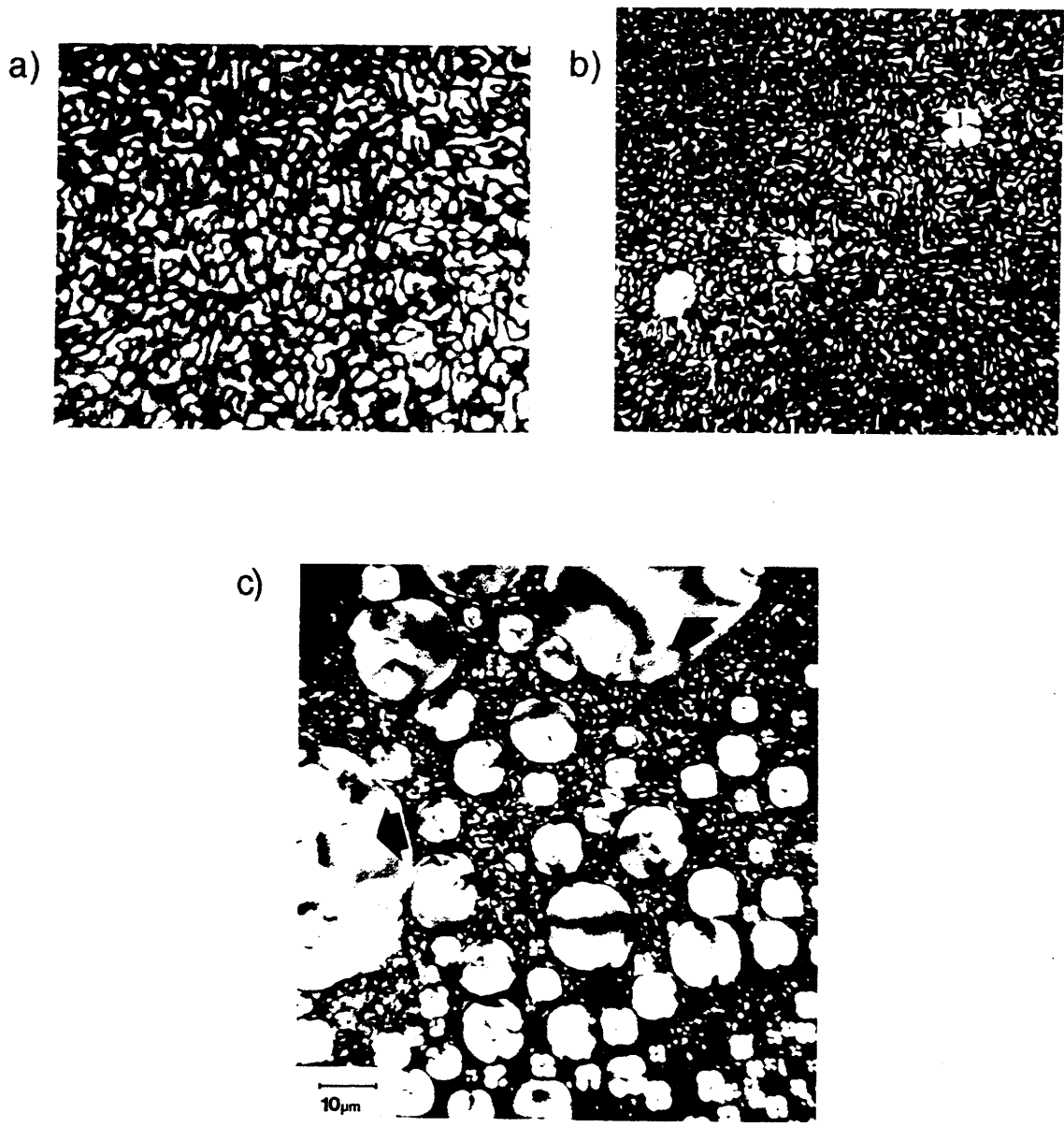
By following the development of nematic domains in an isotropic matrix after cooling below  $T_{ni}$ , using a relatively polydisperse sample, it becomes possible to view nucleation and coalescence events in real time. During early stages of nucleation and growth (low percent conversion) the nematic domains are so small (approx 0.5 microns) that it is not possible to determine the nature of the defects. However at a slightly larger percent conversion (middle stage of domain development), defects of the type  $s=+1$ ,  $c=\pi/2$  are easily detected. This type of defect is generated as a result of the specific anchoring conditions that exist between the sample, the substrate, and the isotropic matrix. The later stage of domain growth is identified by the onset of coalescence into large domains. The

coalescence process always leads to the production of defects of negative strength. Defects of the type  $s=-1$  are formed at impingement sites and tend to be located in the interior of the newly coalesced domain. Defects of the type  $s=-1/2$  are also formed at impingement sites but migrate towards domain boundaries with further annealing. In addition, defect strength is conserved within individual domains due to the differing anchoring conditions. All droplets that nucleate at a low % conversion contain a single defect of strength  $s=+1$ . After domains begin to coalesce at higher % conversion, the defect strength again sums to one. The presence of both negative and positive strength defects leads to annihilation events. After the annihilation process is complete, the domains reconfigured to either a single  $s=+1$  defect or a pair of  $s=+1/2$  defects.

Which defect configuration results from a particular set of coalescence events has little to do with domain ellipticity. Image analysis of 400 domains showed no correlation between ellipticity and domain type.

- [1] Kibble, T.W.B., "Topology of Cosmic Domains and Strings", *J. Phys. A*, **9**, 1387-1398, 1976
- [2] Hill, C.T., Schramm, D.N., Fry, J.N., *Comm. Nucl. Particle Phys.*, **19**, 25, 1989
- [3] Vilenkin, A., *Phys. Rep.*, **9**, 1387, 1989
- [4] Furukawa, H., *Adv. Phys.*, **34**, 703, 1985
- [5] Chuang I., Durrer, R., Turok, N. and Yurke, B., "Cosmology in the Laboratory: Defect Dynamics in Liquid Crystals", *Science*, **251**, 1339, 1991
- [6] Bowick, M.J., Chandar, L., Schiff, E.A. and Srivastava, A.M., "The Comological Kibble Mechanism in the Laboratory: String Formation in Liquid Crystals", *Science*, **263**, 943, 1994
- [7] General discussion from the Faraday Discussions of the Chemical Society, No. 79, 1985, Dr. A.H. Windle's comments p. 186
- [8] Ding, Ding-Kuo and Thomas, E.L., "Structures of Point Integer Disclinations and Their Annihilation Behavior in Thermotropic Liquid Crystal Polyesters", *Mol. Cryst. Liq. Cryst.*, **241**, 103-117, 1994
- [9] Meyer, R., "On the existence of Even Indexed Disclinations in Nematic Liquid Crystals", *Phil. Mag.*, **27**, 405-424, 1972
- [10] Nehring, J. and Saupe, A., "On the Schlieren Texture in Nematic and Smectic Liquid Crystals", *J. Chem. Soc., Faraday Trans. II*, 1972
- [11] Hall, E., Ober, C.K., Kramer, E.J., Colby, R.H., Gillmor, J.R. and Galli, G., *Mater. Res. Soc. Symp. Proc.*, **248**, 113-118, 1992
- [12] Hall, E.E., Robinson, A.A., McNamee, S.G., Ober, C.K., Freidzon, Y.S., *J. Mater. Sci.*, **30**, 2023-2028, 1995
- [13] Percec, V., Shaffer, T.D. and Nava, H., "Telechelics and Macromonomers of a New Class of LCP's: Polyethers of Mesogenic Bisphenols", *Polym. Prepr.*, **25**(2), 45-46, 1984
- [14] Percec, V., Shaffer, T.D. and Nava, H.J., "Functional Polymers and Sequential Copolymers by Phase Transfer Catalysis. 10. Polyethers of Mesogenic Bisphenols: A New Class of Main-Chain Liquid Crystalline Polymers", *J. Polym. Sci., Polym. Lett. Ed.*, **22**, 637-647, 1984

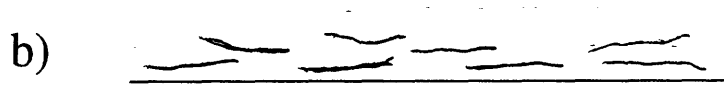
[15] Kilian, A., "Computer Simulations of Nematic Droplets", *Liq. Cryst.*, 4, 1189, 1993



**Figure 3.1:** a) A fine schlieren texture observed in the polymer B-ET after cooling below the isotropic to nematic transition temperature [7]

b) Coarsening domains appear after the fine schlieren texture is annealed

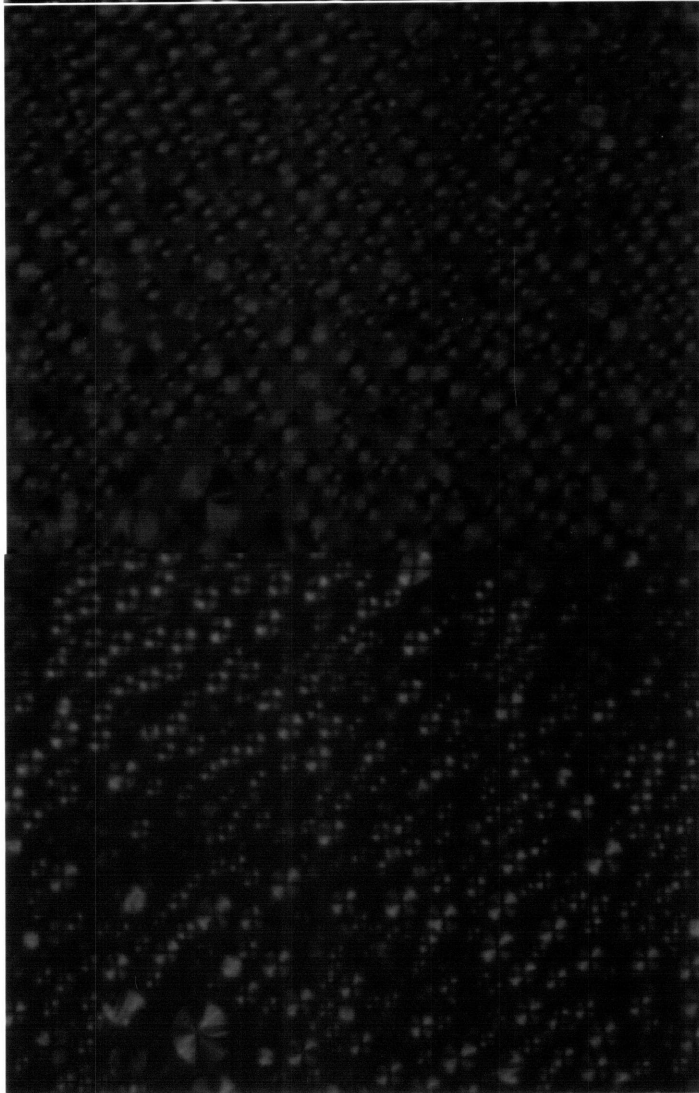
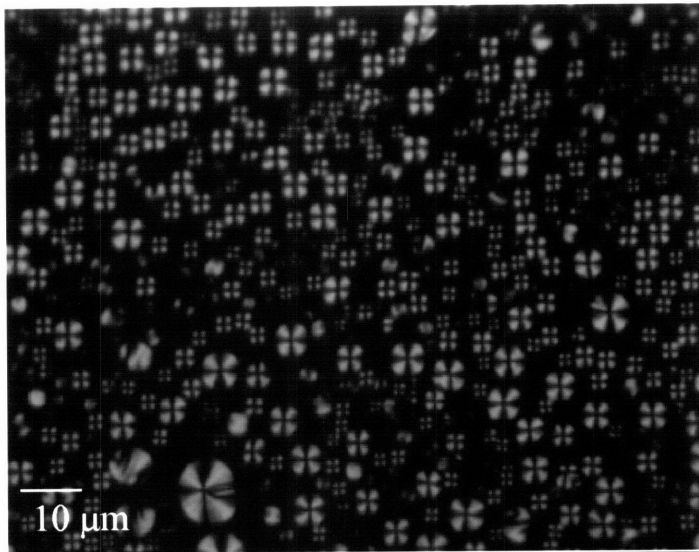
c) Further annealing causes additional nucleation and growth



**Figure 3.2:** a) A schematic depicting homeotropic anchoring. b) homogeneous anchoring

**Figure 3.3:** (following page) a) Nematic domains that appear during early stages of nucleation and growth. Each contains a single  $s=+1$  defect. b) The corresponding color shifts for insertion of a quarter wave plate. c) The corresponding color shifts for insertion of a first order red plate. These results were used to determine that the director was parallel to the boundary of the domains (homogeneous anchoring conditions).





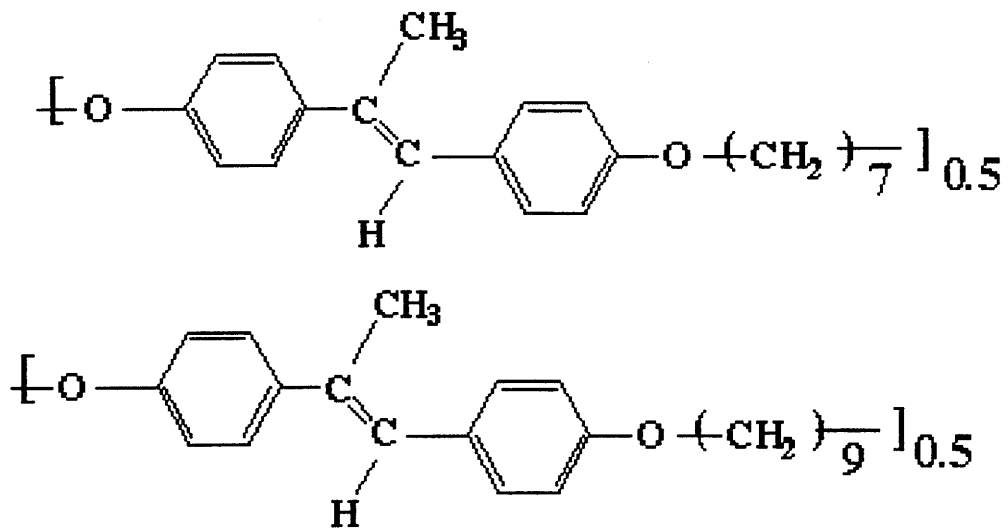


**Figure 3.4:** Chemical structure of DHMS-7,9, a random liquid crystal copolyether. The transition temperatures are as follows:  $T_g=20\text{ }^\circ\text{C}$ ,  $T_{xn}=90\text{ }^\circ\text{C}$ ,  $T_{ni}=170\text{ }^\circ\text{C}$ .

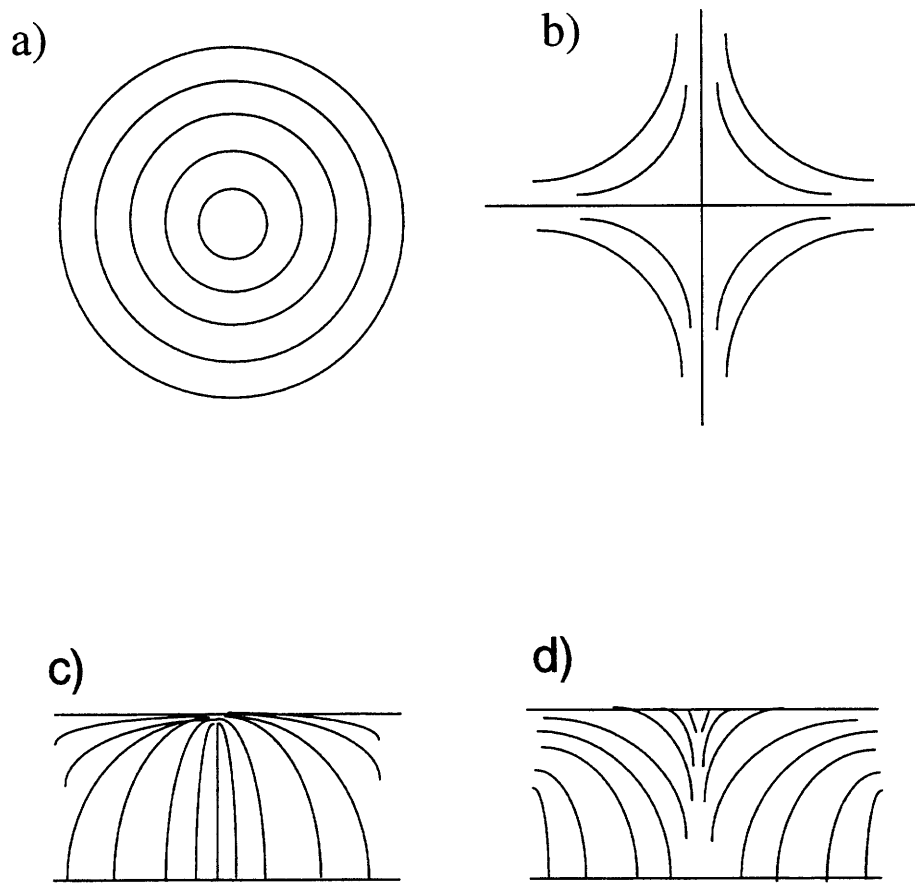


**Figure 3.5:** Schematics depicting the structure of point defects that lie at the surface of a film.[9] a) The top view of an  $s=+1$   $c=\pi/2$  defect. b) The corresponding side view. c) The top view of an  $s=-1$  defect. d) The corresponding side view.

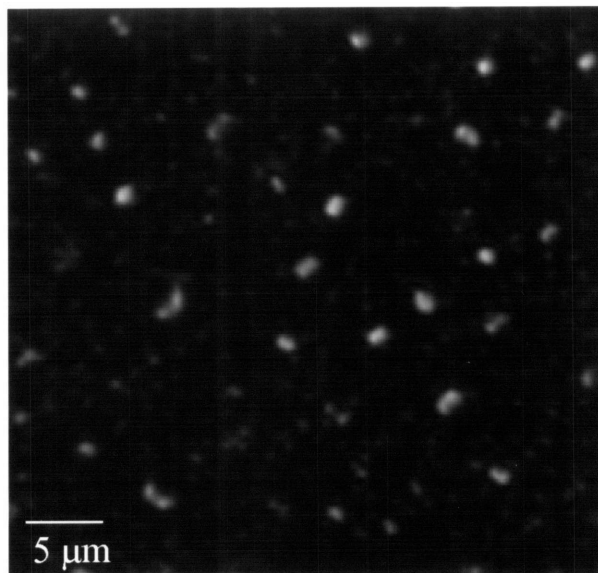


**Figure 3.6:** Image of nematic droplets that appear during early stages of domain development. The bright spots are indicative of liquid crystalline ordering. However it is still too early in the transformation process to determine the exact morphology within the droplets.

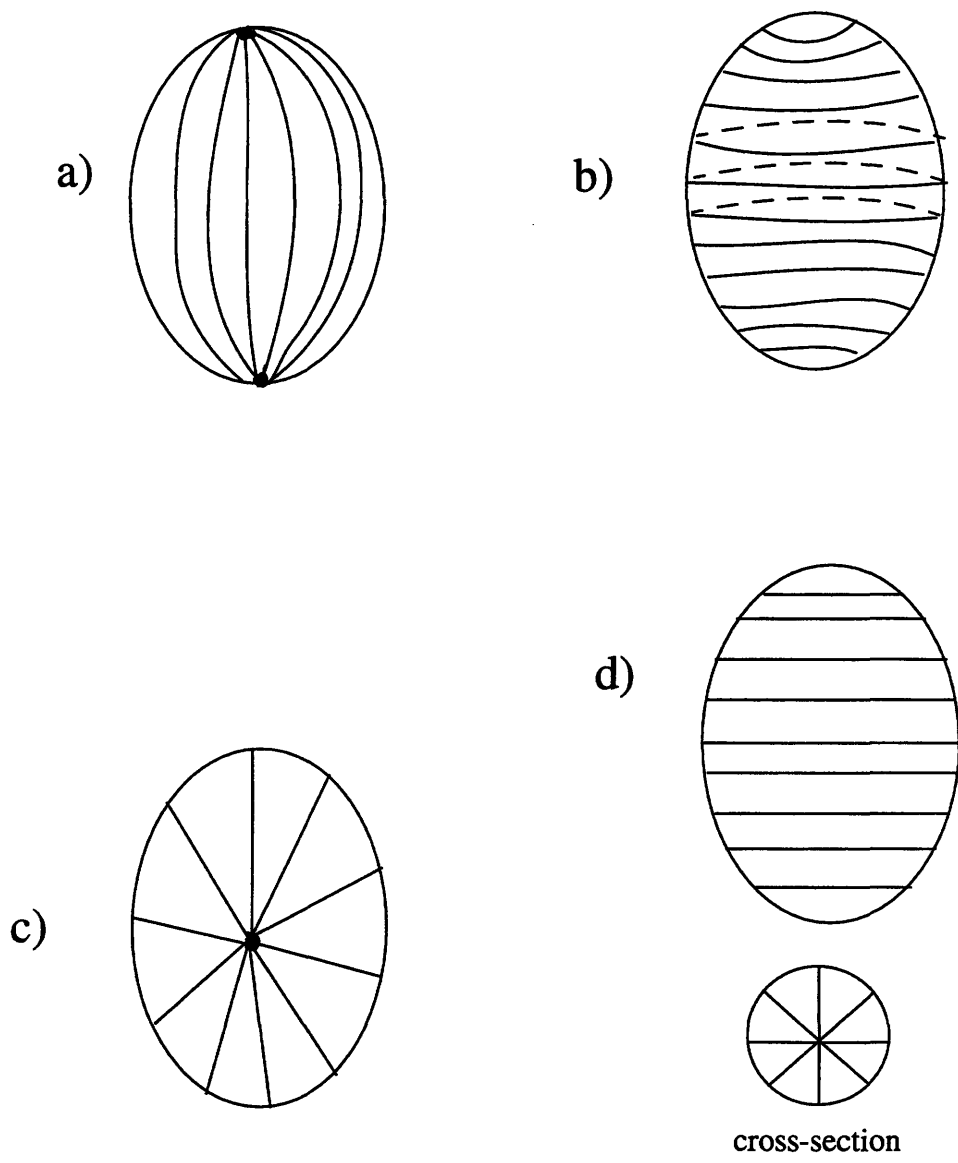


**Figure 3.7:** Schematics depicting the four possible droplet morphologies. a) Tangential configuration, homogeneous anchoring. b) Toroidal configuration, homogeneous anchoring. c) 'Hedgehog' configuration, homeotropic anchoring. d) Axial configuration, homeotropic anchoring.

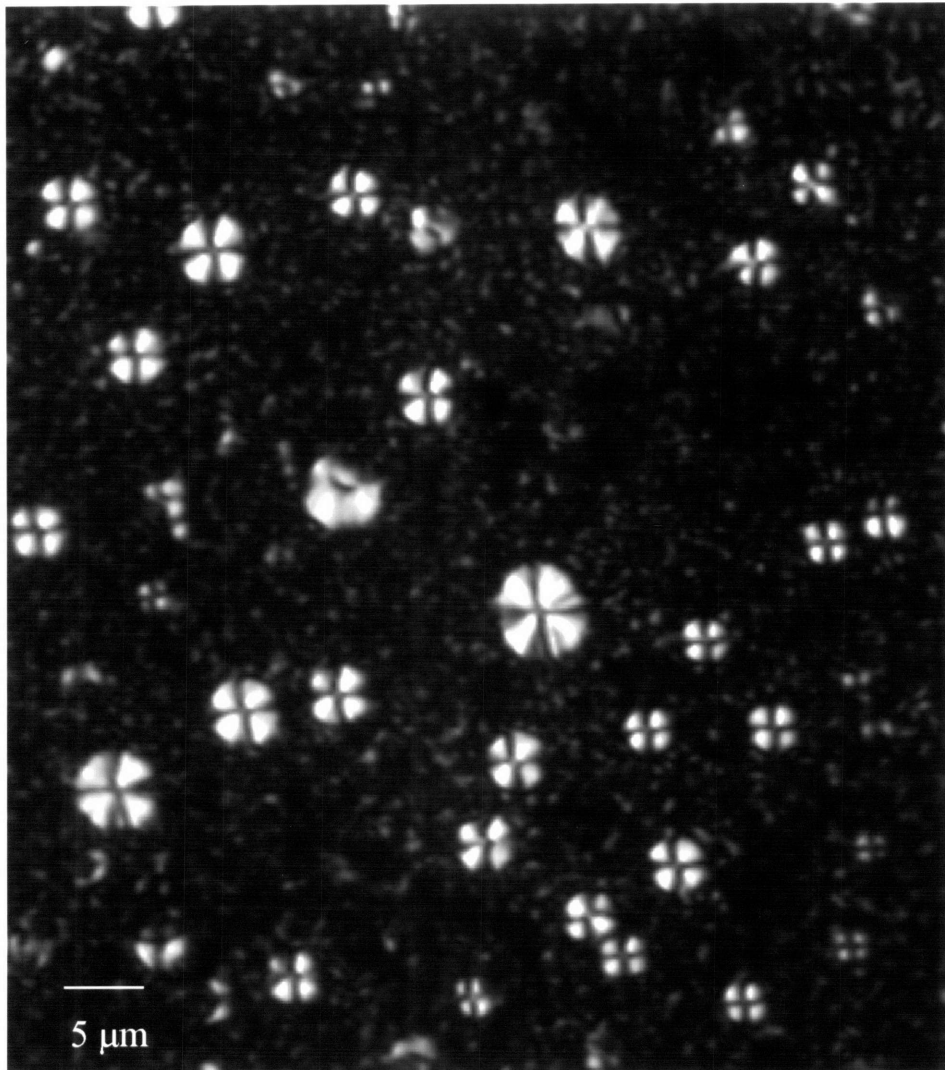


**Figure 3.8:** Example of nematic domains that appear during slightly later stages of domain development. At this stage, a defect can be seen inside each domain. These are of the  $s=+1$ ,  $c=\pi/2$  type as evidenced by the four brush pattern and by banding experiments as well as optical analysis with compensators.

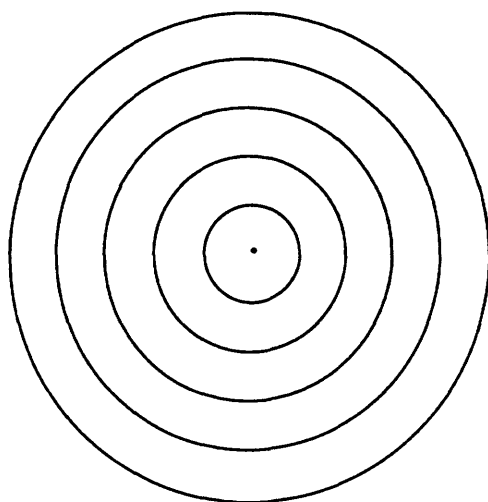


**Figure 3.9:** The director field distribution within middle stage nematic domains. The molecules are parallel to the boundary of the domain which indicates that the anchoring conditions are homogeneous.

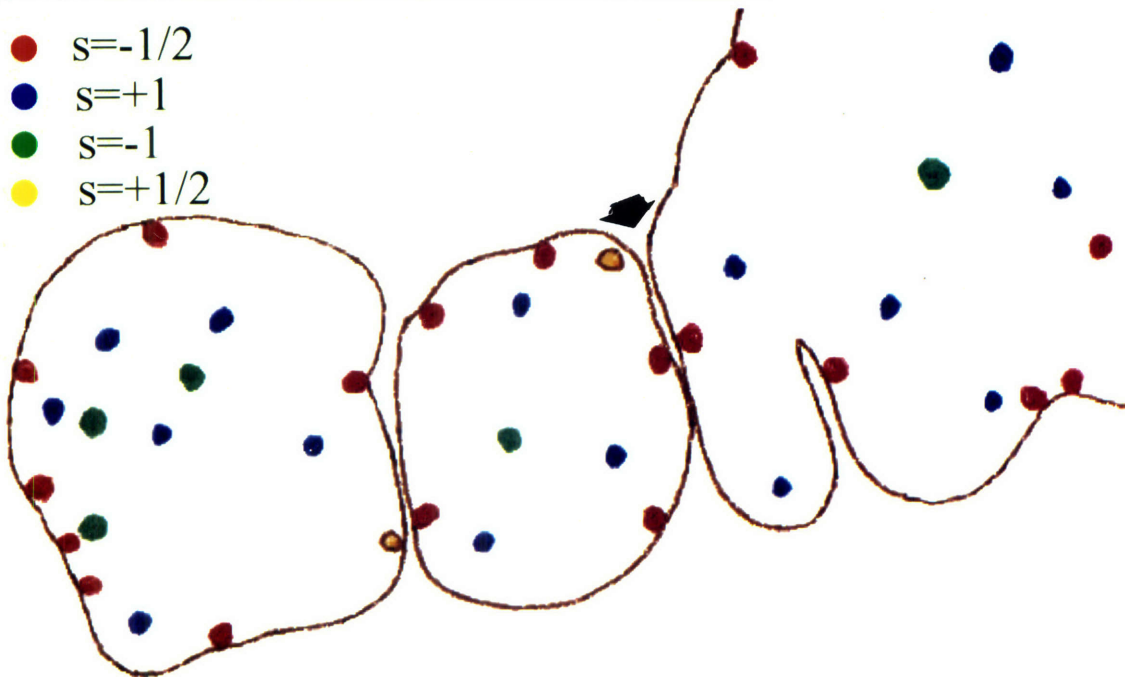


**Figure 3.10:** a) An image of several large domains formed by many coalescence events. b) The corresponding schematic indicating, by color, the location and type of the various defects. Note that the  $s=|1/2|$  defects are located exclusively at the boundaries while the defects of the type  $s=|1|$  are located towards the center of the domains that just coalesced.



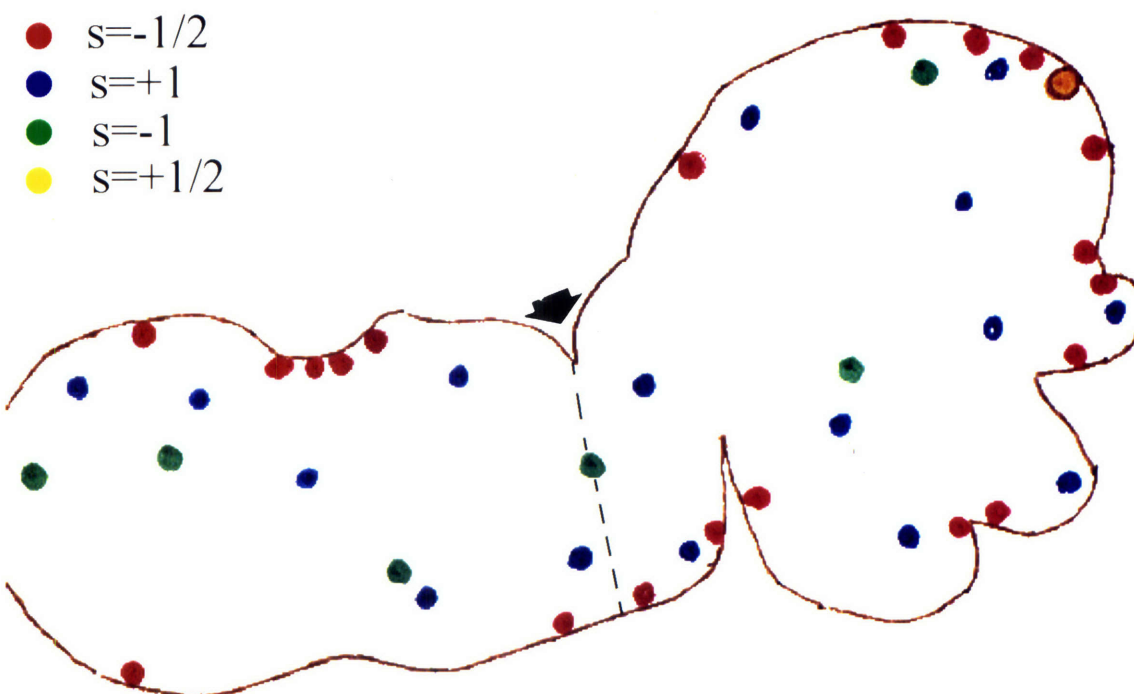
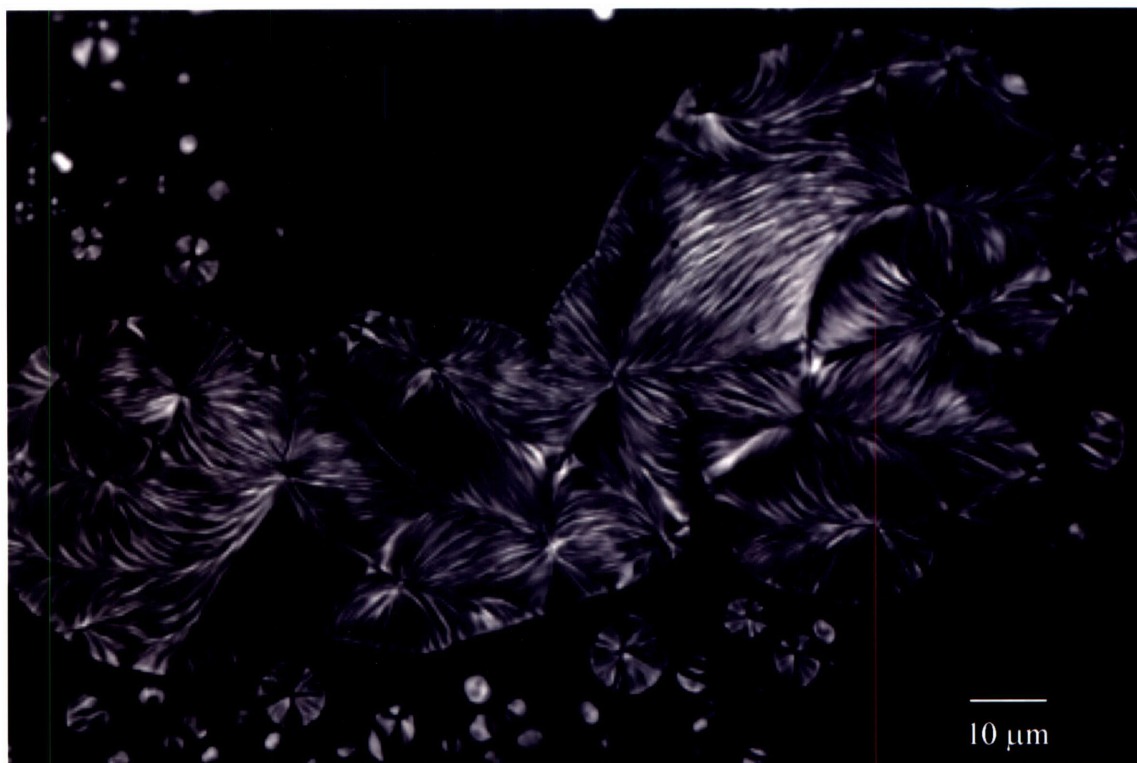


**Figure 3.11:** a) An image taken 20 seconds after Figure 3.10a. b) The corresponding schematic indicating the location and types of defects. The dotted line indicates the region where the domains coalesced and the  $s=-1$  defect was created.

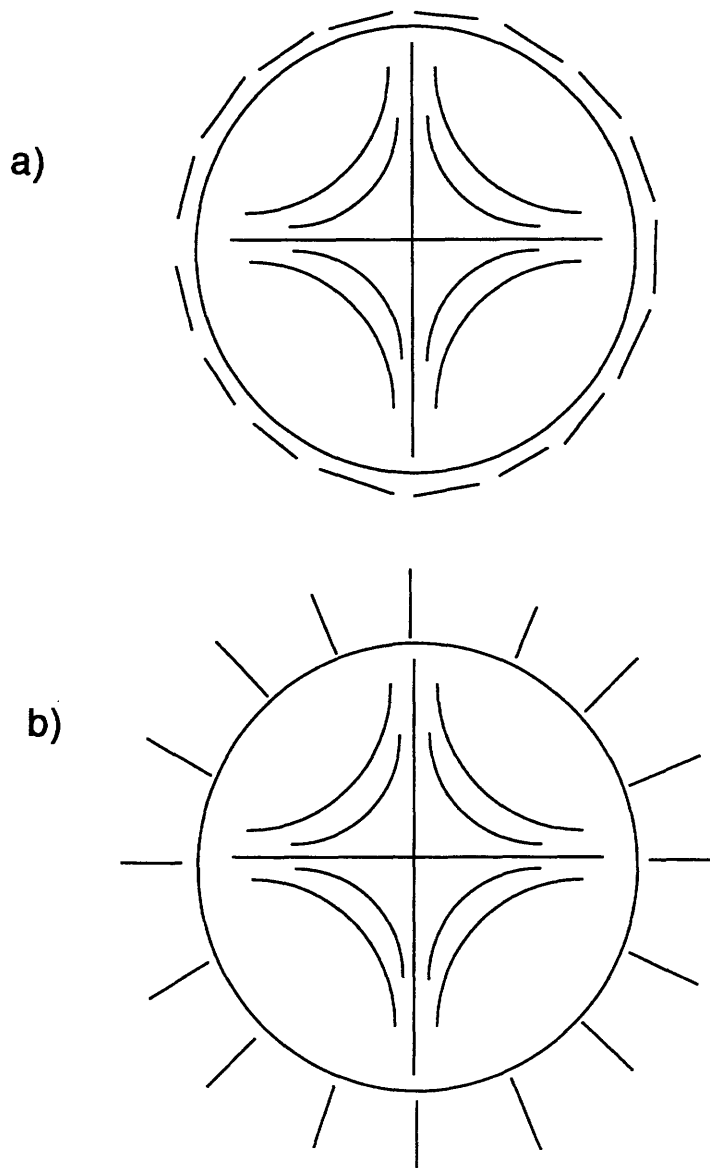


**Figure 3.12:** Schematics illustrating how the  $s=-1$  is incompatible with the nematic domains formed at early stages of domain development. a) homogeneous anchoring. b) homeotropic anchoring

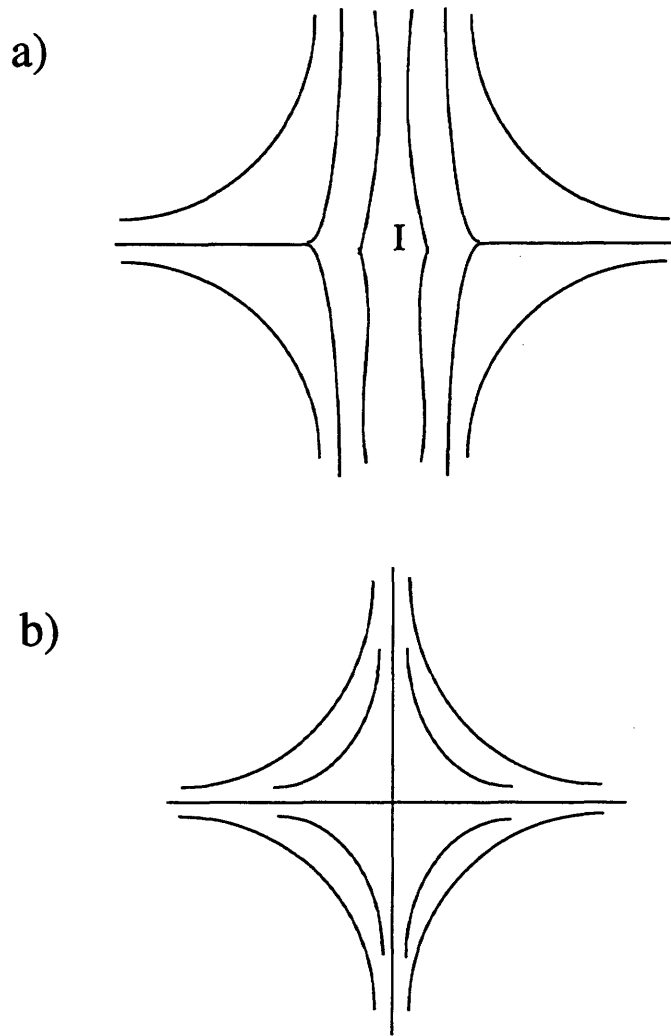


**Figure 3.13:** A model for the formation of an  $s=-1$  defect from the coalescence of two  $s=-1/2$  defects. The label “I” refers to the isotropic phase between the domains. a) A schematic showing two  $s=-1/2$  defects in close proximity, but in adjacent domains separated by a thin region of isotropic material.. b) The state of the system after domain coalescence. The  $s=-1/2$  have coalesced to form an  $s=-1$  defect.

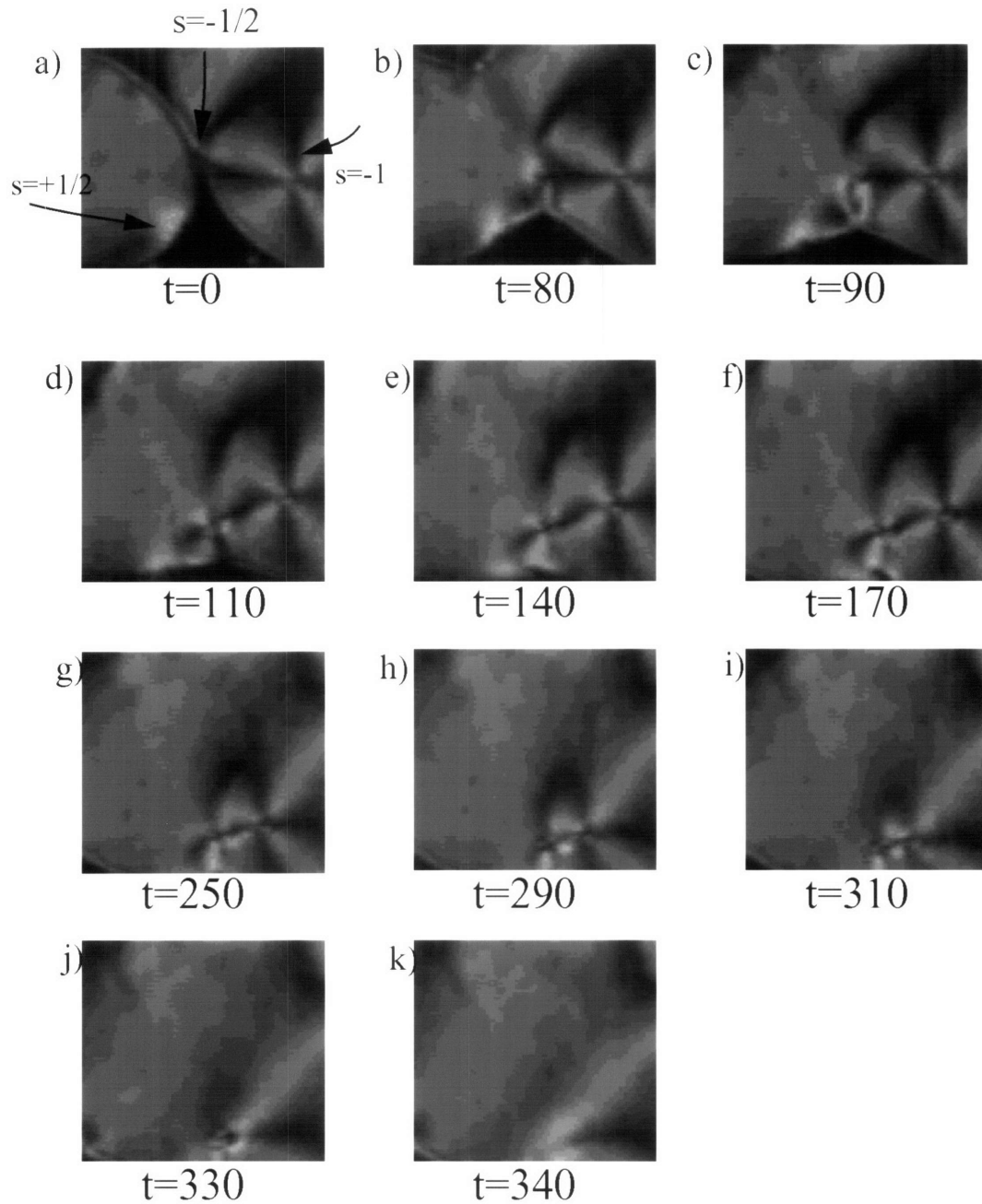


**Figure 3.14:** A video sequence depicting the formation of an  $s=-1$  defect. Time is indicated in seconds. The  $s=-1$  defect is attracted to the  $s=+1$  defect located near the center of one of the coalescing domains. These eventually annihilate each other.

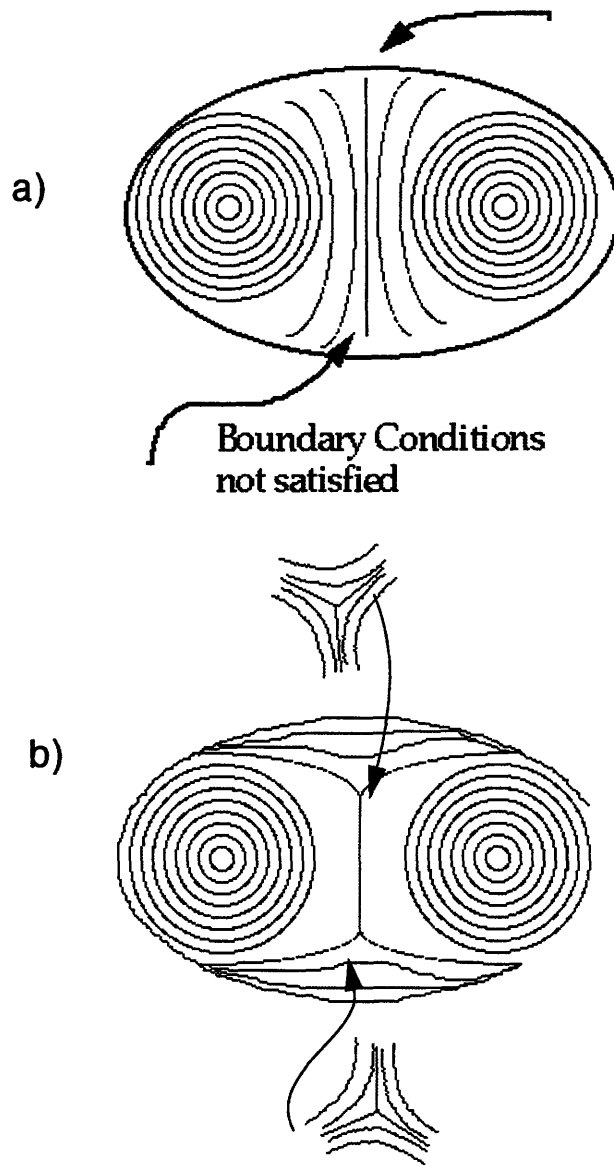


**Figure 3.15:** a) This schematic depicts the repulsive force field that exists between two  $s=+1$ ,  $c=\pi/2$  defects in close proximity. If this ensemble is placed within a domain, the homogeneous anchoring conditions are not satisfied at all locations along the boundary. The arrows mark the problematic locations. b) If homogeneous anchoring is imposed on the ensemble then two new topological defects must be created. These defects are clearly of the  $s=-1/2$  type indicated by the arrows.

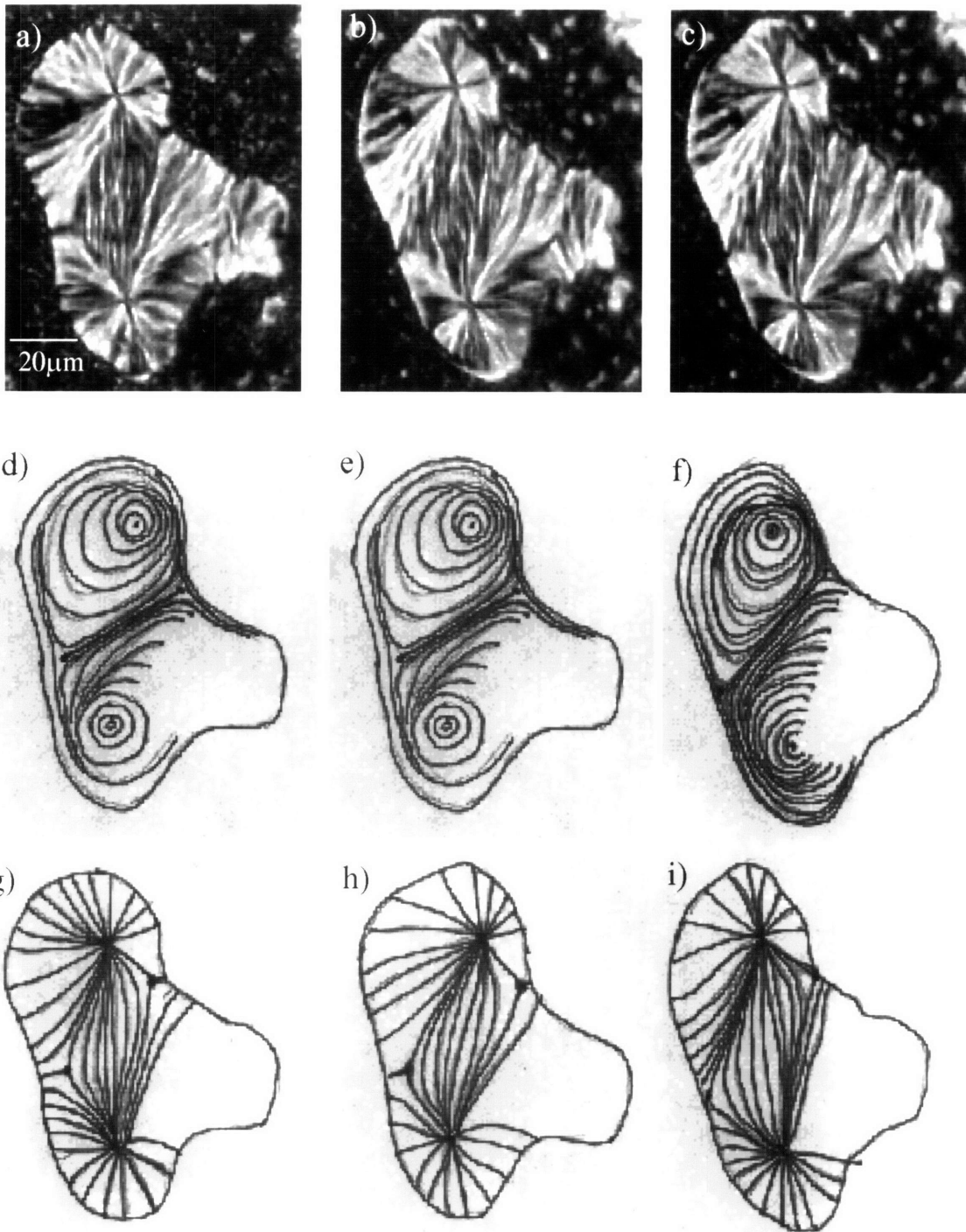


**Figure 3.16:** a-c) a series of images depicting the formation of two  $s=-1/2$  defects from the coalescence of two  $s=+1$  defects. Images taken 10 seconds apart. d-f) The corresponding maps of the director field distribution. g-i) The corresponding maps of the solidification-induced banded texture.

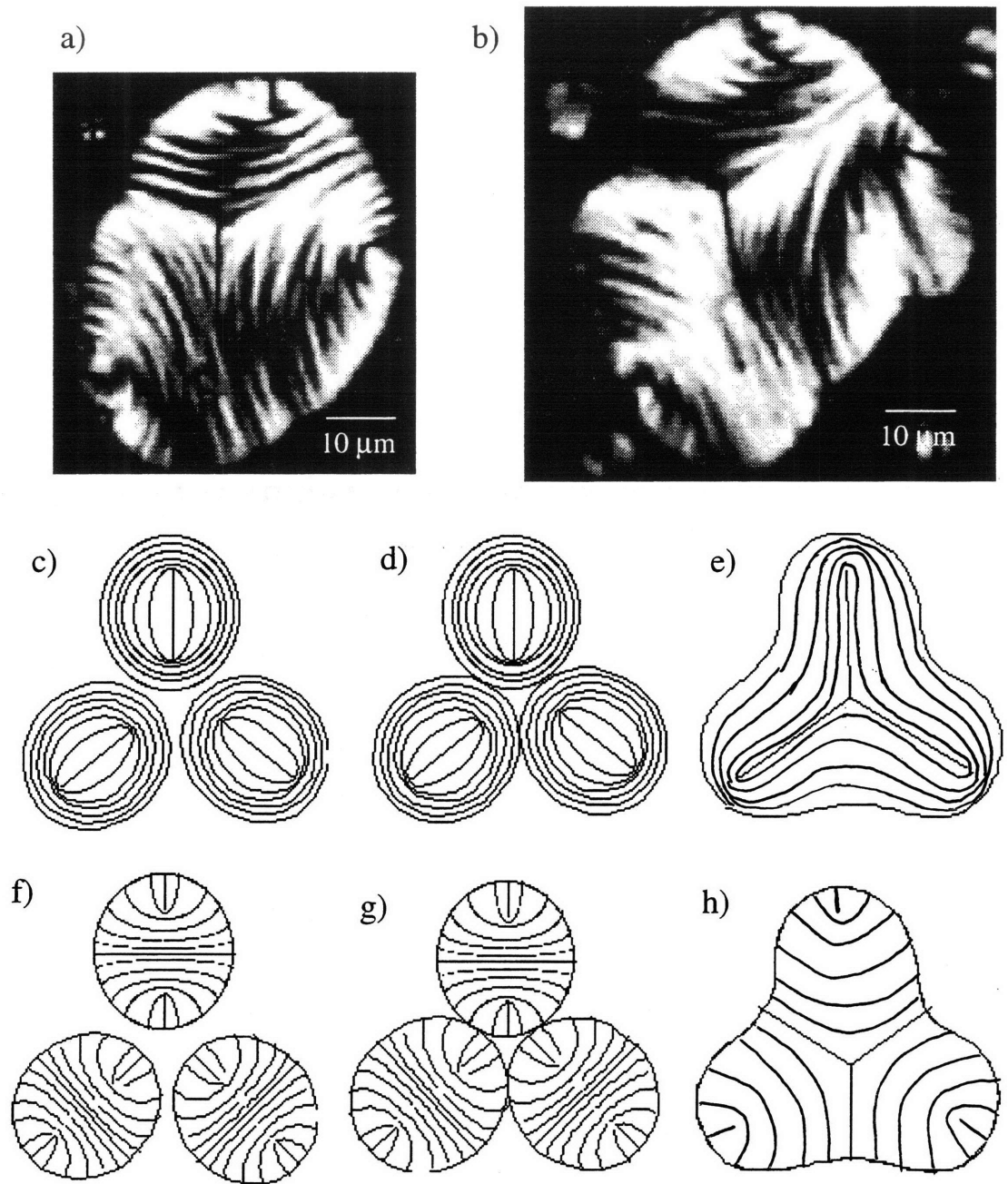


**Figure 3.17:** Two separate examples of a  $s=-1/2$  defect formed by the coalescence of three domains each containing a pair of  $s=+1/2$  defects. d-f) The corresponding maps of the director field distribution. g-i) The corresponding maps of the solidification-induced banded texture. Compare the pattern in “i” with the images in a and b. There is good agreement between experimental results and the proposed model.

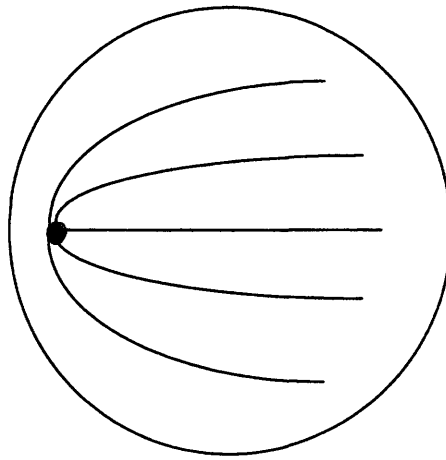
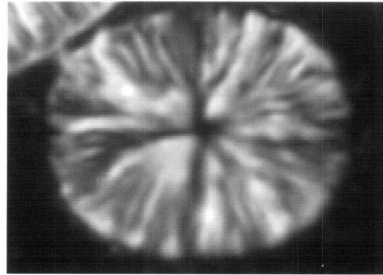
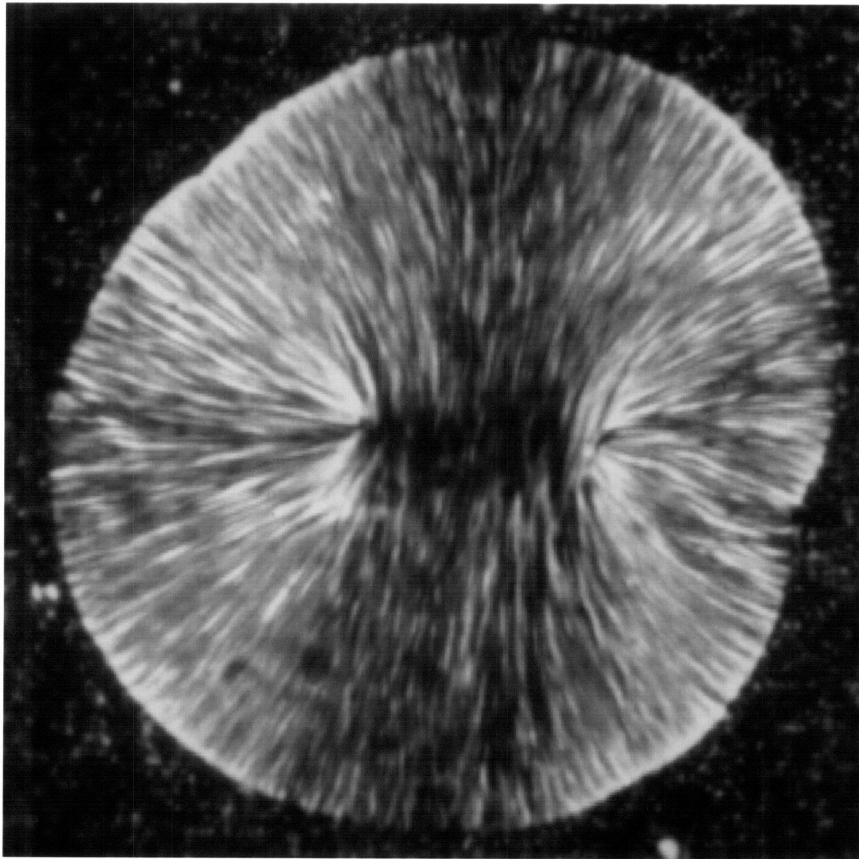


**Figure 3.18:** a) A schematic depicting the incompatibility of a single  $s=+1/2$  defect within a nematic domain formed at early stages. The geometry of this defect make it impossible for the homogeneous anchoring conditions to be satisfied in all locations along the boundary.





— 10  $\mu\text{m}$

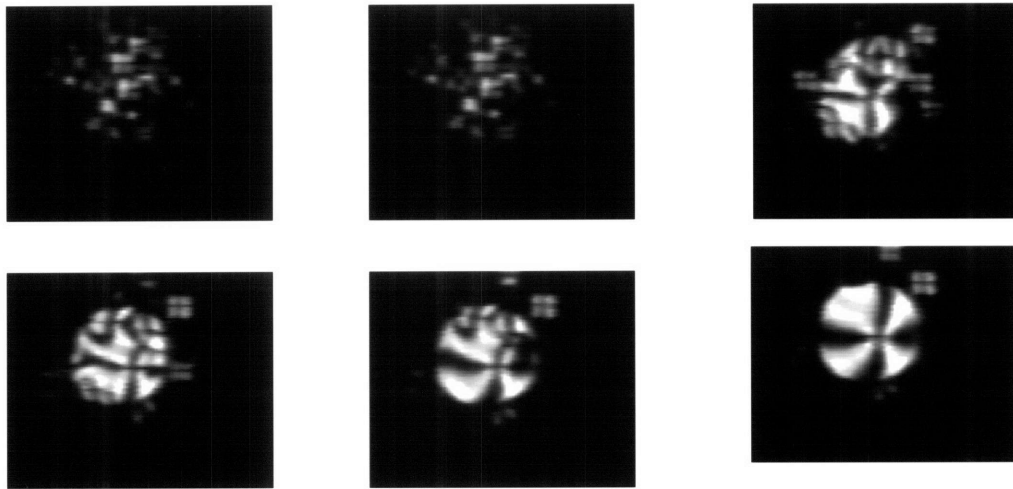


— 10  $\mu\text{m}$

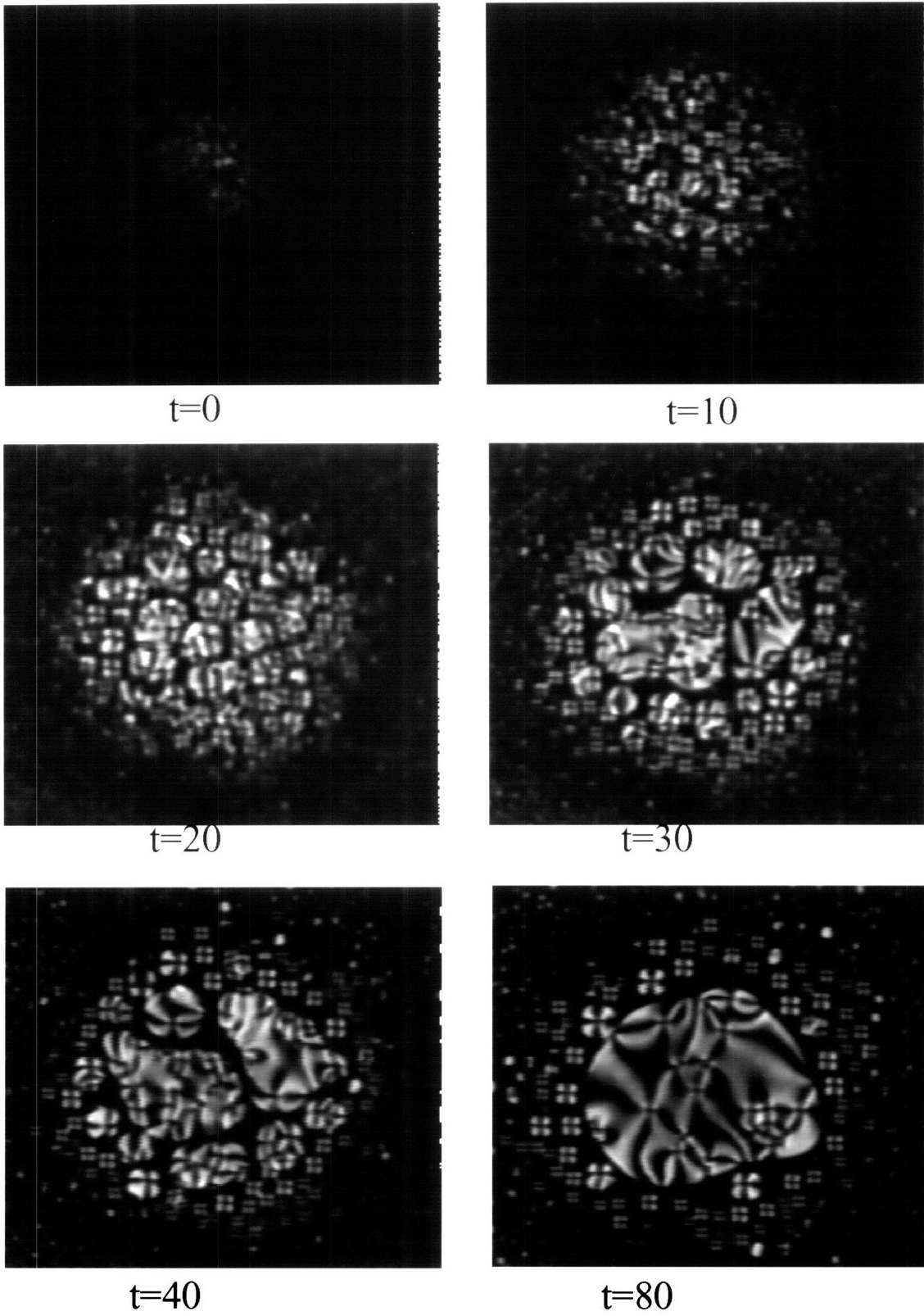
**Figure 3.19:** Images showing the two possibilities for domain recombination.

a) a single  $s=+1$ ,  $c=\pi/2$  defect

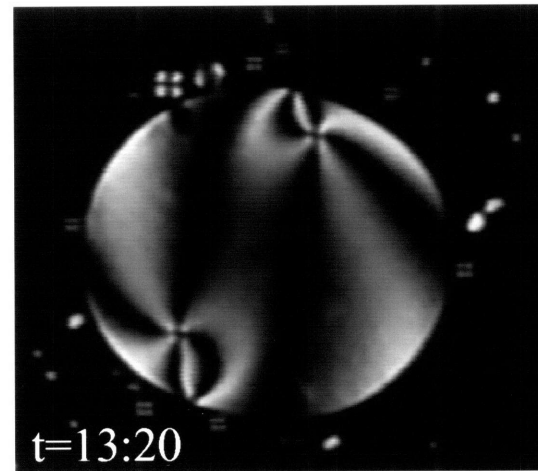
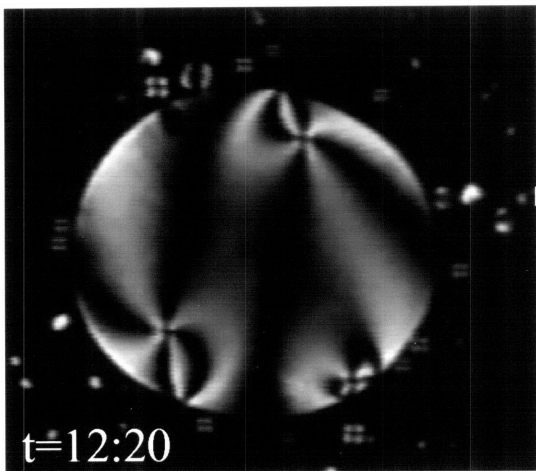
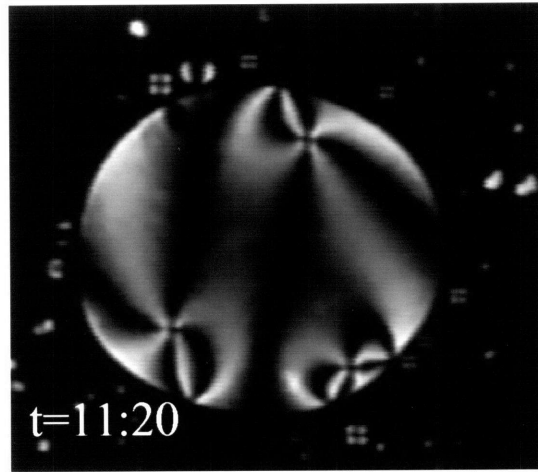
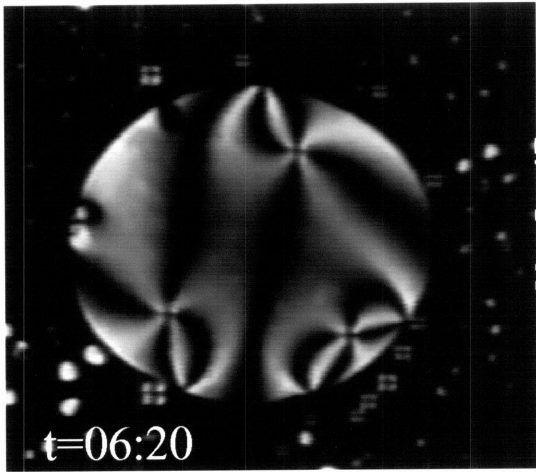
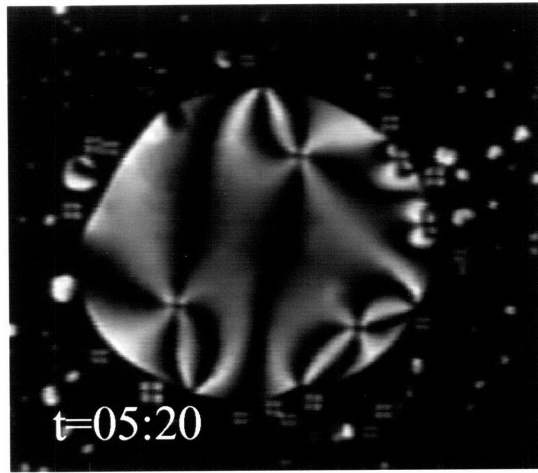
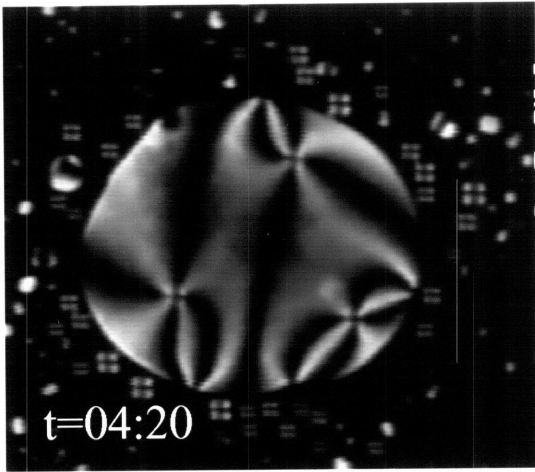
b) a pair of  $s=+1/2$  defects

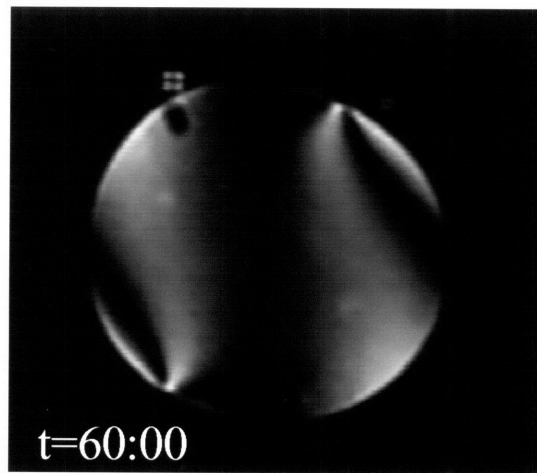
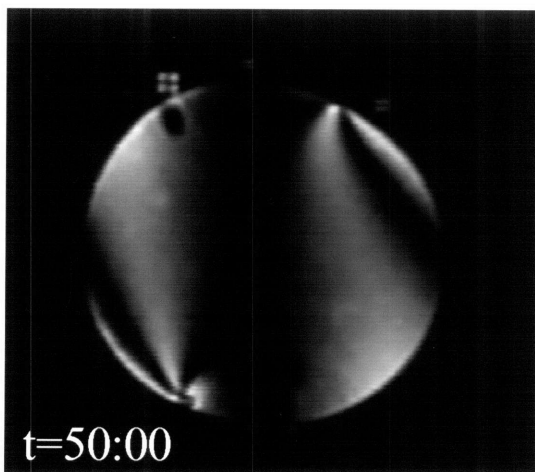
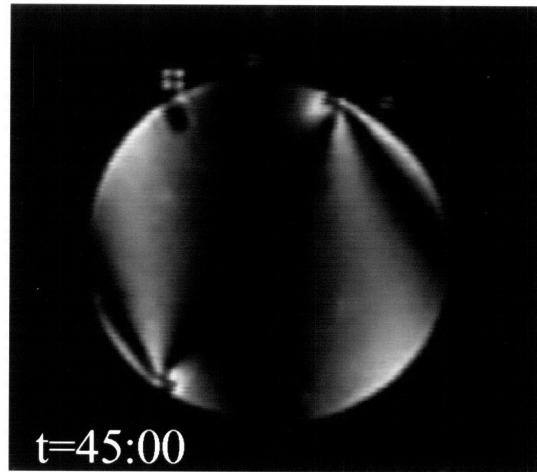
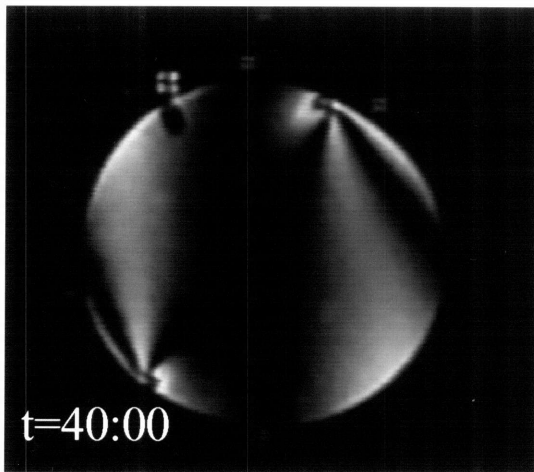
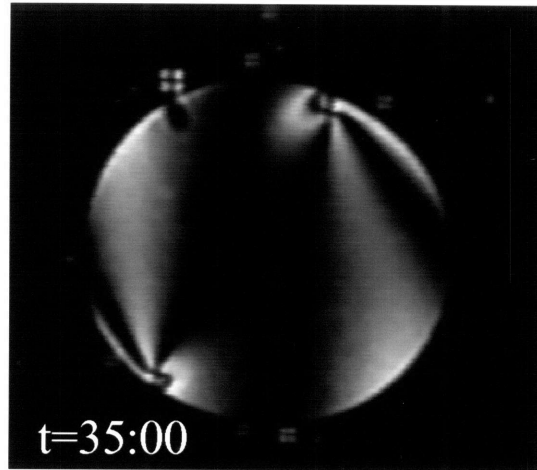
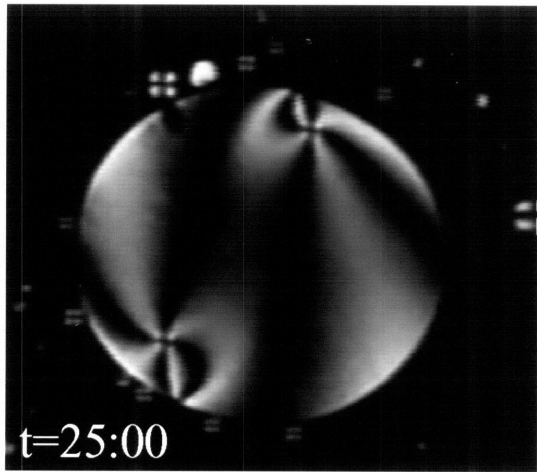


**Figure 3.20:** A video sequence depicting recombination of many small droplets with a single  $s=+1$   $c=\pi/2$  into a single  $s=+1$ ,  $c=\pi/2$  defect.



**Figure 3.21:** Video sequence showing recombination to a pair of  $s=+1/2$  defects





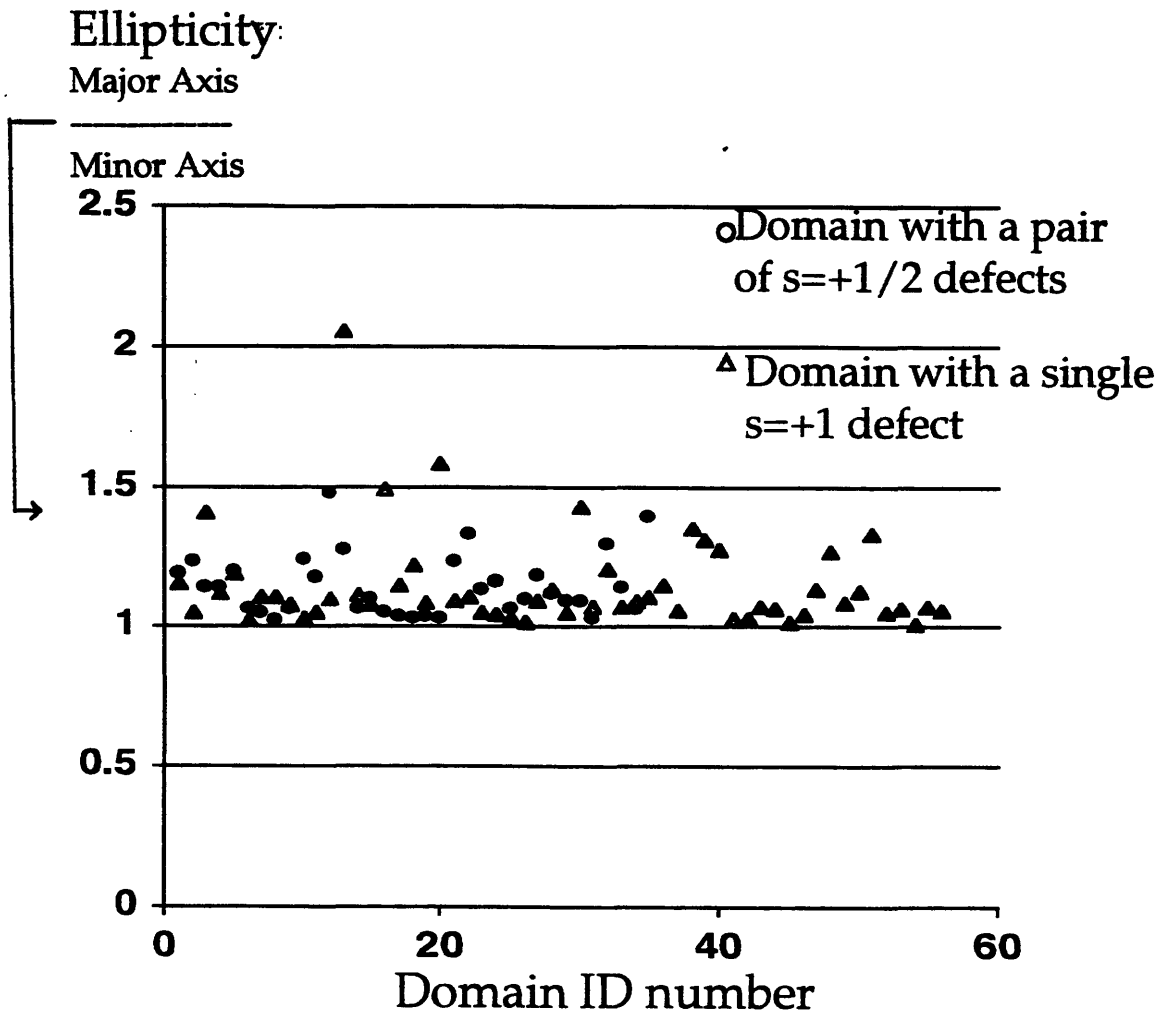


**Figure 3.22:** A plot of ellipticity vs defect type. No correlation exists between these two quantities. However, approximately 90% of the domain reconfiguration events led to the formation of a single  $s=+1$  defect.

## Chapter 4

# Computer Simulations of Static Defect Textures

### 4.1 Introduction

This chapter addresses the subject of high strength defects. For a number of years there has been a controversy as to whether defects of high strength exist. Several research groups have reportedly seen such defects (i.e.  $s=|3/2|$  and  $|2|$ ) under a variety of conditions. These findings will be discussed in detail in the following section. The main section of this chapter uses computer simulations to establish the director field distribution for defects of both low and high strengths. Then a series of simulations are made to illustrate that what appears as a high strength defect may actually be an array of low strength defects that are in close proximity. Finally, I conclude that based on the results of this chapter as well as chapter 3, that defects of high strength are not possible for DHMS-7,9 under quiescent conditions.

### 4.2 Background

Since the energy of an individual defect varies as  $s^2$ , defects of high strength are expected to be rare. Several research groups have reported on the existence of  $s=|3/2|$  and  $s=|2|$  defects[1][2][3][4]. These observations were made on a variety of mesophases using various undercoolings, sample handling procedures (static vs. application of a flow or electric field) and concentration of non-mesogenic components. All apparent cases of  $s>|1|$  were identified via the use of optical microscopy. In most cases even excellent microscopy was not able to unequivocally determine the existence of a single core region. This indicates the importance of using high resolution techniques when carrying out studies of defect structure in liquid crystals.

The first observations of apparent high strength defects were made by Lee and Labes[2]. They performed their studies on mixtures of the small molecule 4-cyano-4'-pentylbiphenyl (CPB) droplets suspended in the lyotropic system disodium cromoglycate-

water-ethylene glycol (weight ratio 15:60:25). This mixture had the characteristics of a microemulsion in that very small droplets of liquid crystal would form in the water phase. The system was mixed either mechanically or ultrasonically and then spread on a microscope slide by shearing with a coverslip. Observations using light microscopy of the defect texture were made immediately after sample preparation. The authors report the existence of singularity points with as many as 16 brushes. Two examples of so-called high strength defects are shown in Figure 4.1. In these micrographs it is difficult to tell whether or not all the dark brushes are emanating from a single core region. It may be possible that they are actually an array of singular points dispersed around a small droplet.

The high strength defects were only seen before the microemulsion broke apart. It was believed that the strong fluctuations at the droplet interface provided a stabilizing effect for defects with  $s > |1|$ . This effect was lost when the microemulsions broke. As a result the high strength defects dissociated into equivalent numbers of the  $s = |1|$  type. The authors qualify their results by stating that it was difficult to distinguish between a “real” high strength defect from several low strength defects (i.e.  $s = |1/2|$  or  $s = |1|$ ) which are in close proximity. The instability of the microemulsion (it broke apart after several minutes) would have made it difficult to conduct more extensive studies.

Additional studies of high-strength defects via light microscopy in liquid crystal mixtures were also made by Madhusudana and Pratibha[1]. They used various small molecule nematic liquid crystals mixed individually with leucoquinizarin which is a non liquid crystalline compound. After cooling though the isotropic to nematic transition temperature, nematic domains formed which later coalesced to produce a schlieren texture. This system exhibited greater phase stability which provided some experimental advantages. These authors reported that defects of strength  $s = |3/2|$  could be observed even after several hours of annealing and up to 30 °C below the nematic to isotropic transition temperature. Upon heating, these defects would stay intact, but isotropic droplets would form in the location of the original defect core. According to the authors, a concentration gradient in this region is what may have led to the stability of the defects with  $s > |1|$ .

The most serious limitation of this study was the interpretation of several of the micrographs. Some defects that are referred to as “high strength” actually appear to the naked eye as lower strength defects connected by a short line defect. An example of this is shown



in Figure 4.2. It is not clear from this particular micrograph that all the brushes are emanating from the same point. In fact it appears as if this defect is actually an  $s=+1$  and an  $s=+1/2$  that are displaced by several microns. This type of problem re-emphasizes the importance not only of careful optical microscopy but the necessity of high resolution techniques.

In 1989, Madhusudana and Pratibha studied the effects of electric fields on morphology of droplets in a cholesteric liquid crystal mixed with a small amount of a non mesomorphic epoxy[4]. The addition of the epoxy not only lowered the transition temperatures but also gave rise to a wide biphasic region that made it possible to obtain stable droplets of up to 50 microns in lateral diameter. In thick sample cells (i.e. 150 microns) they noticed that the tangential anchoring conditions between the cholesteric drop and the isotropic phase led to the formation of an  $s=+2$  defect (see Figure 4.3). Although these studies were conducted only on cholesterics, it suggests that appearance of high strength defects may be dependent upon the specific mesophase and anchoring conditions under consideration.

The most recent work on high strength defects was performed by Viney et al[3]. They were the first to carry out studies using a *single component* nematic liquid crystal. This is important because all the previous studies suggested that high strength defects are stabilized by the surface tension gradients that occur at droplet surfaces or by concentration gradients. Quiescent samples displayed defects of  $s=|1|$  and  $s=|1/2|$  only. Defects of strength  $s=|3/2|$  appeared only after the samples were disturbed by some type of flow field. In this work, the sample was agitated by vigorously moving the top cover slide for a few seconds. The defects of high strength were more frequently seen close to the clearing temperature. Unfortunately, the maximum lifetime of these defects was approximately 30 seconds which made it difficult to conduct more extensive studies. However the fact that they were seen at all was felt to be a result of several conditions including agitation by flow, small undercooling and higher molecular weight.

### 4.3 Computer Methods

This computer simulations in this chapter were produced with Matlab script files prepared specifically for defect generation. A solution to Frank's equations of director field distribution were used for the equiconstant case. The mathematical development of these equations is described in detail in Chapter 1. The form of the equation used in the Matlab script file is shown below:

(4.1)

$$\phi = \sum_i s_i \arctan \left( \left( \frac{y - y_i}{x - x_i} \right) + \text{const} \right)$$

where  $i$  refers to the number of defects that are included in the simulation. To simplify the calculations, a two-dimensional situation was assumed.

The input file to the Matlab script allowed the user to control the following parameters: simulation resolution, number of defects, strength, orientation of the director with respect to the  $x$  axis, and the  $(x_i, y_i)$  location of the  $i$ th defect. The results were in the form of a two dimensional array of numbers representing the orientation of the director at that location in the  $xy$  plane. A map of the actual director field distribution was obtained from a modified form of the `quiver.m` routine in Matlab. This routine typically plots an arrow for each data point in the plot. The end of the arrow opposite the point is placed at the  $(x, y)$  location for the data point in question. This is problematic for plotting director field distributions because gross singularities appear in the plots near the defect cores. To overcome this problem, the `quiver.m` file was changed so that line segments rather than arrows were plotted. In addition, the middle of the line segment was placed at the  $(x, y)$  location of the data point. These changes made it possible to make proper director field distribution plots.

Simulations of polarized light images were made by assuming a linear mapping between director orientation and gray scale level. The output of the 2D array created by Matlab was input to a second script file that rescaled the director orientation angle to a value between 0 and 255 gray levels. Director orientations that corresponded to a polarizer or analyzer direction were set to zero (black) while those at 45 degrees were set to the

maximum gray value of 255 (bright white). The linear gray scale map used for this procedure is shown in Figure 4.4.

#### **4.4 Director trajectories and Polarized Light Simulations for Individual Point Defects**

Simulations of the director field distribution about individual point defects and the corresponding polarized light images are shown in Figures 4.5 to 4.15. The polarized images show the brush patterns that would appear in an actual light microscope under crossed polarizers. In addition, as the defect strength increases, so does the number of brushes, according to the relation: number of brushes= $4*s$ . It should also be noted that defects whose strengths have the same magnitude will look alike under crossed polars. These defect types can be distinguished from one another by rotating the cross polars, inserting compensators in the optical path as well as by using high resolution imaging techniques on polymer samples that are amenable to the lamellar decoration technique.

These simulations can also be used to explain pictorially why defect energy increases as  $s^2$ . As the strength increases, so does the amount of distortion surrounding the core of the defect. As the gradients in the director field become greater, the molecules would find it increasingly difficult to follow the director field distribution. High strength defects would most likely split apart to relieve this strain and lower the total energy of the system.

#### **4.5 Repulsion of Defects of Similar Sign: A single $s=+2$ or two $s=+1$ Defects?**

The energy of defects with  $s>1$  is expected to be high since defect strength varies as  $s^2$ . This should either prevent their formation or at the very least lead to short lifetimes as a result of defect splitting.

The reason for this will first be described from a theoretical point of view. The energy associated with an individual disclination of strength not equal to one is given by the following expression developed by Nehring and Saupe [5]:

(4.2)

$$W = W_c(s) + \pi s^2 dk \ln\left(\frac{R}{r_c}\right)$$

where  $W_c$  is the core energy,  $k$  is a single elastic constant,  $r_c$  is the core radius,  $R$  is the sample radius and  $d$  is the thickness. The minimum energy for a defect of  $s=1$  is:

(4.3)

$$W = W_c(1) + \pi dk(1 - |\epsilon|) \ln\left(\frac{R}{r_c}\right)$$

It can be seen from these equations that the energy of a single  $s=+2$  defect is larger than the sum of the energies of two individual  $s=+1$  defects.

This subject has also been treated by Kleman[6]. For disclinations with integral strength that are expected to have diffuse cores this becomes:

(4.4)

$$W = 2\pi k|s|$$

This implies that a disclination of strength  $s=+2$  would have the same energy as two individual defects of the type  $s=+1$ . However this does not take into account the fact that in actuality the  $s=+2$  defect may have a finite core which would raise its energy and decrease its probability of formation[3].

This can perhaps be seen more clearly from the equation used to describe defect interaction[5]:

(4.5)

$$W = \pi k(s_1 + s_2)^2 \ln\left(\frac{R}{r_c}\right) - 2\pi k \ln\left(\frac{r_{12}}{2r_c}\right)$$

where  $r_{12}$  is the defect separation distance. For two  $s=+1$  defects placed at the same initial location, the energy is equal to:

$$W = 4\pi k \ln\left(\frac{R}{r_c}\right)$$

which is the same solution as the energy of an isolated  $s=+2$  defect. This is a direct result of the fact that defect strengths add mathematically. As the defect separation distance increases, the energy of the system decreases in a logarithmic manner. This suggests that it may be energetically favorable for an  $s=+2$  defect to split into two  $s=+1$  defects with distinct cores. A graphical depiction of this is shown in Figure 4.16. In this plot, equation 4.5 is used in reduced form. The y axis represents the reduced energy which is equal to  $W/(\pi k)$ . The x axis represents a reduced distance of  $r_{12}/2r_c$ . The following values were used for this problem:  $R=10$  microns,  $r_c=0.1$  microns and  $s_1=s_2=+1$ . In practice the first two parameters will depend on the elastic constants and the temperature. The numbers used here represent average values. The dramatic decrease in the repulsive energy with a function of separation is clearly seen in the plot.

This effect can also be shown pictorially using simulations of the director field distribution along with the corresponding polarized light images. What one hopes to gain from such a study is a determination of what separation distance is required for distinguishing individual defect cores.

For these simulations, two defects of the type  $s=+1$ ,  $c=\pi/2$  were placed on a 2D lattice at the same initial location and were then moved apart. The initial simulation for two  $s=+1$  defects in the same location (Figure 4.17) looks exactly like a single  $s=+2$  defect (Figure 4.12) since defect strengths sum mathematically. The next set of simulations show the two  $s=+1$  defects as they are moved apart. The table shown below lists the Figure numbers along with a normalized distance factor  $d/R$  (separation/sample size).

Figure Number	$d/R$
4.17	0
4.18	0.022
4.19	0.044

**Table 4.1: A list of Figure numbers and the corresponding  $d/R$  value**

Figure Number	d/R
4.20	0.177
4.21	0.266
4.22	0.355
4.23	0.444

**Table 4.1: A list of Figure numbers and the corresponding d/R value**

When  $d/R$  is much less than 1, the two  $s=+1$  defects still look exactly like a single  $s=+2$  defect. It is not until  $d/R$  reaches values around 0.2 that the two different defect cores are distinguishable. When  $d/R$  reaches 0.25 the existence of two  $s=+1$  can easily be detected. This suggests that the reports of high strength defects are tentative at best. In order for those studies to have been more conclusive, higher resolution techniques such as TEM, SEM, or AFM should have been used. However, this may not have been possible for the studies that utilized low molar mass liquid crystals.

#### **4.6 Defect Generation Mechanism Experiments, Computer Simulations and the Implications for Defects of High Strength**

The existence of defects of high strength is tentative from energy considerations alone. The computer simulations described in the previous section established that defects of similar sign placed in close proximity will appear as high strength defects especially for small values of  $d/R$ . When these notions are considered in light of the theories put forth for defect generation mechanisms in Chapter 3, the existence of defects of high strength in this system becomes very unlikely.

As discussed in Chapter 3, the only defects that form during early stages of domain development for our system are the  $s=+1$   $c=\pi/2$  type. The specific conditions are discussed in the introduction to chapter 3. Briefly, the polymer DHMS-7,9 was examined at an undercooling of 20 °C with homogeneous anchoring at the air/nematic interface, homogeneous anchoring at the isotropic/nematic interface, and homeotropic anchoring between the coverslip and the nematic phase. In addition the samples were examined in a static sit-

uation - no agitation was used. Defects of high strength would not form during initial stages of domain development because their geometries would not satisfy homogeneous anchoring in all regions of the boundary (see Figure 4.24). This presupposes that anchoring energy is dominant in the total free energy of the defect system. In order for high strength defects to exist they would have to be formed from the coalesce of small domains containing an  $s=+1$  defect.

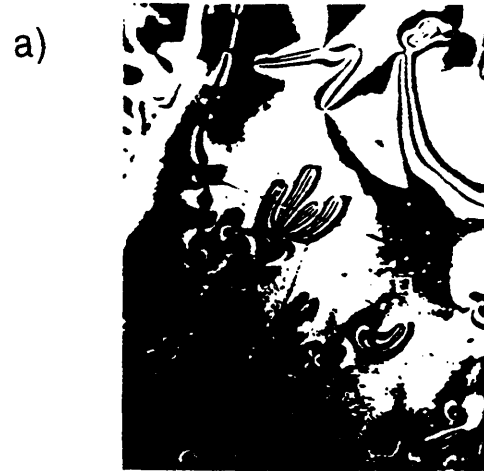
When two domains each with an  $s=+1$  defect coalesce, the resulting ensemble has two new  $s=-1/2$  defects. This would never give the  $s=+2$  defect a chance to form. The presence of the two  $s=-1/2$  defects would cause annihilation events to occur which would prevent the  $s=+1$  defects cores from coming any closer. If one tries to imagine how an  $s=+3/2$  defect might form, the situation would be very similar. It initially seems possible that an  $s=+3/2$  could form from the interaction of an  $s=+1$  and an  $s=+1/2$  defect. A schematic describing this is shown in Figure 4.25. Just as the domains coalesce, the homogeneous anchoring conditions are violated (regions marked with arrows). In order to correct this situation, the director field has to form smooth continuous lines in front of the cusps just as it did for coalescence of two  $s=+1$  defects. When this happens, two new topological defects are created which are of the  $s=-1/2$  type. Thus, the  $s=+3/2$  defect would never form because the defects of negative strength would attract the positive strength defects and prevent them from getting close enough to create the defect of higher strength.

These results are specific for the DHMS-7,9 system examined in detail in chapter 3. Since sample agitation or addition of another phase was not addressed, the claims should not be considered as universal. As discussed in section 4.2 it may be possible for high strength defects to be stabilized by specific anchoring conditions, high core energies, or concentration gradients. However, the results of the computer simulations are significant because they emphasize the limitations associated with optical microscopy. High resolution techniques such as AFM, SEM, or TEM must be used whenever possible to give a true picture of the director field distribution.

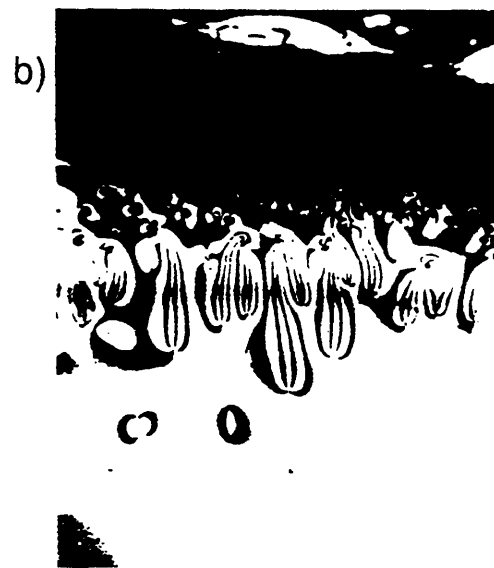




- [1] Madhusudana, N.V. and Pratibha, R., "Studies on High Strength Defects in Nematic Liquid Crystals", *Mol. Cryst. Liq. Cryst.*, **103**, 31, 1983
- [2] Lee, H. and Labes, M.M., "Observation of Apparent High Strength Singularities in Mixtures of Nematic Thermotropic and Lyotropic Liquid Crystals", *Mol. Cryst. Liq. Cryst.*, **82**, 199, 1982
- [3] Viney, C., Brown, D.J., Dannels, C.M., and Twieg, R.J., "High Strength Disclinations in a Rigid Rod Nematic Polytolane", *Liq. Cryst.*, **13**(1), 95, 1993,
- [4] Madhusudana, N.V. and Pratibha, R., "An Experimental Investigation of Electromechanical Coupling in Cholesteric Liquid Crystals", *Liq. Cryst.*, **5**(6), 1989
- [5] Nehring, J. and Saupe, A., "On the Schlieren Texture in Nematic and Smectic Liquid Crystals", *J. Chem. Soc. Faraday Trans. II*, **68**, 1-15, 1972
- [6] Kleman, M., Points, Lines, and Walls, John Wiley and Sons, New York, 1983



(a) 100  $\mu$



100

**Figure 4.1:** Two images from reference [2] depicting possible high strength defects. a) A micrograph of CPB combined with a droplet of DSCG|H<sub>2</sub>O|EG. Possible defects with  $s=+4, +2 \frac{1}{2}$ , are indicated by the arrows. b) A micrograph of MBBA combined with a droplet of DSCG|H<sub>2</sub>O|EG. Singularities from  $s=|1|$  to  $s=|4|$  were reported.

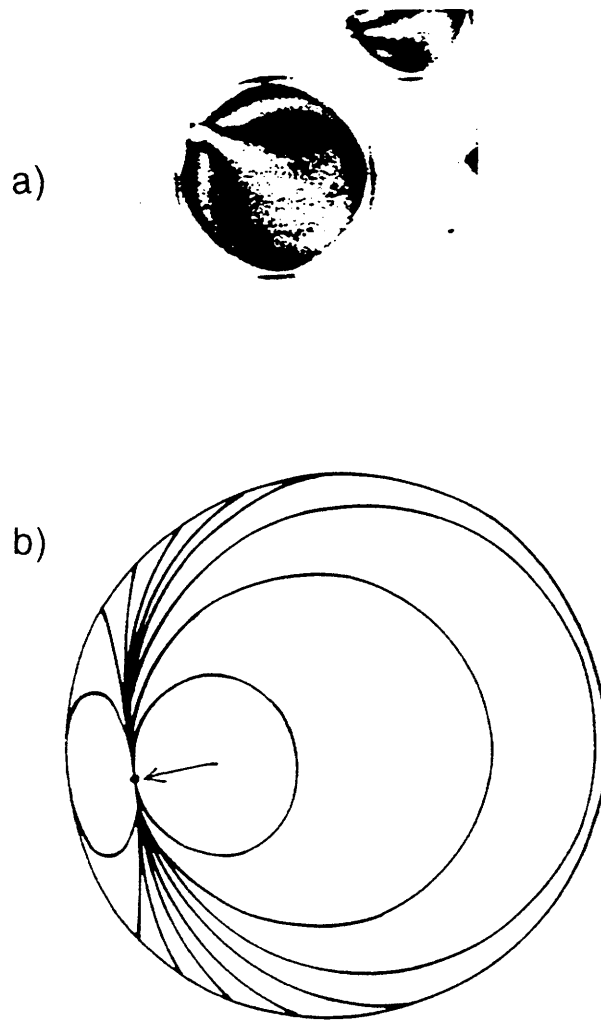


**Figure 4.2:** a) An image of a cholesteric droplet showing a  $\chi$  disclination line. The sample thickness is 150 microns[4]. b) A schematic depicting the director field distribution on the surface of the cholesteric droplet. The singularity point marked by the arrow is an  $s=+2$  defect.

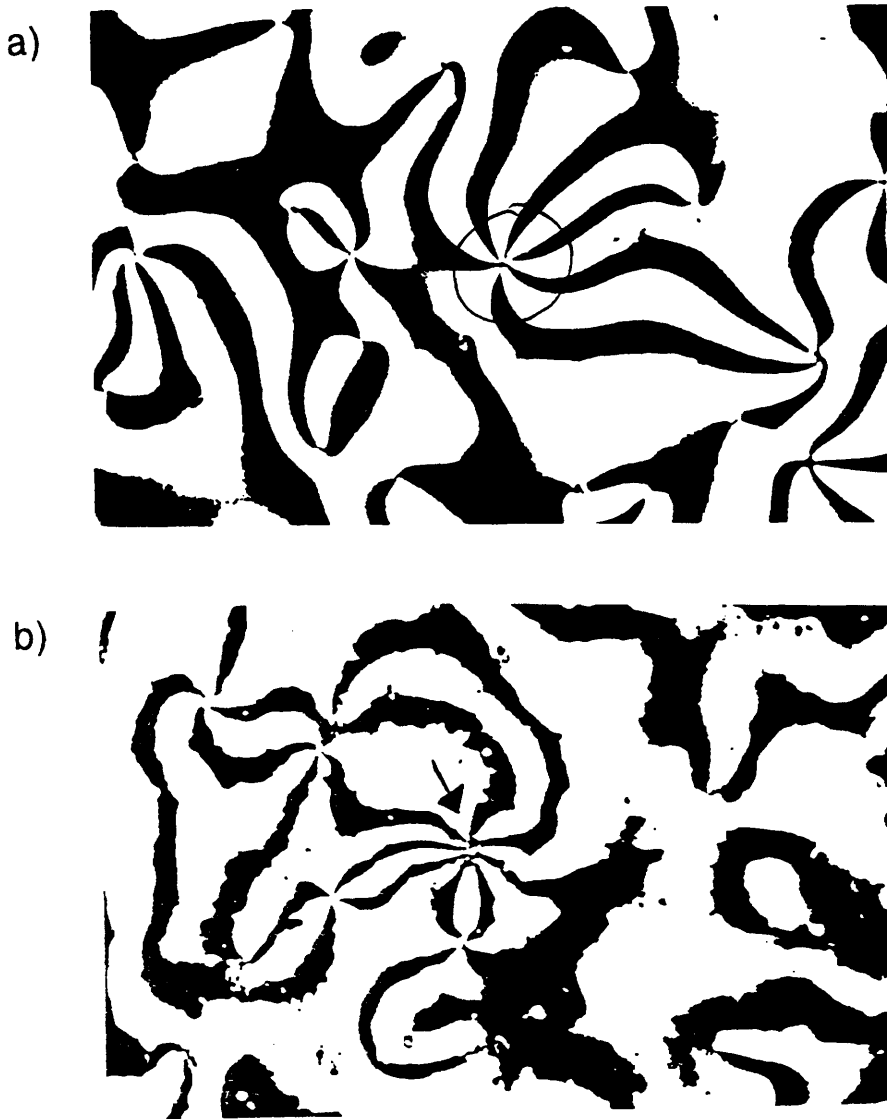


**Figure 4.3:** a) An example of an  $s=+3/2$  defect from reference [1]. The circled region actually appears to be an  $s=+1$  and an  $s=+1/2$  defect connected by a short line defect. It is not clear that the defects occupy the same core region. b) A defect reported by the authors to be of type  $s=+2$ . This actually appears to be two  $s=+1$  defects in close proximity.

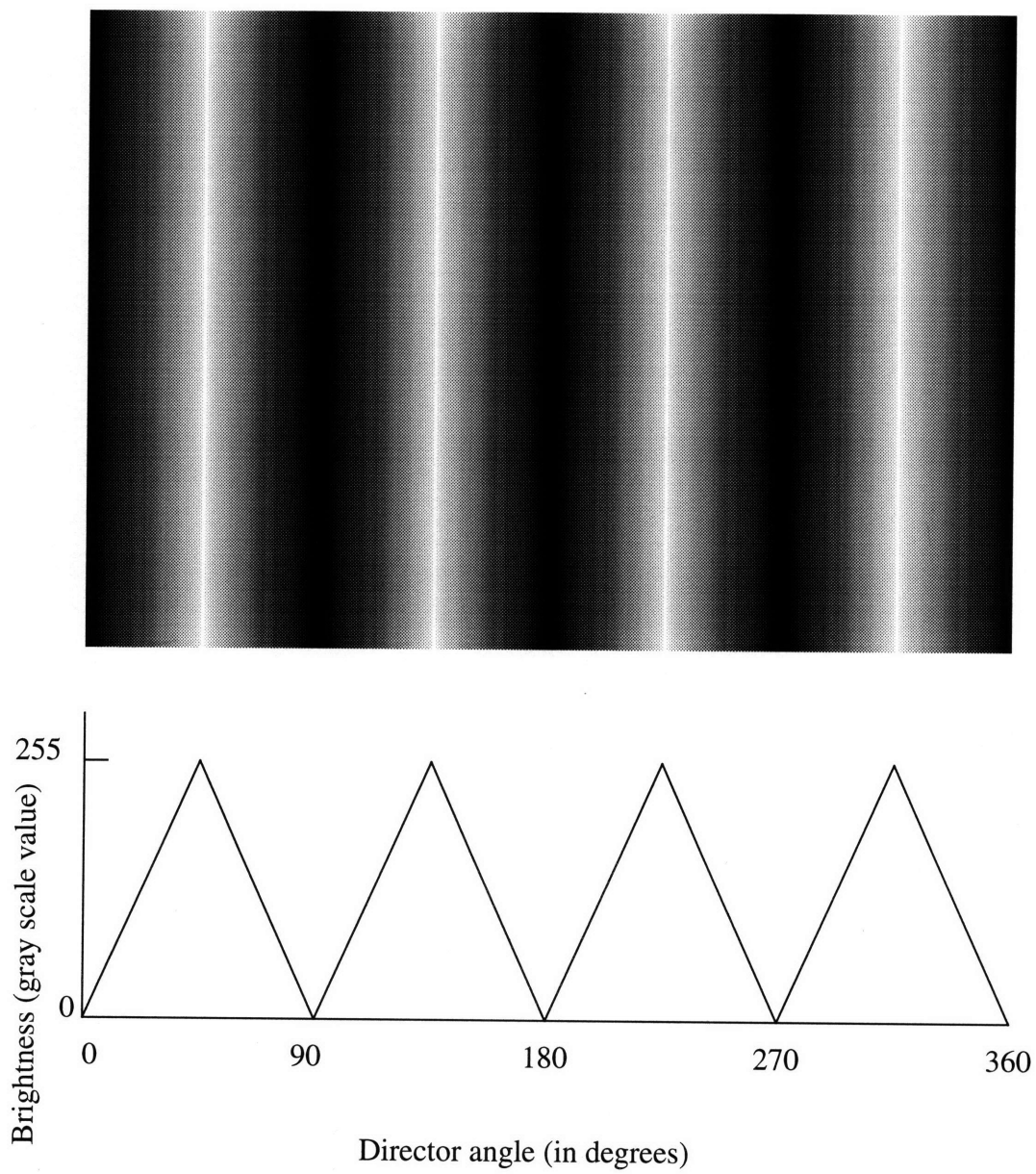


**Figure 4.4:** The linear colormap used for producing the simulated polarized light images

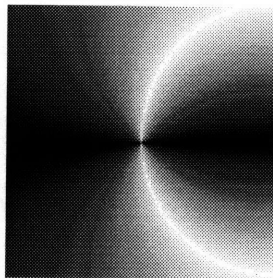
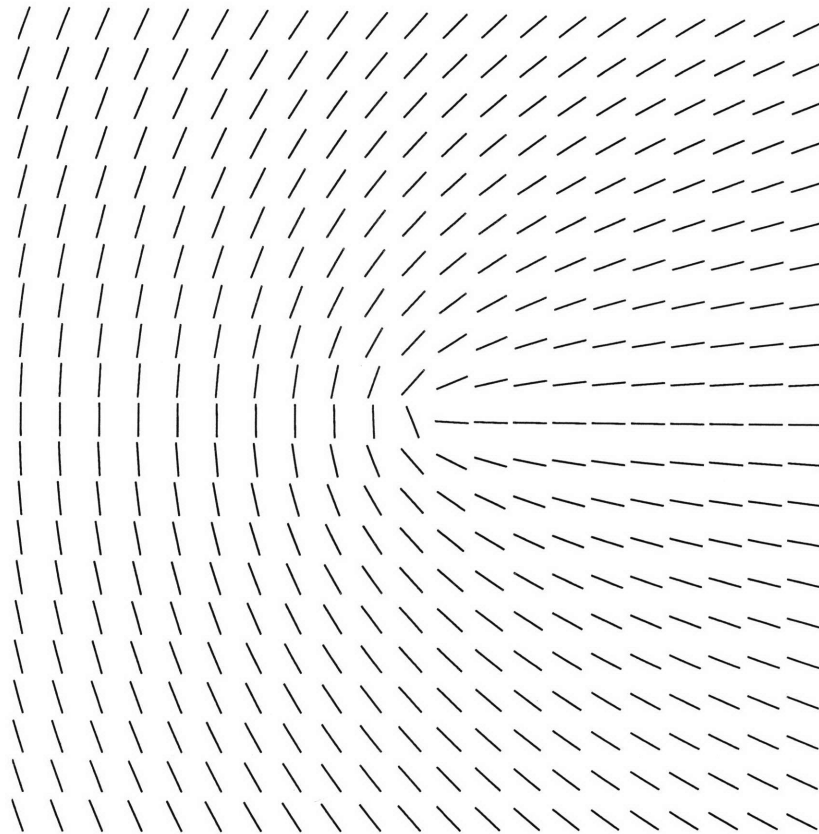


**Figure 4.5:** a) Simulation of the director field distribution for an  $s=+1/2$  defect. b) The corresponding polarized light simulation

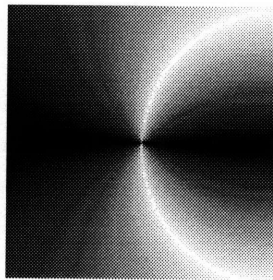
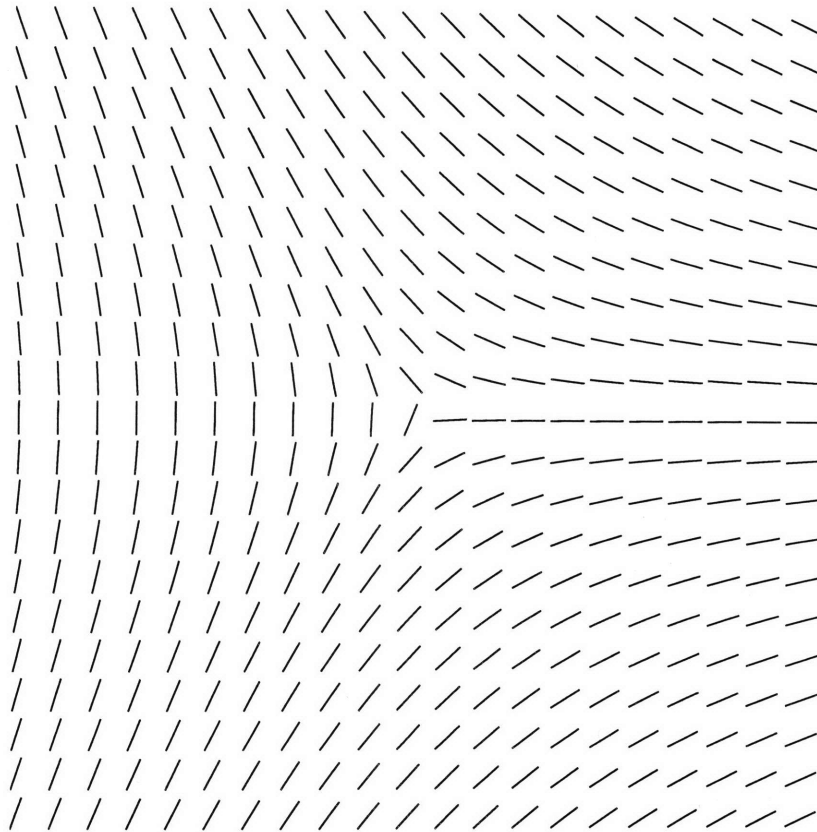


**Figure 4.6:** a) Simulation of the director field distribution for an  $s=-1/2$  defect. b) The corresponding polarized light simulation

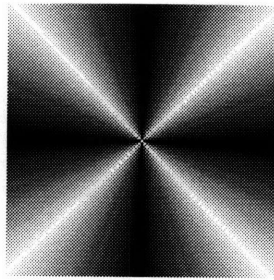
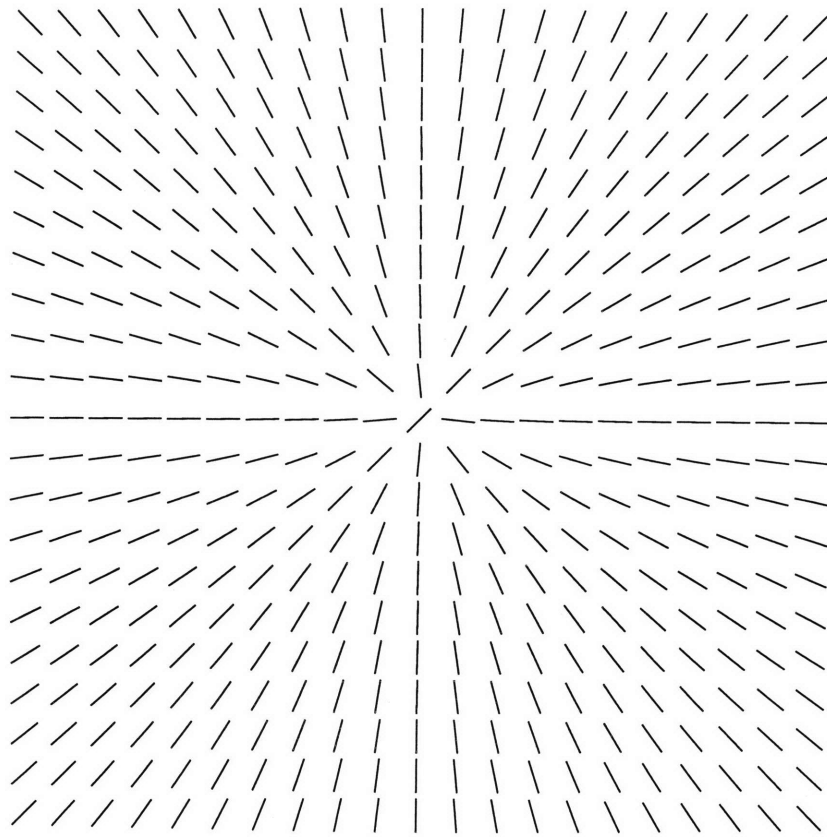


**Figure 4.7:** a) Simulation of the director field distribution for an  $s=+1$ ,  $c=0$  defect. b) The corresponding polarized light simulation



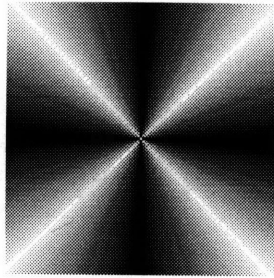
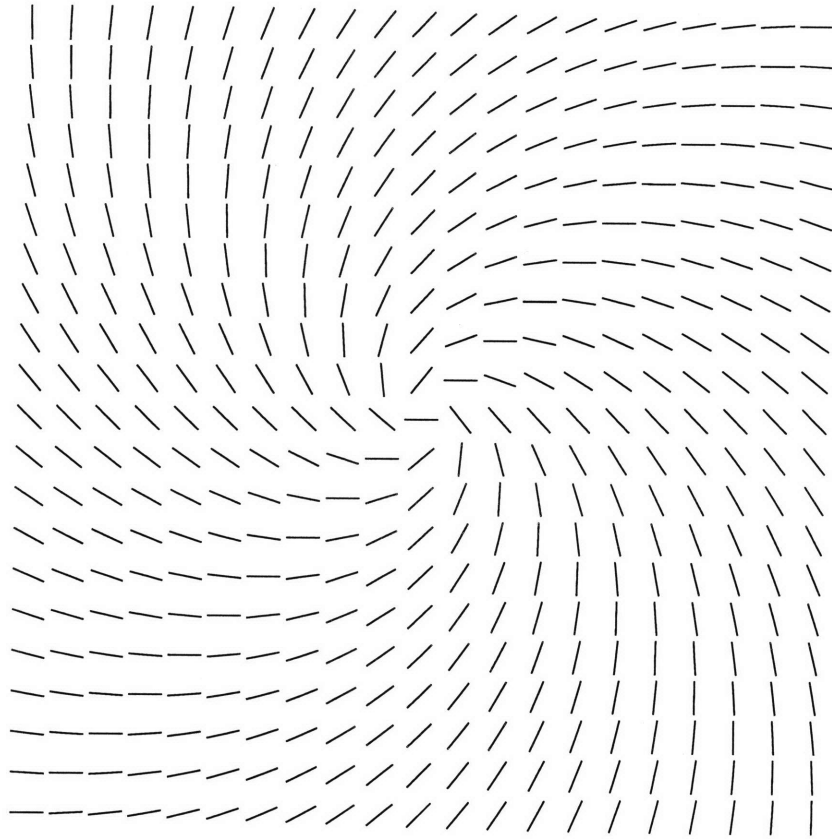


**Figure 4.8:** a) Simulation of the director field distribution for an  $s=+1$ ,  $c=\pi/4$  defect. b) The corresponding polarized light simulation

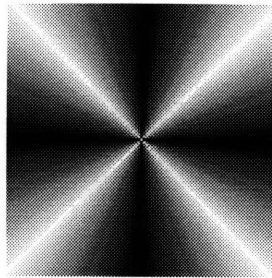
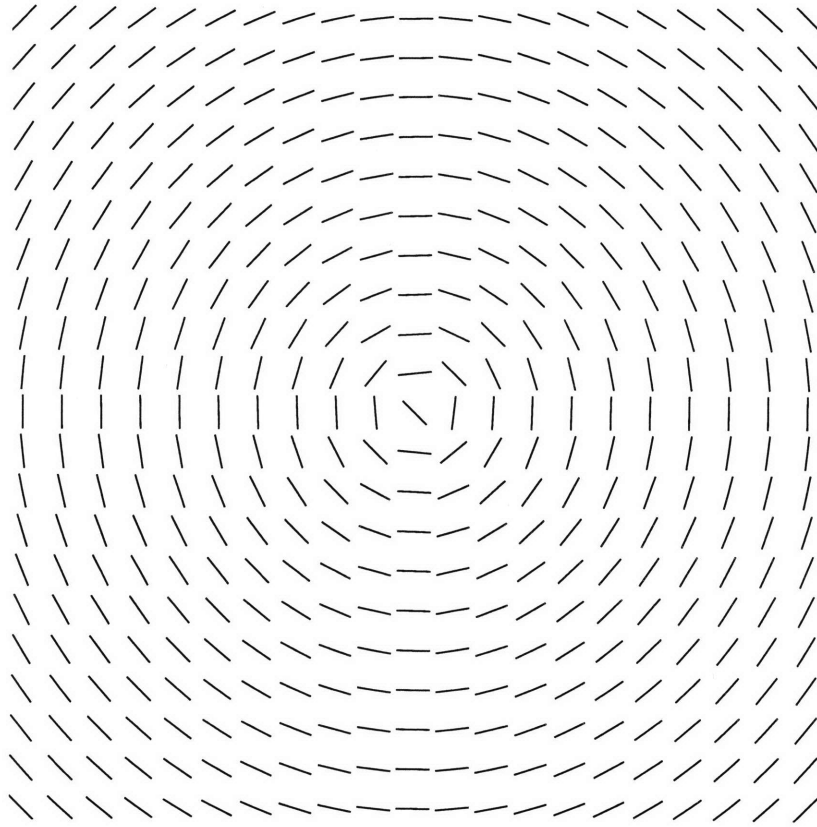


**Figure 4.9:** a) Simulation of the director field distribution for an  $s=+1$ ,  $c=\pi/2$  defect. b) The corresponding polarized light simulation

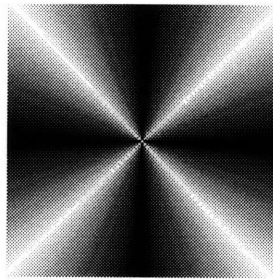
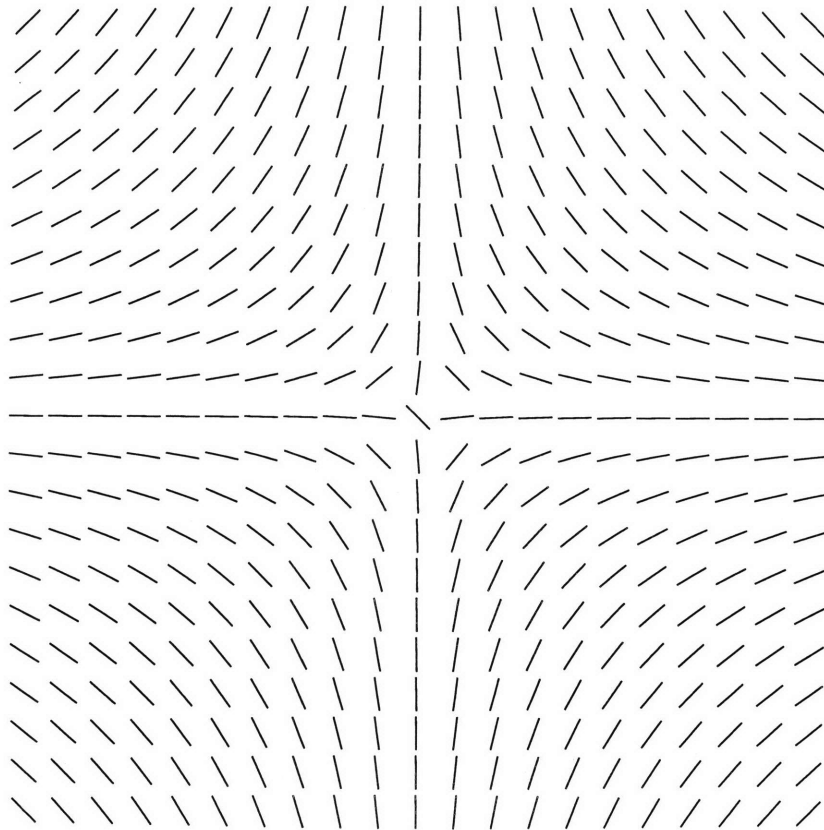


**Figure 4.10:** a) Simulation of the director field distribution for an  $s=-1$  defect . b) The corresponding polarized light simulation

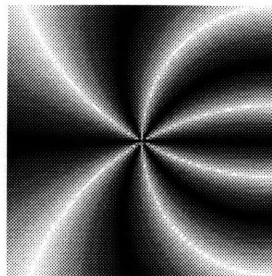
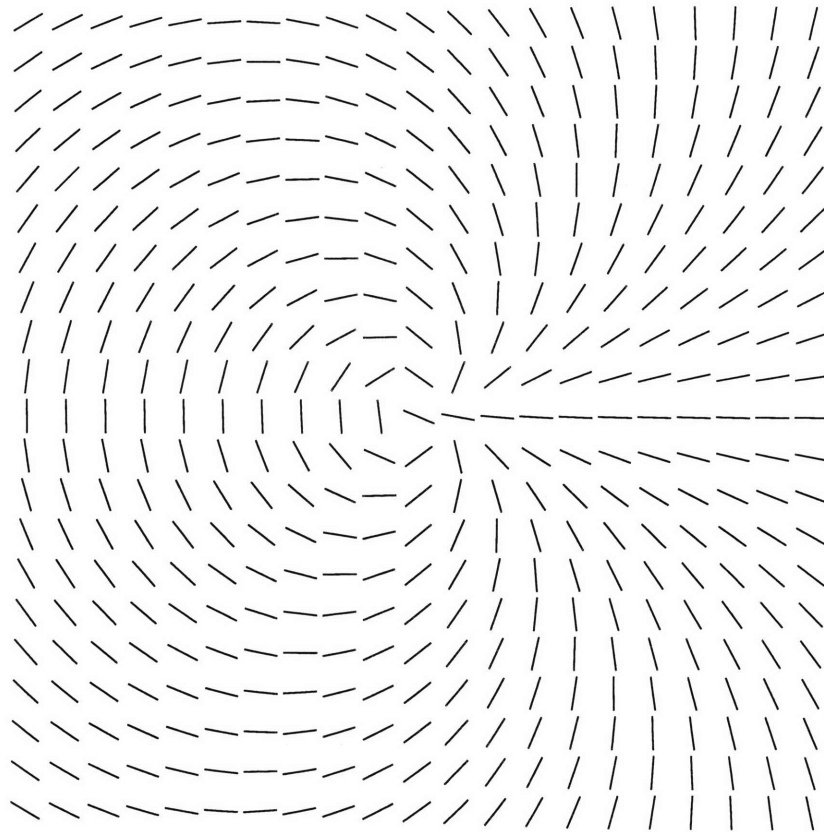


**Figure 4.11:** a) Simulation of the director field distribution for an  $s=+3/2$  defect. b) The corresponding polarized light simulation

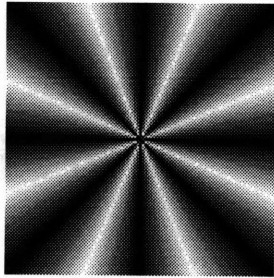
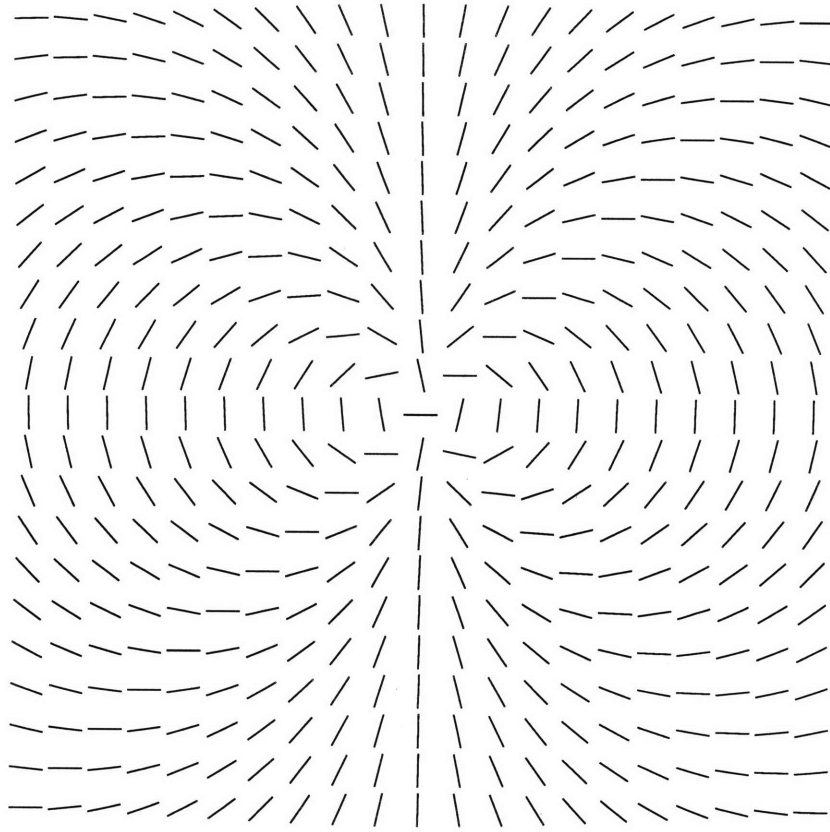


**Figure 4.12:** a) Simulation of the director field distribution for an  $s=+2$  defect. b) The corresponding polarized light simulation

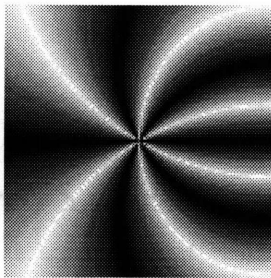
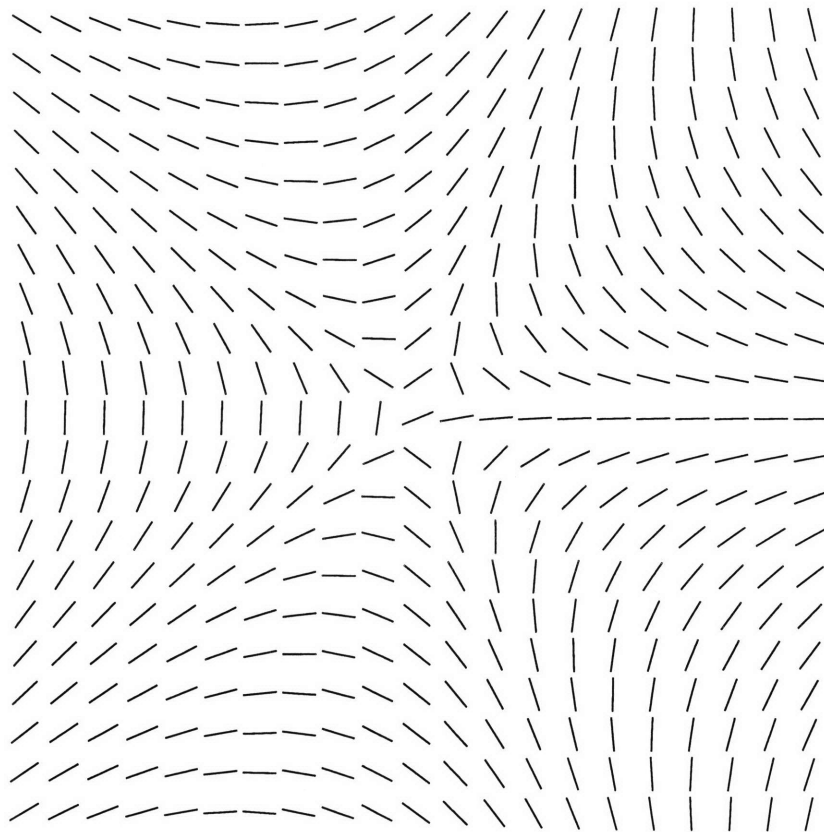


**Figure 4.13:** a) Simulation of the director field distribution for an  $s=-3/2$  defect. b) The corresponding polarized light simulation

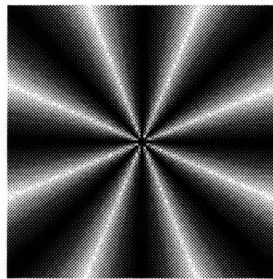
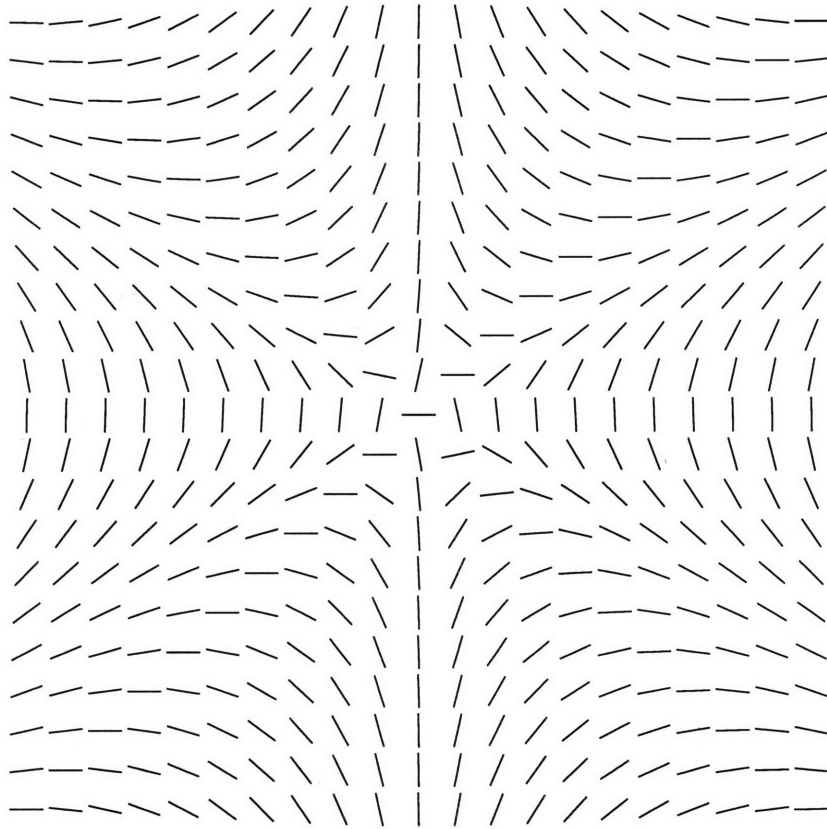


**Figure 4.14:** a) Simulation of the director field distribution for an  $s=-2$  defect. b) The corresponding polarized light simulation

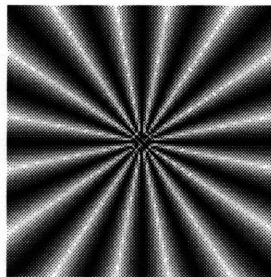
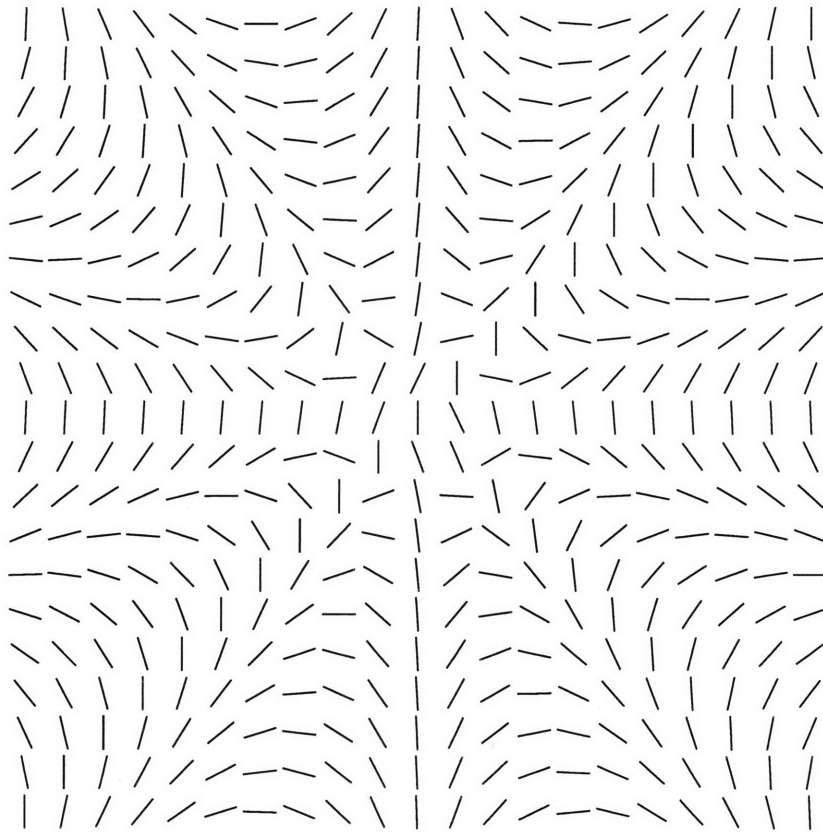


**Figure 4.15:** a) Simulation of the director field distribution for an  $s=+4$  defect. b) The corresponding polarized light simulation





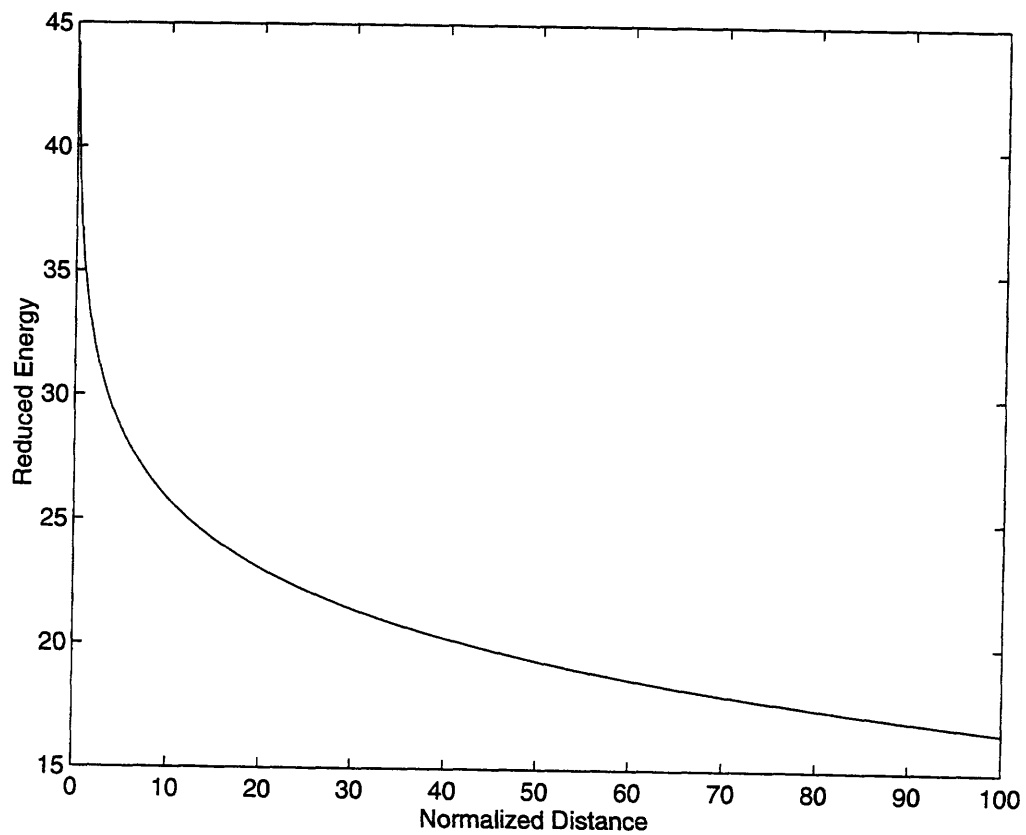


**Figure 4.16:** A plot of reduced energy vs normalized separation distance for two  $s=+1$  defects

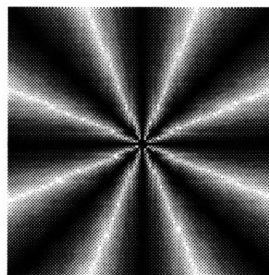
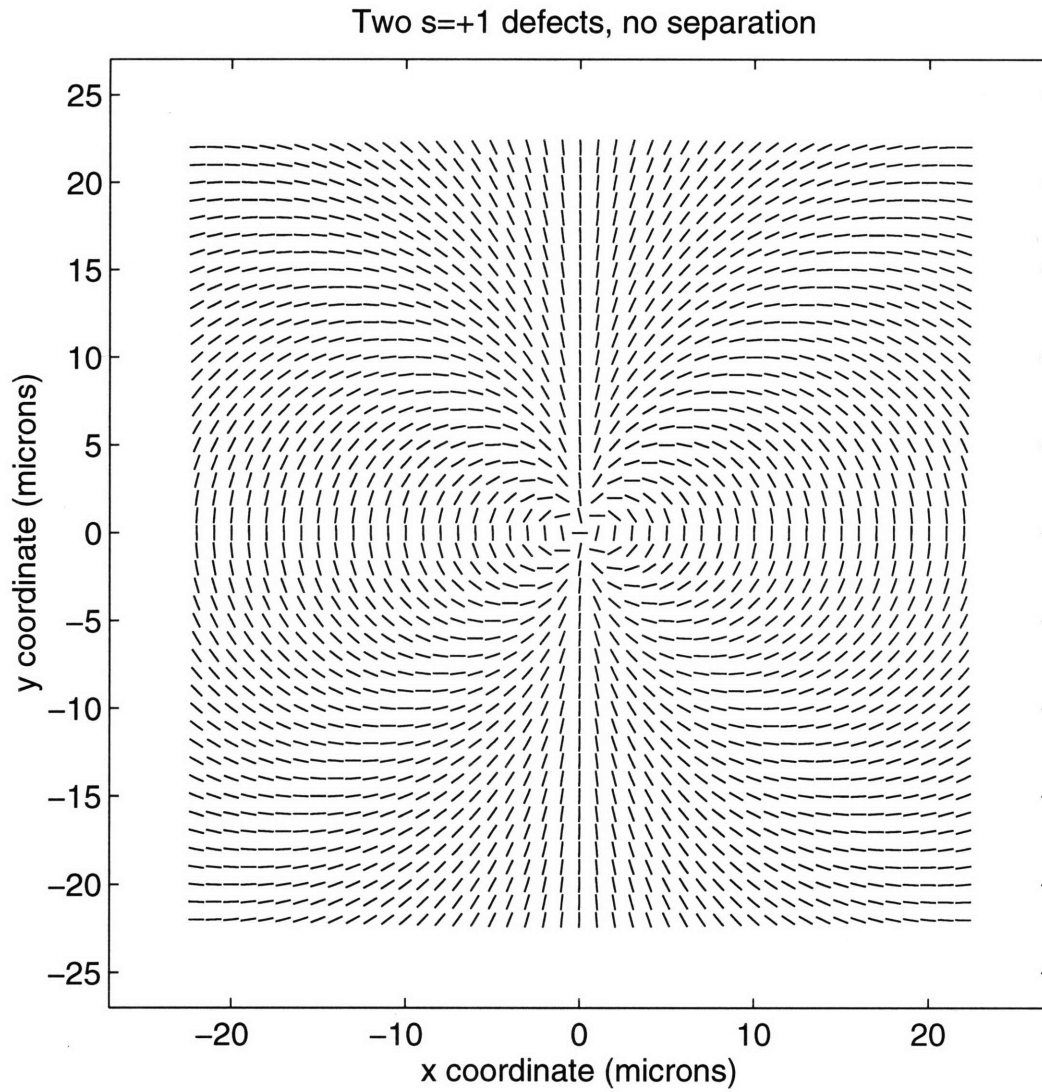


**Figure 4.17:** A simulation of the director field distribution for two  $s=+1$ ,  $c=\pi/2$  defects in the same location.

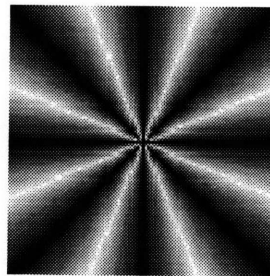
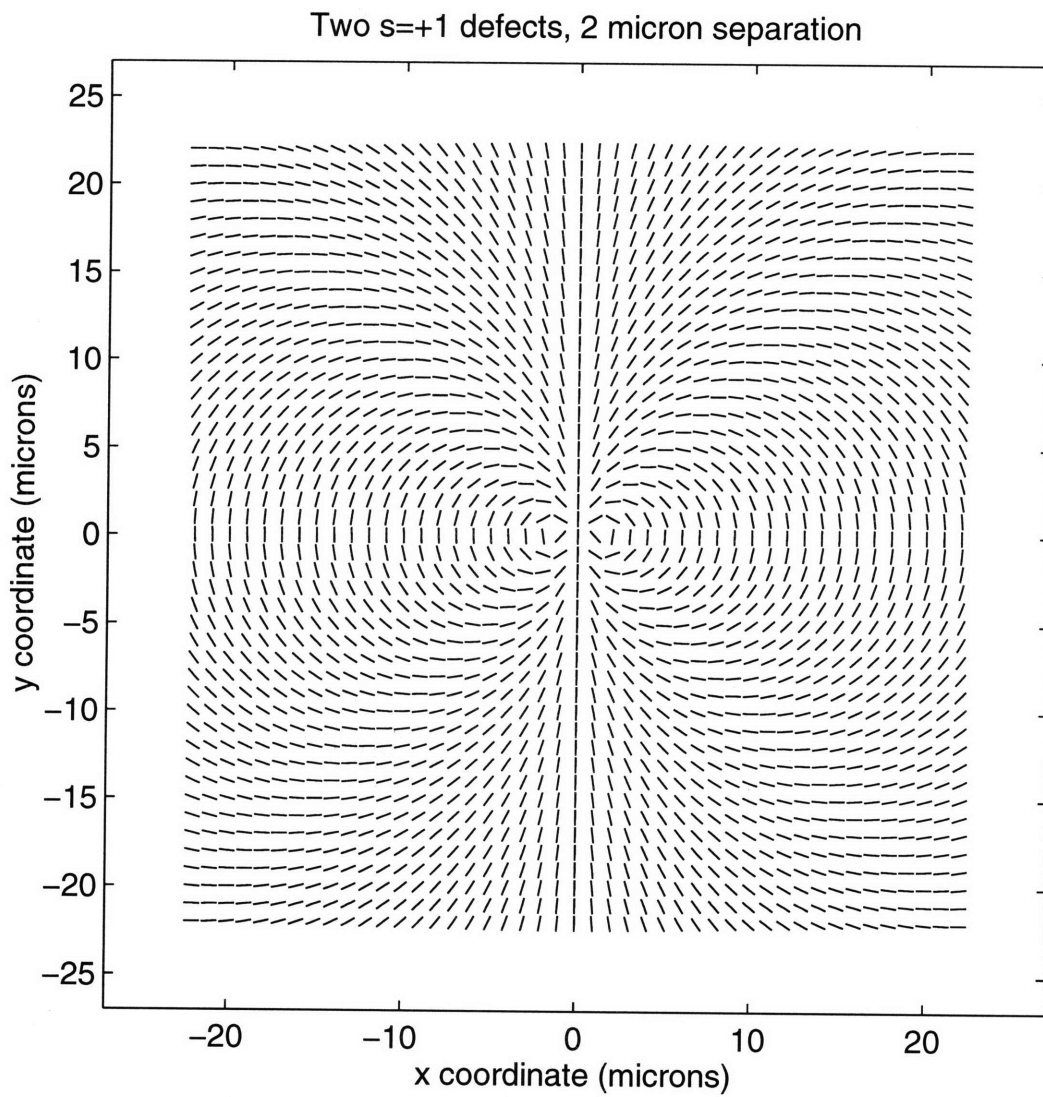


**Figure 4.19:** Two  $s=+1$ ,  $c=\pi/2$  defects with  $d/R=0.044$ . The two cores are indistinguishable

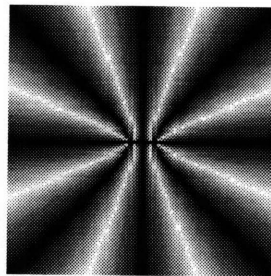
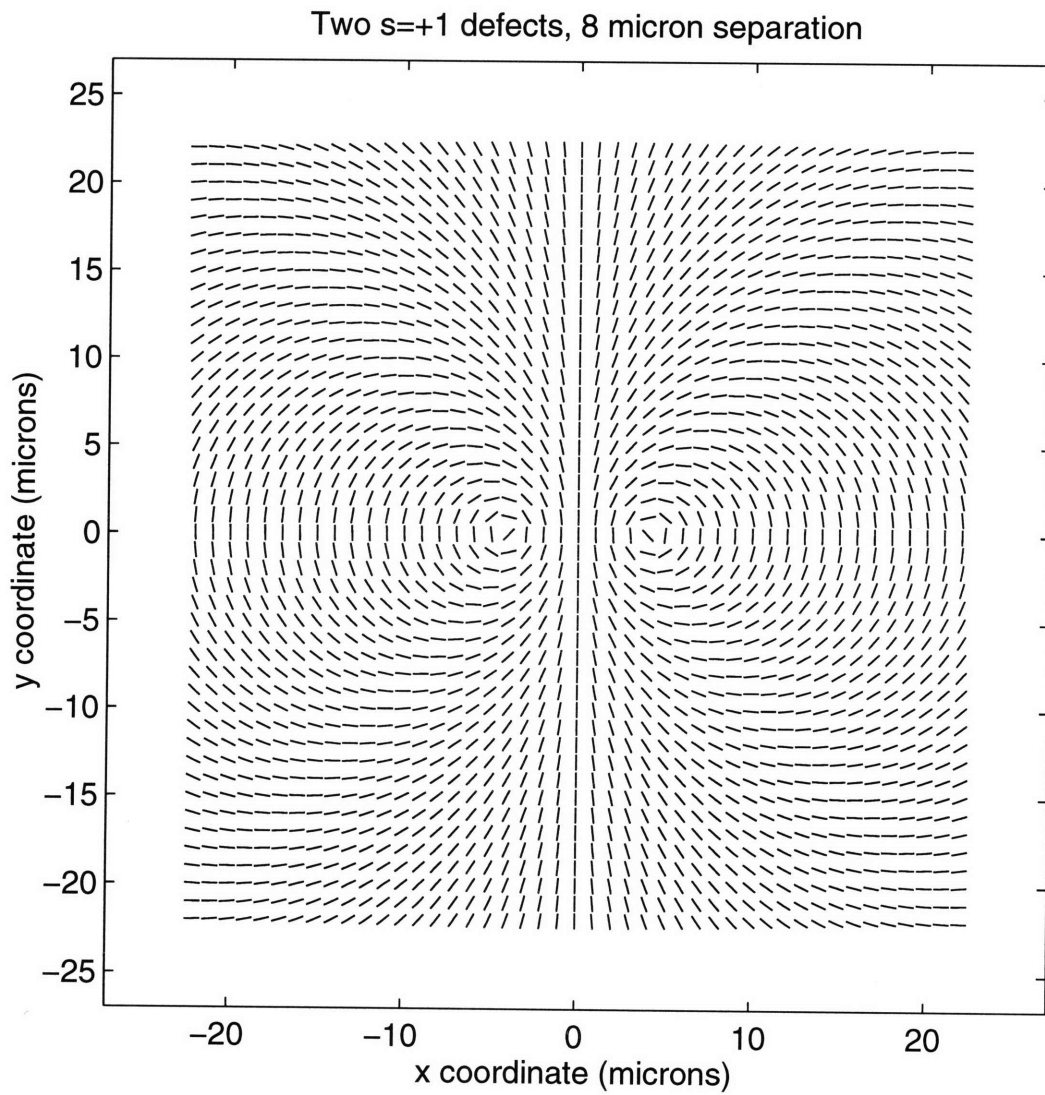


**Figure 4.20:** Two  $s=+1$ ,  $c=\pi/2$  defects with  $d/R=0.177$ . The cores are barely distinguishable.

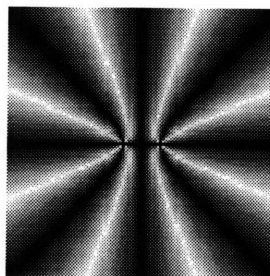
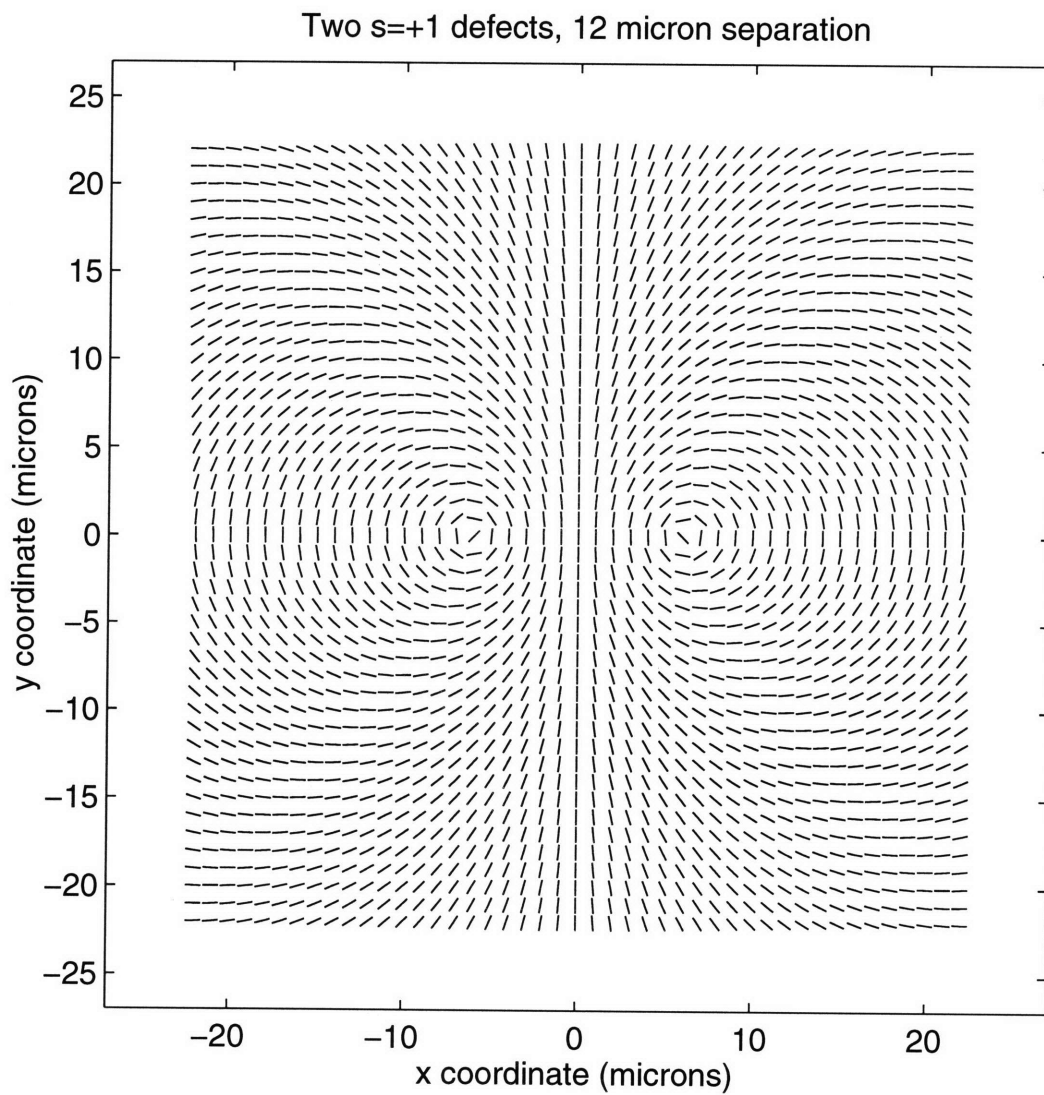


**Figure 4.21:** Two  $s=+1$ ,  $c=\pi/2$  defects with  $d/R=0.266$ . The cores are easily distinguished.

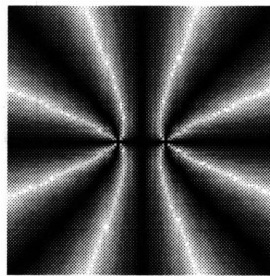
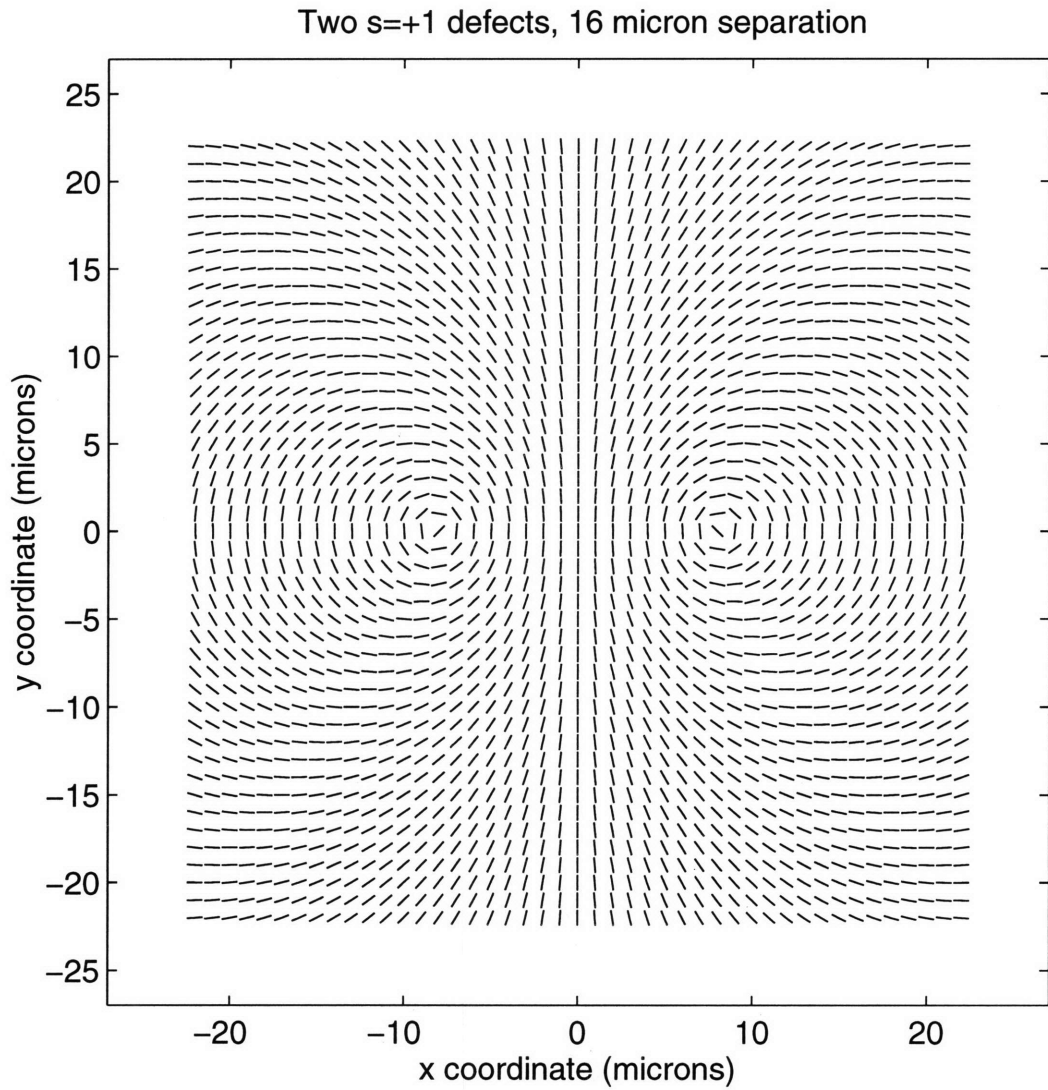


**Figure 4.22:** Two  $s=+1$ ,  $c=\pi/2$  defects with  $d/R=0.355$

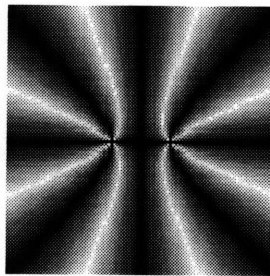
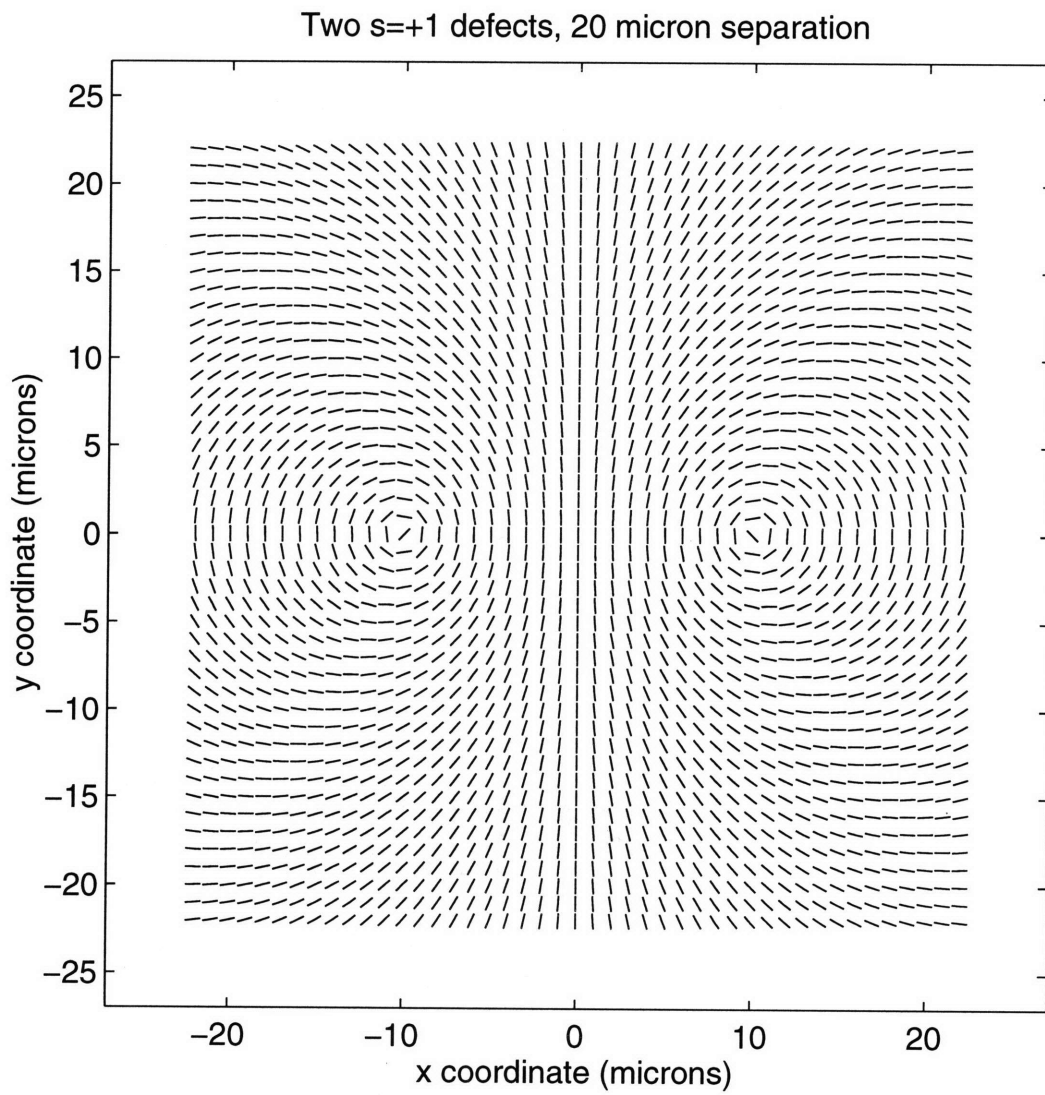


**Figure 4.23:** Two  $s=+1$ ,  $c=\pi/2$  defects with  $d/R=0.444$



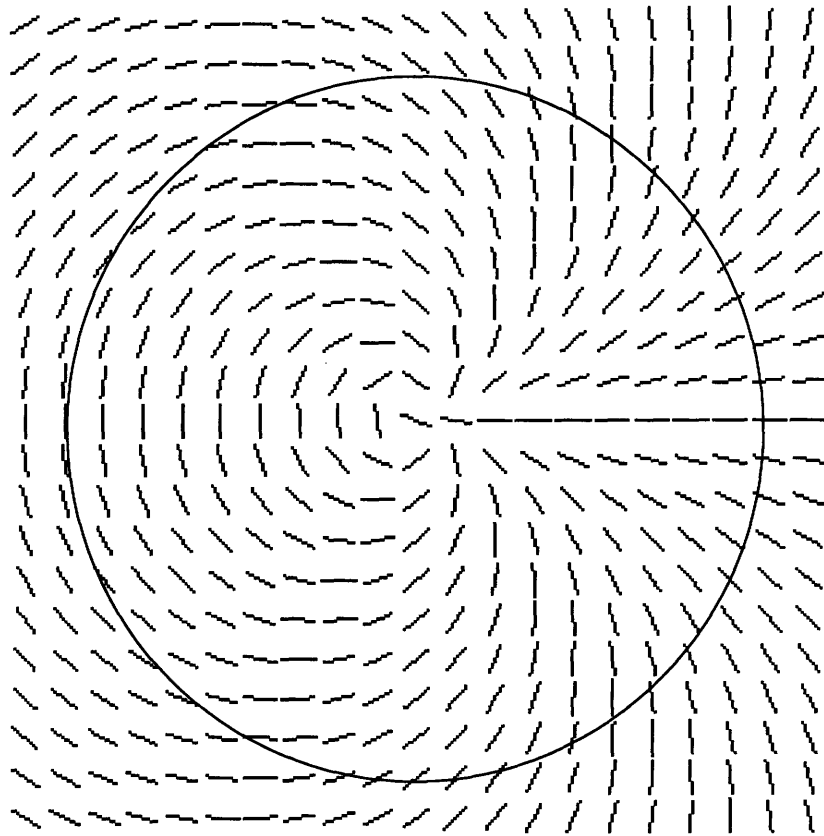


**Figure 4.24:** Incompatibility of an  $s=+3/2$  with anchoring conditions and droplets formed at early stages. This can be seen by the variation of the director angle with respect to the circular boundary.

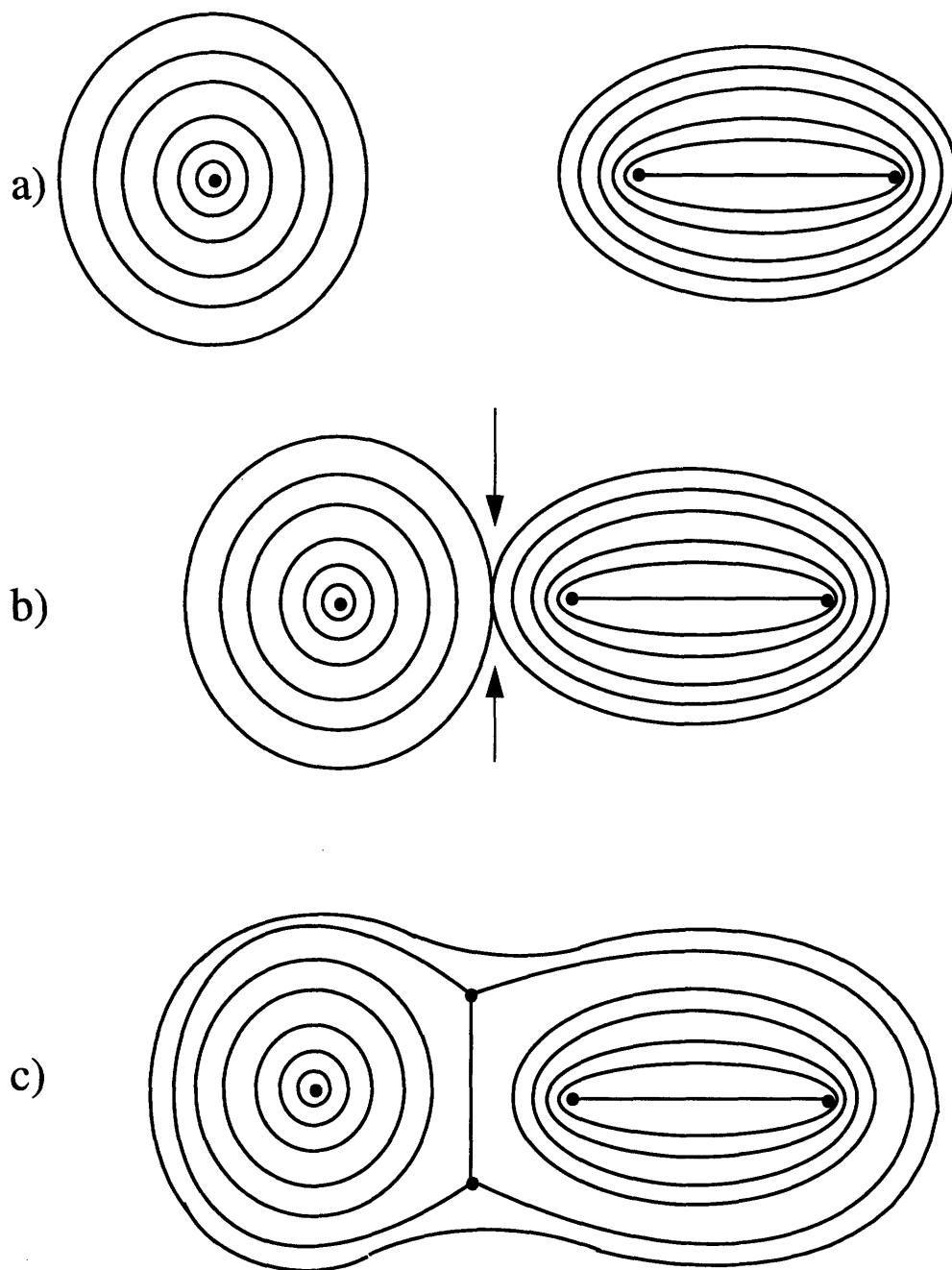


**Figure 4.25:** a) A schematic showing a domain with a single  $s=+1$   $c=\pi/2$  defect that is about to coalesce with a domain containing a pair of  $s=+1/2$  defects. b) The domains just after coalescence. Two sharp cusps form in the regions marked by the arrows. The homogeneous anchoring is violated in these regions. c) Two new topological defects of the type  $s=-1/2$  are formed in front of the cusps in order to satisfy the anchoring conditions.



## Chapter 5

# The Effect of Magnetic Fields on Defect Structure

### 5.1 Introduction

As discussed in Chapter 2, external fields can have a significant effect on the defect texture of a liquid crystal. The original free energy expression derived by Frank[1] in 1958 can be supplemented with additional terms to account for anchoring energy, magnetic field strength, electric field strength, as well as applied strain in order to develop a more general free energy expression. Specific expressions typically involve a competition between a linear elastic term due to the Frank elastic constants and an additional term from the applied field. This competition can lead to new types of defects with structures vastly different from the point and line defects found in the typical “schlieren” texture formed under static conditions.

The elastic constants play an important role in determining the director field distribution about defects situated in an applied field. It seems plausible then that a mathematical analysis of the defect structures would provide a means for extracting these important materials parameters. This chapter describes a methodology for extracting the elastic anisotropy from AFM micrographs of a liquid crystal polymer thin film in an applied magnetic field. A magnetic field was chosen as the external field for two reasons. First, it is relatively easy to control the field direction which is not always true of flow fields. In addition, magnetic fields, unlike their electric counterparts, do not create hydrodynamic instabilities in liquid crystal samples.

The work in this chapter was performed in collaboration with Dr. Ding-Kuo Ding (International Center for Materials Research, Japan), Dr. Bih-Yaw Jin (National Taiwan

University) and Professor V. Percec (Case Western). Dr. Ding provided the AFM micrographs, Dr. Jin assisted in the development of Matlab script files for solving the director field distribution equations, and Professor Percec provided the samples of TPP5 that were used in the experiments.

## 5.2 Theoretical Background

When a liquid crystal of positive diamagnetic anisotropy is placed in an external field, the director orients along the field direction. The orientation process can create a new type of defect known as a “wall” [1][2][3][4][5] This is defined as a defect that separates regions of uniform alignment. Upon crossing a wall the director turns through an angle of  $\pi$ . This chapter will discuss walls formed in magnetic fields. There are three main types of walls [6]. The first is a twist wall where the field is along the z axis and the director is confined to the yz plane and twists about the x axis. As indicated in Figure 5.1a, the director has to twist out of the plane of the page by a factor of  $\pi$  as it crosses the wall. Twist walls are analogous to Bloch walls in magnetic-spin systems [7]. The other two types of walls are referred to as Néel walls. The main difference between them being the proportions of bend and splay distortions they exhibit. A schematic of a Néel bend-splay wall is shown in Figure 5.1b. The field is again applied along the z direction, however the director remains confined to the xz plane. The transition of the director through an angle of  $\pi$  takes place primarily through bend distortions. For the Néel splay-bend wall, on the other hand, the transition takes place mostly through splay distortions (see Figure 5.1c). Walls can terminate in disclinations of opposite sign or can loop back upon themselves [1] [8][9]

Early work on walls in small molecule liquid crystals showed that these defects could be formed as the result of degenerate anchoring with the substrate(s). [2] [9] [10] [11] [12] [13] [14] [15] As a result, both anchoring energy and sample thickness played an important role in the experiments. In particular, it was noted that walls as opposed to disclinations, would be seen if the thickness was less than  $2K/w$ , where K represents a combination of the elastic constants and w represents the anchoring energy per unit area. Donald et al. comment that this relation presents some difficulties for many small mole-

cule liquid crystal systems [16]. In particular they note that the anchoring energy per unit area is often not low enough for this relation to be satisfied for specimens that are thick enough for examination by optical microscopy. These problems can be overcome by treating the substrates to achieve a specific anchoring conditions (usually planar) or by using systems where the anchoring energy per unit area is relatively high.

The director field distribution surrounding wall defects has been studied in detail by several researchers. Donald and Windle [17] have used TEM to study wall defects in sheared films of a liquid crystal polymer. Their study focused on how wall structures were affected by chain end segregation. In particular they were able to identify two wall geometries which could exist in the absence of chain end segregation. One possible type of wall was one that lay in the plane of the sample, while the other was in a plane normal to the film that contained twist distortions.

Walls have also been studied via High Resolution SEM (HRSEM) as well as TEM and optical microscopy by Hudson et al.[18] They extended the lamellar decoration technique of Wood and Thomas [19] by using an etch technique to view director textures in a thermotropic liquid crystal polyester. They found that thicker samples could be viewed directly in the HRSEM, thus eliminating the need for production of replicas. Only a small amount of a conductive coating was necessary for imaging samples at a low voltage. This made it less likely that the surface detail would be obscured. These authors also made theoretical calculations of defect wall structure using an equiconstant approximation. They used the results to extract a value of the characteristic length of the alignment distortions from the micrographs. They did not extend their analysis to the case of elastic anisotropy, noting that such a task involved working with a nonlinear partial differential equation. They did indicate that they were able to use a perturbation expansion to solve for the director field distribution close to the wall.

The first attempt at numerically addressing the effect of elastic anisotropy on the structure of walls was reported by Ding and Thomas.[20] They solved the nonlinear partial differential equation using the Runge-Kutta method to obtain simulations of the director field distribution across a wall as a function of elastic anisotropy. These simulations were used to prepare plots of director angle as a function of distance from a fixed point on the wall. Comparisons with similar plots made from an AFM micrograph made it possible to

extract a value of the elastic anisotropy. This research represented an important advance in mathematical analysis of defect walls. However the authors were able to obtain solutions only for the case when the walls were oriented at either  $0^\circ$  or  $90^\circ$  with respect to the applied field.

In the present work, a general mathematical formalism has been developed to study director orientation near Néel bend and splay walls as a function of both field angle and elastic anisotropy. This subject has not been previously examined in detail due to the difficulty in handling the nonlinear partial differential equation that describes director orientation. The director field distribution across Néel walls can be derived from a free energy density expression. The free energy density for a nematic in a magnetic field is comprised of a linear gradient elastic term and a nonlinear magnetic term:

$$g = \frac{1}{2} \left( k_{11} (\nabla \cdot n)^2 + k_{22} (n \cdot \nabla \times n)^2 + k_{33} (n \times \nabla \times n)^2 - \frac{1}{2} \chi_a (n \cdot H)^2 \right)$$

where  $k_{11}$ ,  $k_{22}$ , and  $k_{33}$ , are the bend, twist, and splay elastic constants,  $H$  is the magnetic field strength, and  $\chi_a$  is the magnetic susceptibility anisotropy[21]. The two terms in the free energy expression balance each other. The linear elastic term tends to disperse distortions, while the nonlinear magnetic term globally reorients the director and localizes the distortions. The latter term is the one responsible for the formation of Néel walls. The equation shown previously can be simplified for thin films, where the director is confined to lie in the plane. In such a situation, no twist is allowed. The only degree of freedom then becomes  $\phi$ , which is the angle between the director and a fixed axis contained in the plane. If a strong magnetic field is applied to a thin film in the plane and the director is confined to the  $xy$  plane then the free energy density can then be rewritten as:

$$\begin{aligned}
g &= \frac{1}{2}(k_{11} \sin^2(\phi) + k_{33} \cos^2(\phi)) \left( \frac{d\phi}{dx} \right)^2 \\
&+ \frac{1}{2}(k_{11} \cos^2(\phi) + k_{33} \sin^2(\phi)) \left( \frac{d\phi}{dy} \right)^2 \\
&+ (k_{33} - k_{11}) \sin(\phi) \cos(\phi) \left( \frac{d\phi}{dx} \right) \left( \frac{d\phi}{dy} \right) \\
&- \frac{1}{2} \chi_a H^2 \cos^2(\phi - \phi_H)
\end{aligned}$$

where  $\phi_H$  is the direction of the magnetic field.

The total free energy of this system can be written as:

$$G = \iint g dx dy$$

The Euler-Lagrange equation that minimizes the total free energy is then:

$$\begin{aligned}
0 &= (k_{11} \sin^2(\phi) + k_{33} \cos^2(\phi)) \left( \frac{\partial^2 \phi}{\partial x^2} \right) \\
&+ (k_{11} \cos^2(\phi) + k_{33} \sin^2(\phi)) \left( \frac{\partial^2 \phi}{\partial y^2} \right) \\
&+ (k_{11} - k_{33}) \sin(\phi) \cos(\phi) \left( \left( \frac{\partial \phi}{\partial x} \right)^2 - \left( \frac{\partial \phi}{\partial y} \right)^2 \right) \\
&+ k_{33} \sin(2\phi) \left( \frac{\partial^2 \phi}{\partial x \partial y} \right) + \chi_a H^2 \cos(\phi - \phi_H) \sin(\phi - \phi_H)
\end{aligned}$$



The total energy remains constant when the coordinates are rotated. Thus the director field of the inversion wall is only a function of a single variable, say  $y$ . Consider the case where an inversion wall is formed at an angle with respect to the applied field. The new axis parallel to the inversion wall is chosen so that the director field is given by  $n = (\cos(\phi)y, \sin(\phi)y)$  and the magnetic field by  $H = (\cos(\phi_H), \sin(\phi_H))$ . The Euler-Lagrange equation then reduces to:

$$0 = (k_{11} \cos^2(\phi) + k_{33} \sin^2(\phi)) \left( \frac{d^2 \phi}{dy^2} \right) + (k_{33} - k_{11}) \sin(\phi) \cos(\phi) \left( \frac{d\phi}{dy} \right)^2 + \chi_a H^2 \cos(\phi - \phi_H) \sin(\phi - \phi_H)$$

This equation can be solved by multiplying by  $\frac{1}{2} \frac{d\phi}{dy}$  and integrating. This yields

$$(k_{11} \cos^2 \phi + k_{33} \sin^2 \phi) \left( \frac{d\phi}{dy} \right) = \chi_a H^2 \sin^2(\phi - \phi_H)$$

where the integration constant vanishes because  $\frac{d\phi}{dy}$  approaches zero as  $\phi$  approaches  $\phi_H$ . The elastic anisotropy,  $\varepsilon = \frac{(k_{11} - k_{33})}{(k_{11} + k_{33})}$ , is now introduced along with a new characteristic length. A dimensionless distance,  $u = \frac{y}{\zeta}$ , can be defined in order to rewrite the above

$$\zeta = \left( \frac{1}{H} \right) \left( \frac{k_{11} + k_{33}}{\chi_a} \right)^{0.5}$$

equation as:

$$(1 + \varepsilon \cos(2\phi)) \left( \frac{d\phi}{du} \right)^2 = \sin^2(\phi - \phi_H)$$

The quantity  $\frac{d\phi}{du}$  is obtained by taking the square root of the previous equation:

$$\frac{d\phi}{du} = \frac{|\sin(\phi - \phi_H)|}{\sqrt{1 + \varepsilon \cos(2\phi)}}$$

This equation can now be integrated to obtain  $u$  as a function of  $\phi$ :

$$u(\phi) = \int_{\left(-\frac{\pi}{2} + \phi_H\right)}^{\phi} \frac{\sqrt{1 + \varepsilon \cos(2\phi)}}{|\sin(\phi - \phi_H)|} d\phi \quad \text{for } (u \geq 0)$$

$$u(\phi) = \int_{\phi}^{\left(-\frac{\pi}{2} + \phi_H\right)} \frac{\sqrt{1 + \varepsilon \cos(2\phi)}}{|\sin(\phi - \phi_H)|} d\phi \quad \text{for } (u < 0)$$

The limits of integration were chosen in order to satisfy the boundary conditions and to avoid singularities. For the simplest case where elastic constants are equal, the Euler-Lagrange equation reduces to:

$$\left(\frac{d\phi}{du}\right)^2 = \sin^2(\phi - \phi_H)$$

where  $u = \frac{y}{\zeta}$ , and  $\zeta$  is the characteristic length equal to  $\left(\frac{1}{H}\right)\left(\frac{k}{2\chi_a}\right)^{0.5}$ . Here  $\zeta$  takes the same value as the traditional magnetic characteristic length,  $\xi$ , defined by deGennes. The analytic solution for the director field in the equiconstant case [9] can now be written as:

$$\phi = \phi_H - 2 \arctan \left[ e^{\left(\frac{y}{\zeta}\right)} \right]$$

where the value of  $\phi$  is equal to  $-\frac{\pi}{2} + \phi_H$  if  $y$  is equal to zero. The value  $\phi$  approaches  $-\pi + \phi_H$  or  $\phi_H$  when  $u$  approaches negative or positive infinity respectively.

### 5.3 Sample Preparation

A main-chain thermotropic nematic liquid crystalline polyether known as TPP5

(1-(4-hydroxy-4'-biphenyl)-2-(4-hydroxyphenyl)propane with 1,5-dibromopentane) with  $\bar{M}_n = 11,200 \frac{g}{mol}$  and a polydispersity of 2.5 was used for this study. The chemical structure is shown in Figure 5.2. The crystal to nematic transition is 148 °C and the nematic to isotropic is 180 °C. A 1-2 micron thin film in the nematic state was sheared on a glass slide using a razor blade. Sample thickness plays an important role in this work. When films are sufficiently thin, a pseudo two-dimensional situation can be made which makes it possible to eliminate twist distortions in the resultant director field distribution.

To create the inversion walls, the specimen was first aligned in a 13.5 T magnetic field at the Bitter National Magnet Lab. The field direction was oriented in the plane of the sample and perpendicular to the shearing direction. The annealing process was conducted at

160 °C for 30 minutes. The sample was then quenched to room temperature at a rate of 10 °C/s using a flow of nitrogen gas. In the final processing step, the lamellar decoration technique [19] was used to cause the sample to partially crystallize into a lamellar morphology. The variations in director field distribution are made visible by AFM of the lamellae which protrude above the film surface by 2-4 nm and are normal to the local director. A Digital Instruments Multimode Atomic Force Microscope and Nanoscope III controller were used to acquire 8 by 8 micron height images of the liquid crystal. The AFM was operated in contact mode and was equipped with 200 micron SiN<sub>3</sub> cantilevers. Typical applied forces were a few mN with scan rates of 5Hz.

#### 5.4 Results and Discussion

The general two-dimensional solution of the director orientation distribution across an inversion wall as a function of field direction for a nematic liquid crystal with elastic anisotropy requires the solution of a two dimensional nonlinear partial differential equation (equation 5.5). Rotation of the coordinate system shows that the problem is actually one-dimensional and therefore much easier to solve (equation 5.9). When the coordinate system is rotated so that the x-axis is along the inversion wall, the y-axis now becomes the only degree of freedom.

Simulations for the director orientation across a Néel wall for the equiconstant case ( $k_{11}=k_{33}$ ) as a function of the orientation of the wall with respect to the field direction are shown in Figure 5.3. The proportions of bend and splay character in the wall depend on the wall orientation. The first plot (Figure 5.3a) shows the case where the wall and the magnetic field are parallel. In this situation the Néel wall has pure bend character. The last plot (Figure 5.3e) shows a pure splay wall that results when the wall and the magnetic field are orthogonal. The results for intermediate angles (Figure 5.3b-d) show how the Néel wall makes a gradual change from bend to splay character. It is evident that a Néel wall formed at 45 degrees to the field (Figure 5.3c) embodies a mixture of both bend and splay.

Note that the director orientation of the Néel bend wall ( $\phi_H = 0$ ) is precisely orthogonal to that of the Néel splay wall ( $\phi_H = 90^\circ$ ). The AFM image in figure 5.4 shows the Néel wall used for the analysis in this chapter. The angle between the wall and the applied field ( $\phi_H$ ) varies gradually as the wall is followed from the lower right to the upper left side of the micrograph. Note that as  $\phi_H$  varies, so does the amount of splay and bend character in that region of the wall.

Based on work of Ding and Thomas [20] the polymer, TPP5 has  $\varepsilon = 0.5$  which implies  $k_{11}=3k_{33}$ , so TPP5 would prefer bend distortions over splay. Note that the polymer MEBB5 described in that publication was renamed to TPP5. Since the lamellae grow perpendicular to the director, what appears in the AFM image as a splay wall is actually a bend wall for the reasons discussed earlier. To determine the director field using the AFM image, we first produce a hand tracing of lines normal to the lamellae. The result is a rough map of the director field which is shown in Figure 5.5a. The region of the wall towards the lower right of the image (i.e.  $\phi_H = -13^\circ$ ) has both splay and bend character. Then as the wall gradually curves and becomes nearly parallel to the field (i.e. the region with  $\phi_H = 13^\circ$ ) the director exhibits much more bend character. In the actual AFM image this is seen as increasing amounts of splay in the lamellae.

In order to obtain a quantitative comparison between data and theory, several criteria were selected. First, the wall (or segments thereof) should be isolated from other walls or defects that might introduce distortions in the director field. Secondly, the wall should have a relatively constant  $\phi_H$ . This is an important criterion because a curved wall actually represents a superposition of many director field solutions of various  $\phi_H$ , a situation which is more difficult to model mathematically. Based on these criteria, the relatively straight portion of the wall at  $\phi_H = 53^\circ$  was selected for the analysis. To produce a more reliable map of the director field than the one from Figure 5.5a, the NIH-Image software package

was used to extract the x-y location of the lamellae (Figure 5.5b). These coordinates were then entered into a Matlab script that reconstructed the lamellar trajectories and then calculated and plotted line segments orthogonal to them (Figure 5.5c). These line segments represent the local orientation of the director field with respect to the lamellae. These segments were then used to reconstruct a more accurate tracing of the entire director field (figure 5.5d) than would be possible using rough hand tracing of the AFM image.

Simulations of the director trajectory as a function of  $\phi_H$  and elastic anisotropy were made using a Matlab script file. Equation 5.9 was solved numerically. Some examples of the results are shown in Figures 5.6a and 5.6b. The former shows several plots which have the same value of elastic anisotropy ( $\epsilon = 0.5$ ) but varying values of  $\phi_H$ . It can be seen that small differences in  $\phi_H$  do not produce large changes in the director trajectory. For example, there is not a great difference between the results for 50, 53 and 55 degrees. However there are significant differences between the results for 53 and either 40 or 60 degrees. A similar situation exists for variations in elastic anisotropy at fixed  $\phi_H$  (refer to Figure 5.6b). The differences between simulations for  $\epsilon = 0.4, 0.5, \text{ and } 0.6$  are almost undetectable. However, large changes in  $\epsilon$  from -1 (easy splay) to +1 (easy bend) produce significant changes in the simulations.

A series of comparisons of theory and experiment will now be shown to illustrate the difference between good and bad fits. NIH Image was used to extract the coordinates of both the simulations and the director field distribution. The result was given to a Matlab script file that fit a polynomial to each set of coordinates. The curve obtained from Matlab was placed on the director field map so that the data and simulations would coincide at locations far from the center of the wall. The equations obtained from these operations were then used to obtain a root mean square error value in y for a fixed range in x, defined as  $\langle R^2 \rangle^{1/2} = \Sigma[(y_{data} - y_{theory})^2]^{1/2}$ . All curves were compared over the same range in x and

with a comparable number of sampling points spread out uniformly along the contour. The simulation in figure 5.7a shows a “bad fit” for  $\varepsilon = 0.5$  and  $\phi_H = 40$  degrees. The corresponding RMS error was 2.96. This high value resulted from the mismatch that occurred close to the centerline of the wall. At locations far from the wall, where the data and simulations are in good agreement, the RMS error is much lower. In these particular regions, the RMS is typically on the order of 0.15.

Another example of a poor fit is shown in figure 5.7b. In this case,  $\varepsilon = -1.0$  and  $\phi_H = 53$  degrees. Far from the wall, the RMS error is again around 0.15, while over the entire contour it increases to a value of 0.72. Figure 5.7c shows an example of a “best fit”, defined as the simulation that produces the lowest RMS error. As can be seen in this plot, there is very little deviation between the simulation and the data. As a result the RMS error is only 0.19, which is only slightly greater than the values obtained far from the wall where the distortions in the director field are much lower. The results from this particular data set show that the elastic anisotropy is approximately 0.5, which corresponds to our earlier measurement of  $k_{11}=3k_{33}$  using TPP5. This indicates that bend distortions are more favorable for this particular polymer. As the comparisons between data and simulation show, sensitivity to elastic anisotropy and wall orientation is greatest close to the centerline of the wall.

## 5.5 Summary

The nonlinear partial differential equation describing director orientation across Néel walls in a liquid crystal polymer was solved in two-dimensions for the general case of elastic anisotropy and variable angle of the wall with respect to the applied field. A computer program was used to create director orientation simulations as a function of both elastic anisotropy and wall angle with respect to the applied field. Experimental measurements of the director distribution were obtained by atomic force microscopy of a polyether

liquid crystal polymer The numerical analysis described in this chapter works best for long portions of a wall that are at a fixed orientation to the applied field and that are also free from the influences of nearby walls and other defects. Good fitting between theory and simulations are obtained when these criteria are met. Calculations of the root mean square error in y values for a fixed range in x were used to make quantitative comparisons between simulations and data. The best fit to the data was selected by a combination of visual inspection and ranking of mean square error values. The fit of a wall at 53 degrees with an elastic anisotropy of 0.5 (i.e.  $k_{11}=3k_{33}$ ) agrees with earlier determinations of the elastic anisotropy of TPP5 the lamellar decoration technique.



- [1] Frank, F.C., "On the Theory of Liquid Crystals", *Disc. Faraday Soc.*, **25**, 19-28, 1958
- [2] Leger, L., *Mol. Cryst. Liq. Cryst.*, **24**, 33, 1973
- [3] Stieb, A. Baur, G., Meier, G., *J. Physique*, **36**, C1-185, 1975
- [4] Ford, J.R., Bassett, D.C., Mitchell, G.R., Ryan, T.G., *Mol. Cryst. Liq. Cryst.*, **180B**, 233, 1990
- [5] Hudson, S.D., Thomas, E.L., *Physical Review A*, **44**, 1991
- [6] Chandrasekhar, S., Liquid Crystals, Cambridge Univ. Press, Cambridge, 1977
- [7] Kleman, M., Points, Lines, and Walls, Wiley, Chichester, 1983
- [8] Mineev, V.P., Volovik, G.E., *Phys. Rev.*, **B13**, 1978
- [9] Helfrich, W., "Alignment Inversion Walls in Nematic Liquid Crystals in the Presence of a Magnetic Field", *Phys. Rev. Lett.*, **21**, 1518-1521, 1968
- [10] Kleman, M. and Williams, C., "Anchoring Energies and the Nucleation of Surface Disclination lines in Nematics", *Phil. Mag.*, **28**, 725-731, 1973
- [11] Meyerhofer, D., Sussman, A., and Williams, R., *J. Appl. Phys.*, **43**, 3685, 1972
- [12] Nehring, J. and Saupe, A., "On the Schlieren Texture in Nematic and Smectic Liquid Crystals", *J. Chem. Soc. Faraday Trans. II*, **68**, 1-15, 1972
- [13] Ryschenkow, G. and Kleman, M., "Surface Defects and Structural Transitions in Very Low Anchoring Energy Nematic Thin Films", *J. Chem. Phys.*, **64**, 404, 1976
- [14] Vitek, V. and Kleman, M., *J. de Physique*, **36**, 59, 1975
- [15] Williams, C., Vitek, V., and Kleman, M., "Surface Disclination lines in 4-methoxy-benzylidene-4-n-butylaniline (MBBA)", *Solid St. Commun.*, **12**, 581, 1973
- [16] Donald, A.M., Viney, C., and Windle, A.H., "Domains and Walls in Thermotropic Liquid Crystalline Polymers: An Optical Microscopy Study". *Phil. Mag. B.*, **52**(5), 925-941, 1985
- [17] Donald, A.M. and Windle, A.H., *Polymer*, **25**, 1235, 1984
- [18] Hudson, S.D., Vezie, D.L., and Thomas, E.L., "Director Textures in Bulk Samples of Liquid-Crystal Polymers", *Makromol. Chem. Rapid. Commun.*, **11**, 657-662, 1990

[19] Thomas, E.L., Wood, B.A., "Mesophase Texture and Defects in Thermotropic Liquid Crystalline Polymers", *Faraday Discuss. Chem. Soc.*, **79**, 1985

[20] Ding, D.K., Thomas, E.L., "Influence of Elastic Anisotropy on the Structures of Néel Inversion Walls in Liquid Crystal Polymers", *Macromolecules*, **26**, 6531, 1993

[21] deGennes, P.G., *The Physics of Liquid Crystals*, Clarendon, Oxford, 1974

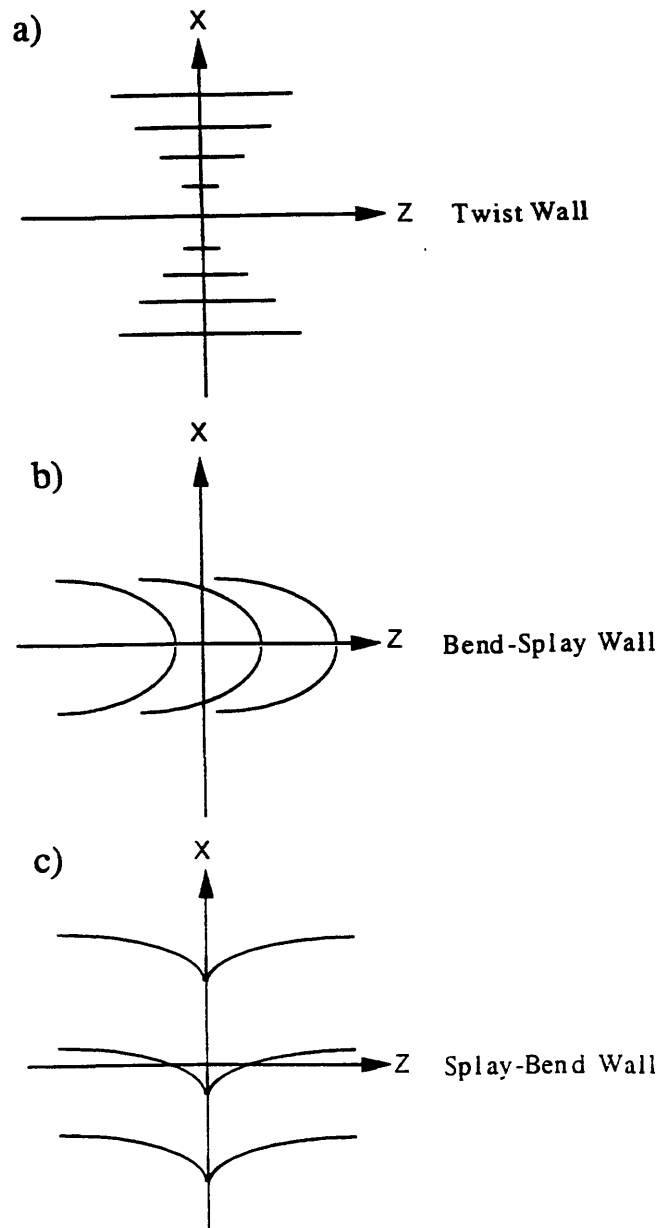


**Figure 5.1:** Schematics depicting the three main types of walls. a) a twist wall that involves out-of-plane deformations b) a Néel bend-splay wall. The director is confined to the  $zx$  plane. The transition across the wall occurs mainly through bend deformations. c) a Néel splay-bend wall. The director is again confined to the  $zx$  plane. The transition across the wall occurs mainly through splay deformations.

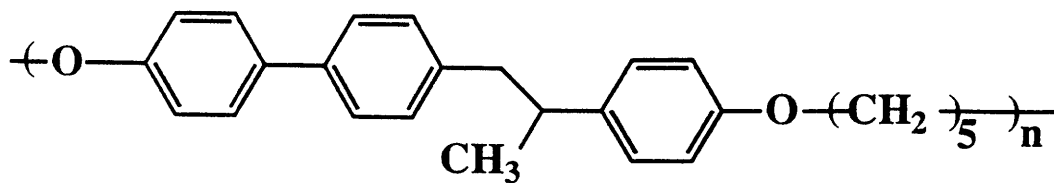


**Figure 5.2:** The chemical structure of TPP5, a liquid crystal polyester. The crystal to nematic transition temperature is 148 °C and the nematic to isotropic transition temperature is 180 °C. TPP5 is ( 1-(4-hydroxy-4'-biphenyl)-2-(4-hydroxyphenyl)propane with 1,5-dibromopentane)

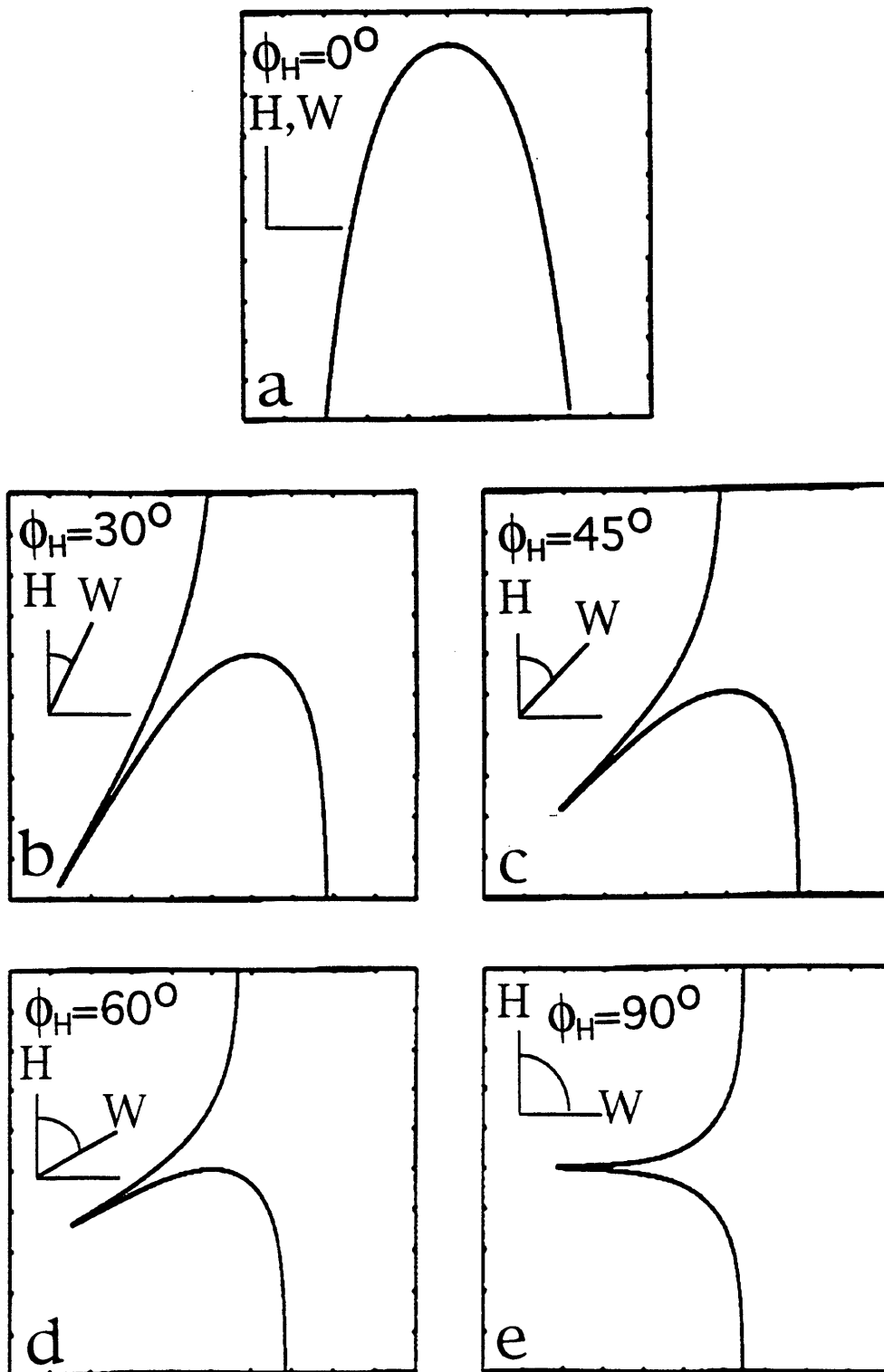


**Figure 5.3:** A series of plots showing the director trajectory across a wall as a function of  $\phi_H$ , the angle between the wall (W) and the applied field(H). In all cases  $\epsilon = 0$  (equiconstant case)

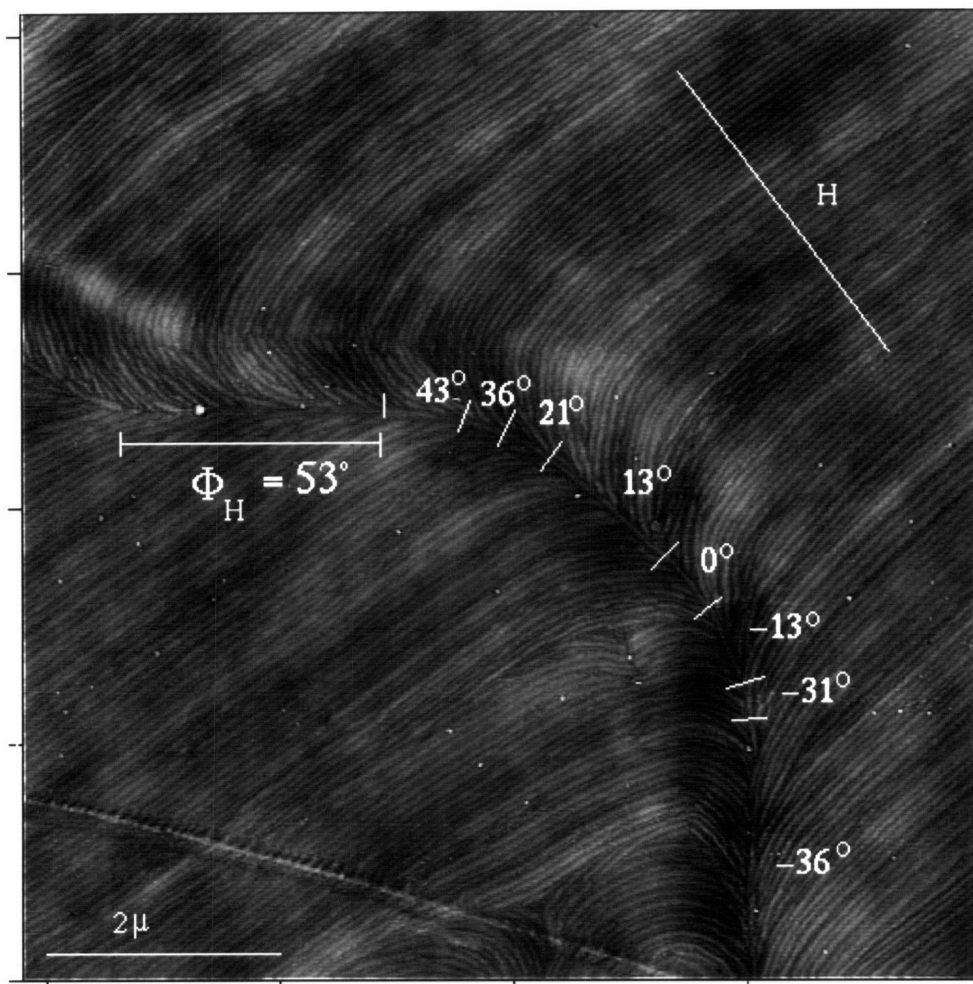


**Figure 5.4:** An AFM image depicting a portion of a Neel wall. The numerical labels indicate the value (in degrees) of  $\phi_H$ , which is the angle between the wall and the applied field. The lines drawn normal to the centerline of the wall separate segments of differing  $\phi_H$ . The straight segment with  $\phi_H = 53^\circ$  was used for the mathematical analysis of the director field distribution.

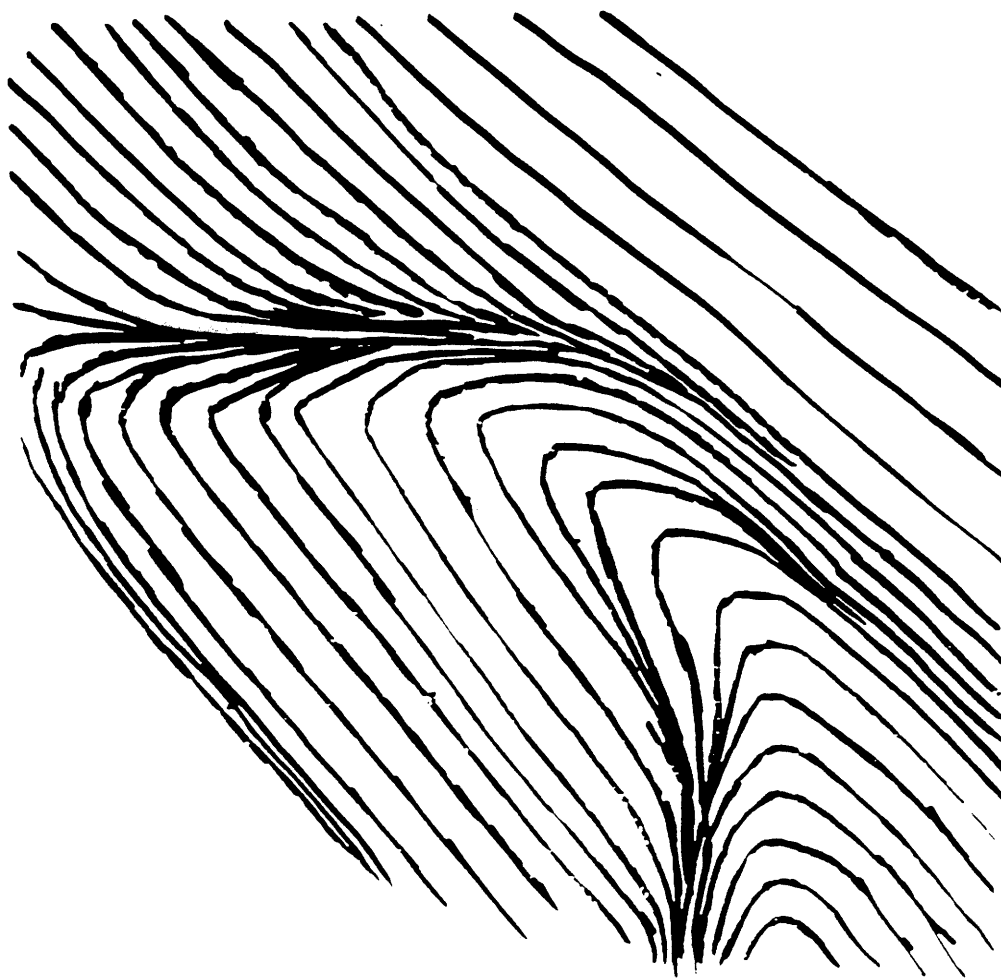


**Figure 5.5:** a) A rough map of the director field distribution produced by hand tracing lines normal to the lamellae in the AFM micrograph of Figure 5.4.

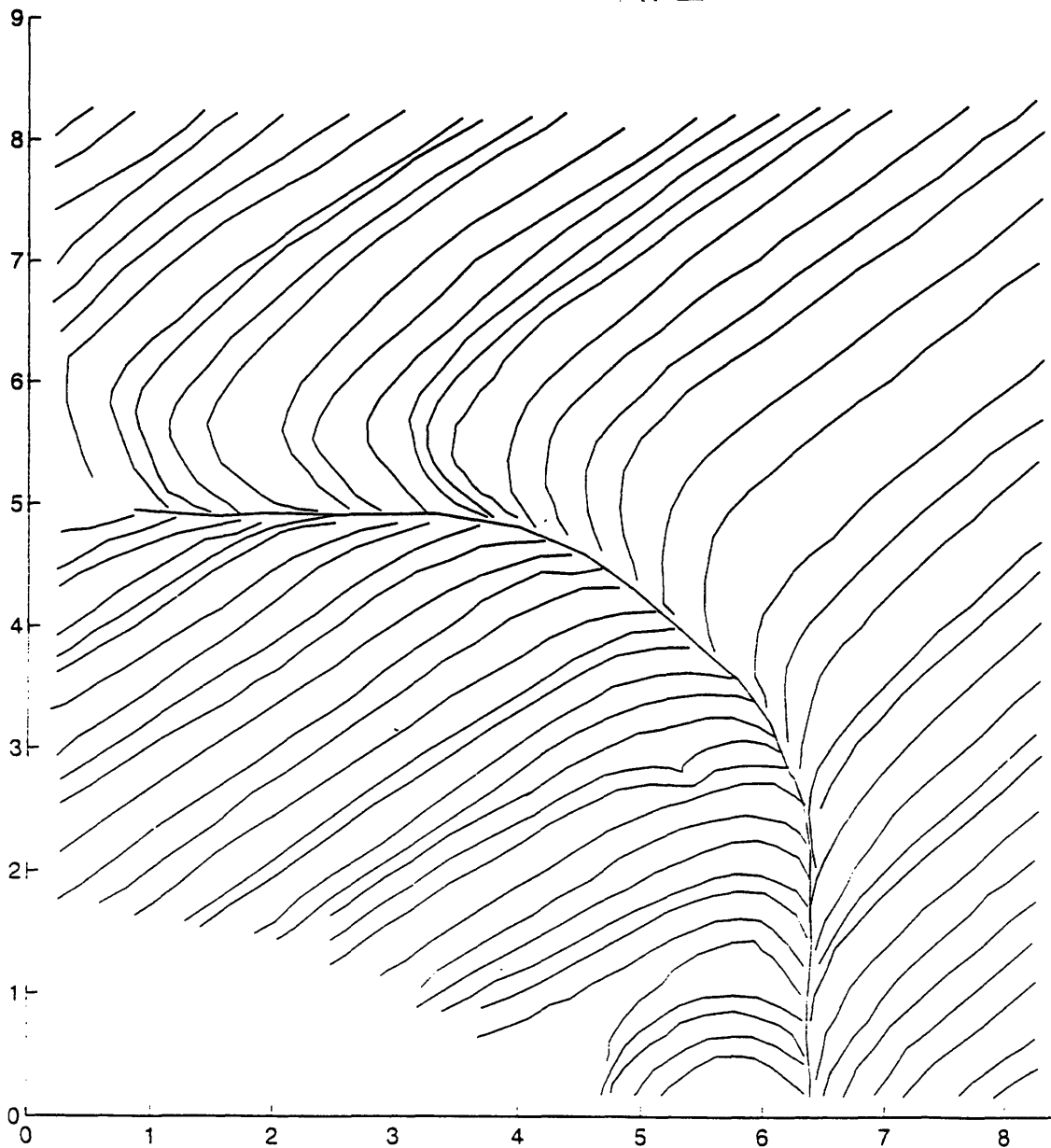


**Figure 5.5 b)** A plot of the lamellar trajectories generated from the AFM micrograph shown in Figure 5.4. The NIH-Image software package was used to extract the coordinates of the lamellae. The results were then given to Matlab which produced the actual plot.



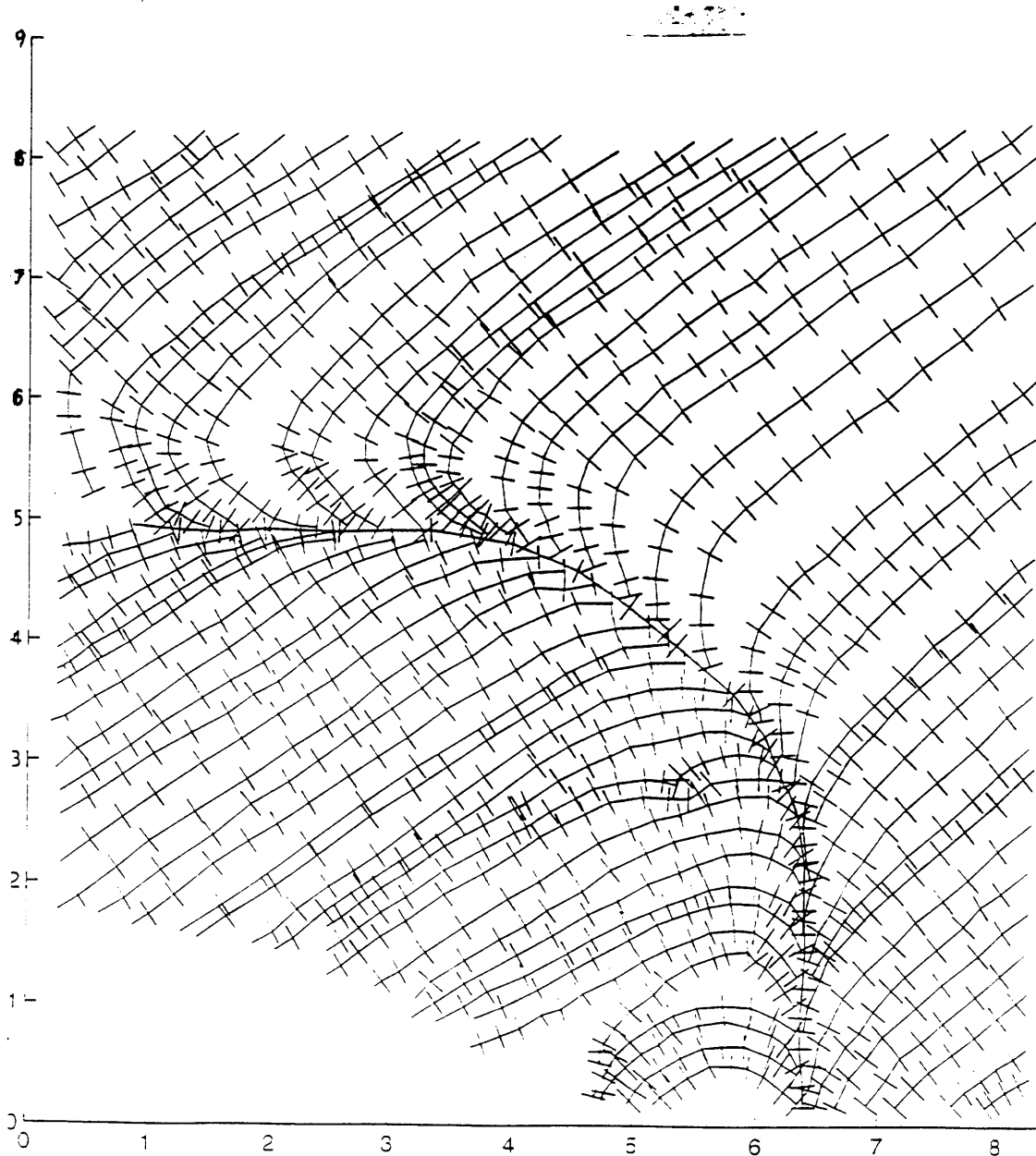


**Figure 5.5 c)** This plot shows the orthogonal line segments generated by Matlab for the purpose of producing a partial map of the director field distribution. A Matlab script file was used to generate the line segments. These segments represent the local director orientation in regions where the director intersects a lamellar trajectory from Figure 5.5b.

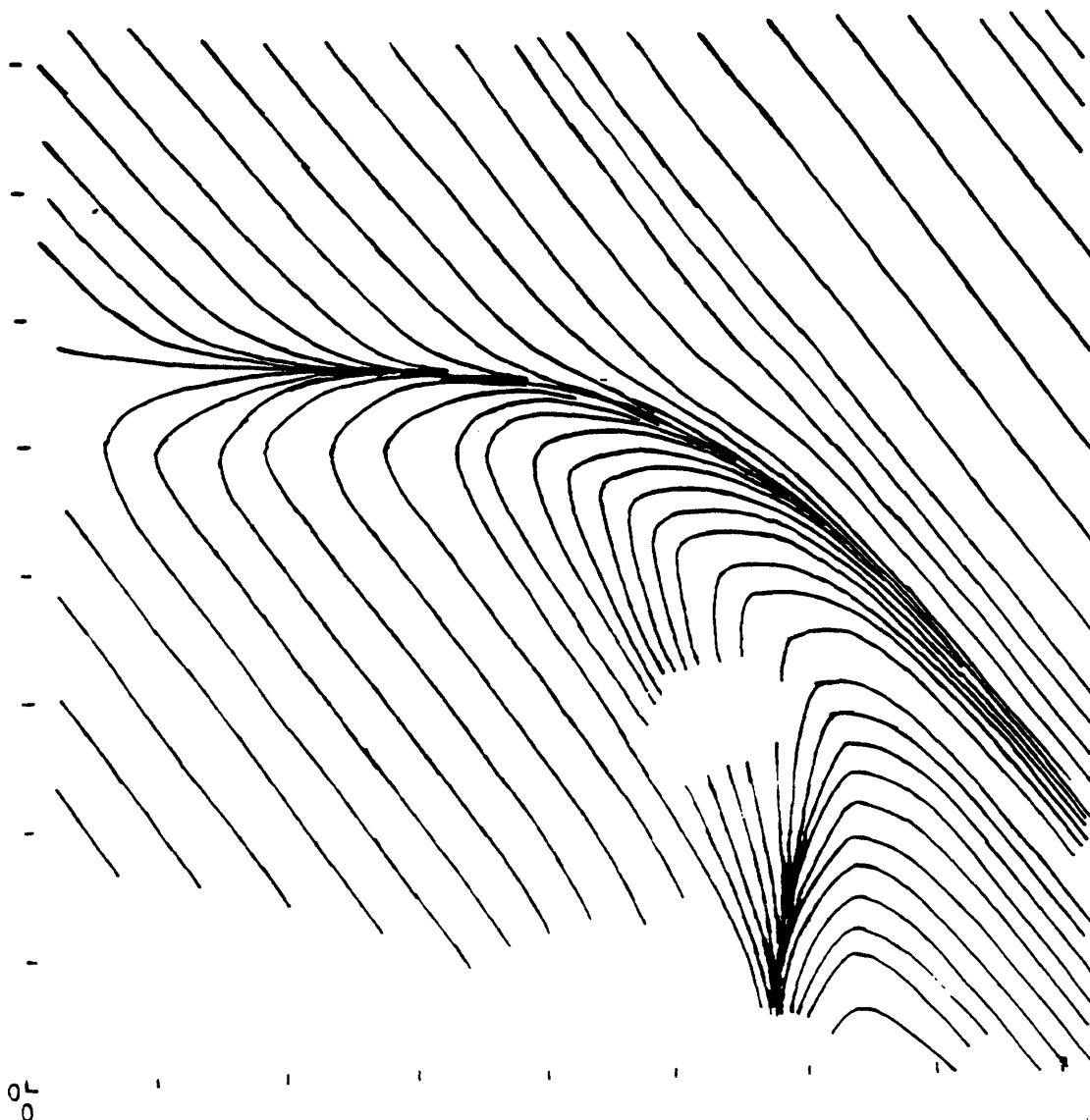


**Figure 5.5 d)** This plot depicts the final map of the director field distribution. The lines corresponding to the director orientation were produced by a small amount of hand tracing along the computer generated line segments from Figure 5.5c.

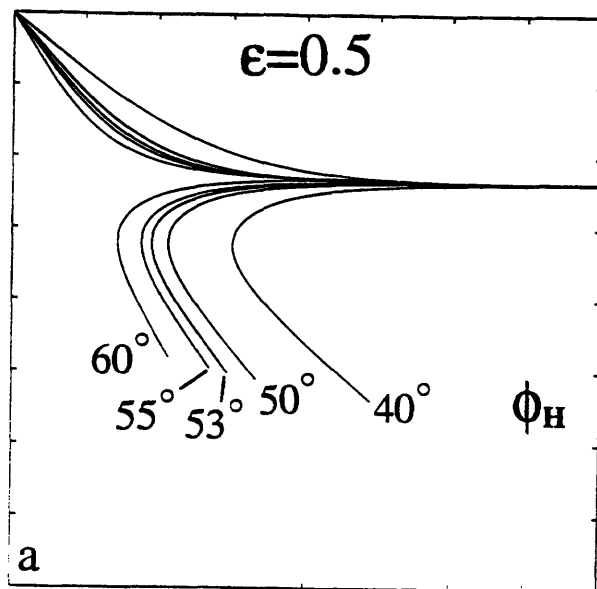


**Figure 5.6:** a) A series of plots showing variations in  $\phi_H$  with  $\epsilon$  fixed at 0.5. Large changes in  $\phi_H$  produce noticeable changes in the director trajectory. Changes of only a few degrees have less of an effect.

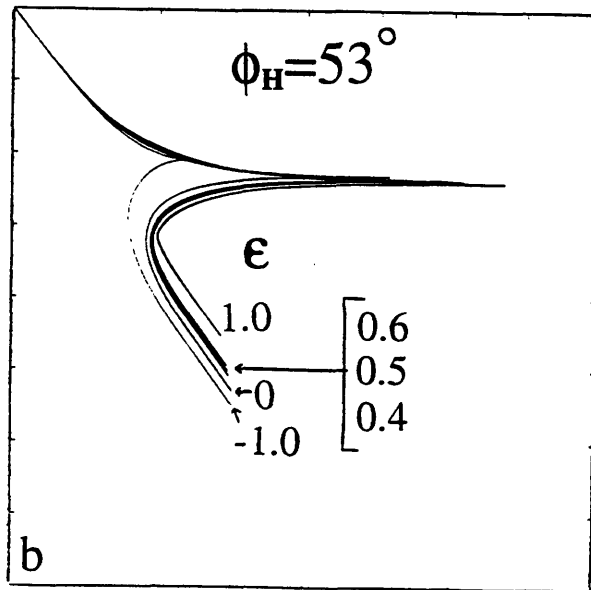


**Figure 5.6 b)** A series of plots showing variations in  $\epsilon$  for  $\phi_H$  fixed at  $53^\circ$ . Small changes in  $\epsilon$  are difficult to distinguish as indicated by the plots for  $\epsilon=0.4, 0.5,$  and  $0.6$ . Large changes in  $\epsilon$  (compare  $\epsilon=1.0$  and  $-1.0$ ) show a marked difference however. The former ( $1.0$ ) clearly shows a higher degree of bend distortion while the latter shows more splay distortion.

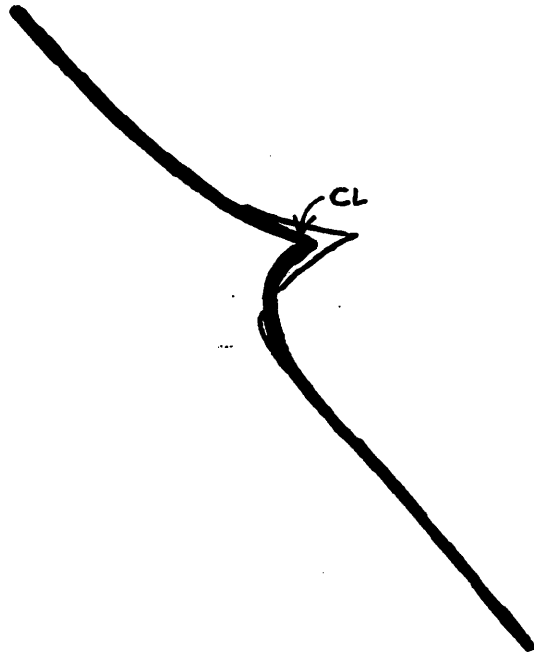


**Figure 5.7 a)** An example of a “bad fit” between the AFM image and simulations. The thick line represents a simulation for  $\epsilon = -1.0$  and  $\phi_H = 53^\circ$ . The thin line represents the data (taken from Figure 5.3d). Far from the wall, the simulation and data do not differ appreciably. However as the centerline (marked “CL”) of the wall is approached, the simulation begins to deviate markedly from the data. This first occurs in the location indicated by the arrow. For this particular simulation the overall rms error was 0.72.

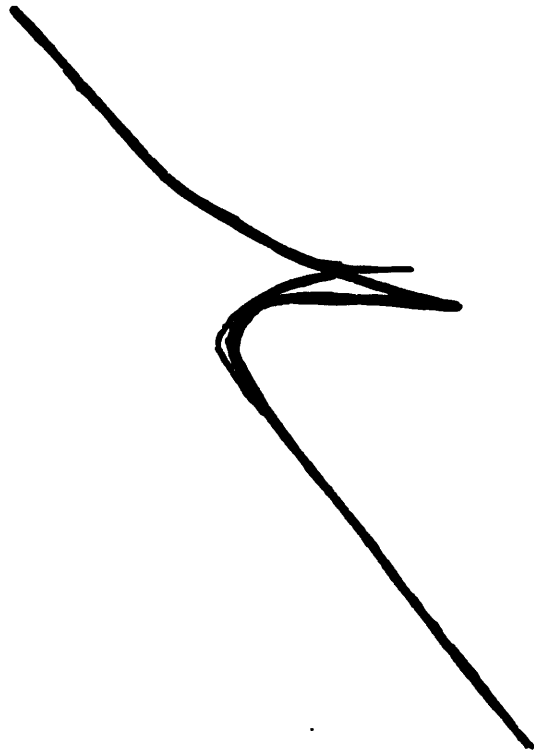


**Figure 5.7:** b) An additional example of a “bad fit” between data and experiment. In this case,  $\phi_H = 40^\circ$  and  $\varepsilon = 0.5$ . The thick and thin lines represent the simulation and data respectively. The mismatch is again most evident in the regions close to the centerline of the wall. The large mismatch in  $\phi_H$  produced a more noticeable difference visually than did the mismatch seen in Figure 5.7a. This is also supported by the larger value of the rms error in this simulation which was 2.96.

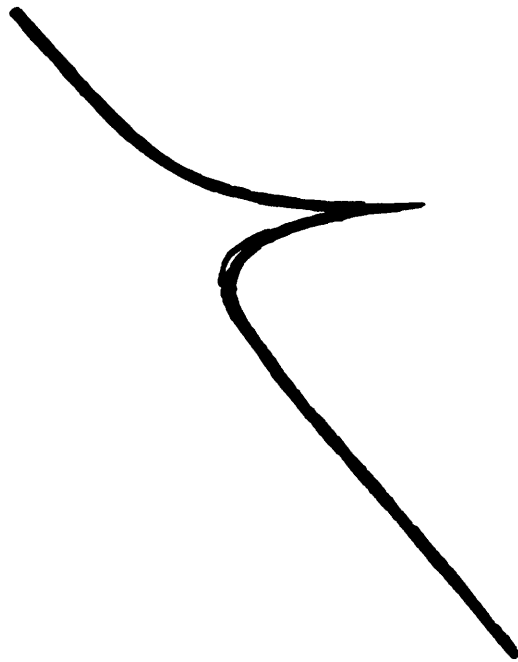


**Figure 5.7 c)** An example of a "best fit" between data and experiment. In this case,  $\phi_H = 53^\circ$  and  $\varepsilon = 0.5$ . The overall rms error, 0.19, in this case, was the lowest obtained from all the comparisons that were made. This is only slightly larger than the rms error corresponding to the fit at regions far from the wall where the distortions are very low.

## Chapter 6

# Curvature Driven Motion in Liquid Crystal Polymers

### 6.1 Introduction

This chapter describes an approach for studying curvature driven motion of disclination loops in liquid crystals. To my knowledge this subject has not been previously examined in the literature. The motivation for this work is to understand the mechanisms by which disclination loops evolve during shear relaxation. It is well known that defects affect viscoelastic behavior, but to date, no quantitative models have been developed that relate defect structure or number density to actual properties such as viscosity. A functional relationship between these parameters would increase the knowledge of structure, property, processing, and performance relationships in liquid crystal systems. A first step towards that goal is to determine what the driving forces are behind disclination loop evolution. This chapter specifically addresses the notion of curvature as an important driving force in this process. Flow visualization techniques are used to study both small molecules and liquid crystal polymers during shear relaxation. Experimental results on contour changes that occur will be compared with theoretical calculations based on level set methods of differential geometry. The implications of the results in terms of structure-property relationships will also be discussed.

### 6.2 Curvature Driven Motion

#### 6.2.1 Background

The motion of surfaces and interfaces is a common research theme throughout the physical sciences. An understanding of how these evolve over time can yield important information on relationships between structure, properties, and materials processing conditions[1]. The speed with which a boundary (2D) or surface(3D) moves can be described in a very general sense by a speed function,  $F[2]$ :



$$F = F(L, G, I)$$

The speed of the entity under consideration is a function of local, global, and independent properties. Examples of each are shown in the following table:

Local	Global	Independent
Curvature	Properties that depend on shape and position	Properties that do not depend on the shape of the front
Normal direction	Diffusion effects	Fluid velocity

**Table 6.1: Examples of local, global, and independent properties that affect the speed function of a moving boundary or surface.**

Determining an expression for the speed function is a complex problem that has been addressed extensively in the literature in many different subject areas. One particularly active area of research has been the study of crystal growth[3][4][5] and evolution of grain boundaries in metals[6][7][8]. These systems are affected by both local properties, such as curvature and global properties such as solute diffusion.

Grain boundaries in a recrystallized metal will move towards their centers of curvature during thermal annealing. The driving force for this type of grain growth is the reduction in the surface energy associated with the grain boundaries which have a positive free energy. A reduction in grain boundary area with thermal annealing has also been reported. These early efforts focused primarily on observation of grain boundary motion as a function of material structure. For example, Beck[9] has also reported that grain boundaries migrate *away* from their centers of curvature when the metal is recrystallizing. In this particular situation, the boundaries that separate the recrystallized material from the cold-worked material are moving in a direction that increases the recrystallized volume. This effect was only seen in the early stages of growth where the recrystallized grains were surrounded by a single deformed grain. This indicates that the motion is opposing the interfa-

cial tension. The energy for this process is supplied by the free energy of cold work that remains in the part of the sample that has not recrystallized.

Additional research on grain growth was carried out by Smith et al. who showed that pressure driven motion was responsible for normal grain growth[10]. Further research was conducted by Smoluchowski[11] and Turnbull[12] who showed that the pressure associated with grain growth caused the boundary to move with a speed  $S=pM=K\sigma M$ , where  $M = Ae^{\frac{-K}{T}}$  is the speed per unit pressure, also referred to as the mobility. They found that when the structure or mode of motion of the boundary did not change with thermal annealing then the speed was directly proportional to the curvature. Deviation from this ideal behavior was found when impurities, strains, and possibly even boundary density became significant. These so-called drag effects fall in the category of global properties.

A review of the effects of drag forces can be found in the book by Sutton and Balluffi[13]. Briefly, a backwards drag force is exerted on a boundary when solute or impurity atoms diffuse along with the boundary at a slower rate than the boundary would normally move. The temperature of the system will help determine if the drag force will have a significant effect on the boundary's mode of motion. This is a direct result of the fact that expressions for atom diffusion must be incorporated into the model for boundary evolution. Several groups have pursued this subject from a theoretical perspective[14][15][16][17]. This is a difficult problem to model which is why the authors note that none of the studies are particularly definitive. There are many factors that can affect the motion of a grain boundary. This includes pinning of an interface by second phase particles as well as by free surfaces. Both can impede the motion of the boundaries and thus have an effect on the microstructure of the material.

A mathematical formalism for describing curvature dependent motion can easily be developed when the motion of a boundary is dependent only on local properties, such as curvature and the direction of the line normal to the segment of the contour[18]. The schematic in Figure 6.1 shows the construction necessary for development of the equations. This schematic shows two curves describing the form of an interface at an initial time  $t$  and a later time  $t+\Delta t$ . The position of the interface is described by a function  $r=r(\theta,t)$  in polar coordinates. The change in this function with time at a constant value of  $\theta$  is defined as:

(6.2)

$$\Delta r = \frac{-v\Delta t}{\sin \psi} = -\frac{M\sigma H\Delta t}{\sin \psi}$$

where  $v$  is the velocity of the interface,  $M$  is the mobility,  $\sigma$  is the free energy per unit area, and  $H$  is the mean curvature. In this equation the velocity is equal to  $M\sigma H$ , which was defined separately by Smoluchowski[11] and Turnbull[12] for situations where thermal annealing did not affect the mode of motion. For plane curves, the following connections can be made among the various parameters in the schematic[19]:

(6.3)

$$H = \frac{\partial \beta}{\partial s} \quad \sin \psi = r \left( \frac{\partial \theta}{\partial s} \right)$$

where  $s$  is the arc length. These can be combined to produce the following non-linear partial differential equation:

(6.4)

$$\lim_{\Delta t \rightarrow 0} \frac{\Delta r}{\Delta t} = \frac{\partial r}{\partial t} = -\frac{M\sigma H}{\sin \psi} = -\frac{M\sigma \partial \beta}{r \partial \theta}$$

Analytical solution to this expression can be obtained in specific situations. In this context, one typically assumes a solution of the form:

(6.5)

$$r(\theta, t) = R(\theta)T(t)$$

When the above equation is inserted into equation 6.4, the following result is obtained:

(6.6)

$$T \frac{dT}{dt} = -\frac{M\sigma}{R^2} \frac{\partial\beta}{\partial\theta} = c$$

where  $c$  is a constant. The determination of the following parameters is more difficult however[13]:

(6.7)

$$\frac{\partial\beta}{\partial\theta} = -\frac{c}{M\sigma} R^2$$

(6.8)

$$\beta_2 - \beta_1 = -\frac{c}{M\sigma} \int_{\theta_1}^{\theta_2} R^2 d\theta$$

In spite of this difficulty, these results show that the interface will shrink towards the origin when  $c < 0$  and expand when  $c > 0$ . At  $c = 0$ , the solution is a straight line which remains stationary. Mullins[18] noted that an interface in the form of a circle will shrink in a self-similar manner when the parameters in the equation take on the following values:  $c < 0$  and  $c = -M\sigma/R^2$  so that  $\partial\beta/\partial\theta = 1$ . This is significant from a general perspective because a similar effect has been seen in many systems, including dislocations, grain boundaries, and antiphase boundaries in metals as well as disclination loops in liquid crystals. In fact, the Grayson theorem from differential geometry[19] states that all simple (i.e. non self-intersecting) closed curves moving under their curvature must shrink to a round point regardless of their initial shape. This important theorem will be used as the basis for studies of disclination loop evolution to be described in subsequent sections of this chapter. All the research described thus far has been solely for surfaces and interfaces rather than on line like defects, which include dislocations in crystals and metals as well as disclinations in liquid crystals.

With respect to dislocation theory, energy calculations are generally made by an approximation of a dislocation line tension. The dislocation is modeled as a flexible string with a line tension associated with it. The line tension is defined as the incremental increase in stored energy with an infinitesimal increase in length[20]:

(6.9)

$$T = \frac{\partial w}{\partial l}$$

This analogy works well when the core irregularities are neglected. However as is usually the case, the line tension is difficult to define[21]. This occurs because the energy of a particular segment of a dislocation line will depend on its interaction with the other segments of the line. This means in effect that the dislocation configuration (i.e. its contour shape) will have an effect on the energy, thus making the line tension difficult to define accurately.

Line tension in disclinations for liquid crystal systems has been considered theoretically by deGennes[25]. He points out that the calculation of the distortions associated with a disclination line are difficult to calculate just as they are for distortions surrounding a dislocation in metals. Simplifying assumptions such as the equiconstant approximation discussed in chapter 1 lead to an analytical solution for the distortions around a disclination line. Refer to that chapter for a more detailed description. The free energy expressions developed in that section can be used to determine the energy per unit length associated with these disclination lines. This has the form:

(6.10)

$$T = \int_a^{\rho_{max}} 2\pi\rho d\rho \frac{1}{2} K \frac{s^2}{\rho^2}$$

where "a" is a lower limit of molecular dimensions and  $\rho_{max}$  is an upper limit defined by the disclination spacing or by the distance between the disclination and a surface. The

variable  $K$  is a single elastic constant and  $s$  is the defect strength. The solution of this equation is shown below:

(6.11)

$$T = \pi K s^2 \ln\left(\frac{\rho_{max}}{a}\right)$$

As discussed by deGennes, the  $\ln$  factor in the equation is generally around 10 which makes  $T$  roughly equal to 30 times the magnitude of the combination of elastic constants.

The energy per unit line length described above can also be described as a line tension. However the analysis is only valid for a one-constant approximation. The line tension is a force that acts tangential to the segment in question. A minimization of line-like energy ( $2\pi RT$ ) causes a disclination loop to shrink rapidly and disappear. Although the mechanism by which the shrinkage occurred was not commented upon, the behavior is very similar to the mathematical theories discussed earlier in this chapter. The notion of this behavior in liquid crystal systems will be discussed in detail in subsequent sections.

It is also interesting to note that when the elastic anisotropy is taken into account several intriguing possibilities arise. The difference between the splay, twist, and bend elastic constants will give rise to disclinations that have different line tensions depending how much of each distortion they contain. It has been pointed out by deGennes and Friedel[25] that a strong anisotropy in the elastic constants translates to a large anisotropy in line tension which can then lead to angular cusps in the disclination line contours. Experimental evidence for this effect will be discussed later in this chapter.

## 6.2.2 Mathematical Algorithms for Studying Curvature Motion

### 6.2.3 Introduction

All of the aforementioned studies have been aided significantly by advances in mathematical analysis, particularly differential geometry. Several algorithms have been developed to study curvature motion. The earliest ones develop a differential equation to describe the motion of a particular curve and determine the form of the rate of change of boundary area as a function of time. More advanced methods developed more recently use

either markers or level sets in order to follow the shape evolution of a space curve or surface.

#### **6.2.4 Algorithms of Differential Geometry - The Marker Method**

While the methods described in section 6.2.1 for evolution of grain boundaries provides a means for following evolution of enclosed area, they do not have the capability of describing how the actual shape of the boundary should change over time. Numerical techniques to accomplish this have been addressed by several groups[25]. The algorithm commonly known as the “Marker” method attempts to follow the evolution of a boundary by dividing it into sections represented by “markers” or “buoys” that are used to parameterize it. It can be seen from the schematic in Figure 6.2 that additional markers should increase the accuracy of the solution. Each marker is moved with a speed  $S$ , which is proportional to its curvature. The positions of the markers over time are determined by approximations to the equations of motion. The connections between the markers are used to determine the shape of the boundary at a specific time. However, there are several problems with the marker method. It is possible for the markers to approach and actually cross over each other, especially for complex geometries where the curvature of the propagating front is building rapidly. This results in a numerical instability. In order to overcome this problem, several additional algorithms need to be employed which involved ad hoc techniques[26].

#### **6.2.5 Algorithms of Differential Geometry - The Level Set Approach**

A type of algorithm, known as a “Level Set” method, offers greater accuracy, flexibility, and ease of use than the marker method. The level set approach was developed by Osher and Sethian in 1988[26]. Instead of following the motion of a set of markers, the algorithm tracks the motion of a surface. The original curve is incorporated into a surface which is designed so that it intersects the  $xy$  plane at the exact location of that curve (see Figure 6.3). Instead of moving the original curve, the entire cone-shaped surface is manipulated instead. To see how the curve changes over time, the cone-shaped surface is translated in the  $Z$  direction to produce a new cross section in the  $xy$  plane at  $z=0$ . The advantage of this

method is that complex topological evolution can be evaluated relatively easily without having to introduce correction algorithms during the process.

Several computer codes are available free of charge which allow a variety of two and three dimensional phenomena to be modeled. The “Surface Evolver”, developed by Ken Brakke, is one such program[27]. This program allows the user to study arbitrary surfaces and has a wide range of adjustable parameters. These include: volume and boundary constraints, boundary contact angles, mean curvature, crystalline integrands, gravity, constraints expressed as surface integrals, and surface tension. The user specifies these parameters as well as a set of points that describe the components of the surface and how they are connected. The surface is then reconstructed as a union of triangles. A gradient descent method is then used to determine how the surface evolves over time subject to the specified constraints.

## **6.3 Evolution of Disclination Loops in Liquid Crystals**

### **6.3.1 Introduction**

The focus of the current study is to understand the physics behind loop contour evolution in liquid crystals. Curvature analysis of disclination lines has not been addressed in the literature up to this point for either small molecule or polymer systems. However, morphological characterization of small molecule systems such as 5CB, 8CB, and DHMS-7,9, indicate that liquid crystals may be amenable to such a study. Disclination loops have been addressed experimentally by many research groups[28][29][30] and have also been treated theoretically by DeGennes[25] among others. The experimental papers focus primarily on disclination loop collapse as a way of determining the scaling laws with respect to line density and loop radius evolution derived from the Kibble mechanism of cosmology. The micrographs in these papers show that disclination loops often evolve in a manner similar to that of grain boundaries in metals. The disclination loops are generated by a pressure induced isotropic to nematic transition in a liquid crystal sample that is held between two thin glass plates. The loops that originally appear as large circles shrink very rapidly in a self-similar manner to a smaller circle. Eventually the loop shrinks to a point and disappears.



This behavior is very closely related to the Grayson theorem discussed in the introduction to this chapter. The theory is applicable no matter how complex the original curve is. A series of simulations depicting this is shown in Figure 6.4. The first simulation shows the original curve that has several sharp points along its contour. The sharp points correspond to the locations that have a very high curvature. After 10 iterations of the Surface Evolver program, the curve changed dramatically as shown in the second simulation in that series. The sharp points have evolved rapidly and been transformed into more gently curved line segments. On the other hand, the regions in the original contour that were more gently curved also evolved more slowly. The subsequent simulations show how the various regions of the curve move towards their centers of curvature until the entire curve is convex everywhere. This condition is reached when the curve reaches an elliptical shape (see the simulation for 30 iterations). This ellipse then shrinks to a circular shape. Once the curve evolves into a circular contour, it shrinks to a smaller circle at an ever increasing rate. This is manifested by the fact that it takes fewer and fewer iterations in order to see a visual difference in the simulation results. As the curvature increases, so does the velocity. This effect can also be seen visually in the way that disclination loops evolve.

This correlation between curvature and velocity suggests that it may be possible to describe disclination loop evolution using mathematical algorithms, such as the level set method described earlier. If this is so, then a study of velocity vs curvature may give insight into the nature of disclination line tension and how it affects the shape and evolution of contours in both small molecule and polymer liquid crystals. This would also be of interest with respect to the formation of defect walls created by applied magnetic fields. Ding [31] has noted that curvature smoothing of inversion walls is evident in their shrinkage and coalescence. That study focused on the formation mechanisms of Neel bend and Neel splay walls and their interaction dynamics. Calculations of wall energy as a function of elastic anisotropy was also examined. It was said that splay walls had a higher velocity than bend walls due to the higher energy of the former. Although energy differences certainly must have played a role in the dynamics, it is also possible that the effects could have been due to curvature as well. In fact, a defect wall loop, has the higher energy splay distortions in the high curvature regions of the loop, while the lower energy bend walls are

located along more gently curved segments. These naturally shrink at different rates as a direct consequence of Grayson's theorem. This similarity also suggests that a curvature analysis may be useful in studying wall dynamics as well.

### 6.3.2 Experimental Procedure

Disclination loop evolution was studied in the small molecule 8CB as well as the polymer DHMS-7,9. The chemical structures of these two materials are shown in Figure 6.5. The molecular weight and transition temperatures are shown below in Table 6.1:

8CB	DHMS-7,9
Mn=300 g/mol	Mn=15,000 g/mol, Mw=20,000 g/mol
Tg=N/A	Tg=20 °C
T <sub>n</sub> =38	T <sub>xn</sub> =95 °C
T <sub>ni</sub> =42	T <sub>ni</sub> =170 °C

**Table 6.2: Molecular weight and transition temperatures for the 8CB and DHMS-7,9 samples used in this study**

A typical disclination loop from each of these samples is shown in Figure 6.6 a and b respectively. It is clear from these optical micrographs that the small molecule system is much simpler and represents a good starting point for curvature analysis.

The CSS 450 shear cell was used to perform the experiments. The sample preparation and machine calibration procedure is described in detail in Chapter 2. For the experiments involving 8CB, the sample was loaded into the shear cell while the plates were at the nematic to isotropic transition temperature. The gap was then set to a value of 100 microns. This value is large enough to minimize the error due to a +/- 5 micron variation in the gap setting but also small enough for sufficient transparency for almost any sample. The sample was annealed in the isotropic state for approximately 2 minutes to erase the sample history. Next, the sample was cooled to 38 °C. No disclination loops were seen initially. In order to generate these within the sample, a program of steady shear at 10 sec<sup>-1</sup> was used. A CCD camera and video recorder were used to follow the disclination behavior in real

time. The resulting defect texture that appeared within a few minutes consisted of long disclination threads as well as disclination loops of various sizes. In general these defects were very gently curved. Whenever an entire disclination loop entered the field of view, the flow was stopped so that the loop relaxation process could be followed. Frames of interest were selected and digitized at a later time.

The experiments involving DHMS-7,9 were handled in a slightly different way. Since the samples with the most readily observable textures were only available in small quantities (i.e. <10 mg) a more simple setup was used to view the disclination loops. The sample was placed on a pre-cleaned coverslip which was heated into the isotropic region. Another coverslip was then placed on top of the polymer to create a sandwich assembly with similar anchoring conditions on each side. The sample was annealed for 10 minutes in the isotropic state following which the temperature was lowered to 150 °C. Upon reaching the nematic state, many disclination loops were evident. Additional disclination loops were created by holding the bottom coverslip in place and oscillating the top coverslip in a rectilinear manner. A CCD camera and video recorder were used to follow the disclination coarsening and relaxation process.

### 6.3.3 Experimental Results

Several examples of disclination loop evolution for 8CB are shown in Figure 6.7. In all cases these loops are shrinking first to an elliptical shape and then to a circular one before they disappear. These loops all have simple contours. In addition their evolution appears to follow the description of curvature driven motion of simple closed curves from the Grayson theorem of differential geometry. It should be pointed out that relatively low shear rates were used for several reasons. First, according to the results of Mather et al [32] on 8CB, it is known that the disclination line density increases with shear rate according to the power laws described in Chapter 2. It is difficult to follow the evolution of individual disclination contours when the defect separation distance is very low. In addition, a high defect density would also be problematic in terms of disclination interactions. This was discussed in detail in Chapter 5 for magnetic field effects in a two dimensional situation. The mathematical analysis of wall defects presented in that chapter are only valid for large separation distances between walls or other defects that might distort the director field dis-

tribution. One can imagine that similar difficulties might arise for flow field effects in three dimensions. Disclination loops that are created during flow can interact in complex ways, the mechanisms of which are not well understood.

In contrast to 8CB, disclination loops in the polymer DHMS-7,9 were much more complicated. A series of images depicting the evolution of some typical defect contours are shown in Figure 6.8. The first image in the series (Figure 6.8a) was taken while the sample was being sheared. At this point not much light is able to pass through the sample due to the high defect density. A close examination of this image reveals a highly entangled network of defects. The defect density is so high that it is impossible to follow the contour of an individual defect. The second image (Figure 6.8b) shows the sample 30 seconds after cessation of shear. A significant amount of coarsening has taken place to the point where the defects are much easier to see. It is now possible to follow small segments of individual defects.

The third image (Figure 6.8c) shows the sample 60 seconds after cessation of shear. Several large disclination loops can now be seen in their entirety. Note that the contours of these loops are much more complicated than those of 8CB. The arrows indicate the loop that will be discussed and analyzed later in this chapter. Several locations of high curvature can be seen along its contour. These will be referred to as “feature A”. A region of lower curvature is referred to in the image as “feature B”. The tracings shown in Figure 6.8d were made directly from the micrographs and indicate how this particular loop evolved over time. The time between tracings is 30 seconds unless indicated otherwise. The high curvature seen in feature “A” evolves rapidly as can be seen in the first few tracings. In contrast, feature “B” which is more gently curved evolves more slowly. In fact, it is very difficult to detect any difference in that particular region during the first few minutes of relaxation. These observations indicate that DHMS-7,9 may also be suitable for a curvature analysis.

## **6.4 Curvature Measurement Algorithms**

### **6.4.1 Introduction**

The approach of Allen and Rondeau[126] was used as the basis of the curvature measurement algorithms. Digitized images were used exclusively in this work to eliminate errors due to shifting and rotation of scanned images. This leads to scatter in the data which will be discussed in more detail in the following section on error analysis. All micrographs were given as input to the NIH-Image program. The point selection tool was used to extract the x-y coordinates of the disclination contours. The datafiles were ultimately used as input to a Matlab script file that reconstructed specific segments of the disclination contours. A series of curve fitting routines were then used to determine the order of the polynomial that best fit each set of data points. Comparisons were made between two sets of curves, one of which was selected as a reference( $t=t_0$ ). The parameters supplied by the curve fitting routines were used to calculate the first and second derivatives for the reference curve over the entire range in x applicable to that particular disclination structure. A point of interest,  $x_i$ , on the original curve was then selected for the curvature analysis. The value of the original polynomial as well as the first and second derivatives were calculated at this point. The results were used to determine the equation for a line normal to the original curve at the point  $x_i$ . The curvature at the point  $x_i$  on the reference curve was then calculated.

A new equation was obtained by subtracting the equation for the line normal to the original curve from the equation of the disclination contour at a later time  $t_1$ . The roots of this new equation then represented the set of intersection points of the two curves in question. This information made it possible to calculate the curvature at the corresponding location on the second equation for the disclination contour. The overall curvature was calculated an arithmetic mean of the curvatures on each individual curve. The velocity was calculated by determining the displacement of the second curve with respect to the reference and then dividing by the corresponding time step.

#### 6.4.2 Error Analysis

Several test problems were designed in order to evaluate the efficacy of the aforementioned algorithm. The first problem measured a velocity vs curvature relationship for a large circle (curve 0) shrinking to a smaller one (curve 1). Since the curvature does not vary around the perimeter of a circle, the curvature should remain constant. As a result, a

plot of velocity vs curvature should yield a single point. A plot of the upper half of the circles used for these calculations is shown in Figure 6.9. The larger curve (curve 0) was used as the reference curve ( $t=t_0$ ). For this particular problem, no errors are introduced due to contour digitization, image registration, or irregular flow.

A plot of velocity vs curvature for this set of curves is shown in Figure 6.10. The data points do not all fall on the same point, but are somewhat spread out. The deviation is very small which indicates that the errors due to digitization of the contours and the subsequent curvefitting routines are not significant. The algorithm fails however when lateral shift occurs. The plot in Figure 6.9 also shows a small circle (curve 2) that is identical to the other small circle (curve 1) but is shifted along the positive x axis. A plot of velocity vs curvature is shown in Figure 6.10. There is a significant amount of scatter in the data which gives meaningless results. This emphasizes the importance of image registration as well as careful observation of flow behavior. If one analyzes images that are significantly affected by lateral flow then the results may not be accurate.

Simulations of loop evolution using the Surface Evolver program were also used to test the theoretical model. The input to the program was a rather jagged disclination loop obtained from shearing experiments conducted on the liquid crystal polymer DHMS-7,9. A digitized image of the original loop is shown in Figure 6.11a. A sequence of images were then calculated with this program to show how the curvature should evolve theoretically over time. The results are shown in Figure 6.11 b-n. The high curvature regions in the original image (feature "A") become smoother in a short period of time while the low curvature regions evolve more slowly. This was confirmed by velocity vs curvature measurements that were made on feature "A" for all the iterations shown in the Figure. The plot shown in Figure 6.12 fits a straight line remarkably well, indicating that the curvature measurement algorithm is working well and also confirming the curvature driven motion that is seen in the simulations.

However, there is one very significant difference between the simulations and the experiments. In the experiments (Figure 6.8), a pinching-off process can be seen in the tracings obtained at later times. This occurred when opposite ends of the disclination loop

became attracted to each other. This is similar to the effect seen in electrostatics where oppositely charged parallel wires will attract. The pinch-off process in this particular loop led to the creation of a sharp cusp on the original defect which evolved very rapidly presumably due to the high curvature in that region. This process also left behind a very small elliptical loop which shrank rapidly before it disappeared. The pinch-off did not occur in the simulations (refer to Figure 6.11). If one simulates a plane curve with the contour of the loop in Figure 6.80, pinch-off will not occur either. Instead the regions of the curve that are very close together will actually move outward since their centers of curvature are in the direction opposite the center of gravity of the curve. These regions will not move inward until the entire curve becomes convex everywhere. This confirms that loop pinch-off is certainly not a local property.

It is also possible that drag forces acting over a long period of time (i.e. 20-30 minutes) could be playing a role as well. At early times during shear relaxation when the local curvature tends to be high, the effects of curvature dominate loop motion. At late times when the high curvature regions have been eliminated, the motion is dominated by forces of attraction between opposite loop segments and also presumably by drag forces acting on the system.

#### 6.4.3 Curvature Motion in Liquid Crystals

Curvature motion studies in both small molecules and polymers were made using the procedures described in the experimental section of this chapter. Data recording was made with a CCD camera attached to a VCR so that experiments could be recorded over long time periods (up to 1 hour). Individual frames were selected and digitized at a later date. Analysis was performed only on disclination loops that were in full view at all times so that the entire contour could be analyzed. In addition loops were analyzed only if they were not tilted and were not close to bounding surfaces or impurities that could pin them or affect their motion.

A series of loops in the liquid crystal 8CB were digitized and compiled into a single plot that is shown in Figure 6.13. The time between each image is about one second. The first two images clearly illustrate that the high curvature regions evolve much more rapidly

than the low curvature regions do. Some lateral shifting is evident, but at least from a visual comparison it appears that the high curvature regions are not affected as much. A plot of velocity vs curvature was prepared from measurements made on the regions indicated by arrows in the figure. A plot of velocity of curvature is shown in Figure 6.14. Different symbols are used to plot values for low, medium and high curvature ranges. The results seem to follow a straight line only when within each individual range. Over the entire range of the data ( $2.8 \times 10^{-4}$  to  $0.8$  1/microns) the plot has a much different form. It appears as if the plot follows a power law with an exponent around 0.5. The most significant manifestation is in the levelling off that occurs in the high curvature region. Curvatures that are extremely high (around sharp points for example) can not move with ever increasing velocities. In theory, (from a mathematical point of view) an infinitely sharp point should have an infinite velocity, but this violates the basic laws of physics. In reality, there should be a point at which the drag forces due to such things as viscosity and molecular diffusion begin to overcome the curvature driving forces that are generating motion in the opposite direction.

Measurements of velocity vs curvature were also made on the polymer DHMS-7,9. A series of digitized curves (made from the data of Figure 6.8) used for this purpose are shown in Figure 6.15a. It is apparent that lateral shifting is occurring in addition to a small amount of rotation. This would make it difficult to obtain accurate results with the curvature measurement algorithm. However the tracings in the figure do indicate at least visually that curvature driven motion is taking place. The high curvature regions which appear as a series of oscillations in the disclination contour gradually become damped out. It can also be seen very clearly that the individual segments of the curve are moving towards their centers of curvature. The decreasing of the separation distance as a function of time between the curves also shows that the velocity decreases as the curvature becomes smaller. When the curves are shifted laterally and rotated slightly they can be more or less superimposed to eliminate a slight amount of the original mismatch. The resulting tracing is shown in Figure 6.15b. For the purpose of comparison with the small molecule system, a plot of velocity vs curvature was made for DHMS-7,9. The result is shown in Figure 6.16. There is a significant amount of scatter in the data, leading to ambiguous results for the relationship between velocity and curvature. However, it was encouraging that the



measured velocities were much lower for curvatures of the same magnitude that were seen in the small molecule system. This is a result of the different viscosities of the materials. While DHMS-7,9 is being studied at a much higher temperature, its viscosity is also much higher than it is for 8CB which means that drag forces should impede the motion of disclination loops in the former much more than they would for the latter. Even though it was not possible to determine the speed function of DHMS-7,9 accurately, the good agreement between the experimental results and the theoretical calculations for contour changes indicate that curvature is playing an important role in the disclination loop motion.

It is also interesting to note that disclination loops in DHMS-7,9 are consistently more complex than in the small molecule 8CB. The former almost always contains loop structures that each have several regions with large curvatures. This is manifest as wave-like oscillations along the contour of the loop. These features were never seen in 8CB. It should be noted that the defect density in DHMS-7,9 has not been measured as a function of shearing conditions, but it appeared to be high just based on a visual inspection. A high defect density makes it very likely that many coalescence and annihilation events are taking place during shear relaxation. The fact that viscosity is higher for polymers than for small molecules indicates that the disclinations in DHMS-7,9 should evolve more slowly than for 8CB. This may explain why the same loop interaction events do not lead to complex structures in 8CB. Even if multiple interactions were taking place, complex contours would evolve very rapidly. These notions are supported by the relative magnitudes of the loop velocities that were seen in the plots of velocity vs. curvature. A model for the possible origin of complex loop structures is shown in Figure 6.17. Several relatively simple loops are shown in the first schematic. These eventually coalesce and anneal to produce the final structure shown in the second illustration. The likelihood that such a model represents reality is also suggested by the experimental results on domain coalescence in static situations. This was discussed in detail in chapter 3. Large, complicated domains of nematic phase were formed from the coalescence of many smaller domains. Eventually the cusps formed upon coalescence gradually became smoother during annealing as surface tension and anchoring conditions acted on the domains.

## 6.5 Summary

A mathematical formalism for curvature driven motion was applied to a study of disclination loop evolution in both 8CB (a small molecule) and DHMS-7,9 (a liquid crystal polymer). Theories originally developed to study grain boundary evolution in metals were combined with level set methods of differential geometry to determine if disclination loop evolution obeyed similar physical laws. Velocity vs. curvature measurements on simulations of loop evolution yielded data that fit a straight line. This is the expected result when curvature is the only driving force. This positive result confirmed that the curvature measurement algorithm performs properly under the appropriate conditions (i.e. no lateral shift).

Simulations of loop evolution were in qualitative agreement with data taken at early times for the polymer DHMS-7,9. The regions of high curvature in both the simulations and the data evolved very rapidly and in a similar manner. The simulations began to deviate from the data at late times during the experiment (i.e. 30 minutes). This is manifested in loop pinch-off events. Loop pinch-off is accelerated by drag forces acting on the loop as well as forces of attraction between opposite ends of the loop itself. Although it was not possible to determine an exact relationship for the speed function of either DHMS-7,9 or 8CB, the velocity vs. curvature measurements did indicate that relaxation was taking place more slowly in the former. This result is to be expected when there is a large difference in the viscosities of the systems.

The mathematical analysis described in this chapter worked best for segments of disclination loops that were free from the influences of nearby defects, impurities and constraining surfaces. As discussed in the introduction to this chapter, surface anchoring and attractive forces between disclinations can influence the mobility of these defects. As is the case with metals as well, any changes in the mode of motion of a boundary will lead to deviations from the ideal (i.e. proportionality) behavior of velocity and curvature expressions.

- [1] Carel, R., Thompson, C.V., and Frost, H.J., "Computer Simulation of Strain Energy Effects vs Surface and Interface Energy Effects on Grain Growth in Thin Films", *Acta. Mater.*, **44**(6), 2479-2494, 1996
- [2] Sethian, J.A., Level Set Methods: Evolving Interfaces in Geometry, Fluid Mechanics, Computer Vision, and Materials Science, Cambridge University Press, Cambridge, 1996.
- [3] Chorin, A.J., *Computat. Phys.*, **57**, 472, 1985
- [4] Langer, J.S., *Rev. Mod. Phys.*, **52**, 1, 1980
- [5] Langer, J.S. and Muller-Krumhaar, H., "Mode Selection in a Dendrite-Like Non-linear System", *Phys. Rev. A*, **27**, 499-514, 1983
- [6] Harker, D. and Parker, E.R., "Grain, Phases, and Interfaces", *Transactions, American Society for Metals*, **34**, 156, 1945
- [7] Smith, C.S., "Grains, Phases, and Interfaces", *Transactions, American Institute of Mining and Metallurgical Engineers*, **175**, 15, 1948
- [8] Burke, J.E., "Some Factors Affecting the Rate of Grain Growth in Metals", *Transactions, American Institute of Mining and Metallurgical Engineers*, **180**, 73, 1949
- [9] Beck, P.A., "Interface Migration in Recrystallization", *Metal Interfaces, 33rd National Metal Congress and Exposition*, Oct. 1951, p. 208-247.
- [10] Smith, C.S., in *Metal Interfaces, American Society for Testing Materials*, 56, 1952
- [11] Smoluchowski, R., "Theory of Grain Boundary Motion", *Phys. Rev.*, **83**, 69, 1951
- [12] Turnbull, D., "Theory of Grain Boundary Migration Rates", *J. Metals*, **3**, 661, 1951
- [13] Sutton, A.P. and Balluffi, R.W., Interfaces in Crystalline Materials, Oxford Science Publications, Oxford, 1995
- [14] Cahn, J.W., "The Impurity Drag Effect in Grain Boundary Motion", *Acta Metall.*, **10**, 789, 1962
- [15] Lucke, K. and Stuwe, H.P., *Acta Metall.*, **19**, 1087, 1971

- [16] Hillert M. and Sundman, B., "A Treatment of the Solute Drag on Moving Grain Boundaries and Phase Interfaces in Binary Alloys", *Acta Metall.*, **24**, 731, 1976
- [17] Westengen, H. and Ryum, N., "On the Effect of Solute Atoms on Grain Boundary Migration", *Phil. Mag. A.*, **38**, 279, 1978
- [18] Mullins, W.W., *J. Appl. Phys.*, **27**, 900, 1956
- [19] Grayson, M., "The Heat Equation Shrinks Embedded Plane Curves to Round Points", *J. Diff. Geom.*, **26**, 285, 1987
- [20] Hirth, J.P. and Lothe, J., Theory of Dislocations, McGraw Hill, New York, 1968
- [21] Hirth, J.P., Jossang, T., and Lothe, J., *J. Appl. Phys.*, **37**, 100, 1966
- [22] Herring, C., in Kingston, W.E. (ed.), The Physics of Powder Metallurgy, McGraw-Hill, New York, 1951
- [23] Frank, F.C., in Gjostein, N.A. and Robertson, W.D.(eds.), Metal Surfaces, American Society of Metals, Cleveland, Ohio, 1, 1963
- [24] Mullins, W.W., in *ibid.*, p. 17
- [25] deGennes, P.G., The Physics of Liquid Crystals, Clarendon Press, Oxford, 1975
- [26] Osher, R. and Sethian, J.A., "Fronts Propagating with Curvature-Dependent Speed: Algorithms Based on Hamilton-Jacobi Formulations", *J. Computat. Phys.*, **79**, 12-49, 1988
- [27] Brakke, K.A., The Surface Evolver Manual, 1994
- [28] Pargellis, A.N., Mendez, J., Srinivasarao, M. and Yurke, B., "Dynamics of Monopole Annihilation by Type=1/2 Strings in a Nematic Liquid Crystal", Physical Review E., **53**, No. 1, 1996
- [29] Chuang, I., Durrer, R., Turok, N. and Yurke, B., "Cosmology in the Laboratory: Defect Dynamics in Liquid Crystals", *Science*, **251**, 1339, 1991
- [30] Bowick, M.J., Chandar, L., Schiff, E.A. and Srivastava, A.M., "The Cosmological Kibble Mechanism in the Laboratory: String Formation in Liquid Crystals", *Science*, **263**, 943, 1994
- [31] Ding, Ding-Kuo, Ph.D. Thesis, Massachusetts Institute of Technology, 1994

[32] Mather, P., Grizzuti, N., Heffner, G., Ricker, M., Rochefort, W.E., Seitz, M., Schmidt, H-W and Pearson, D.S., "Synthesis and Characterization of a Semiflexible Liquid Crystalline Polyester with a Broad Nematic Region", *Liq. Cryst.*, 1995

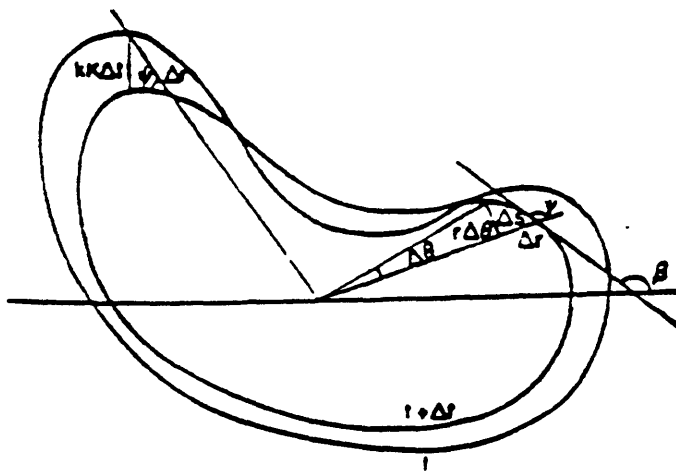
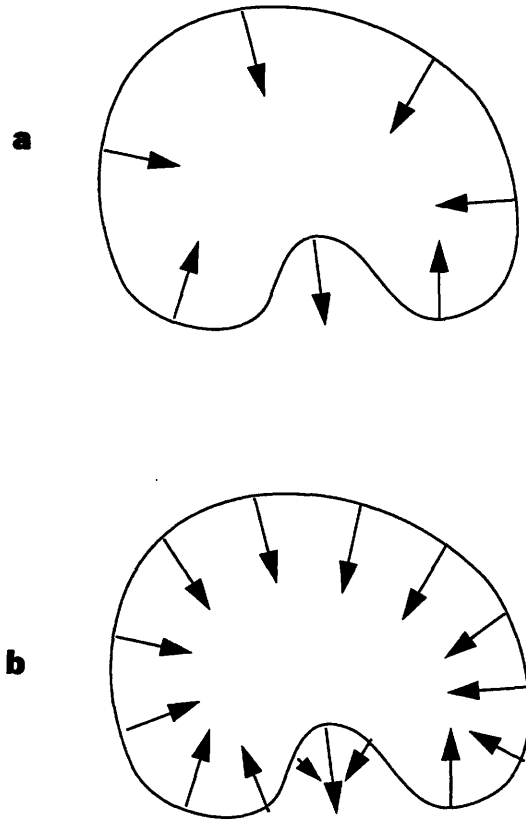
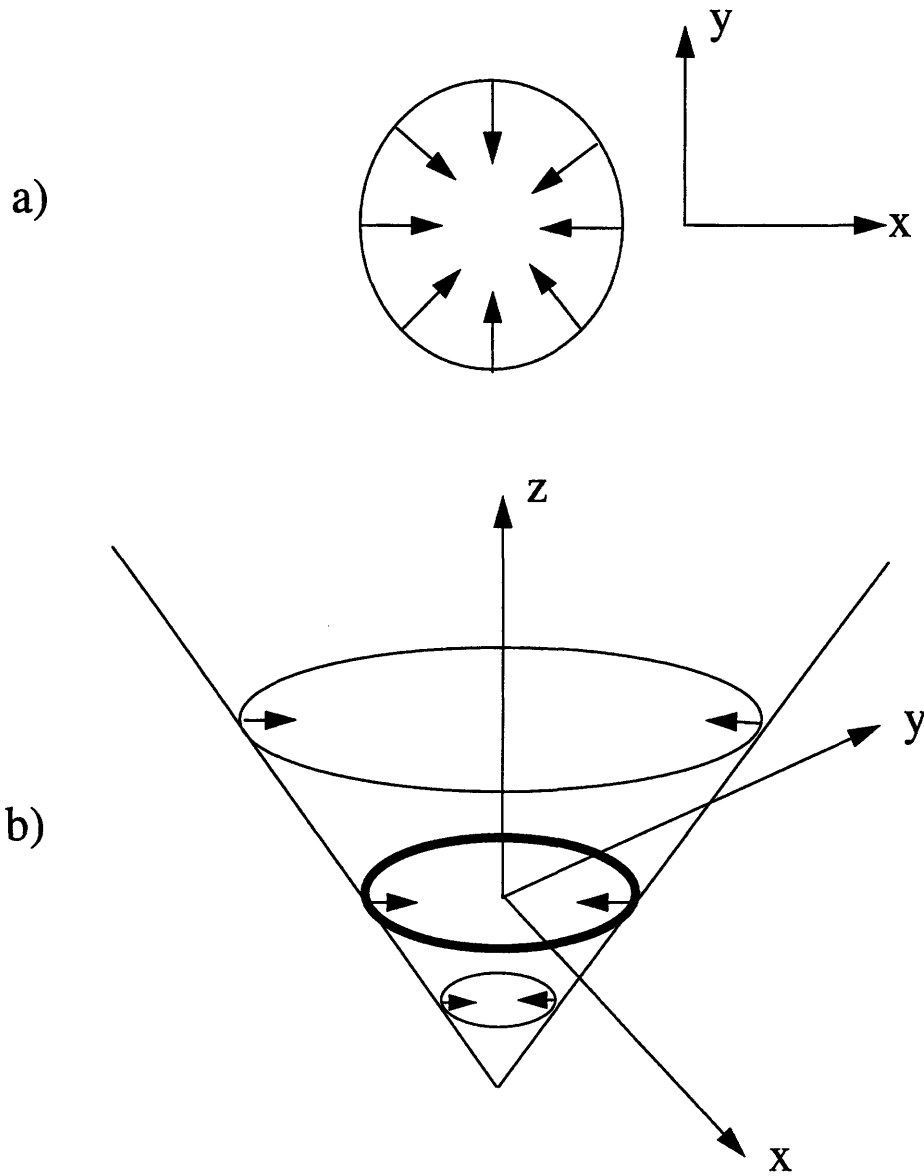


FIG. 1. Right section illustrates definitions; left section derivation of the curvature rule.

Figure 6.1: A schematic depicting the geometry used for the basis of the early curvature driven boundary motion algorithms (after R. Courant).



**Figure 6.2:** a) A schematic depicting a curve with a low marker density. b) An identical curve with a high marker density. The arrows indicate the direction of motion of the curve segment at that location. The local motion is toward the center of curvature. A higher marker density would yield a more accurate solution as can be seen pictorially in the two schematics.



**Figure 6.3:** A schematic depicting the basic elements of the level set algorithm. a) This schematic shows a view of a two-dimensional circular surface that lies in the  $xy$  plane. The arrows indicate the direction of motion of the curves. b) This schematic depicts the cone-shaped level set function. The moving front (schematic a) is the intersection of the surface and the  $xy$  plane. Other slices of the level set function taken at different heights along the  $z$  axis represent the front at different times.



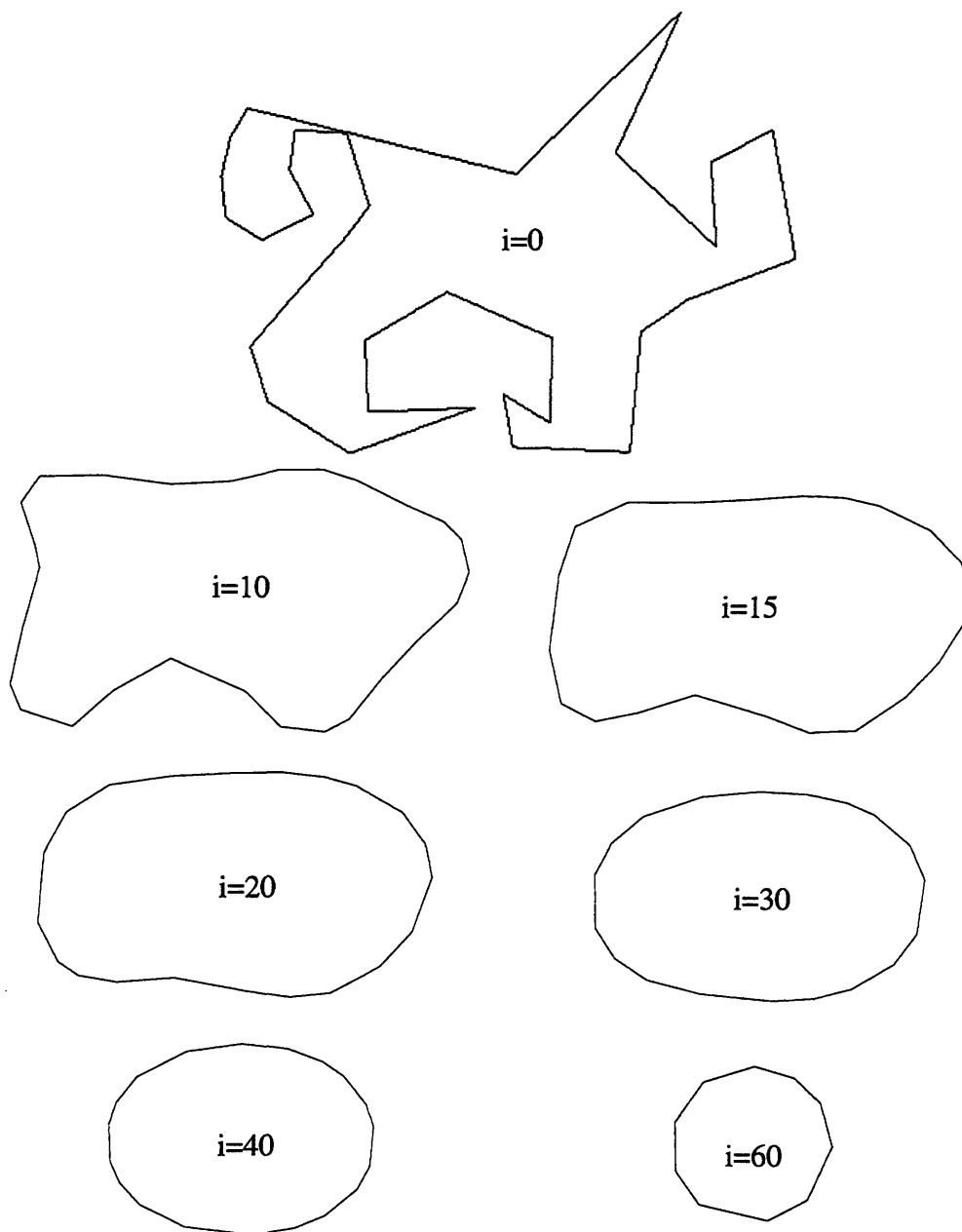
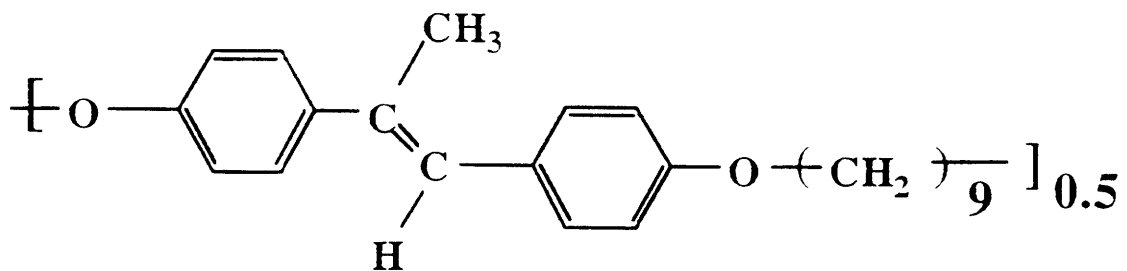
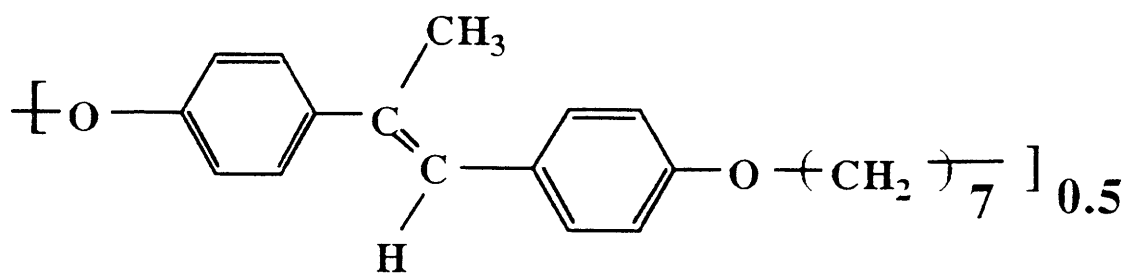
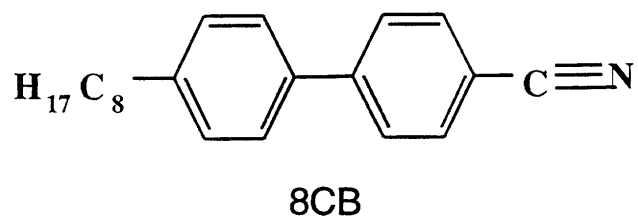


**Figure 6.4:** A series of two dimensional simulations produced with Surface Evolver that depict a complex curve evolving under its curvature. The first simulation ( $i=0$  iterations) depicts the original curve. Initially, the high curvature regions (i.e. the sharp points) become smoother ( $i=10$  iterations). In subsequent simulations the curve evolves first to an elliptical shape and then to a circular one before it disappears (at  $i=70$  iterations).



DHMS-7,9

**Figure 6.5:** The chemical structure of 8CB and DHMS-7,9

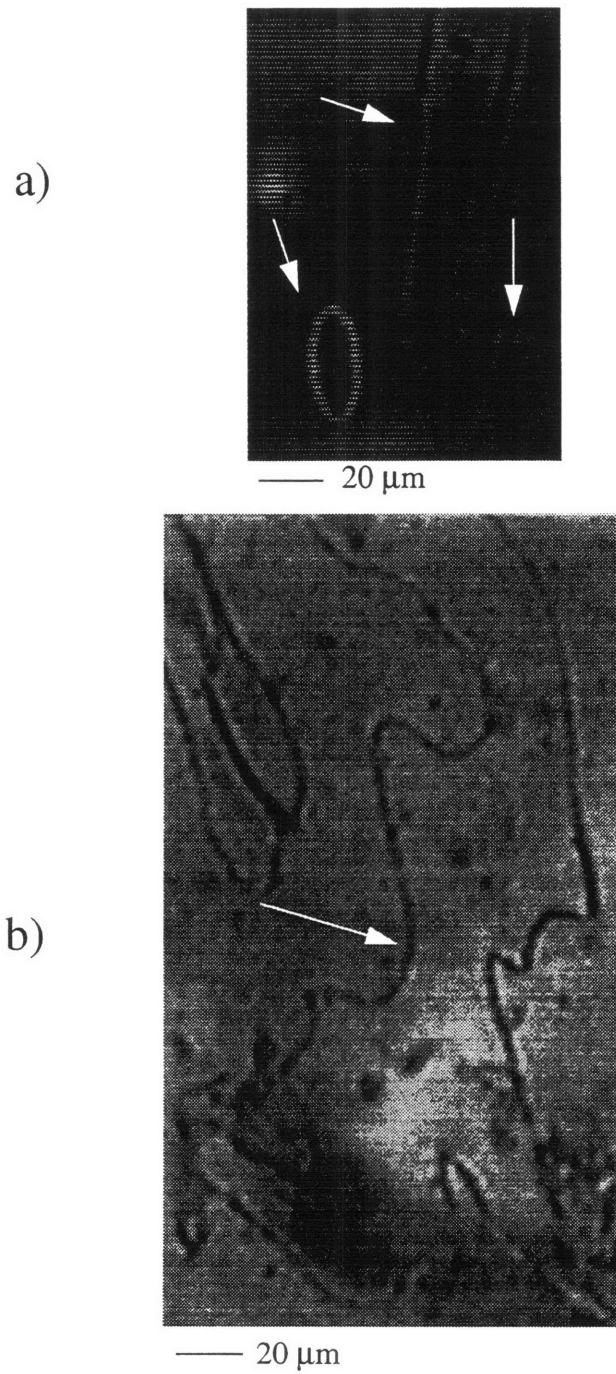
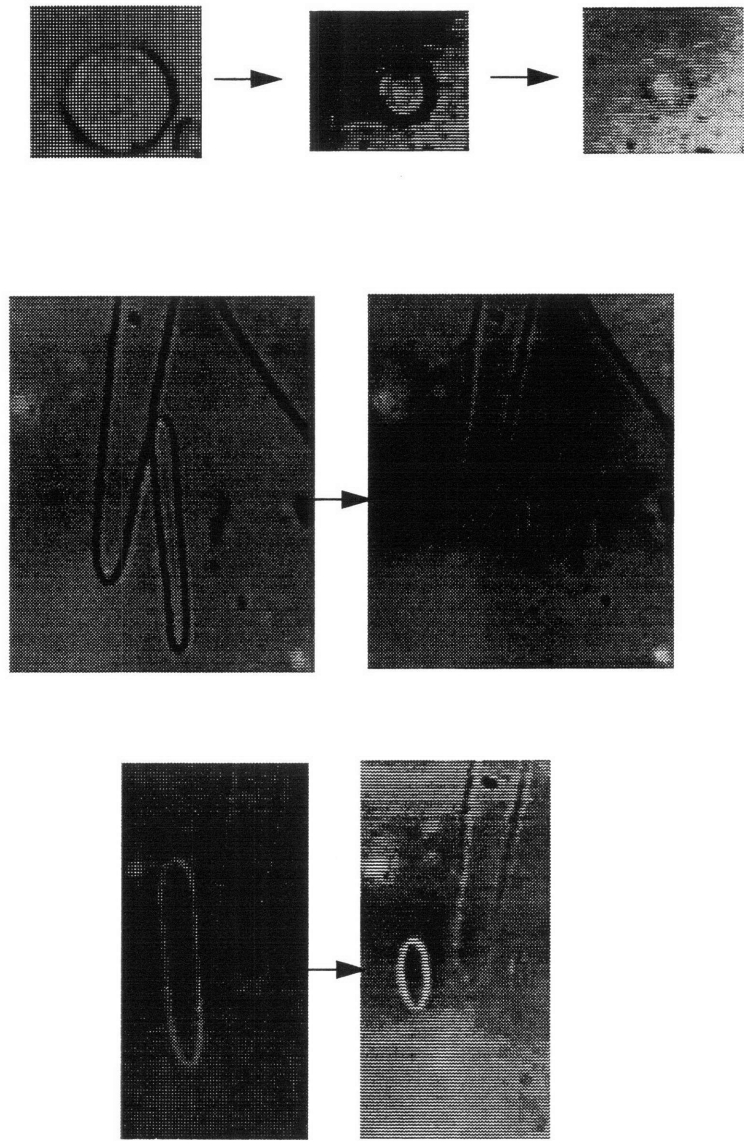


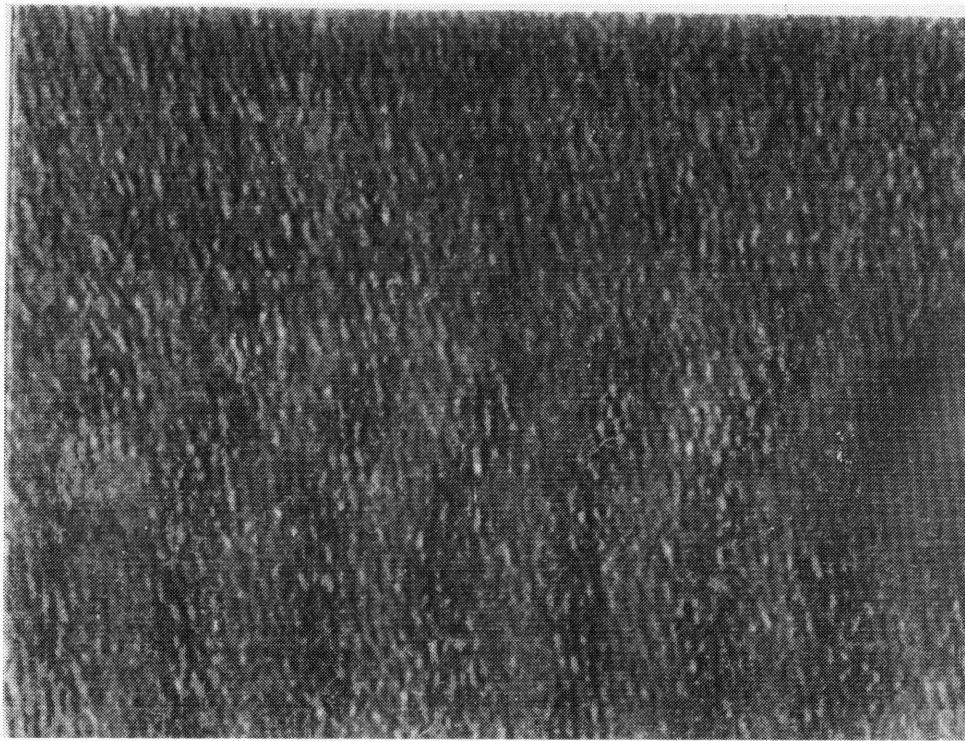
**Figure 6.6:** a) Examples of typical disclination loops in 8CB. Three disclination loops are identified by the arrows. b) An example of a typical disclination loop in the polymer DHMS-7,9. The arrow marks the location of the loop that is analyzed in this chapter. Note that the disclination loops in the polymer are much more irregular and jagged

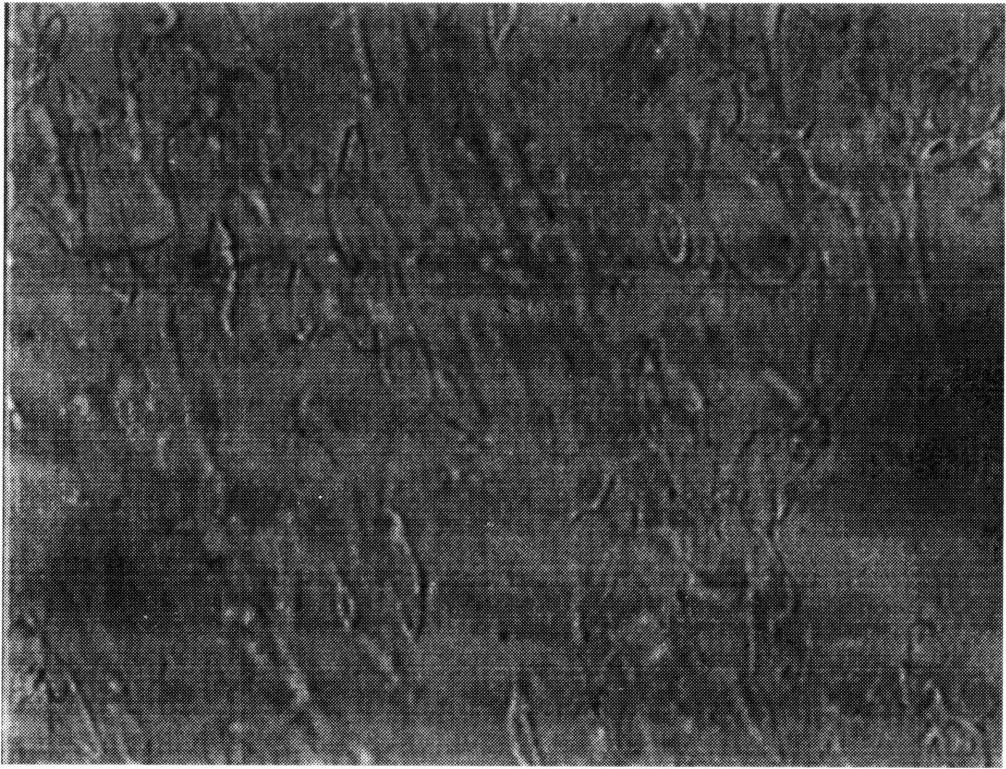


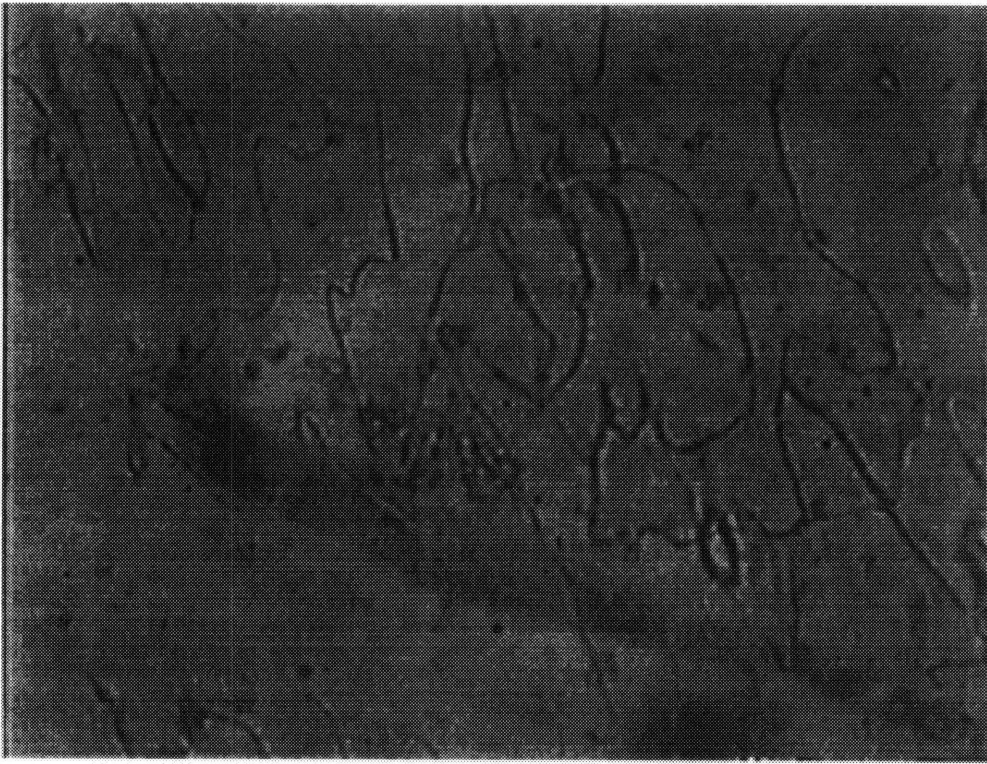
20  $\mu\text{m}$

**Figure 6.7:** Several examples depicting disclination loop evolution in 8CB

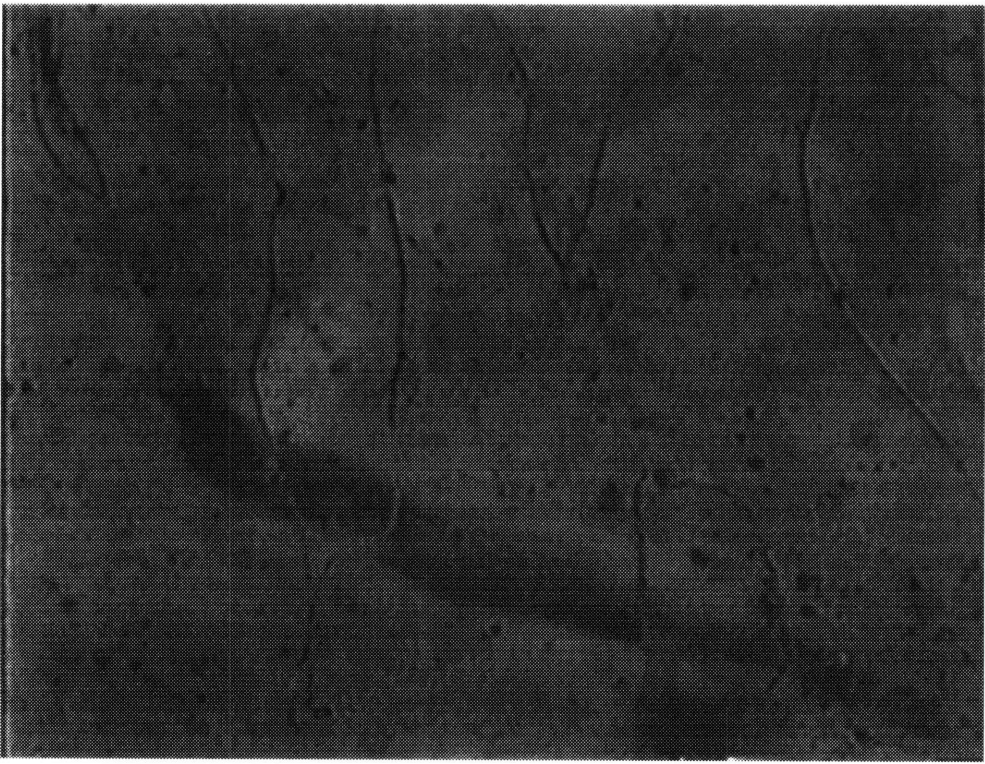
**Figure 6.8:** A series of images depicting disclination loop evolution in the polymer DHMS-7,9. (see the Following Pages). The first image shows the sample while it is being sheared between two coverslips. The disclination density is high enough so that no individual defect contours can be traced. After cessation of shear, the sample relaxes and the texture coarsens. This is evidence by a dramatic decrease in the disclination density with time. The second image shows the sample 30 seconds after cessation of shear. At this point, small segments of the disclination contours can be traced. After an additional 30 seconds (image 3), several large and irregularly shaped disclinations can be seen. Region “A” contains some high curvature segments while region “B” contains more gently curved segments. These two regions will be used for a subsequent mathematical analysis. The fourth image shows the system after about 30 minutes.











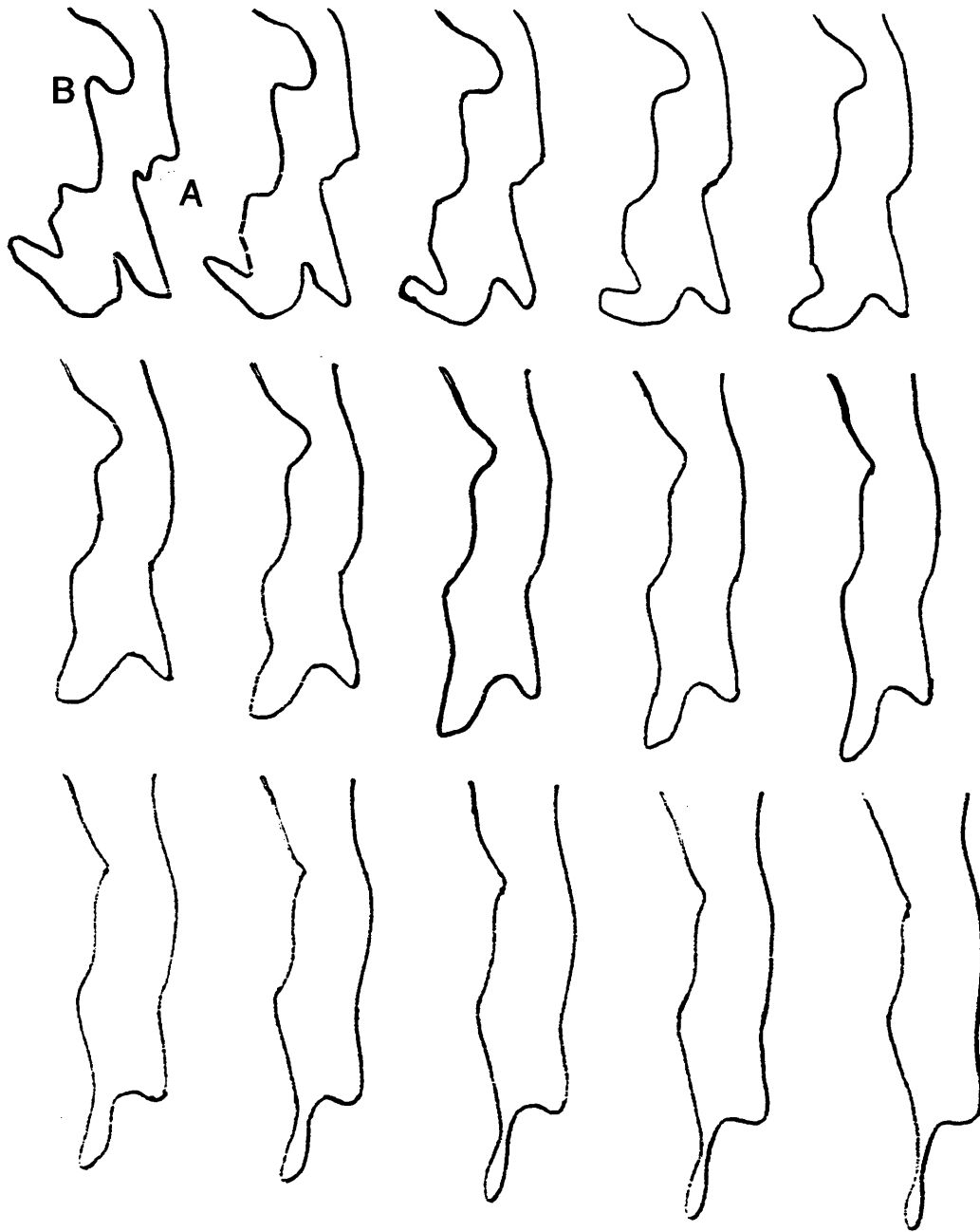


**Figure 6.8** A series of tracings made from the series of micrographs showing disclination loop evolution in DHMS-7,9. Note that at late times during the experiment, a pinch-off phenomena is observed which occurs presumably due to the effects of fluid drag and attractive forces between opposite ends of the disclination loops.

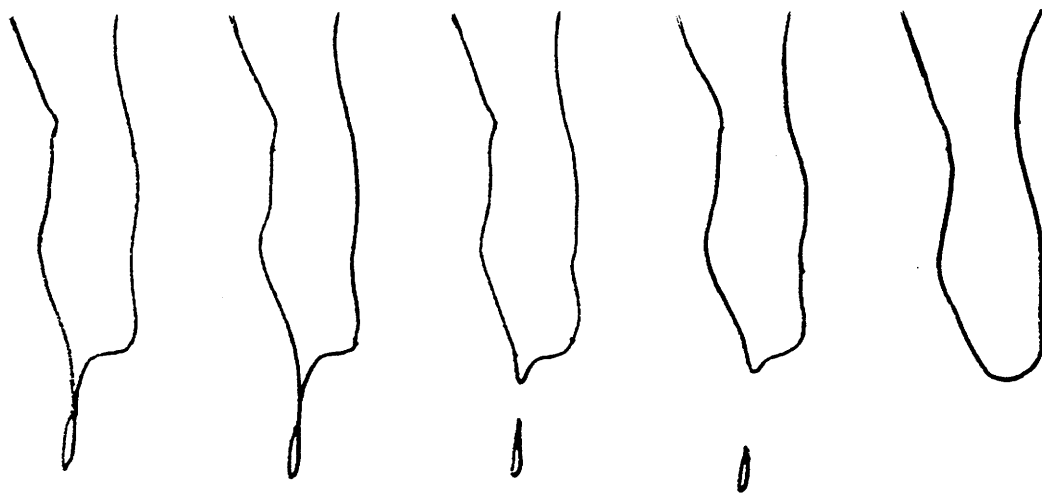


**Figure 6.8: continued**

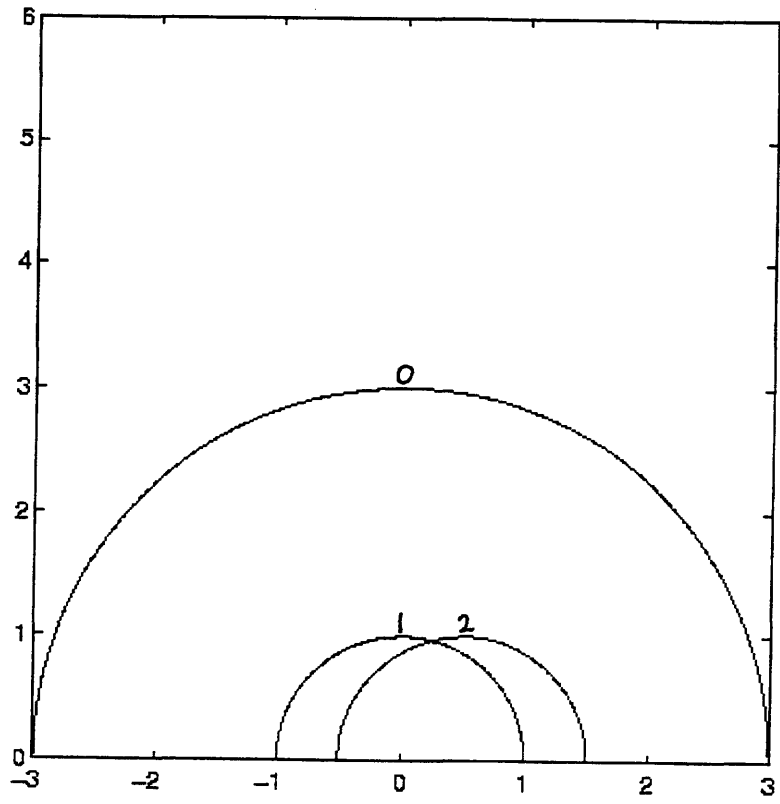


**Figure 6.9:** A schematic showing the circular contours used to test the curvature measurement algorithms. The xy coordinates of each contour was subsequently obtained using NIH-Image. The large circle represents the contour at  $t=t_0$  while the smaller circle represents the contour at a later time after it has evolved solely due to curvature forces. The second smaller circle is identical to the other except that it is shifted laterally.

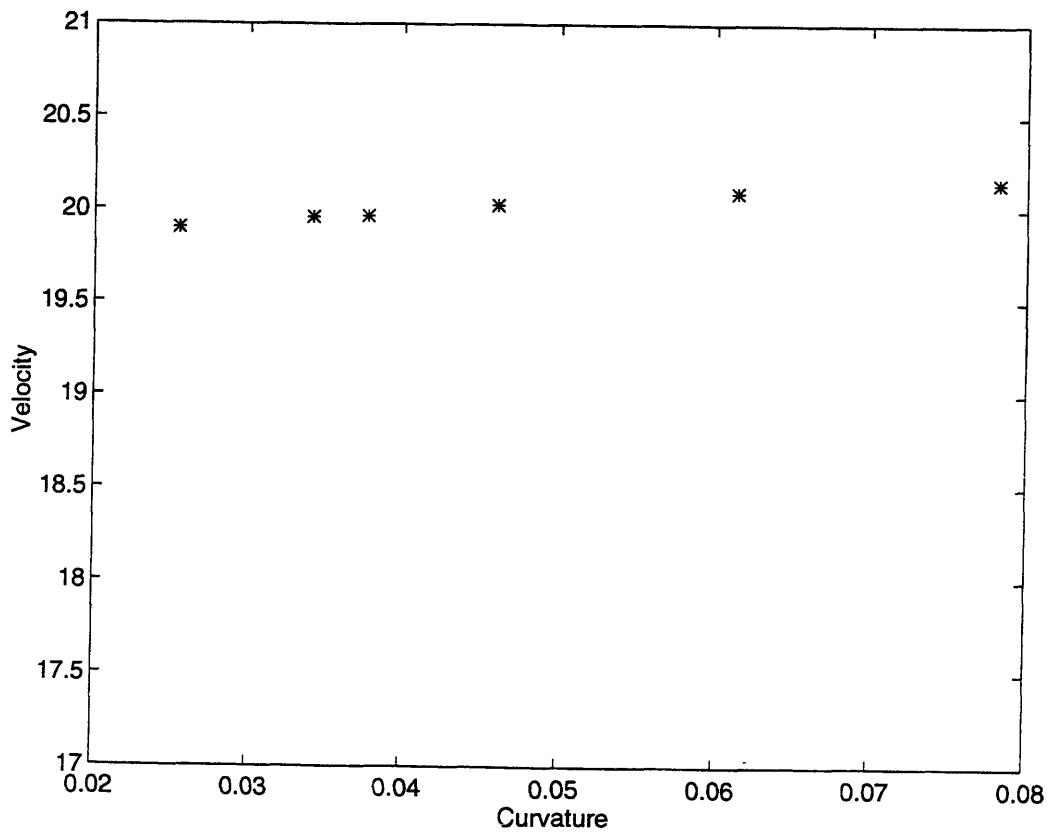


**Figure 6.10:** A plot of Velocity vs. Curvature for the contours of Figure 6.9. The data points should ideally be at the same (x,y) location since the radius of curvature of the circles does not change. The small deviation seen here is a result of the point digitization process made with NIH-Image as well as the curvature measurement algorithm itself.

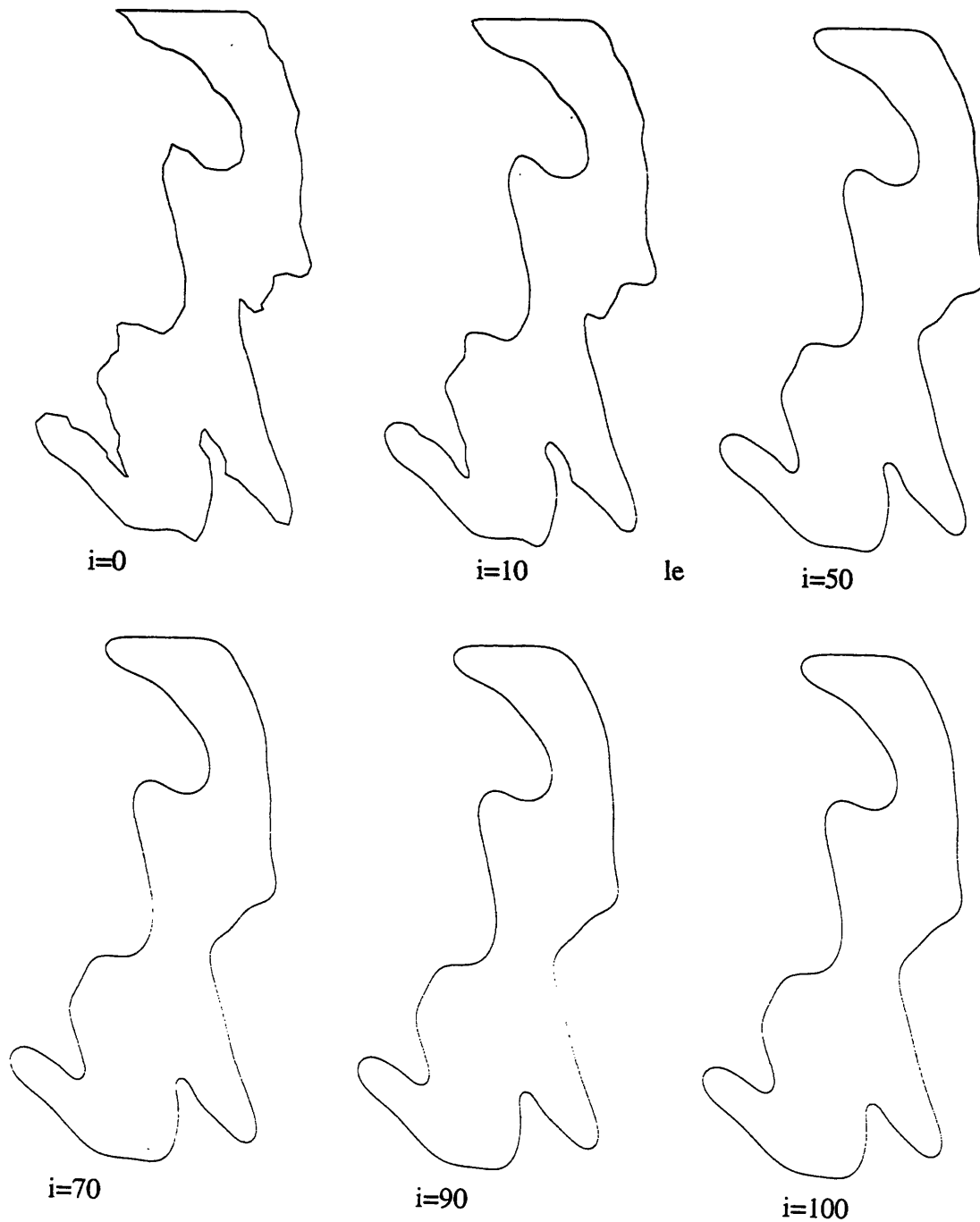


**Figure 6.11:** The first schematic represents digitized data taken from Figure 6.8c. The subsequent images are simulations of loop evolution made with the Surface Evolver program. The label “i” refers to the number of iterations of the program.

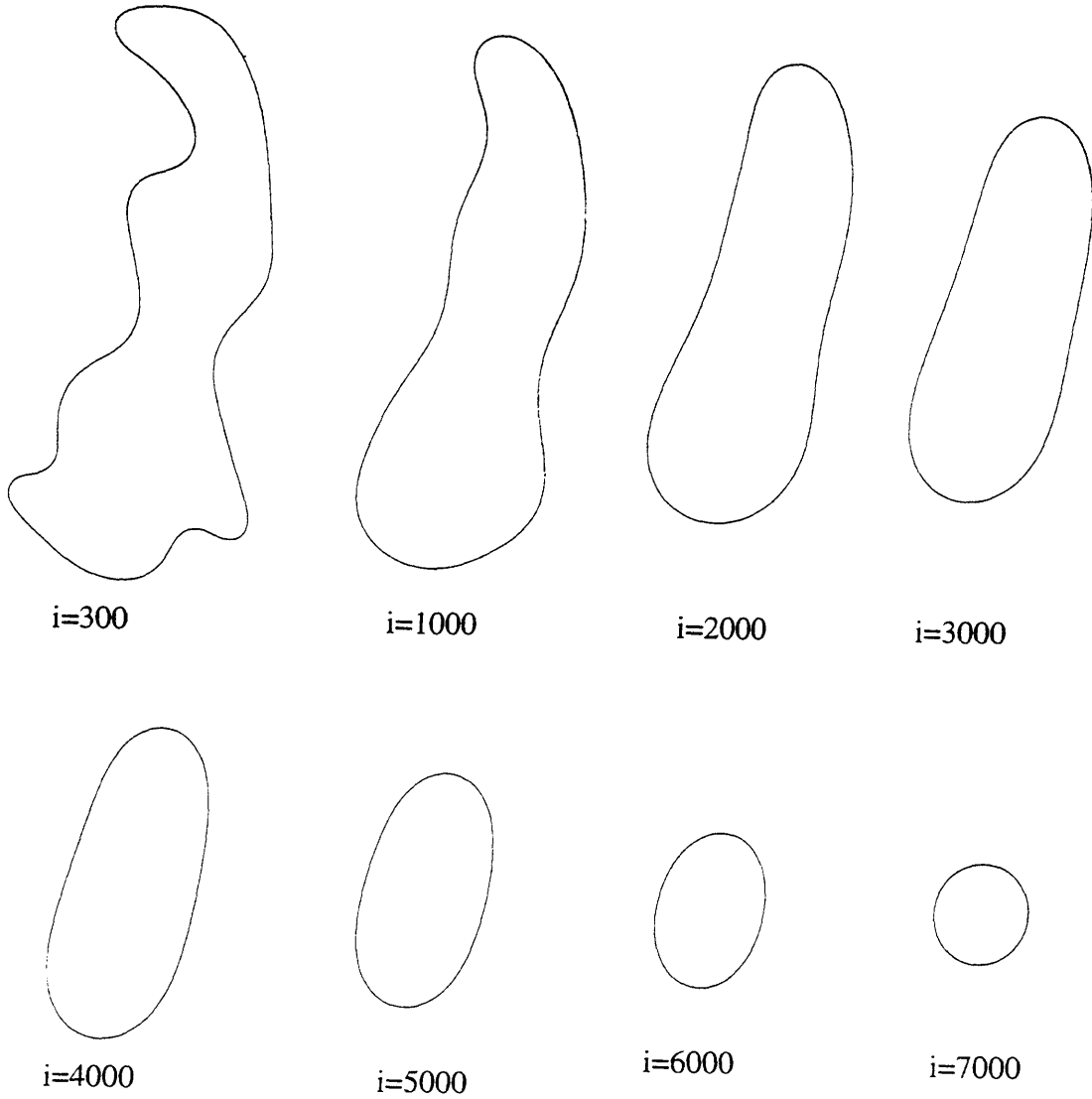


**Figure 6.11: continued.**

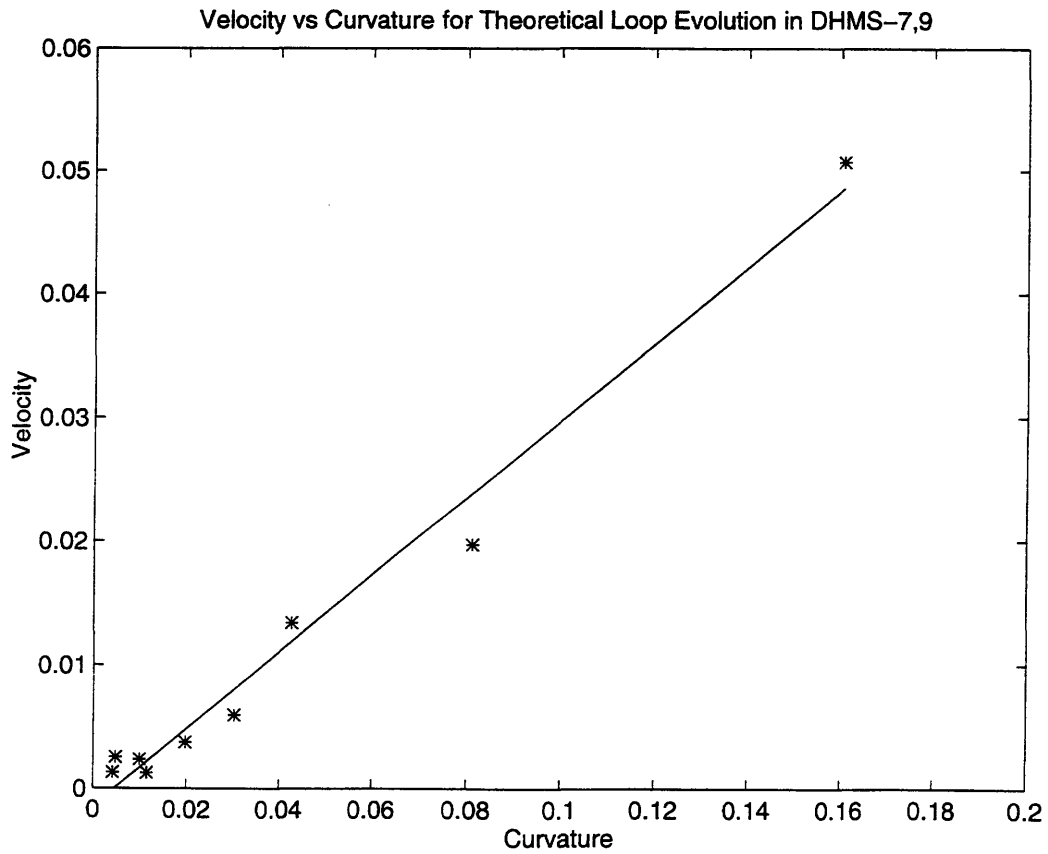


**Figure 6.12:** A plot of velocity vs. curvature for the theoretical loop evolution shown in Figure 6.11. The data fits a straight line remarkably well, indicating that the curvature measurement algorithm can yield results that are expected from mathematical theories.



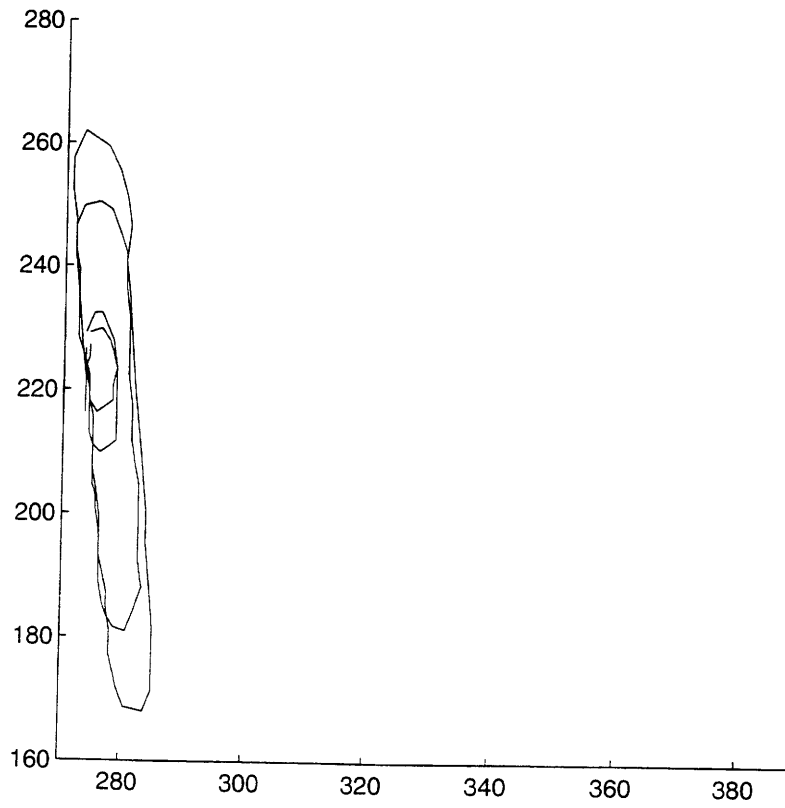


**Figure 6.13:** The above schematic shows a loop evolution process in 8CB. The data was digitized with NIH-Image. Some lateral shift can be seen in the image. However it is clear that the high curvature regions (i.e. the ends of the ellipses) are evolving more rapidly than the low curvature regions.

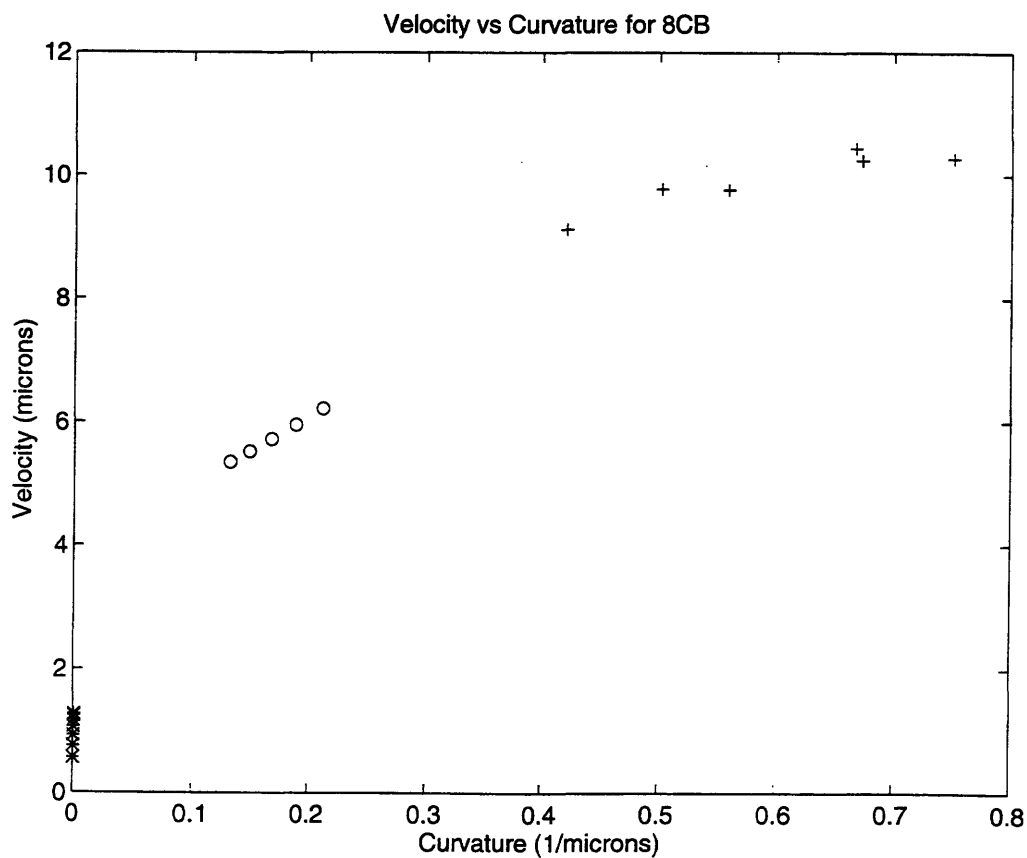


**Figure 6.14:** A plot of velocity vs. curvature for 8CB based on the digitized images in Figure 6.13. The data does not fit a straight line plot. Rather, a leveling-off occurs in the high curvature regime. This is most likely a result of fluid drag and possibly even molecular diffusion that can oppose the direction of motion of the curvature driving force..

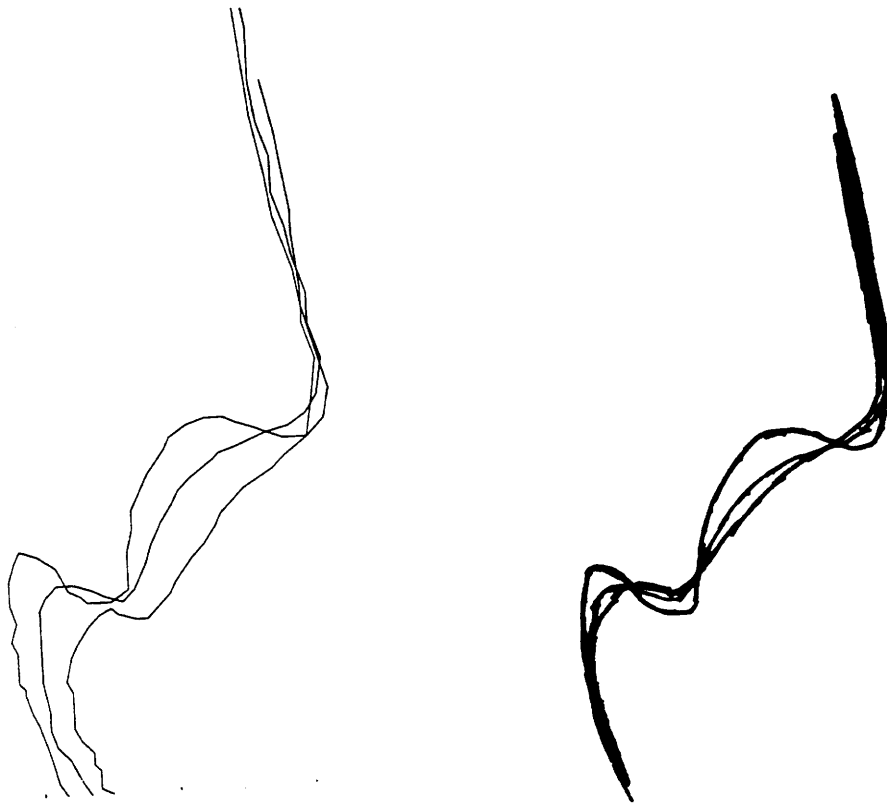


**Figure 6.15:** a) A series of digitized loop contours for the polymer DHMS-7,9. Some lateral shift as well as rotation is evident. b) The curves overlay somewhat when shifted and rotated.

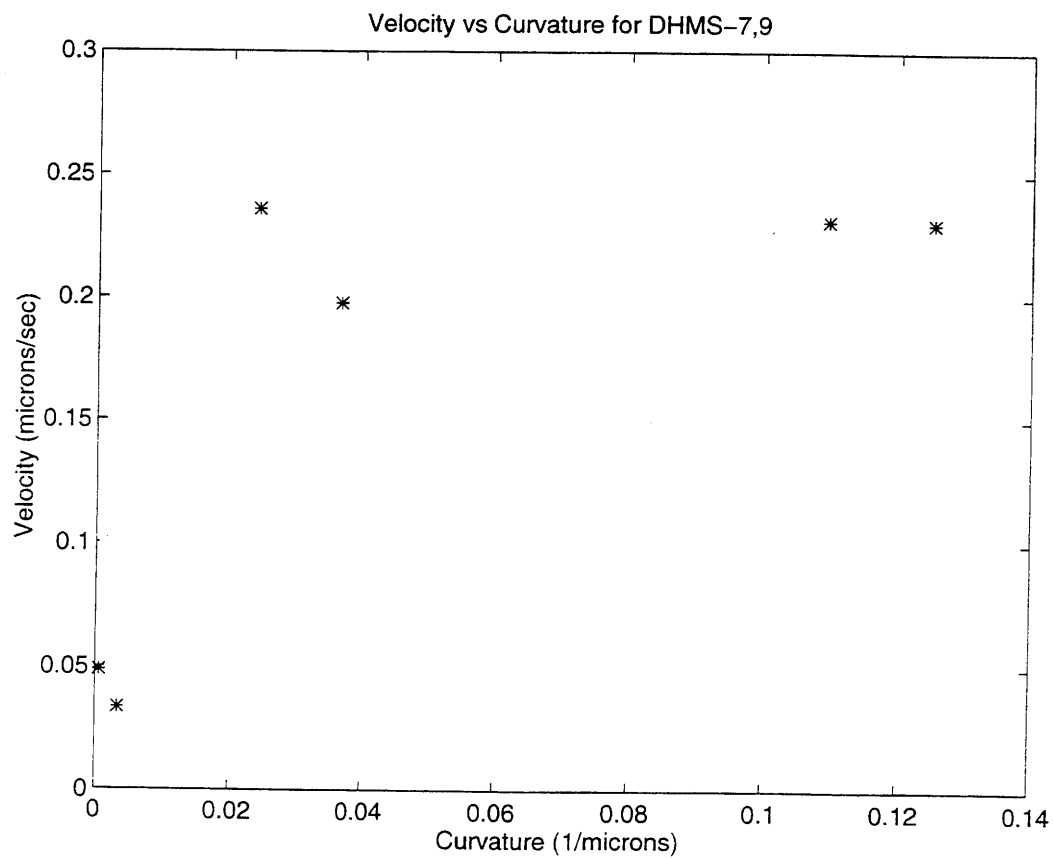


**Figure 6.16:** A plot of velocity vs curvature for DHMS-7,9 based on the digitized data shown in Figure 5.15. A significant amount of scatter can be seen even for a small number of data points. This is most likely a result of the lateral shifting that occurred.

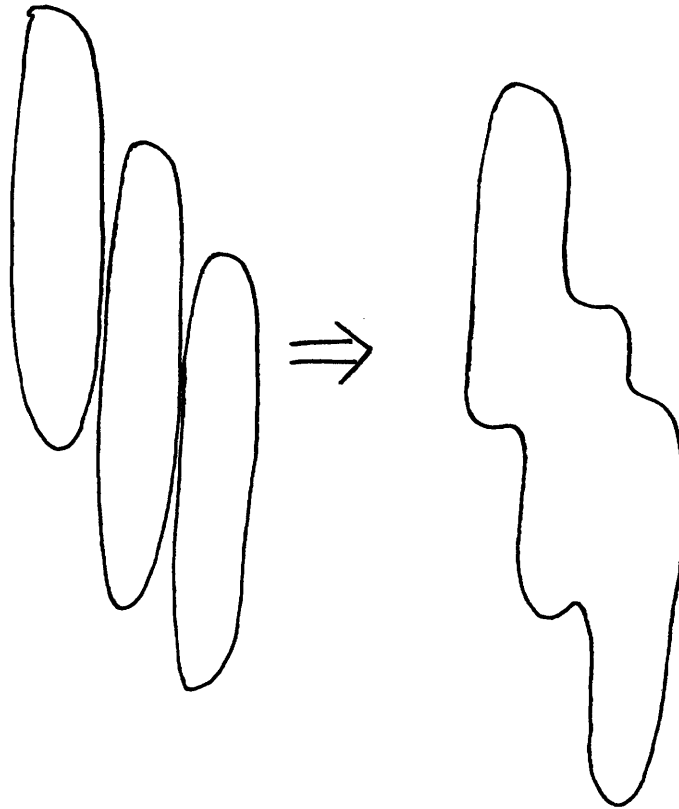


**Figure 6.17:** A series of schematics depicting how loop coalescence could lead to the formation of new disclination loops with many regions of high curvature along their contours.

# Chapter 7

## Summary

### 7.1 List of Conclusions

#### 7.1.1 Defect Generation Mechanisms

To my knowledge this is the first time that the nucleation and growth of nematic droplets has been examined in detail with an emphasize on the underlying mechanisms for defect formation. The following conclusions were made from this part of the study:

1) Defects of the type  $s=+1$ ,  $c=\pi/2$  formed in the polymer DHMS-7,9 as the growing nematic domains responded to the anchoring conditions between the nematic and isotropic phases.

2) Formation of defects with  $s=-1/2$  was required when two  $s=+1$  defects coalesced and formed a new individual domain. A competition between anchoring conditions and the force of repulsion between the  $s=+1$  defects made it necessary to create the  $s=-1/2$  defects at the boundary of a domain in order to avoid violating the anchoring conditions.

3) Defects with  $s=-1$  were created as a result of domain impingement. This particular defect only occurred at later stages of nucleation and growth after many large domains and coalesced.

4) Defect annihilation events lead to formation of a single  $s=+1$  approximately 80 percent of the time. This is indicative of the fact that the polymer prefers bend distortions more than it does splay.

#### 7.1.2 Magnetic Field Effects

This is the first time that a generalized mathematical approach has been used to study the director field distribution in the vicinity of a defect wall. A numerical solution to the nonlinear partial differential equation describing the director field is solved for arbitrary field angle and elastic anisotropy. The results of the mathematical methods for determin-

ing the elastic anisotropy were in excellent agreement with experiments done by others using different methods.

### 7.1.3 Curvature Driven Motion of Disclination Loops

This is the first time that curvature motion in liquid crystal polymers has been examined in detail both from a mathematical and experimental perspective. Curvature plays an important role in loop evolution especially at early times during shear relaxation. At late times however, the properties of the fluid (viscosity, drag forces etc.) and loop-loop interactions cause the motion to deviate from the ideal case where curvature is directly proportional to the velocity. The results of this part of the thesis will lend some insight into how to model the effects that fluids can have on defect structure and behavior. This in turn may lead to a greater understanding of structure/properties/processing relationships.

## 7.2 Thesis Research

The principal contribution of this thesis is the development of the mechanisms by which the various types of point defects are created in a liquid crystal system. The nucleation and growth process of nematic domains in an isotropic matrix was followed in real time using videomicroscopy. The results showed that the four main types of defects ( $s=+1$ ,  $s=-1$ ,  $s=+1/2$  and  $s=-1/2$ ) were created during different stages of nucleation and growth. In addition each of these was created by different mechanisms. The effects of anchoring between the nematic and isotropic phase had a strong influence on the defect morphology. The homogeneous anchoring between these phases was responsible for the formation of  $s=+1$  defects during initial stages of nucleation and growth. The same anchoring conditions imposed at later times during the process resulted in the formation of defects of negative strength when domains containing defects of positive strength coalesced. Higher resolution images of the director field distribution patterns were studied using sequential quenching in conjunction with a solidification-induced banding technique. A statistical analysis of the defect types was used to determine that the polymer DHMS-7,9 had an elastic anisotropy greater than zero, indicating that bend distortions are more favorable than splay for this system.

The subsequent effects of both magnetic and flow fields were also studied. Mathematical techniques were used to predict the effects that both of these external fields would have on the evolution of the resulting defect textures. Magnetic fields created defect walls which had a structure that was highly dependent on the elastic anisotropy. Computer analysis was used to extract a value of the elastic anisotropy of the liquid crystal TPP5. The elastic anisotropy of 0.5 extracted from the micrograph was in agreement with the value obtained from other types of measurements. An elastic anisotropy of 0.5 was indicative of a splay elastic constant that was three times greater than the bend elastic constant. This indicates that bend distortions are more favorable for this particular system.

A study of disclination loop evolution during shear relaxation showed that curvature is an important driving force for loop motion. At early times during the experiments, high curvature regions evolved rapidly and followed a contour evolution sequence that was very similar to computer calculations). Disagreement between theory and results became significant when disclination loops began to slow down, presumably due to drag forces and loop-loop attraction. Actual plots of velocity vs curvature for several test problems showed that the curvature measurement algorithms used in this thesis can provide accurate results under the proper conditions (i.e. no lateral shift). Analysis of both small molecule and polymer systems also indicated that the algorithm is sensitive enough to be able to distinguish between the motion of 8CB vs. DHMS-7,9. The latter has a higher viscosity and as a result had lower values for velocity vs curvature. Even though it was not possible to determine exactly what type of relationship existed between velocity and curvature, the good agreement between data and experiment at early times suggested that this area is ripe for further research.

### **7.3 Suggestions for Future Work**

The idea that coalescence of domains can lead to defect production is not unique to liquid crystals. The mechanisms discussed in chapter three have counterparts in several areas of condensed matter physics, including bubble formation in Higgs phases and vortex produc-



tion in superfluid helium. In fact, the so-called vortex tangles in the latter bear a strong resemblance to the threaded texture in liquid crystals subjected to shearing flows. The mechanism by which the latter is created is still not well understood. However an insight into these mechanisms may be gained from examining superfluidity in more detail.

The basic mechanisms behind vortex production are described in *Physics Today*, October, 1987. The section on computer modelling work is particularly interesting because it shows how a well ordered vortex tangle is affected by changes in the flow of the superfluid. What starts off as a series of perfectly circular vortices, arranged on a cube (one vortex per face) gradually deforms as the superfluid mixes with normal fluid. Over time the original structure is completely deformed and what is left is a dense network of vortices that have a string-like appearance. As the mixing of the superfluid and normal fluid progresses the vortices become more entangled, to the point where individual contours cannot be distinguished in their entirety. The dense tangle of vortices that is found over long times seems to be a direct result of the mixing process. It is quite possible that disclination thread production in liquid crystals subjected to flow may also be modelled in a similar way.

It is currently felt that disclination production during shear flow can occur in several ways: nucleation on dust particles or impurities, at the boundary layers, or at the edges of the sample (ie the boundary between the rheometry cell and air). The mechanisms by which these occur is not well understood. What is known, however is that the magnitude of the Ericksen number seems to be related to disclination density in the form of a power law relationship. The Ericksen number, as discussed in Chapter 1, is dependent upon several materials parameters as well as the shear rate. To date no modelling work has been done to predict what the presence of various anchoring conditions, edge effects, or impurities should have on the flow behavior of disclinations in liquid crystals. A fruitful area of research would be to attempt to model this in detail and study how various flow conditions affect disclination spacing and interaction. In this work it would also be necessary to develop a description of the mechanisms by which the disclinations interact once the disclination spacing becomes low enough. The work in chapter 6 showed that level set methods of differential geometry are a useful tool for predicting the way in which disclination loop contours evolve over time during shear. However it did not address disclination

interaction from a theoretical point of view due to the problems associated with attractive forces between disclinations that were not possible to model using the present programs. If such an effect could be accounted for, the interaction and evolution of disclinations could be described in more detail and given as input to the rheological modelling work. With a knowledge of this and other parameters such as line tension, it may be possible to understand exactly what type of flow conditions and patterns lead to defect multiplication and splitting. Since defect density is thought to have a significant effect on the properties of a liquid crystal, the rheological properties should also be evaluated in the simulations.

The curvature measurement algorithms discussed in chapter 6 could also be applied to the motion of coalescing defect walls that are created by applied magnetic fields. Research conducted by Dr. Ding-Kuo Ding during his PhD thesis work showed that walls seemed to move with a velocity that was dependent on the local curvature of the wall contour although this was never proven or discussed in detail. The success of the curvature measurements in this show that the curvature analysis methods can provide accurate results that could certainly be applied to a wide range of systems.